Electronic Properties of ALD Zinc Oxide Interfaces and its Implication for Chalcopyrite Absorber Materials

vorgelegt von

Diplom-Ingenieur
Eike Janocha
aus Seesen

angefertigt am Helmholtz-Zentrum Berlin für Materialien und Energie

eingereicht an der Fakultät IV - Elektrotechnik und Informatik
der Technischen Universität Berlin
zur Erlangung des Akademischen Grades

Doktor der Ingenieurwissenschaften
Dr.-Ing.

genehmigte Dissertation

Promotionsausschuss:

Vorsitzender: Prof. Dr. Wolfgang Heinrich
Gutachter: Prof. Dr. Bernd Rech
Gutachter: Prof. Dr. Christian Pettenkofer
Gutachter: Prof. Dr. Wolfgang Jäger

Tag der wissenschaftlichen Aussprache: 05.03.2012

Berlin 2012

D 83

Abstract

Electronic Properties of ALD Zinc Oxide and its Implication for Chalcopyrite Absorber Materials

Eike Janocha

With its capacity as a transparent conductive oxide (TCO), zinc oxide (ZnO) is currently used in a wide field of applications, for instance as the front contact in thin-film solar cells. Nowadays, in thin-film chalcopyrite solar cells the heterojunction with the p-doped chalcopyrite absorber is formed by a thin n-type cadmium sulfide buffer layer. Due to environmental considerations and due to disadvantages in the deposition process, it is desirable to replace the cadmium sulfide layer by an alternative Cd-free buffer material. To understand the processes at the interface in detail, well-defined single-crystalline chalcopyrite absorber films in the technologically relevant (112) orientation are used. Onto these absorber layers, ZnO was then grown onto the layers by atomic layer deposition (ALD). Due to its unique self-limiting growth mode, ALD allows a controlled deposition of single ZnO monolayers. In this work a UHV-compatible ALD deposition chamber was designed, assembled and commissioned. A constant deposition rate of 3.0 Å/cycle was determined in a temperature regime between $200 - 225$ °C, the so-called ALD window. The electronic and chemical properties of the interfaces were investigated by means of X-ray photoelectron spectroscopy (XPS), ultraviolet photoelectron spectroscopy (UPS) and synchrotron-radiation photoelectron spectroscopy (SR-PES) at the BESSY II facility. Auger parameter analysis of the initial growth of ALD-ZnO on $CuInSe_2$ (112) and comparison to reference samples indicates the formation of an intrinsic $ZnIn_2Se_4$ (ZISe) boundary layer having a thickness of only one monolayer. Combined XPS and UPS analysis allows the investigation of the electronic properties of the $CuInSe_2|ZnIn_2Se_4|ZnO$ heterostructure, resulting in a detailed picture of the band alignment at the interfaces. Furthermore, this thesis presents a new water-free ALD process for ZnO deposition using metal-organic diethylzinc (DEZn) and molecular oxygen (O_2) as reacting precursors. Zinc oxide films usually show significant n-type doping and it is commonly stated that intrinsic point defects as well as interstitial hydrogen atoms play a major role in the doping mechanism. To reduce the amount of hydrogen in the ZnO, an alternative oxygen precursor to H_2O was introduced and successful atomic layer deposition was demonstrated. The ALD window of the water-free ALD process is shifted slightly towards lower temperatures, located between $185 - 210$ °C and a growth rate of 5.0 Å/cycle was observed. This significant increase indicates a completely different reaction mechanism not limited by steric hindrance effects of the ethyl ligands as in case of standard ALD of ZnO. A detailed comparison of two ZnO films deposited with both, water-free ALD and the standard precursor combination is presented. Both show an additional oxygen photoemission peak that is assigned to a surface hydroxide in the case of H_2O-ALD and a O_2^{2-} dumbbell defect in the case of water-free ALD. Additional non-destructive photoemission depth-profiling and annealing experiments do not show further significant differences in the chemical and electronic properties of both ZnO films.

Zusammenfassung

Electronic Properties of ALD Zinc Oxide and its Implication for Chalcopyrite Absorber Materials

Eike Janocha

Zinkoxid (ZnO) in seiner Eigenschaft als transparenter elektrischer Leiter wird heute in vielen Anwendungen eingesetzt, beispielsweise als Frontkontakt für Dünnschicht-Solarzellen. Dort wird der Heteroübergang zwischen dem p-dotierten Chalkopyrit Absorber heutzutage noch mit einer dünnen Schicht aus n-CdS erzeugt. Da es wünschenswert wäre das Schwermetall Cadmium sowohl aus Umweltaspekten, als auch aufgrund unvorteilhafter Produktionsbedingungen zu vermeiden, sind in den letzten Jahren starke Forschungsanstrengungen in dem Feld sogenannter alternativer Pufferschichten zu vermerken.
Um die Prozesse an der Grenzfläche des Absorbers im Detail zu verstehen werden in dieser Arbeit einkristalline Chalkopyrit Absorber in der technologisch relevanten (112) Kristallorientierung hergestellt und verwendet. Auf diese Absorber wurde ZnO mittels Atomic Layer Deposition (ALD) gewachsen. ALD hat den Vorteil, dass durch sein selbstlimitierenden Wachstumsmodus einzelne ZnO Monolagen definiert abgeschieden werden können. Dafür wurde eine UHV-kompatible ALD Anlage aufgebaut und in Betrieb genommen. In einem Temperaturbereich zwischen $200 - 225$ °C, dem sogenannten ALD Fenster, wurde eine konstante Wachstumsrate von 3.0 Å/Zyklus bestimmt.
Untersucht wurden die chemischen und elektrischen Eigenschaften der Grenzfläche mittels Röntgen-, Ultraviolett- und und Synchrotron-Photoelektronenspektroskopie am BESSY II. Eine Analyse des Auger Parameters während des initiellen Wachstums von ALD-ZnO auf $CuInSe_2$ (112) und der Vergleich mit Referenzproben deutet auf die Bildung einer intrinsischen $ZnIn_2Se_4$ Grenzschicht hin, welche eine Dicke von nur einer Monolage aufweist. Die Kombination aus XPS und UPS erlaubt die Untersuchung der elektronischen Eigenschaften der $CuInSe_2|ZnIn_2Se_4|ZnO$ Heterostruktur und liefert ein detailliertes Bild der elektronischen Bandanpassung an den jeweiligen Grenzflächen.
Zudem wird in dieser Arbeit ein neuer wasserfreier ALD Prozess zur ZnO Abscheidung mittels Diethylzink (DEZn) und molekularem Sauerstoff (O_2) präsentiert. ZnO zeigt üblicherweise eine starke n-Dotierung, hervorgerufen durch intrinsische Punktdefekte, sowie von Wasserstoff-Zwischengitteratomen. Um den Wasserstoff-Anteil im ZnO zu reduzieren wurde ein alternativer Sauerstoff-Lieferant zum H_2O benutzt und der erfolgreiche ALD Prozess gezeigt. Das ALD Fenster der wasserfreien ALD ist leicht zu niederigeren Temperaturen verschoben ($185 - 210$ °C) und zeigt eine Wachstumsrate von 5.0 Å/Zyklus. Der Anstieg deutet auf einen grundlegend unterschiedlichen Reaktionsprozess hin, der nicht durch sterische Hinderung der Ethyl-Liganden limitiert wird. Im Vergleich beider Methoden zeigt sich, dass beide ZnO Filme jeweils eine zusätzliche Sauerstoff-Komponenten aufweisen. Im H_2O-ALD Prozess wird diese durch eine Hydroxid-Oberflächenkomponente erzeugt, wohingegen der Ursprung beim wasserfreien ALD Prozess ein O_2^{2-} dumbbell Defekt ist. Zerstörungsfreie Photoemissions-Tiefenprofilierung zeigen keine weiteren wesentlichen Unterschiede der chemischen und elektronischen Eigenschaften beider ZnO Schichten.

Eidesstattliche Erklärung

Ich versichere an Eides statt, dass ich diese Dissertation selbständig verfasst habe. Die benutzten Hilfsmittel und Quellen sind in der Arbeit vollständig angegeben. Die Dissertation ist bis auf die gekennzeichneten Teile noch nicht veröffentlicht worden. Ich habe weder früher noch gleichzeitig ein Promotionsverfahren bei einem anderen Fachbereich bzw. einer anderen Hochschule beantragt.

Berlin, den 28.11.2011

(Eike Janocha)

Contents

1 Motivation

During the last decades, the global energy consumption increased dramatically and there is no indication that this trend reverses in the near future. Especially, the emerging markets in newly industrialized countries like China or India, will double the demand for energy in the next 50 years. In 2010, about 81 % of the total energy is produced by burning fossil fuels such as coal or natural gas[1]. Since these resources are very limited, renewable energies are the only alternative for future energy production. Today, most of the power generated by renewable energies comes from biomass and wind power. Solar energy is one of the most promising candidates for future power production. Neglecting the difficulty of efficient storage, solar energy is able to cover the global demand for energy by itself. The high growth rates of the photovoltaic market of $30 - 40$ % per year[2] show that the investment in solar energy is of increasing interest, which is also supported by governmental subsidies in some countries such as Germany.

Nowadays, about 80 % of the photovoltaic energy is produced by solar cells based on crystalline or polycrystalline silicon. The indirect band gap of silicon and the resulting absorber layer thickness of at least 100 μm is one of the major disadvantages of these first-generation devices. To reduce the material consumption, thin-film solar cell technologies were developed. Besides Si-based thin-film solar cells, this second solar cell generation is based on direct band gap absorber materials like CdTe, GaAs or CIGS chalcopyrites, reducing the required amount of absorber material drastically by a factor of 100. To motivate this thesis, basic knowledge about chalcopyrite-type thin-film solar cells is required. Hence, the following section will give an introduction of its working principle, the different materials used and how they are typically deposited in current production lines. After a short discussion of the most important materials properties, the aim of this thesis will be motivated and a short outline of this thesis will be presented in the end of this chapter.

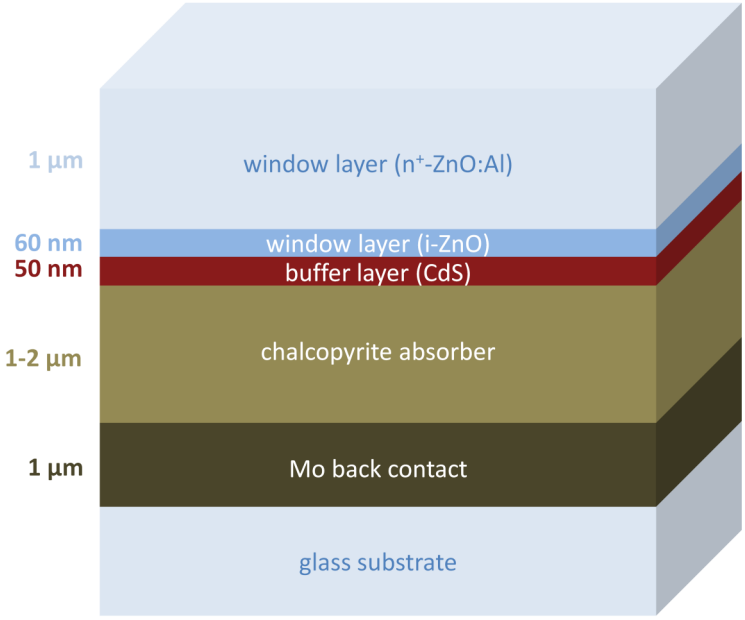

Figure 1.1: Current design of a thin-film chalcopyrite solar cell. Please note, that the film thicknesses of the buffer layer and the intrinsic zinc oxide (i-ZnO) are not to scale.

1.1 Chalcopyrite Solar Cells

Chalcopyrite absorber layers used for photovoltaics are based on I-III-VI_2 $CuInSe_2$ compound materials. The current conversion efficiency world-record is 20.3 % achieved at the Zentrum für Sonnenenergie- und Wasserstoff-Forschung Baden-Württemberg (ZSW) for laboratory-scale devices[3]. This is the highest efficiency not only for chalcopyrite-based thin-film solar cells, but the record of polycrystalline thin-film solar cells at all. The design of such a commercially available chalcopyrite solar cell is shown in Fig. 1.1. The key component of the chalcopyrite solar cell is its absorber layer, that is usually deposited by a co-evaporation process of the individual elements on a 1 μm thick molybdenum back contact. This electrically conducting back contact is usually deposited onto a sodium-containing soda-lime glass substrate by sputter deposition. To separate the charge carriers created in the absorber layer by incident light, a junction has to be formed with the p-type chalcopyrite material. Today, this is done by a thin layer of n-type CdS deposited by a chemical bath deposition (CBD) process. It is this heterojunction, mainly determining the overall efficiency of the solar cell. On top of the buffer layer, a transparent front contact is deposited by sputter deposition. Usually, a combination of a thin intrinsic zinc oxide (i-ZnO) and heavily n-doped ZnO:Al is used and shows a beneficial effect on

the device efficiency. Especially the influence of the i-ZnO is still under discussion [2].
In the following, the absorber layer, the buffer layer and the transparent front contact materials are discussed in detail, since they play a crucial role for this thesis, while the substrate, the Mo back contact and the role of Na for the device efficiency are not treated in this work. For more detail it is referred to several reviews that give additional information about the role of the substrate and the back contact [2;4–6].

1.1.1 Chalcopyrite Absorber

As mentioned above, chalcopyrite absorber layers presently used in thin-film solar cells are usually based on $CuInSe_2$. It crystallizes in a tetragonal chalcopyrite structure (space group $I\bar{4}2d$) having lattice lattice parameters of $a = 5.77$ Å and $c = 11.54$ Å according to Shay and Wernick [7]. The chalcopyrite lattice can be derived from the cubic zinc blende structure of binary II-VI compound semiconductors like ZnSe by occupying the zinc lattice sites alternately by copper and indium atoms, respectively [6]. Both crystal structures,the one of ZnSe (cubic zinc blende) and $CuInSe_2$ (tetragonal chalcopyrite lattice), are illustrated in Fig. 1.2, respectively.

$CuInSe_2$ absorbers have very attractive properties to convert sunlight efficiently into electrical energy. Its direct band gap of $E_g = 1.04$ eV [6] results in a high optical adsorption coefficient ($\approx 10^5$ cm^{-1}) [2] and hence, the thickness of the absorption layer can be reduced significantly with respect to indirect band gap materials such as silicon. The band gap energy of the semiconducting absorber material has a strong influence on the device

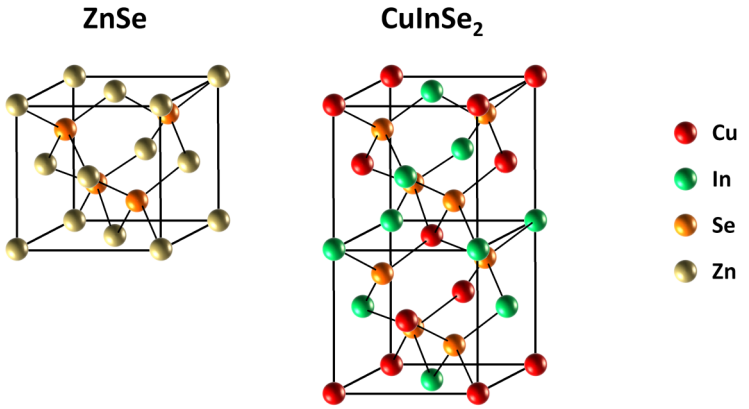

Figure 1.2: (left) zinc blende crystal structure of a II-VI compound such as ZnSe; (right) chalcopyrite unit cell of a $CuInSe_2$ I-III-VI_2 compound

efficiencies. There are basically two parameters that influence the solar cell's efficiency: on the one hand, the amount of photons absorbed in the active layer and on the other hand the losses in the device that lower the electrical energy created per photon[4]. While a small band gap would increase the amount of photons absorbed, at the same time, the electrical losses would increase, where a larger band gap would be advantageous. There is an optimum band gap that represents a compromise between the absorption efficiency and electrical losses at $E_g = 1.5\,\mathrm{eV}$[4]. Hence, $CuInSe_2$ with its band gap of 1.04 eV is not an ideal absorber material. Fortunately, the band gap of $CuInSe_2$ can be increased by substituting parts of the indium by gallium. Depending on the Ga content, the band gap can be varied continuously in a range between $1.04 - 1.68$ eV. In practice, $Cu(In,Ga)Se_2$ absorbers are produced with a [Ga]/[In+Ga] ratio of $20 - 30$ %, resulting in a band gap of approximately $1.20 - 1.25\,\mathrm{eV}$[4] to achieve optimum device characteristics.
Besides the band gap engineering by changing the gallium concentration, the doping of the chalcopyrite plays a crucial role for the solar cell efficiency. Doping in chalcopyrites is controlled by intrinsic point defects that are likely to form due to their low defect formation energies during growth of the material[8]. High-efficiency photovoltaic cells have p-type absorber layers, that are achieved by growing the material Cu-poor. There, copper vacancies [V_{Cu}] are the dominant acceptors, resulting in p-type doping of the absorber. The existence of an $CuIn_3Se_5$ ordered defect compound at the surface of the chalcopyrite and its influence on the junction formation has been heavily discussed in the past. Much more information about the ordered defect compound is presented in the thesis of Hofmann[9] and is not discussed here in detail.

1.1.2 Buffer Layer

To form a junction with the p-type absorber layer, in today's production lines n-type CdS buffer layers are deposited onto the chalcopyrite absorber. Commonly, this is done by a chemical bath deposition (CBD) process, where the absorber is put into a chemical solution of Cd ions and thiourea[6]. Besides a very homogeneous junction formation across the whole surface area, the CBD CdS deposition process has some additional advantages, as it protects the absorber surface from damage of the subsequent ZnO sputter deposition. Additionally, the treatment in the chemical bath will also remove natural oxides that can form at the chalcopyrite's surface during the process.
Nevertheless, the usage of cadmium sulfide and the chemical bath deposition process itself

have some disadvantages and both are subject of intensive research activities in the last years. One drawback of the chemical bath deposition process is its incompatibility with the vacuum deposition processes in the production line. Currently, the devices have to be removed from the vacuum after absorber evaporation, to deposit the CdS in the chemical bath. On the one hand, breaking the in-line production process is economically not very advantageous. On the other hand, breaking the vacuum can lead to oxidation of the surfaces and can influence the device characteristics. Hence, having a vacuum compatible process for the buffer layer deposition would be beneficial for the solar cell production.
The second disadvantage in today's chalcopyrite solar cell production is the usage of cadmium. CdS is known for its high toxicity and it is known for being responsible for causing cancer. Hence, additional safety regulations are required for the employees[6]. The environmental risks of cadmium also result in legal regulations for selling cadmium-containing devices in some countries[10], for instance Germany as one of the biggest markets for photovoltaic devices today. Besides those legal issues, substituting the CdS by a different material is also of interest from the technological point of view. To avoid the absorption of incident light in the window and buffer layer, materials with wide band gaps are beneficial for the device performance. With a band gap of $E_g = 2.4$ eV, light in the spectral region between $350 - 550$ nm will be absorbed by the CdS[10]. Hence, an alternative buffer material with a band gap energy exceeding the one of CdS could increase the solar cell efficiency.
In recent years, several new materials and deposition methods have been investigated in terms of their benefits in chalcopyrite thin-film solar cell production. Even though the best efficiencies are still achieved with CBD-CdS buffers, promising results are reported using alternative buffer layers that are Zn- or In-based materials. Among those, ZnS with a band gap energy of 3.8 eV[11] has been studied extensively[10], just like In_2S_3 ($E_g = 3.0$ eV[12]) and ZnSe ($E_g = 2.7$ eV[11]). Various vacuum compatible deposition techniques were applied, for instance sputter deposition, co-evaporation, ion layer gas reaction (ILGAR) and atomic layer deposition (ALD). The latter often shows best results among the alternative deposition techniques, most likely due to its excellent interface formation with the subjacent chalcopyrite[10;13–15].
It has also been found, that the efficiencies of devices with sulfide-based buffer layers can be increased, when the material additionally contains some oxides or hydroxides[5]. Studies of the interface formation of Zn(O,S) buffer layers deposited by ALD on polycrystalline Cu(In,Ga)Se_2 absorber layers have been carried out by Yousfi et al.[16] and Platzer-Björkman et al.[15], showing the feasibility of atomic layer deposition for the solar

cell production process. Also direct ZnO growth on the chalcopyrite absorber layer has been investigated by those groups using atomic layer deposition[14;17]. As expected, the resulting efficiencies of those buffer-free solar cells did not reach the world-record cells of 20.3 %. But 14.6 % achieved with ALD-ZnO is close to the 15.0 % record for buffer-free CIGS|ZnO structures grown by sputtering[18] or the ILGAR method[10] and emphasizes the potential of atomic layer deposition to substitute the chemical bath deposition process in the near future.

1.1.3 Zinc Oxide

The front contact of a chalcopyrite solar cell has to fulfill two requirements: on the one hand, it has to be sufficiently conductive as it acts as the counter electrode to the Mo back contact. On the other hand, it has to be as transparent to the incident sunlight as possible to avoid undesired absorption in the window layer. There are not many materials that fulfill both of those requirements. Often, tin-doped indium oxide (ITO, also known as indium tin oxide) is used for this purpose. The limited resources are one of the indium is one of the disadvantages of this material, increasing the costs of the devices. In today's chalcopyrite solar cell production, zinc oxide (ZnO) is used as transparent conductive oxide for the front contact, showing a wide direct band gap of $E_g = 3.36 - 3.44$ eV[19;20] and hence being a promising candidate for the transparent front electrode in solar cells. Zinc oxide is a binary II-VI compound semiconductor that usually crystallizes in a hexagonal wurtzite structure (space group $P6_3mc$), where each oxygen anion is surrounded by four zinc cations[20]. The crystal structure of hexagonal wurtzite ZnO is illustrated in Fig. 1.3 in side-view (top) and from the top (bottom). ZnO in (0001) orientation can have two different surface terminations, zinc or oxygen, respectively. If zinc is the surface-terminating element, one speaks of (0001) ZnO, while an oxygen-terminated surface is defined as $(000\bar{1})$ ZnO. According to Özgür et al.[20], the lattice parameter of ZnO are reported being $a \approx 3.25$ Å and $c \approx 5.20$ Å, respectively. Small deviations in the experimentally determined lattice constants are caused by point defects present in the crystal. Those point defects, like interstitial zinc atoms [Zn_i] or oxygen vacancies [V_O] have very low formation energies and are also discussed being responsible for the natural n-type doping of ZnO crystals[20]. For use as front contact, this n-type conductivity is additionally increased by heavily doping the ZnO by aluminum as a group III element.

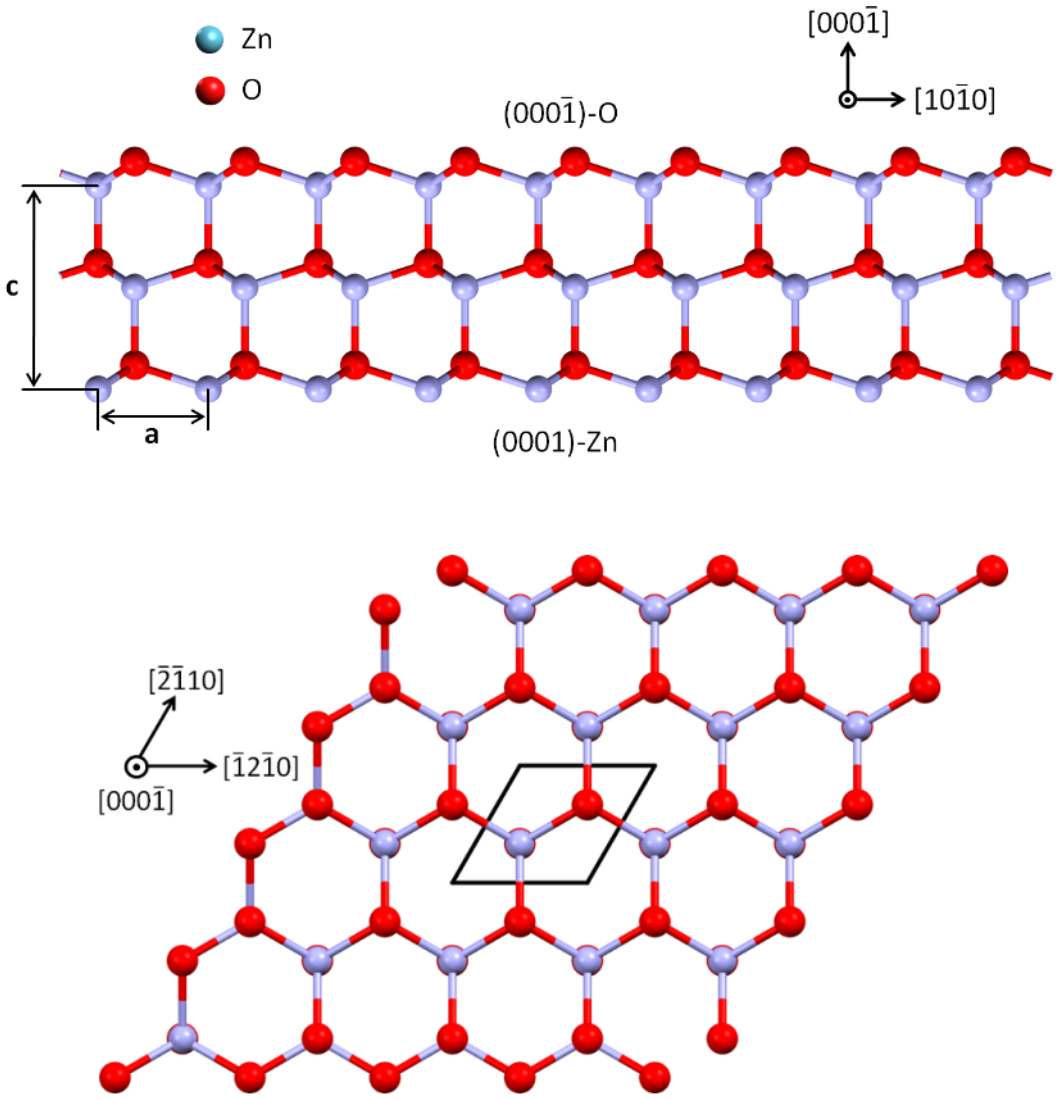

Figure 1.3: Illustration of the crystal structure of wurtzite zinc oxide in two different viewing directions.

While additional n-type doping is easily achieved, the same is not true for p-type doping of zinc oxide. Over the last years, extensive research was done trying to find an effective and reproducible method to achieve p-type conductivity in ZnO. Most promising dopant candidates discussed in the scientific community are nitrogen, phosphorus or arsenic atoms, substituting the oxygen in the ZnO lattice. High quality p-type ZnO would result in various new applications, for instance in the field of optoelectronic devices[20]. Difficulties in p-type doping of ZnO and other wide band gap semiconductors (like GaN, ZnS and ZnSe) are caused by several factors. Compensation of the p-type doping effects by the native point defects mentioned above ($[Zn_i]$, $[V_O]$) is one of them.
Another crucial role might be the presence of hydrogen in the zinc oxide crystal. While hydrogen is known for being amphoteric in most semiconducting materials (i.e. it can act as both, donor or acceptor[19]), this is not the case in ZnO. Here, interstitial hydrogen always acts as a donor, resulting in additional compensation of potential acceptor dopants[19;20].

1.2 Objectives and Outline of this Thesis

To understand the high efficiencies achieved by direct ZnO deposition on chalcopyrite absorbers, earlier work of our group investigated the direct ZnO deposition by metal-organic molecular beam epitaxy (MOMBE) on epitaxial $CuInS_2$[21] and $CuInSe_2$[22]. Since polycrystalline chalcopyrite absorbers tend to grow in a preferred (112) orientation[23], both absorber systems were grown in this technologically important (112) orientation. The epitaxial nature of the absorber substrate allows detailed investigation of the interface formation and the electronic band alignment of the two materials. Those studies indicated no direct ZnO deposition on the chalcopyrite, but the formation of an intrinsic buffer layer consisting of ZnS in case of $CuInS_2$ and ZnSe for $CuInSe_2$ absorbers. The electronic band alignment determined from photoelectron spectroscopies indicated beneficial properties of the $CuInX_2$ - ZnX - ZnO interface (X=S,Se) for photovoltaic devices. To investigate the interface formation between epitaxial $CuInSe_2$ and ZnO grown by atomic layer deposition is one of the objectives of this thesis. Besides an investigation of the chemical interface formation, the electronic band alignment can be determined by in situ photoelectron spectroscopies. This will result in a detailed picture of the processes at the interface, responsible for the efficiencies achieved for the buffer-free chalcopyrite solar cells.

As mentioned above, hydrogen plays a crucial role for the electronic properties zinc oxide. Hydrogen incorporation into the zinc oxide crystal is very difficult to prevent, as it is present in virtually every deposition technique available for ZnO growth. In atomic layer deposition for instance, H_2O is usually used as the oxygen precursor and therefore provides a possible hydrogen source in the grown zinc oxide layer. To reduce the amount of hydrogen in the ZnO deposition chamber, a water-free ALD process would be advantageous, using an alternative to H_2O as oxygen precursor. There are only few oxidizing agents, which demonstrated successful atomic layer deposition of ZnO. While in the past $ZnCl_2$ and O_2 were used as precursors for ZnO atomic layer deposition, nowadays, metal-organic zinc precursors such as diethylzinc ($Zn(C_2H_5)_2$) are preferred. Even though there are few studies of alternative oxygen precursors for the ZnO atomic layer deposition using diethylzinc, most of them either use reactive ozone (O_3) or a plasma-enhanced deposition technique. Due to their high reactivities, both processes can have negative influences on the electronic and optical properties of the zinc oxide films deposited. In this study, the first successful atomic layer deposition of diethylzinc and molecular oxygen (O_2) is presented, that results in ZnO films of comparable chemical and electronic qualities to the standard water-based ALD process.

This thesis is structured as follows:
After this motivation chapter, an introduction to the analytical techniques used in this thesis is given. Afterwards, several deposition techniques relevant for this work are shortly presented in Chp. 3. One objective required for the success of this thesis was the design, assembly and initial operation of an UHV-compatible atomic layer deposition system for ZnO growth. The results are presented in Chp. 4, followed by the second goal of this thesis: the investigation of the $CuInSe_2$|ZnO interface in Chp. 5. Finally, in Chp. 6 the results of water-free ZnO atomic layer deposition using a precursor combination of diethylzinc and O_2 are presented.

2 Methods of Surface Analysis

In the following chapter, some basic information about the methods of surface analysis used in this thesis are presented. It is mainly focused on the sample characterization by photoelectron spectroscopies, but also gives a short introduction about other techniques, such as low-energy electron diffraction (LEED).

2.1 The Integrated System

All surface analysis techniques used in this thesis are sensitive to the utmost atomic layers of the material under investigation. Therefore, any surface modifications in between the sample preparation (for instance a deposition step) and its characterization have to be avoided. This is achieved by carrying out all experiments under ultra-high vacuum (UHV) conditions in a combined deposition and analysis system called the *Integrated System* (IS). An illustration of this complex system is shown in Fig. 2.1. The base pressure in this system is usually below $5 \cdot 10^{-10}$ mbar, except for some deposition chambers, where source gases cause higher pressures. Several types of vacuum pumps (rotary vane pumps, turbo molecular pumps, ion getter pumps, sublimation pumps) are necessary to create such low pressures. In comparison with high vacuum conditions, where only pressures of about 10^{-7} mbar have to be reached, this is not only much more cost-intensive, but also very time consuming. For instance, to remove water from the walls of the vacuum system after it has been vented and exposed to air, it has to be baked-out for several hours up to days at about 130 °C, until UHV conditions are achieved. Nevertheless, UHV conditions are of utmost importance to maintain ultra-clean and unmodified surfaces after preparation of the samples. Several deposition techniques in the Integrated System allow to investigate

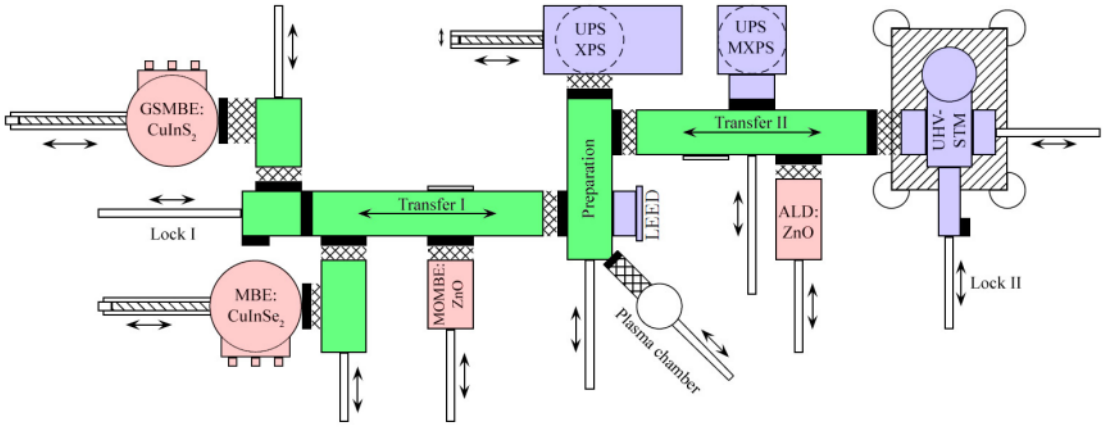

Figure 2.1: Schematic drawing of the Integrated System, an ultra-high vacuum system combining several deposition chambers (red) and surface analysis systems (blue). Samples can be transferred in the UHV by transport systems (green), allowing in situ analysis without any sample modification between deposition and analysis.

the interface formation and properties of different material combinations. Those are in particular: $CuInSe_2$ molecular beam epitaxy (MBE), $CuInS_2$ gas-source MBE (GS-MBE) and ZnSe thermal evaporation. In addition, zinc oxide can be deposited via atomic layer deposition (ALD) and metal-organic molecular beam epitaxy (MOMBE). Since most of the techniques were used in this work, they are treated in detail later in a separate chapter. In Fig. 2.1, all deposition chambers are colored in red.

The samples are mounted on small transferable sample holders, that allow in situ surface characterization by transferring the specimen under UHV conditions from the deposition chambers into several analysis systems. The disadvantage of those sample holders is the limitation of the specimen sizes to 0.8×0.8 cm^2 at most. Samples are usually introduced into the IS by one of two load locks.

Various surface analysis techniques are available, labeled in blue in Fig. 2.1. The main components are two X-ray photoelectron spectroscopy (XPS) systems, one equipped with a monochromized Al Kα X-ray source, the other one with a Mg/Al dual X-ray source. Both chambers are equipped with helium discharge lamps, allowing the valence band investigation with ultraviolet photoelectron spectroscopy (UPS). Additionally to the photoemission spectroscopies, the Integrated System allows to investigate the surface struc-

ture of the samples by low-energy electron diffraction (LEED), as well as creating images of the surfaces by scanning tunneling microscopy (STM).

Furthermore, the Integrated System allows to anneal the samples either under UHV conditions, in oxygen and hydrogen atmospheres or to sputter clean samples by bombardment with high energetic argon ions. This is usually very useful to prepare clean reference materials.
One useful feature of the Integrated System not illustrated in Fig. 2.1 is a battery-powered transfer box. It allows to transport a sample from the laboratory to an analysis system at the BESSY II synchtrotron radiation facility under UHV conditions. More information about the BESSY II and the application of synchtrotron light in this work is given later in Sec. 2.2.3.

2.2 Photoelectron Spectroscopies

When Albert Einstein explained the photoelectric effect in 1905 [24], he provided the basis for one of todays most powerful analytical techniques to investigate electronic properties of materials, namely the photoelectron spectroscopy (PES). Using Max Planck's concept that energy only exists in discrete levels, he explained the energy transfer of a photon with energy $E = h \cdot \nu$ by exciting an electron which then might escape the atom. Both were awarded the Nobel Prize in Physics, Planck in 1918 and Einstein in 1921. Depending on the photon excitation energy one distinguishes between different types of photoelectron spectroscopies:

- ultraviolet photoelectron spectroscopy (UPS) with photon energies $\lesssim 120$ eV
- X-ray photoelectron spectroscopy (XPS) with excitation energies of ≈ 1 keV
- hard X-ray photoelectron spectroscopy (HAXPES) with energies $\gtrsim 5$ keV

In the this chapter, the basic principles of X-ray and ultraviolet photoelectron spectroscopy will be shortly discussed. For those readers who want to gain deeper insight into this topic there are lots of textbooks available dealing with photoelectron spectroscopy [25–28].

2.2.1 X-ray Photoelectron Spectroscopy

Using the concept of the photoelectric effect, Kai Siegbahn and his co-workers developed the instrumentation to investigate chemical properties of materials surfaces. In addition, he developed the theory of XPS and established the term *electron spectroscopy for chemical analysis* (ESCA). For his contributions to the field of surface science, also Siegbahn was awarded the Nobel Prize in Physics in 1981. Since photoelectron spectroscopies can provide much more information about materials than its chemical properties, as shown later in this section, nowadays the term X-ray photoelectron spectroscopy (XPS) became commonly used.

In XPS, a sample is irradiated by X-ray photons of a specific known energy. The photons can transfer their entire energy to core-electrons in the material, which then are able to escape the atom. Those photoelectrons are energetically separated by an electron spectrometer and counted. It is the kinetic energy of those photoelectrons that contain information about the chemical environment of the emitting atom. The individual processes during photoemission spectroscopy, beginning with creating a characteristic X-ray photon and resulting in photoemission spectra with several spectral features, are discussed now in detail.

Figure 2.3 shows the configuration of an XPS system as it is used in this work. First, X-rays have to be created at the X-ray source by accelerating a high-energy electron beam in the range of $10 - 15\,\mathrm{keV}$ onto an anode material to create holes in its core levels. Electrons from outer shells of the atom will fill up this hole, emitting characteristic radiation of specific energy at the same time. In practice, X-ray source anode materials

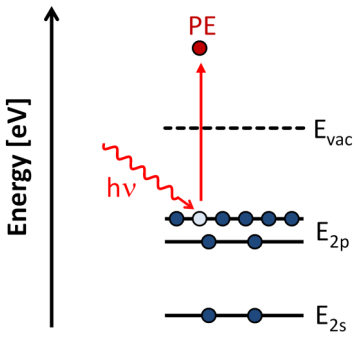

Figure 2.2: Simplified energy scheme of the photoelectron creation by energy transfer of incident X-rays with an energy $h\nu$.

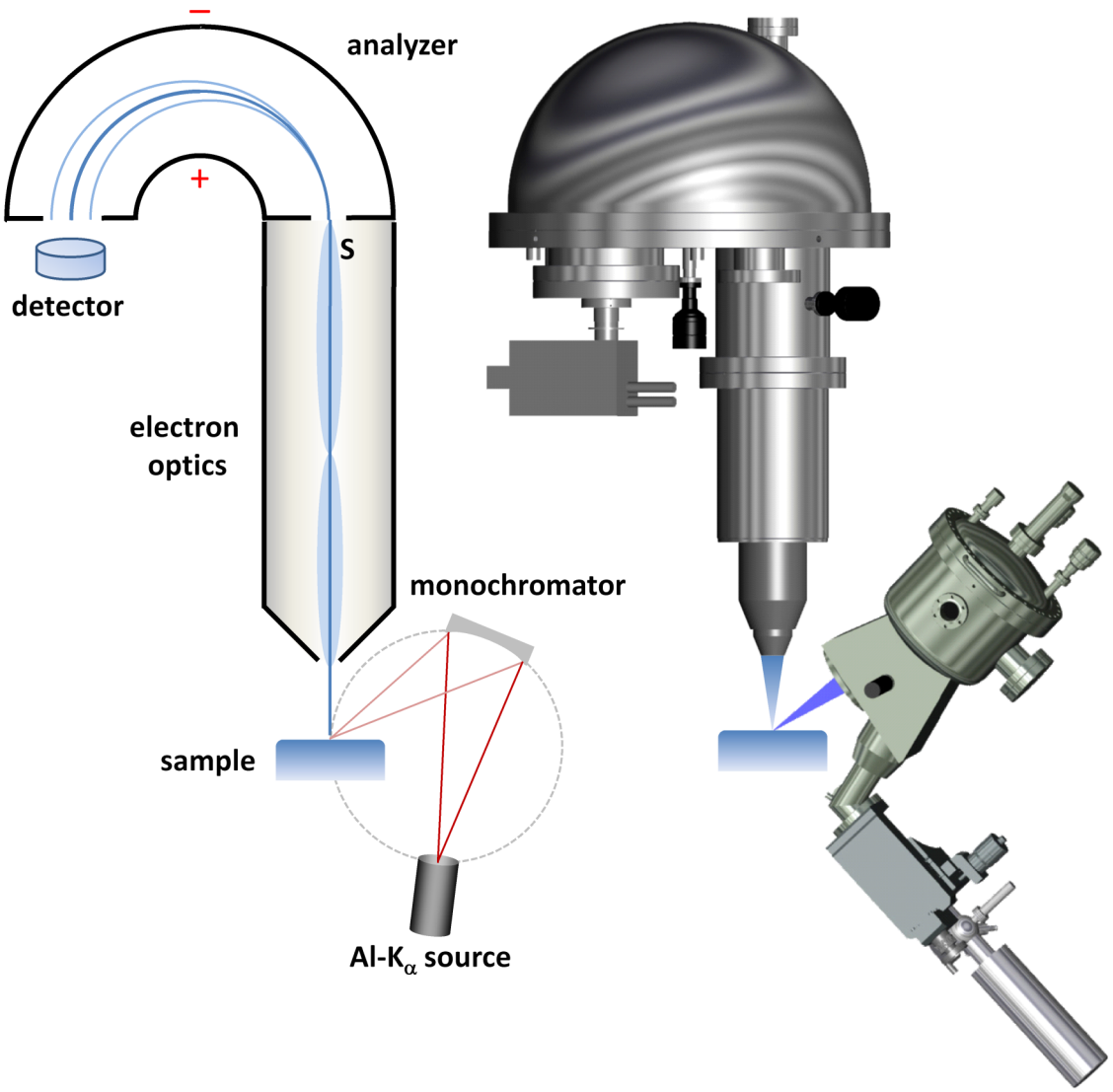

Figure 2.3: Schematic illustration of the monochromized X-ray photoelectron spectroscopy analysis system mainly used in this work. Explanation of the different parts is given in the text.

are usually either magnesium or aluminum creating characteristic X-rays of 1253.6 eV (Mg Kα) and 1486.6 eV (Al Kα), respectively[26], where 1 eV = $1.6 \cdot 10^{-19}$ J. Since most of the energy of the incident electrons is released in form of heat, anodes have to be water cooled to prevent thermal degradation.
In Fig. 2.4 a spectrum of characteristic Al Kα radiation is shown. The Kα radiation is quite complex and is composed of two different Kα lines where the Kα_1 line corresponds to the $2p_{3/2} \rightarrow 1s$ transition and the Kα_2 line arises from a $2p_{1/2} \rightarrow 1s$ transition. Their intensity difference originates from the different number of electrons in the $2p_{1/2}$ and $2p_{3/2}$ energy states. In addition, a couple of satellite lines are present which are not shown in Fig. 2.4.

To increase the energy resolution of the X-radiation, a monochromator is used to separate the Al Kα_1 line from the Al Kα_2 radiation and all satellite lines. To do so, a quartz crystal is used to diffract the X-rays from the source and to focus it onto a sample. Aluminum anodes are the most commonly monochromized X-ray sources. This is due to the fact that the Kα_1 wavelength of 0.83 nm and the quartz lattice spacing of the $(10\bar{1}0)$ planes (0.425 nm) fulfill the Bragg relationship $n\lambda = 2d \sin\theta$ at an angle of 78°[26] so that only the Al Kα_1 line is diffracted. As illustrated in Fig. 2.3, the X-ray source, the monochromizing crystal and the sample have to be positioned on a spherical surface called the Rowland sphere, to satisfy the Bragg condition. Using a monochromator significantly

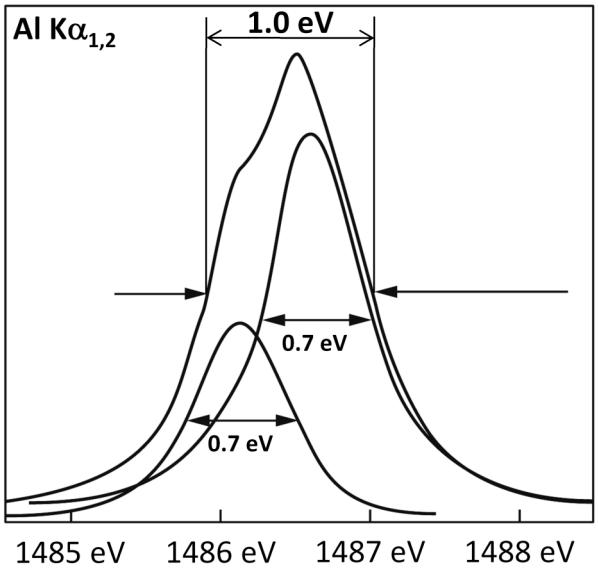

Figure 2.4: Energy distribution of characteristic Al Kα radiation. The illustration is taken from Alford et al.[28]

increases the quality of the photoemission spectrum due to removing unwanted signal contributions from other spectral lines as the Al Kα_1. Even though it lowers the X-ray intensity reaching the sample and having higher costs, the benefits in spectral quality predominate the drawbacks.

Once the X-rays reach an atom of the sample surface, three different interactions may occur[27]:

1. the photon may pass through the atom without any interactions
2. the photon is scattered by an electron and loses some energy
3. the photon transfers its entire energy to an electron, which then is ejected as a photoelectron

It is the third event X-ray photoelectron spectroscopy is based on. To gain insight on the information achieved by photoelectron spectroscopies, we have to take a look at the interaction of photons and the electrons in the material. One has to differentiate between *initial state* and *final state* effects. In its initial state, before the incident photon interacts with the atom, the negatively charged electrons are bound to the atom by the positively charged nucleus. The closer an electron is located at the nucleus, the higher its binding energy, i.e. the stronger it is bound to the nucleus. Hence, the atomic number (the number of protons in the nucleus) influences the binding energies of the electrons. This binding energy can relatively easy be determined using photoelectron spectroscopies. Hence, it is providing information about the elements present in the sample.

The binding energy (BE) and the measured kinetic energy (KE) of the emitted photoelectrons have first been related to each other by Einstein in his work about the photoelectric effect[24] according to Eq. 2.1:

$$E_{\text{bin}} = h\nu - E_{\text{kin}} \tag{2.1}$$

The excitation energy $h\nu$ of the incident X-rays is a known parameter determined by the X-ray source used. In solid materials there is an additional amount of energy necessary to remove the electron out of the crystal. This additional energy is called the work function

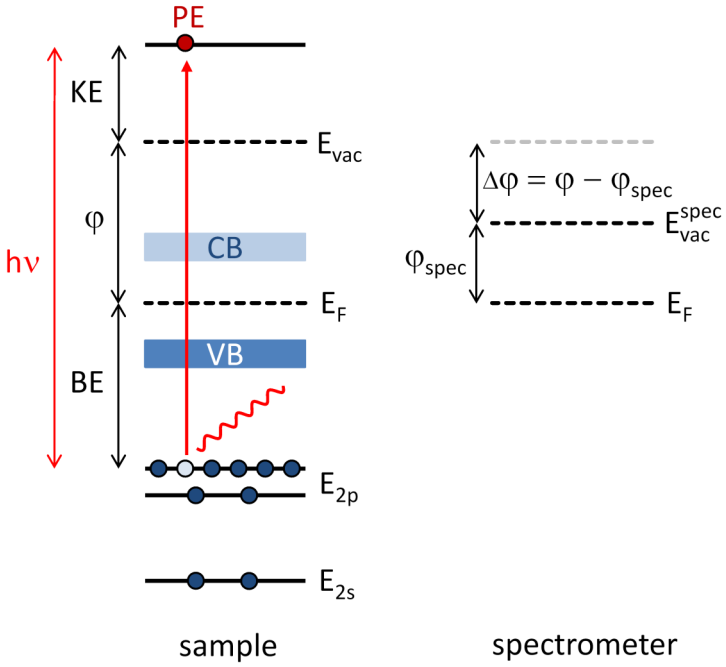

Figure 2.5: (left) energetic situation of an electron in the sample; (right) work function of the spectrometer, if sample and spectrometer are in electrical contact

(φ), which has to be considered in the Einstein equation:

$$E_{\text{bin}} = h\nu - E_{\text{kin}} - \varphi \tag{2.2}$$

The work function is defined as the energy required by an electron at the Fermi energy to escape the crystal, i.e. to reach the vacuum energy E_{vac}: $\varphi = E_F - E_{\text{vac}}$. A schematic representation of the processes in a photoemission process is shown in Fig. 2.5 on the left hand side. As shown on the right, one also has to take into account the work function of the spectrometer.

Because sample and spectrometer are in electrical contact, both are also in a thermodynamical equilibrium. Hence, their Fermi levels are equal and the energy an electron has to overcome to be ejected from the crystal reduces by $\Delta\varphi = \varphi - \varphi_{\text{spec}}$, where φ_{spec} corresponds to the work function of the spectrometer. Including the work function of the spectrometer in Eq. 2.2 results in:

$$E_{\text{bin}} = h\nu - E_{\text{kin}} - \varphi + (\varphi - \varphi_{\text{spec}}) = h\nu - E_{\text{kin}} - \varphi_{\text{spec}} \tag{2.3}$$

φ_{spec} can be determined during calibration of the spectrometer using clean Cu, Ag and Au metal samples. Once calibrated, it can be assumed to stay constant as long as the spectrometer is maintained under ultra-high vacuum conditions.

It is not only the atomic number that is responsible for the binding energy of the electrons, but also its chemical environment. If an atom forms chemical bonds to other atoms, their valence electrons, responsible for chemical bonding, will redistribute depending on the electronegativities of the bonding partners. This changes the electrostatic potential felt by the core-electrons, which in turn can result in a change in the binding energies of the core-electrons. This change is called *chemical shift* and contains information on the bonding situation of elements in a sample.

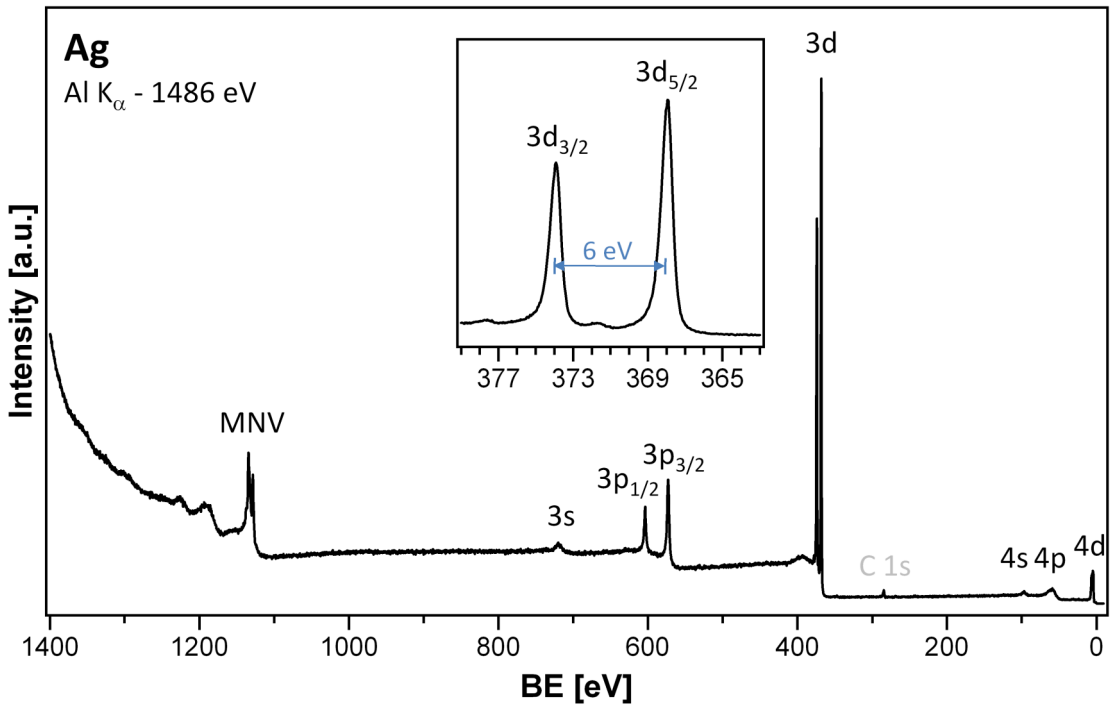

Figure 2.6: X-ray photoelectron survey spectrum of Ag. The major photoemission and Auger transition peaks are labeled. The small spectral features around 371.5 eV and 377.5 eV originate from plasmon losses of the photoelectrons. The spectrum has been recorded with monochromized Al K_α radiation with $h\nu = 1486.6$ eV

A survey spectrum of a metallic Ag sample is presented in Fig. 2.6 to exemplify a typical photoemission spectrum. The X-ray source was a monochromized Al Kα anode with $h\nu = 1486.6$ eV. Survey spectra like this are useful to get an overview about the elements present in a sample. They are recorded over a broad range of binding energies with a lower energy step size of typically 0.5 eV to reduce recording times. The most prominent feature in Fig. 2.6 is originating from Ag 3d electrons at binding energies of about 368 eV and 374 eV, respectively. This is shown in detail in the inset recorded with an smaller energy step size of only 0.05 eV. Another initial state effect is shown in this inset is the spin-orbit splitting of two electron states of same energy but different spin. The magnetic interaction between the electron's spin (up or down) and its orbital angular momentum leads to the splitting into two components. In case of d-orbitals as in the example of Ag 3d they split into $3d_{3/2}$ and $3d_{5/2}$ with a difference in binding energy of $\Delta BE = 6$ eV in this particular case. The intensity ratio between those two peaks is $d_{3/2} : d_{5/2} = 2 : 3$. Other less prominent photoemission lines in Fig. 2.6 belong to electrons of the 3p state around 600 eV, that split into $p_{1/2}$ and $p_{3/2}$ with an intensity ratio of 1 : 2. In case of Ag, the core-electrons of deeper energy levels than 3s are not visible using Al Kα radiation since their binding energies (e.g. 3352.6 eV for Ag $2p_{3/2}$ electrons[29]) exceed the excitation energy of 1486 eV. The survey spectrum also provides information about the contamination of the sample surface. In case of the Ag example, the surface was sputter cleaned by Ar^+ ion bombardment and only small traces of carbon are present at the surface indicated by the C 1s photoemission peak at 284 eV.

In X-ray photoelectron spectroscopy, there is another important feature that contributes to the photoemission spectra. Those features arise from X-ray excited Auger electrons, as illustrated in Fig. 2.7 in a simplified form.

On the left hand side of Fig. 2.7, the process of creating the core-hole by ejection of a photoelectron is demonstrated again. On the right, this particular hole is refilled by an 3d outer shell electron to reduce the total energy of the excited atom. For reasons of energy conservation, the surplus energy of this process has to be emitted either in form of an X-ray photon or by ejecting a so-called *Auger electron*. Its kinetic energy depends on the energy level of the emitted photoelectron, the initial state of the electron that fills up the core-hole and on the state the Auger electron has been prior to being emitted to the vacuum. Hence, the kinetic energy is independent of the excitation energy of the incident photons. For historical reasons, for Auger electrons are labeled in X-ray notation, whereas for photoelectrons the spectroscopic notation is used. In spectroscopic notation,

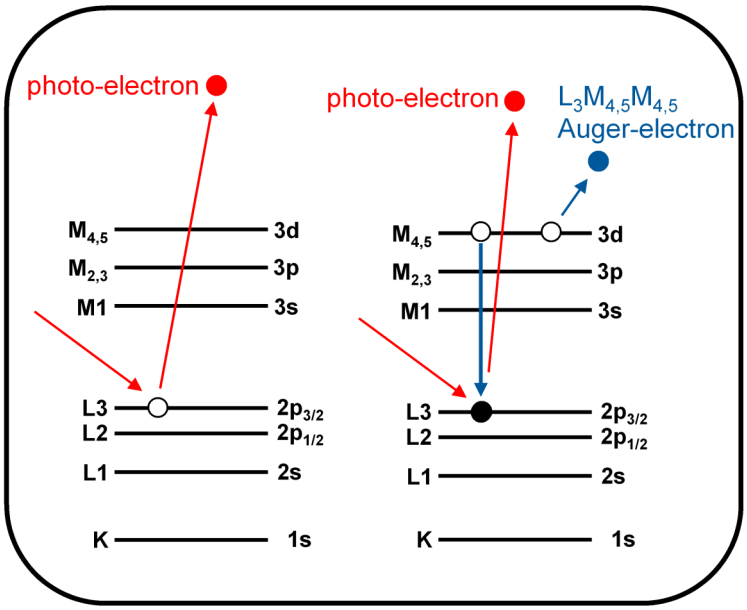

Figure 2.7: Schematic illustrations of the excitation of an photoelectron by absorption of an X-ray (left) and the emission of an Auger electron created by a relaxation process (right)

the electron states are a combination of the principal quantum number $n = 1, 2, 3, 4$, the angular momentum l = s, p, d, f and the total angular momentum quantum number $j = l + s$, where s is the spin of the electron, i.e. $s = 1/2$ or $(-1/2)$. In X-ray notation, n is expressed by the capital letter K, L, M, N followed by suffixes 1, 2, 3, 4, ... which represent the various combinations of l and j. Table 2.1 summarizes the most important electron states and their particular notation.

The combination of the three energy levels that determine its kinetic energy is used to

Spectroscopic	X-ray notation
1 s	K_1
2 s	L_1
2 $p_{1/2}$	L_2
2 $p_{3/2}$	L_3
3 s	M_1
3 $p_{1/2}$	M_2
3 $p_{3/2}$	M_3
3 $d_{3/2}$	M_4
3 $d_{5/2}$	M_5

Table 2.1: Spectroscopic notation and X-ray notation for photo- and Auger electrons

label an Auger electron. In Fig. 2.7 the photoelectron was ejected from the $2p_{3/2}$ (i.e. L_3) state and filled up by an electron of the $3d_{3/2}$ or $3d_{5/2}$ (M_4 or M_5) shell. The Auger electron is released from the same energetic state and therefore the Auger electron is labeled $L_3M_{4,5}M_{4,5}$. This example has been chosen since it is the most prominent Auger transition in case of zinc and of great importance for this work as shown later.

In many cases, additional analysis of the Auger lines in a photoemission spectrum provides more chemical information about the sample than just measuring the photoelectrons. In fact, the shift in kinetic energy of the Auger electrons might exceed the shift in binding energy of the photoelectrons significantly[30]. In general, this occurs for materials that are electrically conducting and when the initial vacancy is in one of the inner electron shells. In case of zinc compounds Wagner et al.[30] showed that the Zn photoelectrons show almost no shift in binding energy, while the corresponding Auger lines can shift several electron volts. This deviation can be explained by differences in the ionized states: if the atom emits a photoelectron, its final state remains singly ionized. This affects the outer shell electrons that can be emitted as Auger electrons. Therefore, electrons emitted from an ionized atom in form of an Auger electron will be more sensitive to the chemical environment than photoelectrons emitted from atoms in their ground state[31]. Wagner[30] combined the photoelectron binding energies and the kinetic energy of the corresponding Auger electrons in his concept of the so-called *Auger parameter* α as an empirical method to determine the chemical state of an atom in a sample. The Auger parameter is defined as:

$$\alpha = E_{\text{bin}}(\text{photoelectron}) + E_{\text{kin}}(\text{Auger electron}) \tag{2.4}$$

His concept is based on the idea that the energy difference between photoelectron and Auger electron of an element is fixed for particular compounds. In addition, the combination of kinetic energy of the Auger electron and the binding energy of the photoelectron cancel out effects due to surface dipoles or band bending and make work function corrections unnecessary. It has also the advantage of being independent on the excitation energy, which allows for comparing measured data with the results of other groups independent on the X-ray source used. There are two database of experimentally determined Auger parameter available in the internet worth being mentioned: one the one hand an extensive database of the National Institute for Standards and Technology (NIST)[29] and on the other hand one database provided by the UK Surface Analysis Forum[32]. A

comprehensive review of the Auger parameter concept can be found elsewhere[30;33].

An unwanted but important spectral feature to be aware of are X-ray satellite features. Those features arise due to the differences in excitation energy of the different X-ray lines in case of not using a monochromator (c.f Fig. 2.4). Fortunately, those features can nowadays easily be removed during data evaluation by aid of proper software routines. Additional final state effects that can occur in the photoemission spectra like plasmon energy loss features, multiplet splitting, shake-up and shake-off peaks will not be discussed here but are treated in various text books[26–28].

Photoelectron spectroscopies are very surface specific techniques. Even though the X-rays with energies usually used in XPS can penetrate about 1000 nm into the sample, the distance an electron can travel through matter without losing energy (and hence their information content) is much smaller. The distance an electron can travel without undergoing inelastic collisions is called the *inelastic mean free path* (IMFP) of an electron. According to Seah and Dench[34] the IMFP λ for inorganic compounds can be calculated by Eq. 2.5:

$$\lambda = \left(\frac{2170}{E_{\text{kin}}^2} + 0.72\sqrt{aE_{\text{kin}}} \right) \cdot a \tag{2.5}$$

a is the monolayer (ML) thickness of the material the electron travels through, expressed in nanometers. To determine the monolayer thickness for ZnO, we assume a crystal growth without a preferred growth direction. One can then calculate the monolayer thickness via the volume of the unit cell V and its number of atoms n:

$$a^3 = \frac{V}{n} = \frac{(\vec{a} \times \vec{b}) \cdot \vec{c}}{n} \,, \tag{2.6}$$

where the volume can be calculated forming the triple product over the basis vectors of the unit cell ($\vec{b} = \vec{a}$). Solving Eq. 2.6 results in a ZnO monolayer thickness of:

$$a = \sqrt[3]{\frac{(\vec{a} \times \vec{a}) \cdot \vec{c}}{n}} = \sqrt[3]{\frac{0.325^2 \cdot \cos 30^\circ \cdot 0.52}{4}} = 0.228 \text{ nm} \tag{2.7}$$

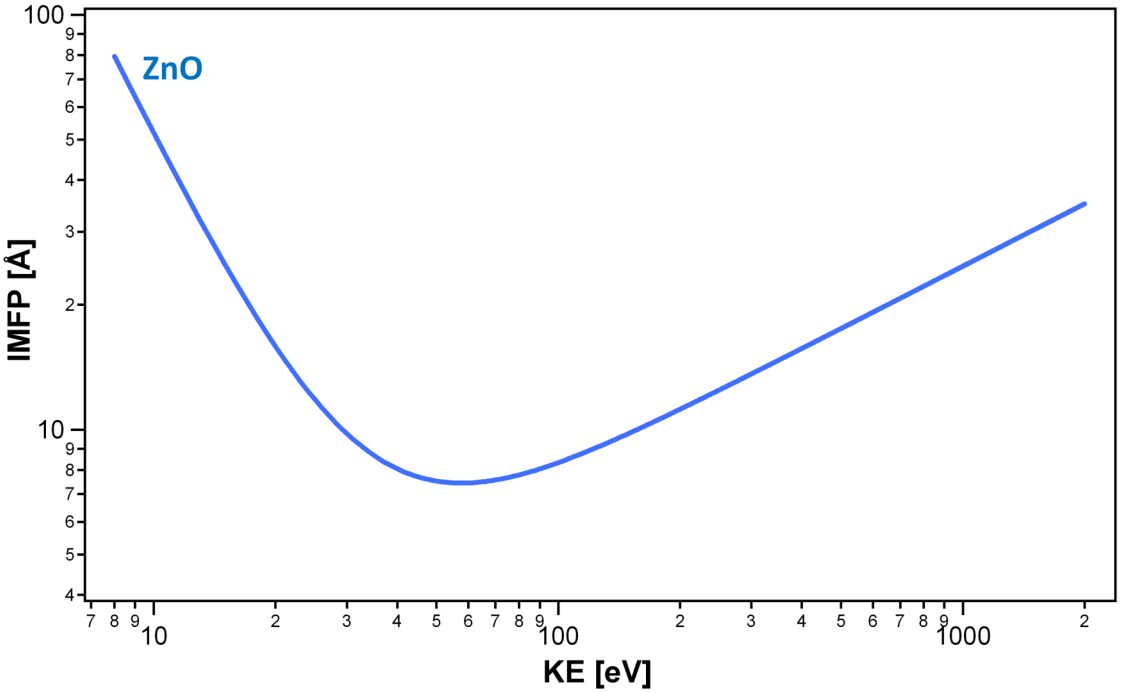

Figure 2.8: Calculated inelastic mean free path (IMFP) of photoelectrons in zinc oxide depending on their kinetic energy.

In case of ZnO, Fig.2.8 shows the IMFP calculated by Eq. 2.5 plotted against the kinetic energy of the excited photoelectrons. Even if the absolute values of the electron IMFP are just a rough estimate, it gives an idea about the surface sensitivity of the technique. Since the IMFP is a statistical value it does not mean that electrons excited deeper in the material than the IMFP do not contribute to the measured photoemission signal. 95 % of all photoelectrons escape from the so-called sampling or information depth of 3λ which results in a surface sensitivity of roughly 10 nm in photoelectron spectroscopy experiments. As mentioned above, the calculated IMFP is just a rough estimate. The actual values are difficult to determine and not only depend on the kinetic energy of the electrons but also on the density of the material the electrons have to penetrate, its composition and crystal structure.

Those electrons that are able to escape the crystal without losing energy contribute to the characteristic photoemission peak containing chemical information. In addition, there are photoelectrons that lost some energy by inelastic scattering processes but still have enough energy to escape the work function of the surface. Those photoelectrons contribute to a cumulative background signal which increases after each photoemission line in the spectrum also visible in Fig. 2.6. This background signal increases continuously towards

lower kinetic energy and has to be considered during quantification as shown later in this section.

Once an electron has been ejected from the sample, its kinetic energy has to be determined using an electron spectrometer. As illustrated in Fig. 2.3 those spectrometers are composed of three components: electron optics to retard the incident electrons, an electron analyzer to separate the electrons with respect to their kinetic energy, and a detector to count the electrons.
Nowadays, the most common electron analyzers are energy dispersive *concentric hemispherical analyzers* (CHA) also illustrated in Fig. 2.3. A CHA consists of two hemispheres in between an electric field is applied such that the outer hemisphere is more negative and the inner hemisphere more positive with respect to the potential at the center line[27]. This potential at the center of the analyzer is called the *pass energy* E_{pass}.
Electrons that enter the entrance slit of the analyzer with $E_{\text{kin}} \approx E_{\text{pass}}$ are deflected by the electric field, pass through the analyzer and are counted by a multichannel detector behind the exit slit. Electrons that enter the entrance slit with kinetic energies much higher than the pass energy will hit the outer hemisphere, those with much lower kinetic energies will be attracted by the inner hemisphere and will also not contribute to the measured signal.

Quantification

The quantification of the measured raw data usually includes two steps: the removal of the unwanted inelastically scattered secondary electron background and a peak fitting routine to determine the position and intensity of the photoemission peak. In this work, background subtraction is done by subtraction of a Shirley function[35] from the measured spectra. The Shirley background is illustrated by the blue shaded area in the left part of Fig. 2.9.
After removing the secondary electron background, a software-controlled peak fitting routine was applied to the data. It simulates the intensity distribution of the photoemission signal by a Voigt profile, which is a convolution of a Lorentzian and a Gaussian profile. Integration of the line profile then results in the particular peak intensity, as shown in Fig. 2.9 (b). To get comparable peak positions, it is important to calibrate the position of the Fermi energy and the energy scale of the spectrometer from time to time. Both is done by defined reference materials. Using clean metal surfaces, the position of the Fermi

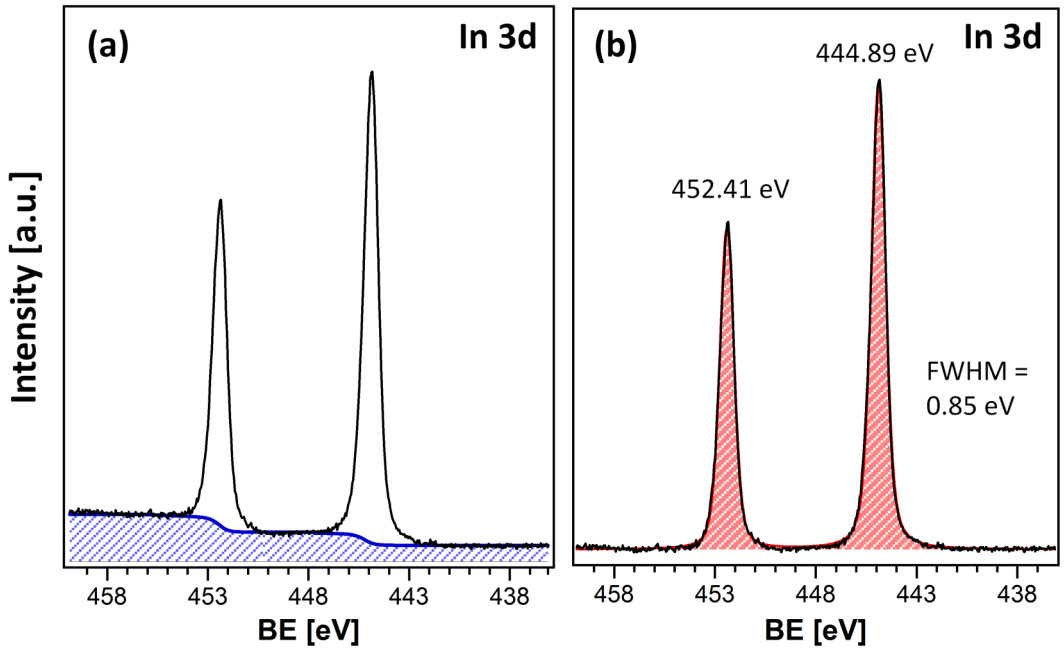

Figure 2.9: (a) inelastically scattered secondary electron background removal by applying a Shirley function (blue); (b) peak fitting by a Voigt profile. The integrated peak area (red) gives the peak intensity.

edge defines the energetic reference point for the core-level spectra. In addition, clean copper, silver and gold samples are used to calibrate the spectrometer for slow electrons (Cu), electrons of medium energy (Ag) and fast electrons (Au), respectively.

Many factors have influences on the measured peak intensity. According to Wagner et al. the detected photoemission intensity is given by Eq. 2.8[36]:

$$I = n \cdot f \cdot \sigma \cdot \Theta \cdot y \cdot A \cdot T \cdot \lambda \tag{2.8}$$

The contributing parameters are in particular:
I = photoemission intensity of a specific element per time unit [s^{-1}]; n = particle density of the element [cm^{-3}]; f = photon flux of the X-ray source [cm^{-2} s^{-1}]; σ = photoionization cross section of the particular element; Θ = angular efficiency of the spectrometer; y = photoelectron yield; A = surface area under investigation [cm^2]; T = transmission function of the spectrometer; λ = inelastic mean free path of the photoelectrons in a specific material.

	Zn $2p_{3/2}$	O 1s	Cu $2p_{3/2}$	In $3d_{5/2}$	Se 3d
Al Kα	23.93	3.1	20.28	13.89	2.22
Mg Kα	3.726	0.711	5.321	4.359	0.853

Table 2.2: Collection of the atomic sensitivity factors (ASFs) used in this work for compositional analysis in both XPS systems of the Integrated System.

While some of those parameters such as the illuminated area A, the angular efficiency Θ and the photon flux f can be assumed to be equal for different elements under investigation, some of them are material specific. In particular, this is of importance in compositional analysis, when comparing the individual photoemission intensities among each other. To simplify the compositional analysis, there are *atomic sensitivity factors* (ASFs) S_x provided by the spectrometer manufacturers for each element and their specific electron transitions. The atomic sensitivity factors used in this thesis are given in Tab. 2.2 for both XPS systems, respectively. They are given for a fixed angle between X-ray source and electron analyzer of 54.7°. There are differences in magnitude between the ASFs for Al Kα and Mg Kα radiation. They occur due to different normalization of the factors: while the data for Al Kα are normalized to the carbon 1s photoemission line, the ones for Mg Kα are normalized to F 1s. With those sensitivity factors, in compositional XPS analysis Eq. 2.8 reduces to:

$$I = n \cdot S_x \tag{2.9}$$

Hence, for zinc oxide the composition is given by:

$$\frac{[\mathrm{Zn}]}{[\mathrm{O}]} = \frac{n_{\mathrm{Zn}}}{n_{\mathrm{O}}} = \frac{I_{\mathrm{Zn}} : S_{\mathrm{Zn}}}{I_{\mathrm{O}} : S_{\mathrm{O}}} \tag{2.10}$$

Another useful feature of the photoemission intensity used in this thesis is the possibility of directly calculating the thickness of an overlayer by the attenuation of the substrate's photoemission signal(s). The only requirement is, that the overlayer has to be thin enough to allow photoelectrons of the substrate to travel-through without any inelastic scattering, i.e. its inelastic mean free path λ.
To determine its attenuation, one has to characterize the substrate prior to deposition of the overlayer by means of X-ray photoelectron spectroscopy. An easy way to calculate the film thickness after deposition of the overlayer is given by Seah and Dench [34]:

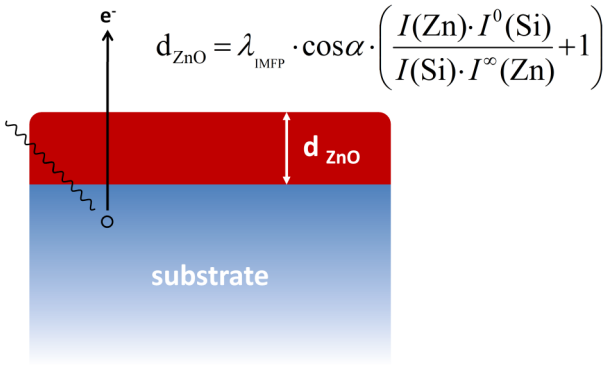

Figure 2.10: Schematic drawing of the overlayer thickness determination by attenuation of the substrate's photoemission attenuation and simultaneous increase of the overlayer photoemission signal according to Jablonski and Zemek [37].

$$I = I_0 \cdot \exp\left(-\frac{d}{\lambda}\right) \Rightarrow d_{overlayer} = -\lambda \cdot \ln\left(\frac{I}{I_0}\right) \tag{2.11}$$

where d = thickness of the overlayer; λ = inelastic mean free math of the particular photoelectron in a specific material; I = measured intensity of the substrate; I_0 = intensity of the substrate before overlayer deposition.

In this work, a more precise way to calculate the overlayer thickness reported by Jablonski and Zemek has been used [37]. Additionally to the attenuation of the substrate, they take into account the increase of the overlayer signal. In Eq. 2.12 the overlayer thickness calculation is presented for the case of ZnO deposition on a silicon substrate:

$$d_{ZnO} = \lambda(\text{Si } 2p_{3/2}) \cdot \cos\alpha \cdot \left(\frac{I(Zn) \cdot I^0(Si)}{I(Si) \cdot I^\infty(Zn)} + 1 \right) \tag{2.12}$$

There, α is the emission angle of the photoelectrons with respect to the surface normal. For normal emission (i.e. 90° with respect to the surface or 0° with respect to the surface normal), the $\cos\alpha$ term has no influence on the measurement, since $\cos(0°) = 1$.
To be able to calculate the overlayer thickness according to Eq. 2.12, one has to determine the intensity of the overlayer signal much thicker than the information depth of the substrate's signal $I^\infty(Zn)$. This has to be done just once for all subsequent measurements if the analysis system remains unchanged. A schematic drawing of the overlayer thickness determination with X-ray photoelectron spectroscopy is shown in Fig. 2.10.

In almost all XPS experiments the angle between sample surface and the electron optics remains constant at 90° with respect to the surface normal. Even though photoelectron spectroscopy is a very surface sensitive technique, in some cases it can be of advantage to further decrease the information depth of the photoelectrons. There are basically two ways to obtain increased surface sensitivity. One possibility is to reduce the inelastic mean free path of the photoelectrons by lowering the kinetic energy of the photoelectrons according to Fig. 2.8. Since the kinetic energy is directly connected to the excitation energy of the photon source (cf. Eq. 2.1) and each X-ray source has only one specific photon energy, it is usually not possible to reduce the IMFP by lowering the electron's kinetic energy in the laboratory. As shown later in this chapter, it is possible to vary the excitation energy using synchrotron radiation. Since those facilities are usually not available and measurements are very cost-intensive, there is a second way to reduce the information depth of the photoelectrons in the laboratory by reducing the exit angle of the photoelectrons with respect to the surface normal. Fig. 2.11 illustrates those *angle-dependent* XPS experiments. In the following, the exit angle is always denoted with respect to the surface, i.e. normal emission corresponds to 90°.

For normal photoelectron emission, the information depth ($\approx 3\lambda$) is identical to the *effective* information depth of the photoelectrons. If one changes the angle between the

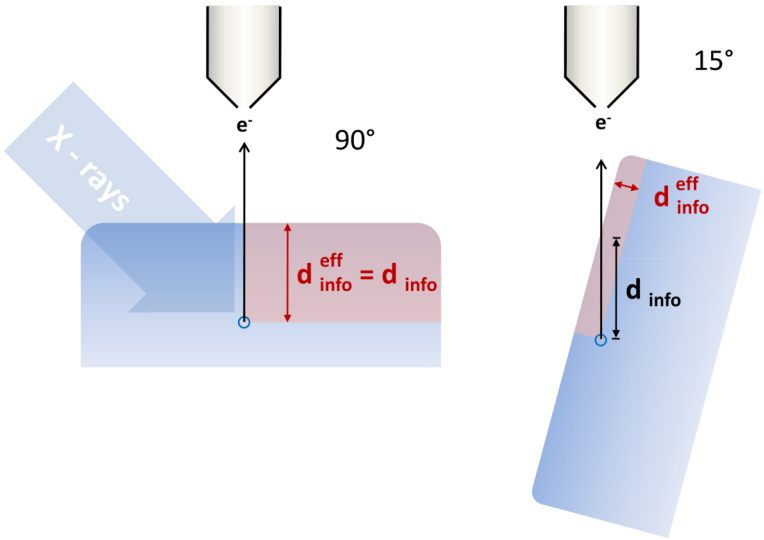

Figure 2.11: Illustration of angle-resolved XPS measurements to reduce the effective information depth of the photoelectrons. This increases the surface sensitivity of the measurements without changing the excitation energy of the X-ray photons.

surface and the electron optics, the path the electrons have to travel to escape the sample increases. Since λ remains constant, the effective information depth decreases and the measurements become more surface sensitive. This is illustrated at the right-hand side of Fig. 2.11. This allows to create non-destructive depth-profiling for instance of the samples' composition and is applied later in this work.

Accuracy of XPS measurements

Estimating the *absolute* error of photoemission spectroscopy experiments (in terms of the photoemission peak intensity and the accuracy in binding energy determination) is not trivial, since there are some parameters which might cause large inaccuracies. For instance, when calculating the thickness of an ZnO overlayer by attenuation of the substrate's photoemission signal (cf. Eq. 2.12), inaccuracies contributing from the peak fitting procedure (< 5 %) can usually be neglected, since the significant error arises from large uncertainties of the electrons inelastic mean free path (≈ 40 %[37]). Fortunately, the *relative* error, comparing the results of the experiments performed in the Integrated System under the same conditions among each other, is much smaller. These relative errors usually contribute mainly from data evaluation like the background removal procedure or peak fitting. Here, the inaccuracies depend on the signal-to-noise ratio of the measured signal, which in turn improves with increasing the overlayer thickness, as demonstrated in Fig. 2.12 for a very thin ZnO layer (left) and a film thickness in the range of the information depth (right).

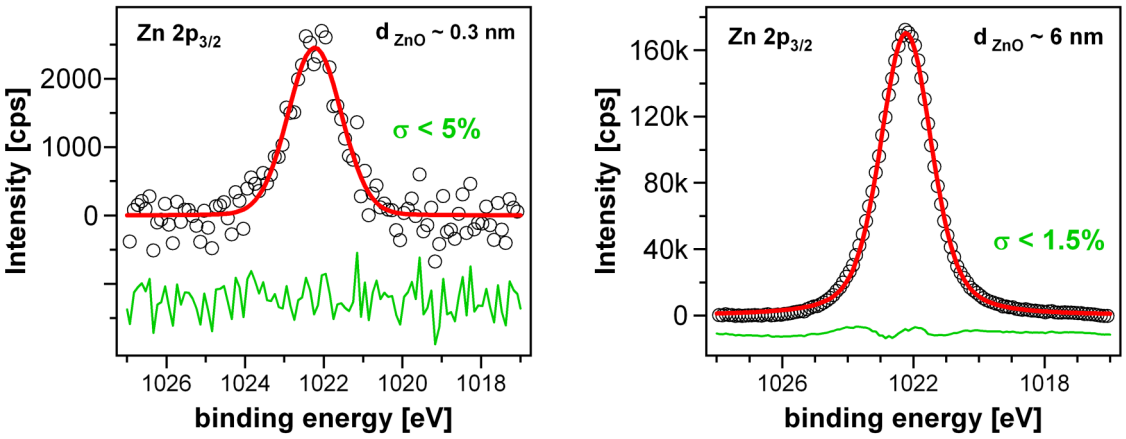

Figure 2.12: (left) Zn $2p_{3/2}$ peak fit of a very thin ZnO layer, resulting in an inaccuracy of $\sigma \approx 5$ % (right) same peak fitting of a thick ZnO film results in a smaller peak fitting error of only $\sigma \approx 1.5$ %

In case of a thin ZnO overlayer, the error of the data evaluation σ was determined being $\sigma \approx 5\,\%$, represented by the difference spectrum between the measured and the fitted data (green). With increasing film thickness, the signal-to-noise ratio decreases for the elements present in the overlayer, resulting in an relative error of only about 1.5 %. At the same time, the signal-to-noise ratio of the substrate's photoemission signals increases due to their decreasing peak intensity. Since the overlayer thickness is calculated from the attenuation of these signals, the relative error of film thickness determination also depends on the overlayer thickness as discussed just recently, being 5 % at most.
In angle-dependent XPS experiments, an additional error results from inaccuracies in adjusting the emission angle by tilting the sample. Assuming an error of 1° at most, the $cos\alpha$ dependency of the peak intensity given in Eq. 2.12 results in an additional error of 2 % for small emission angles. For normal emission, the error is only about 0.2 % per degree deviation from the surface normal and hence can be neglected. Besides an error in peak intensity determination, one also has to consider inaccuracies in determination of the peak's position. Since the spectrometer was calibrated by well-defined reference samples, the absolute error is very small, usually assumed being below 0.1 eV.

2.2.2 Ultraviolet Photoelectron Spectroscopy

While X-ray photoelectron spectroscopy contains information about the core-level electrons, ultraviolet photoelectron spectroscopy (UPS) allows analysis of the valence electron states that form interatomic bonds between the atoms. Instead of using high energy X-rays to excite the photoelectrons, UPS uses ultraviolet radiation of a helium discharge lamp, resulting in an excitation energy of $h\nu = 21.22$ eV for the He I transition. This low excitation energy is not able to excite core-level electrons but can emit loosely bound photoelectrons of the valence band. The helium discharge lamp does not only provide very intense photons of the He I discharge, but also He II_α of $h\nu = 40.8$ eV and He II_β with $h\nu = 48.0$ eV energy. As in X-ray photoelectron spectroscopy, satellite peak contribute to the measured spectra, that have to be removed for quantitative analysis. The line width of the He I line of only 3 meV results in very high energy resolution of the valence band spectra, usually limited by the energy resolution of the electron analyzer [28].

A typical valence band spectrum of a semiconductor recorded by He I irradiation is shown in Fig. 2.13 (a). One can directly determine the work function of the material by the position of the secondary electron cutoff at the high binding energy side of the

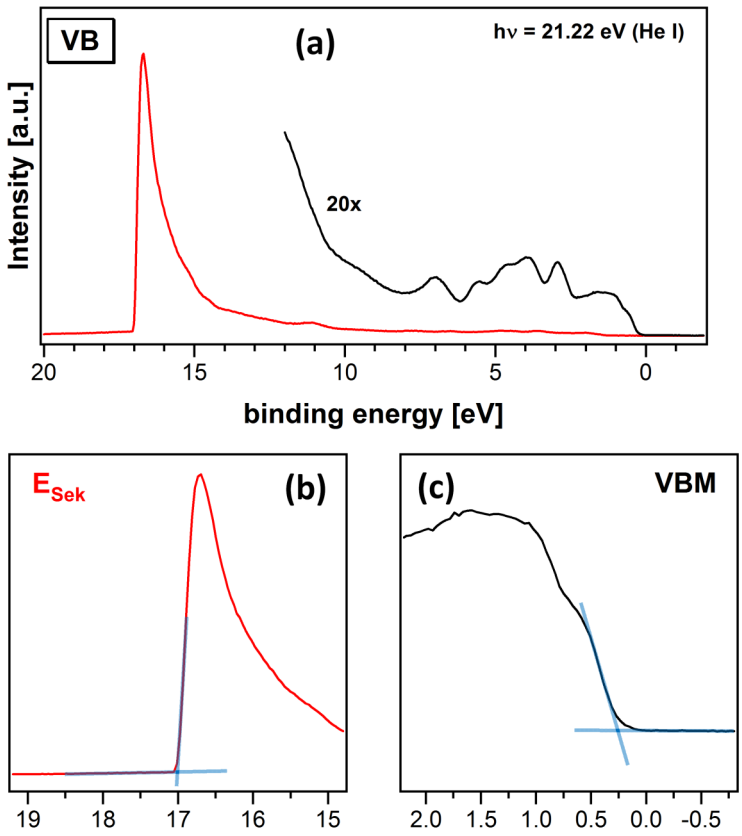

Figure 2.13: (a) Ultraviolet photoelectron spectrum containing the valence band structure of a semiconductor; (b) secondary electron cutoff; (c) valence band maximum

spectrum. An enhancement of the secondary electron cutoff is shown in Fig. 2.13 (b). The work function ϕ is simply calculated by subtraction of the secondary electron cutoff energy from the excitation energy of the He I discharge ($h\nu = 21.22$ eV):

$$\phi = h\nu - E_{\text{sec}} \tag{2.13}$$

At the low binding energy side of the valence band spectrum, the valence band maximum (VBM) can be determined. The easiest way is to do a linear extrapolation of the valence band edge. This is illustrated in Fig. 2.13 (c) by the blue lines. The point of intersection corresponds to the valence band maximum of the semiconductor material. Knowledge of the VBM and the secondary electron cutoff E_{sec} directly results in the ionization energy E_{ion} of the material:

$$E_{\text{ion}} = h\nu - E_{\text{sec}} + E_{\text{VBM}} \tag{2.14}$$

In addition, knowledge of the band gap width E_g between the conduction band minimum and the valence band maximum of the semiconductor results in the electron affinity of the sample. The band gap energy is known from literature values. One has to be aware that those values are usually determined for bulk crystals and the actual band gap for ultra-thin films can differ from those values. Nevertheless, the electron affinity can be calculated according to Eq. 2.15:

$$\chi = \phi + E_{\mathrm{VBM}} - E_g \tag{2.15}$$

The combination of UPS and XPS is a very powerful method to investigate the heterointerface of two semiconducting materials. Especially the in situ deposition and analysis of semiconductor A on semiconductor B is of interest in this work and can help to investigate the electronic band alignment of the heterocontact. This contact is of utmost importance for the efficiency of electronic devices, such as for instance solar cells and therefore detailed knowledge of the band alignment is required. More details about the band alignment is given later in Chp. 5.

2.2.3 Synchrotron Radiation

In contrast to laboratory X-ray sources, which are limited to one specific photon energy due to the defined electron transitions in the anode material, synchrotron radiation provides tunable radiation in a wide energy range. Unfortunately, synchtrotron radiation cannot be created in the laboratory but requires large electron acceleration facilities, what limits their every day use in science and technology.
The experiments presented in this thesis were all performed at the BESSY-II synchrotron radiation facility in Berlin, where a cooperative research group of the University of Cottbus, the University of Darmstadt and the Helmholtz-Center Berlin operate the U49/2-PGM2 beam line. The close vicinity of the synchtrotron radiation facility allows to transport the samples from the laboratory to the BESSY II beam line under ultra-high vacuum conditions.

Fig. 2.14 illustrates the principle of the BESSY II synchrotron radiation facility. Bunches of electrons are injected into the inner synchrotron ring, where they are accelerated to energies of 1.7 GeV, resulting in velocities close to the speed of light. After the electrons have been accelerated, they are injected into the electron storage ring, with a circumference

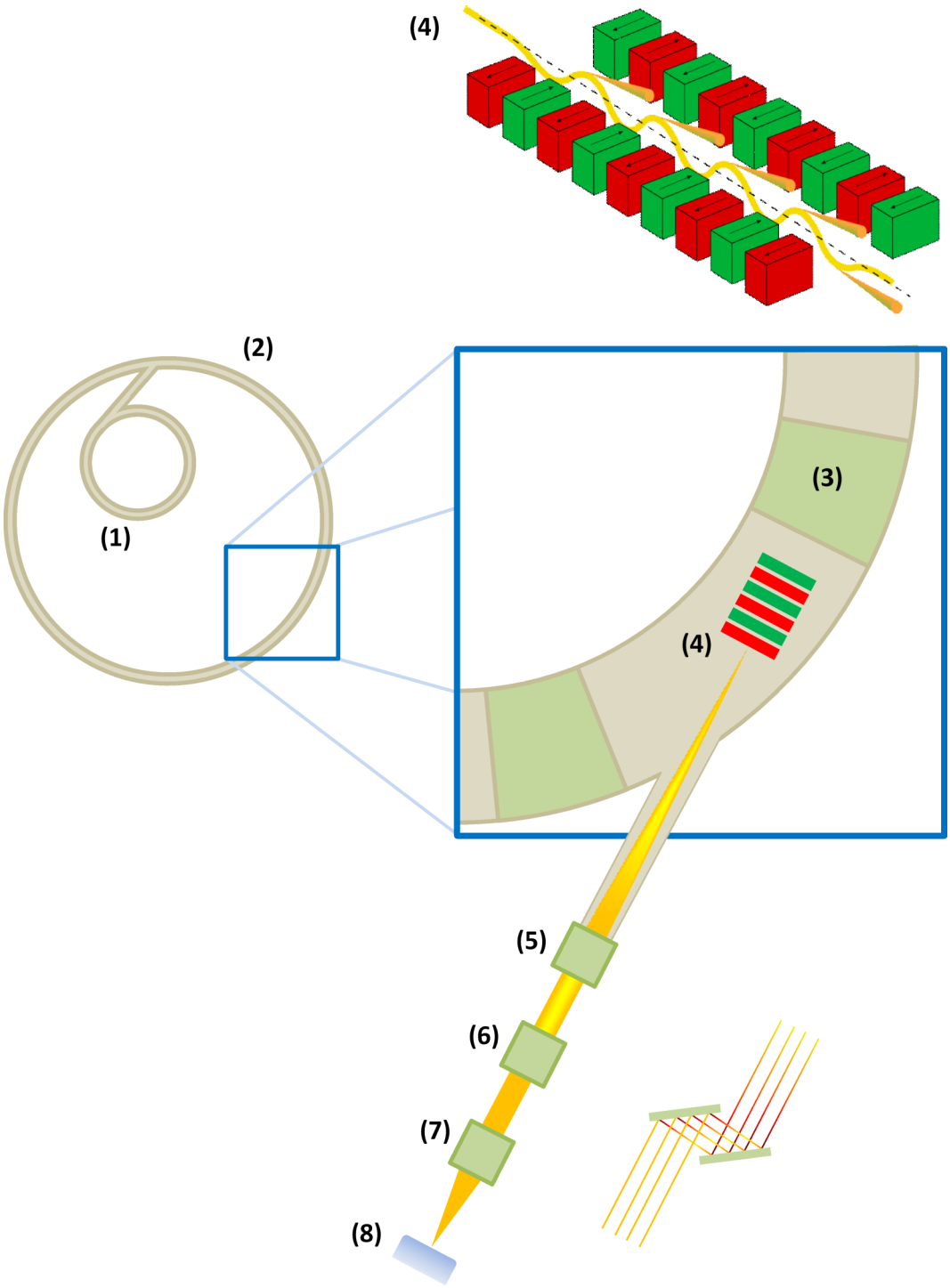

Figure 2.14: Schematic of the BESSY synchtrotron radiation facility: (1) electron accelerator; (2) electron storage ring; (3) bending magnets; (4) undulator; (5) collimating mirror; (6) monochromator; (7) toroidal mirror; (8) sample

of 240 m. There, bending magnets and undulators force the electrons to circulate around the storage ring for a long period of time. Forcing a charged particle into a circular orbit, they are accelerated radially and emit a continuum of light, the so-called synchtrotron radiation. For the U49/2-PGM2 beam line, this synchtrotron radiation is created and inserted into the beam line by an undulator, as illustrated in Fig. 2.14. An undulator is composed of a linear periodic structure of dipole magnets. Their static magnetic fields force the electrons into a sinusoidal oscillation, thus emitting intense synchtrotron light. This light enters the beam line as a cone with a small divergence angle. After entering the beam line, a cylindrical mirror is used to collimate the beam. This parallel beam of light them enters the monochromator, where the desired photon energy is chosen. This particular beam line is able to provide energies in a range between $86 - 1890$ eV. After monochromization, the light beam is focused onto the sample, resulting in a small illuminated area of high intensity. Synchrotron radiation photoelectron spectroscopy (SR-PES) offers very high spectral resolution and excellent signal-to-noise ratios. But it is its tunable radiation source that allow some unique experiments and makes synchrotron radiation a powerful tool in physics and materials science.
In X-ray photoelectron spectroscopy, photons of constant energy create photoelectrons of different kinetic energies. As discussed earlier, the distance an electron can travel in a crystal without undergoing inelastic scattering events (i.e. the inelastic mean free path) depends on the kinetic energy of the photoelectrons. Hence, the photoelectrons contributing the spectra can have their origin in different depths of the material, possibly resulting in significant errors during data evaluation. The tunable excitation energy of the photons allow to excite photoelectrons with specific kinetic energy according to Eq. 2.1. According to Fig. 2.8, the information depth of the SR-PES experiments can be chosen either very surface sensitive (for low kinetic energies) or electrons can be created deeper in the material. Recording a range of different kinetic energies will result in non-destructive depth profiling of the surface under investigation.

Quantification

Quantification of the SR-PES data is much more time consuming than in case of X-ray photoelectron spectroscopy. In contrast to XPS experiments, where the flux of incident photons on the surface can be assumed being constant, this is not the case for the synchrotron radiation. Here, the photon flux depends on several factors, such as the selected photon energy, the amount of photons rejected by the exit slit, and the electron beam

current in the electron storage ring. A proper way to normalize the spectra to allow comparability between the different measurements is to measure the intensity of the incident photons with a GaAs photodiode. The spectra are normalized according to Eq. 2.16:

$$I_{\mathrm{norm}} = I^0 \cdot \frac{X \cdot Y_{\mathrm{diode}}}{I^0_{\mathrm{ring}} \cdot \sigma} \tag{2.16}$$

To normalize the measured photoemission spectra of intensity I^0, the diode current I_{diode} and the current in the storage ring $I^{\mathrm{ref}}_{\mathrm{ring}}$ have to be determined for the applied excitation energy / exit slit combination. This results in a factor $X = I^{\mathrm{ref}}_{\mathrm{ring}}/I_{\mathrm{diode}}$ to normalize the spectra with respect to the ring current I^0_{ring} when a particular spectrum has been recorded. The yield of the GaAs diode Y_{diode} is also energy-dependent and has to be determined. Its characteristic curve is well-known for the photon energy range used in this work. σ in Eq. 2.16 describes the ionization cross-section of a particular chemical element. This is also energy-dependent and can be obtained from reference works, such as the work of Yeh and Lindau[38].
Since there are several factors contributing to the normalization of the measured data, the error in data evaluation is expected to be increased with respect to the laboratory XPS work. Due to the very good signal-to-noise ratio, the error of data evaluation of I^0 can be expected being below 1.5 %. The ring current of the storage ring does not change significantly during the particular measurements. The absolute error is approximated being below 0.5 % for $I^{\mathrm{ref}}_{\mathrm{ring}}$ and I^0_{ring}, respectively. Additionally assuming the error of Y_{diode}, I_{diode}, and σ each with 1 % at most, the total error of I_{norm} can be estimated estimated being below 6 %. As in case of XPS, the energy scale of the spectrometer was calibrated by standard reference samples, resulting in an absolute error below 0.1 eV of the peak's energy position.

2.3 Low-Energy Electron Diffraction

Applying low-energy electron diffraction (LEED) is a very useful tool to characterize crystalline surface structures. Even though the focus of this work is on photoelectron spectroscopy, LEED has been used to verify the quality of the substrate surfaces for the subsequent ZnO deposition experiments.

The basic principle of electron diffraction in a crystal is illustrated in Fig. 2.15. A collimated beam of electrons, typical kinetic energies are in a range between $20 - 200$ eV, is

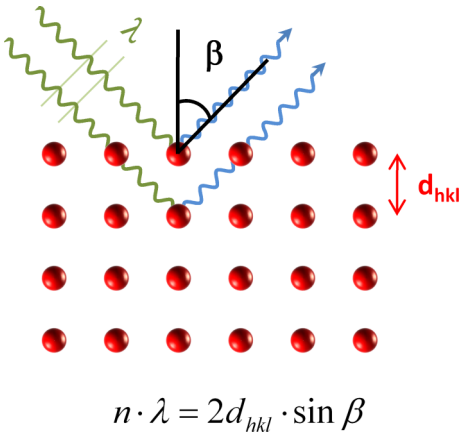

Figure 2.15: Principle of electron diffraction at a crystal surface.

directed on a crystal surface. The electrons are created in a hot cathode and accelerated to the substrate by a couple of electrodes. The electrons interact with the crystal an electrons can be elastically scattered. In some cases, the path difference of the scattered electrons match the Bragg condition $n\lambda = 2d_{\mathrm{hlk}} \cdot sin\beta$, resulting in constructive interference of the scattered electrons. In reciprocal lattice, the Bragg condition can be expressed as $\mathbf{G} = \mathbf{k_j} - \mathbf{k_0}$, where $\mathbf{G}$ corresponds to the reciprocal lattice vector, while $\mathbf{k}_0$ and $\mathbf{k}_j$ represent the wave vectors of the incident and diffracted beams, respectively.

Fig. 2.16 shows a combination of the reciprocal lattice and the spot pattern observed for LEED experiments. The electrons that fulfill Bragg's law, i.e. where the Ewald sphere intersect a reciprocal lattice point, appear as bright diffraction spots on the luminescent screen. Hence, the diffraction pattern provides a direct reproduction of the reciprocal lattice. For detailed information about the technique and its information content it is referred to various text books[39–41]. In this work, LEED is only used to check the crystalline quality of the prepared substrates. In addition, the presence of a secondary electron background can give an indication about the cleanliness of the prepared surface.

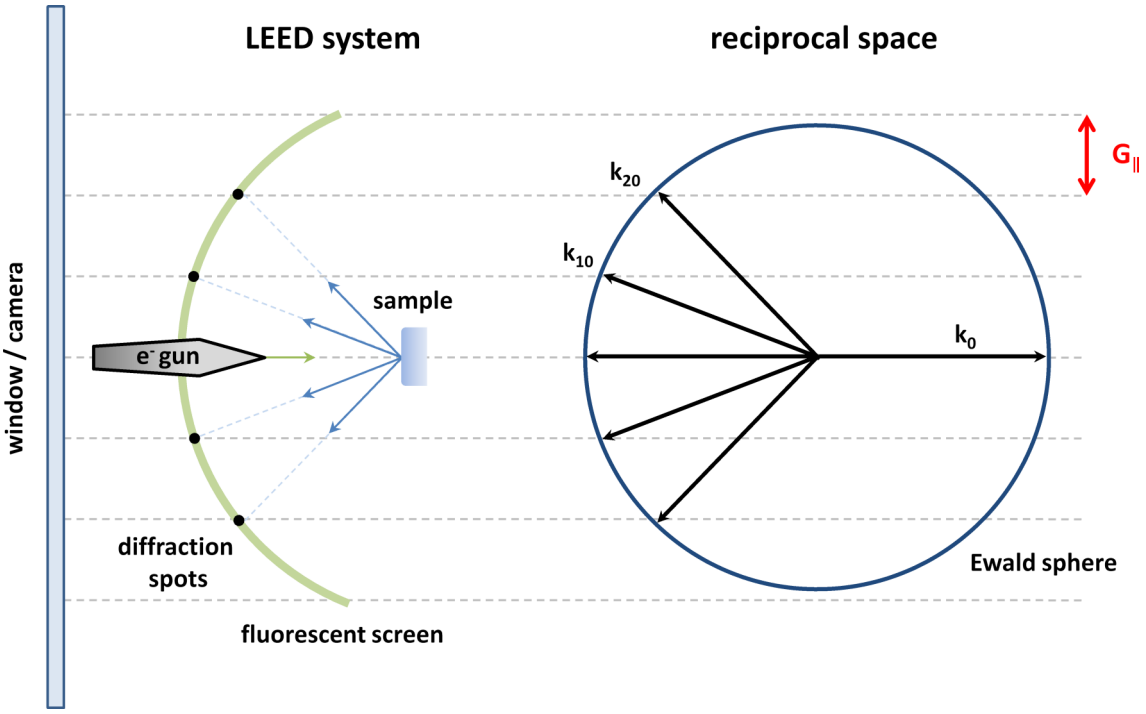

Figure 2.16: Illustration of a LEED diffraction pattern formation by constructive interference of diffracted electron fulfilling Bragg's law.

3 Thin-Film Deposition

Nowadays thin-films are used in a wide field of applications as for instance in thin-film chalcopyrite solar cells as introduced in Sec. 1.1. Producing thin-films from the vapor phase is of great importance and the processes occurring when atoms or molecules impinge on a materials surface are crucial for the quality and properties of the films produced. In the following chapter, first some general remarks about the atomic events of initial layer growth are presented. Afterwards examples of several important vapor phase deposition techniques are given and their particular advantages and disadvantages are discussed.

3.1 General Issues of Thin-Film Deposition

There are a couple of different processes in thin-film growth as the adsorption of the gas phase atoms and molecules on the surface to be coated, surface diffusion of the adsorbed species, re-evaporation processes and the final film formation. The structural properties of the formed films depend on both, the conditions in the deposition system as well as the combination of the substrate and film materials. The conditions in the deposition system will vary for the different techniques and hence their influence on the film structure will be discussed in the particular sections.

First we will take a look at the atomic processes when a molecule approaches a surface. To be deposited on the substrate it has to be bound to the surface, a process known as adsorption. Usually one distinguishes two types of adsorption mechanisms and that is physisorption and chemisorption, respectively. Figure 3.1 illustrates the differences between both adsorption mechanisms in an energetic manner. If a molecule reaches the surface from the vapor phase it will feel an attractive force which accelerates it towards the surface. Even it is, from a thermodynamic point of view, energetically favorable for

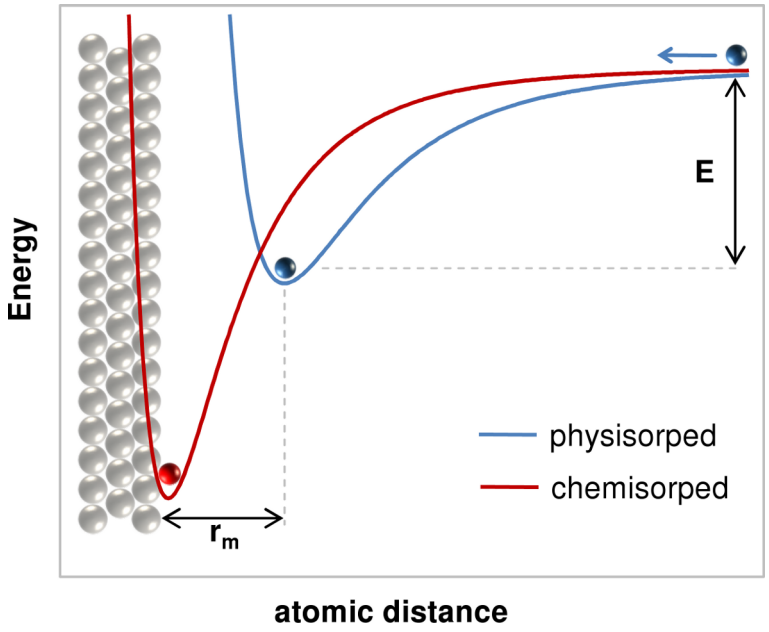

Figure 3.1: Energetic conditions of atoms approaching a surface where they either are physisorped by weak van-der-Waals forces or strongly bound when chemical bonds are formed between surface and adsorbed atom in a chemisorption process.

the arriving molecule and the substrate's atoms to react and form a chemical bond, the interatomic bonds in the arriving molecule might be too strong to reorganize spontaneously. In this case, the molecule will remain loosely bound at the surface bound by electrostatic van-der-Waals forces. In Fig. 3.1 this process is illustrated in terms of a Lennard-Jones potential which is the result of attractive and repulsive forces affecting the incident molecules. Mathematically, the Lennard-Jones potential can be expressed as shown in Eq. (3.1):

$$E = \epsilon \left(\left(\frac{r_m}{r} \right)^{12} - 2 \left(\frac{r_m}{r} \right)^{6} \right) \tag{3.1}$$

As shown in Fig. 3.1 the Lennard-Jones potential will form a well of depth ϵ which defines an energetically favorable position r_m for the molecule to remain at. To form a stable chemical bond to the surface the physisorbed atom in the potential well of the blue curve first requires some extra energy to break some intramolecular bonds. This is illustrated by the energy barrier between the potential well of the blue curve and the intersection point with the red curve. The additional energy might be provided by thermal heat which allows the atom to overcome the energetic barrier. Chemical bonds are formed and the adsorbed atom is strongly bound, i.e. it is chemisorbed at the substrate's surface. On the

other hand, if the energy required to change from the physisorped state to the chemisorbed state is higher than the binding energy between molecule and surface, it is more likely for the adsorbed molecule to desorb from the surface.

Once a molecule is adsorbed on the surface it might move to a neighboring surface site which is not occupied by other molecules adsorbed from the vapor phase. Depending on the surface coverage (and therefore on the deposition rate of the material on the surface) surface diffusion might be more or less favorable. Generally speaking, the lower the deposition rate, the higher the surface diffusivity. This, in turn, results in improved structural quality of the deposited films.

When a thin-film of material B is deposited onto a substrate A the film is desired to grow with uniform thickness distribution across the whole surface area. In practice, the morphology of the deposited film depends on a couple of properties of both the substrate as well as the material to be deposited.

Much of the thin-film structure achieved during deposition from the vapor phase can be attributed to surface energies of the substrate γ_{SA}, the film material γ_{SB} and the energy of their interface γ_{AB}. The surface energy is a quantity that expresses the additional amount of energy of a surface compared to the energy of the bulk crystal. At the surface the bonding conditions of the particular atoms differ from that in the bulk because there is no partner to form bonds with which results in dangling bonds. By reconstruction, i.e. reorganization of the surface atoms, the number of dangling bonds can be reduced and the surface energy is lowered. An illustration of the different surface energies for a material B deposited on a substrate A is given in Fig. 3.2.

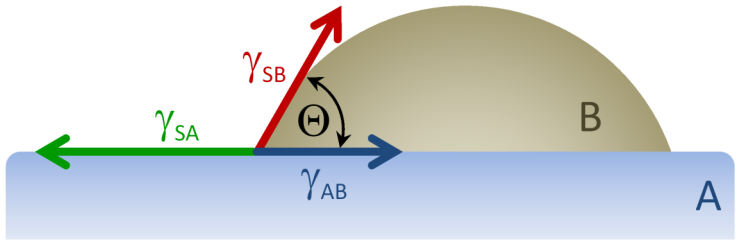

Figure 3.2: Contact angle Θ in case of deposition of a material B onto a substrate material A. γ_{SA} denotes the surface energy of the substrate, γ_{SB} the one of the deposit B and γ_{AB} the interface energy between A and B.

It is common to express the surface energies in terms of the contact angle Θ. Mathematically, this can be described by Young's Equation given in Eq. (3.2).

$$\gamma_{SA} = \gamma_{SB} + \gamma_{AB} \cdot \cos\Theta \tag{3.2}$$

Desired is a contact angle of $\cos\Theta = 0°$ where the material does not form a droplet but spreads over the whole surface area and forms a thin-film. This is the case when the film deposited onto material A lowers its surface energy by saturating the dangling bonds without further reconstruction. On the other hand, if the surface energy of material A is increased by depositing film B the film will tend to minimize the covered area of the substrate. This will lead to the formation of islands of material B. A third mode of thin-film growth is the so-called Stranski-Krastanov or layer-plus-island growth mode. In this process first some monolayers are deposited in a layer-by-layer mode and beyond a critical thickness, depending on lattice strain and the chemical potential, the film continues growing in an island growth mode. All three possibilities, layer-by-layer (or Frank-van der Merwe) growth, island (or Volmer-Weber growth), and Stranski-Krastanov growth are illustrated in Fig. 3.3.

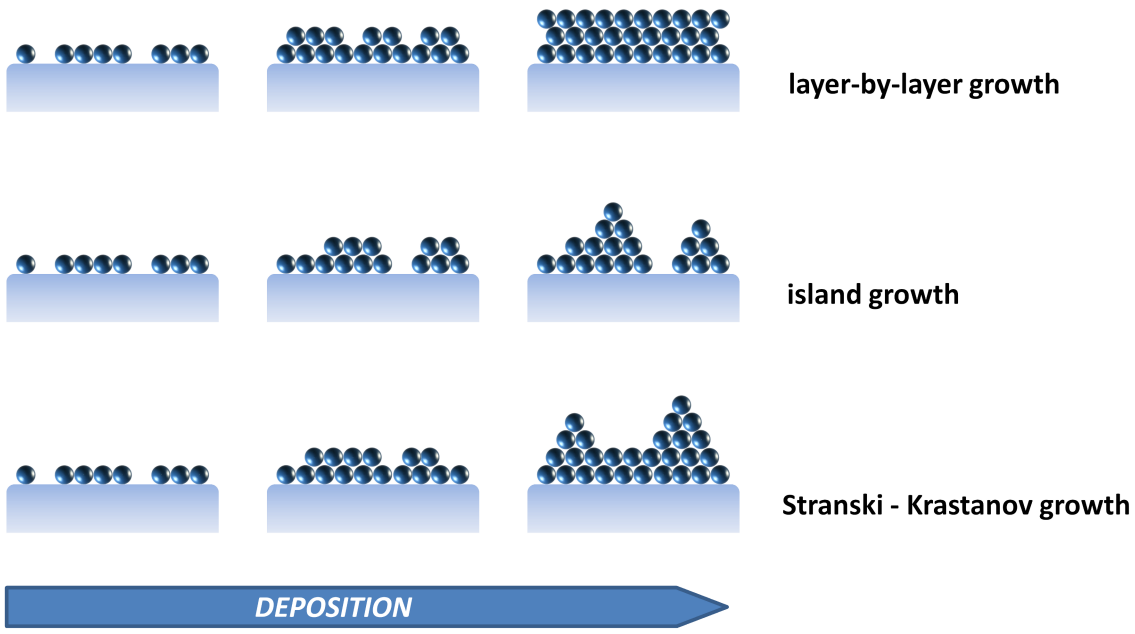

Figure 3.3: Three different growth modes observed during thin-film growth: (top) layer-by-layer growth, (middle) island growth, (bottom) Stranski-Krastanov growth

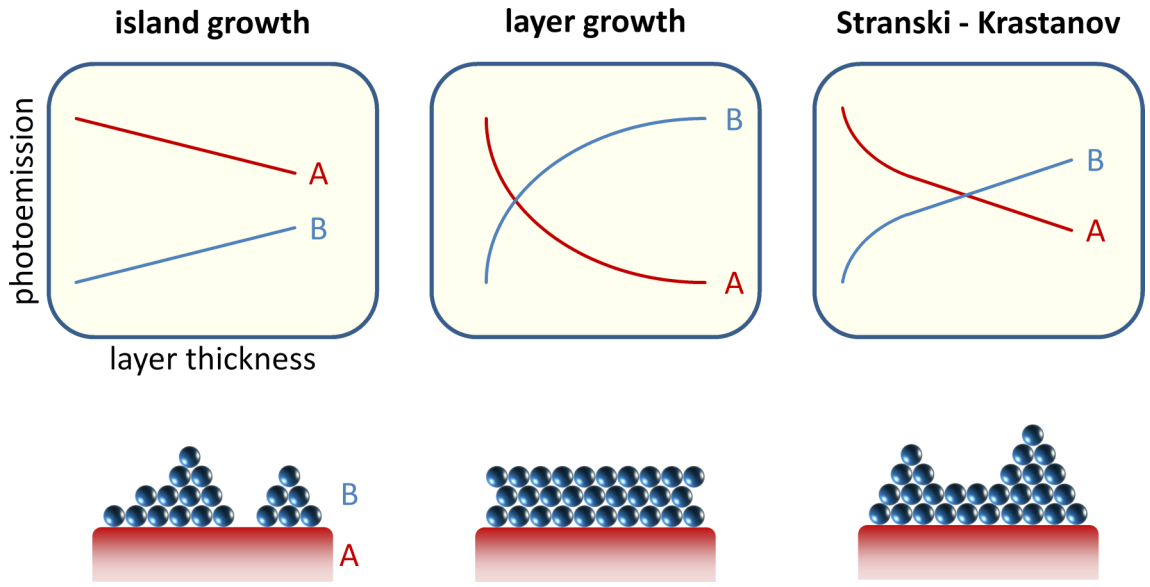

Figure 3.4: Photoemission signal characteristics for the three different primary thin-film growth modes. The attenuation of the substrate photoelectrons A and the increase of the film material B can be measured in situ during the initial growth.

Surface energy is not the only factor influencing the growth mode. Lattice mismatch is another important one. If the lattice constants between substrate material and deposit do not fit a layer-by-layer growth is not very likely. Therefore, even if a deposit would lower the surface energy of the substrate there may be an energetic favor of growing in an island growth mode.
Which type of growth mode occurs in the initial growth regime of the thin-film can be measured by photoelectron spectroscopy. As long as the deposited film is thin enough for photoelectrons of the substrate to escape the growth mode can be determined by the attenuation of the substrate signal and the increase of the film signal as shown in Fig. 3.4.

Another point of interest in crystalline thin-film deposition is the orientation of the growing film. In case of island growth, polycrystalline films are formed whose grains usually try to reduce the density of dangling bonds by growing in a preferred orientation to the substrate[42]. The distribution of crystallographic orientations is called the texture of the film and can be measured by X-ray diffraction techniques. Epitaxy is the most perfect way of growing a material B onto a material A. It results in a single-crystalline film which has taken on the lattice structure and crystal orientation of the subjacent substrate. One distinguishes between two types of epitaxial growth, homoepitaxy and heteroepitaxy, respectively. In homoepitaxy the substrate and the deposited film consist

of the same material and therefore their structural properties match perfectly. In contrast, in heteroepitaxy the deposit and the substrate material differ from each other. Therefore, their lattices will usually not match perfectly which leads to lattice strains in the beginning of the overlayer growth. This can influence the electronic properties of the interface as will be shown later in this work. For further details of thin-film growth the reader is referred to the books of Ohring[43] and Rockett[42].
Generally, one can divide the wide field of thin-film deposition techniques into the two major classes of physical vapor deposition (PVD) and chemical vapor deposition (CVD). The following two sections will give an overview of their basic properties, their differences and their particular advantages and disadvantages with respect to the final film properties.

3.2 Physical Vapor Deposition

From an historic point of view physical vapor deposition is one of the oldest thin-film deposition techniques. The most widely used methods are thermal evaporation of a hot source material and sputter deposition where the material to be deposited is removed from a solid target by impact of high energy gaseous ions, usually Ar^+. The momentum transfer during ion impact evaporates the target material which is then deposited onto the substrate. The use of an ionized sputter gas results in a higher background pressure during film deposition. In contrast, thermal evaporation is operated under high vacuum conditions ($p = 10^{-6}$ mbar) and hence it shows beneficial results in terms of film purity and the deposition rate is increased with respect to sputter deposition. Since sputter deposition has not been used in this thesis it will not be treated here in more detail. For further reading there are various textbooks (e.g.[43;44]) giving extensive reviews of sputter deposition techniques. Instead, we take a closer look at thermal evaporation and a techniques that is closely related and of utmost importance, namely molecular beam epitaxy (MBE).

3.2.1 Thermal Evaporation

In thermal evaporation processes a crucible containing the source material to be deposited as a thin-film is heated resistively. This heating process converts the condensed phase of the deposit into its vapor phase. If those atoms reach a substrate in the deposition

chamber they condense and form a thin film as described in Sec. 3.1. Hence, it is obvious that the key parameter determining the deposition rate of the film is the temperature of the evaporation source. A relation between temperature T and vapor pressure p of a material is given by the Clausius-Clapeyron equation[44]:

$$\frac{dp}{dT} = \frac{L}{T(\nu_g - \nu_c)} \tag{3.3}$$

where L is the amount of energy needed to evaporate 1 mol of material, ν_g its molar volume in the gas phase, and ν_c the molar volume in its condensed state. Assuming that L is independent on temperature, the vapor can be described with the ideal gas law and assuming that the volume of an amount of material is much larger in its vapor phase than in its solid state, i.e. $\nu_g \gg \nu_c$, Eq. (3.3) can be written as:

$$\log_{10} p = -\frac{A}{T} + B \tag{3.4}$$

where A and B are constants that can be experimentally determined. In case of zinc selenide (ZnSe) evaporation one can find reported values[45] for $A = 6250 \pm 187.5$ and $B = 3.762 \pm 0.41$. Figure 3.5 plots the calculated vapor pressure of ZnSe over the temperature range interesting for ZnSe evaporation.

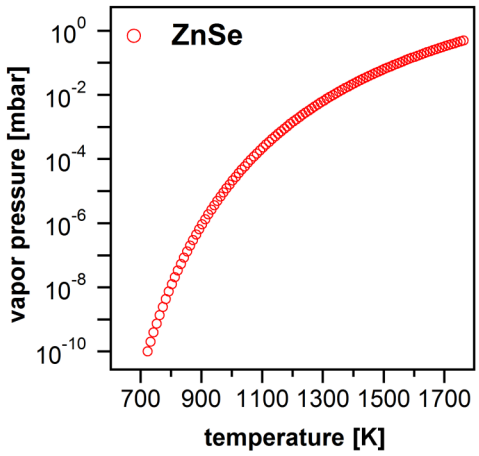

Figure 3.5: Calculated ZnSe vapor pressure during evaporation at different source temperatures. The vapor pressure was calculated by the Clausius-Clapeyron equation using $A = 6250$ and $B = 3.762$

While metal sources vaporize mostly in the form of single atoms the same is usually not valid evaporating compounds consisting of two elements A and B. There are only few compounds which evaporate congruently, i.e. in a single vapor phase AB(g) without dissociation. Examples are fluorides like CaF_2 or some simple oxides like SiO[44] due to their strong interatomic bonds. Most other compounds decompose during heating because of differences in the vapor pressures of their elemental components, i.e. they vaporize non-congruently. This can lead to a change in composition in the deposited film with respect to the stoichiometric source material. Usually those films tend to be metal-rich. A typical reaction for chalcogenides like ZnSe where the compound dissociates into two vapor phases can be expressed as:

$$AB(s) \rightarrow A(g) + B(g)$$

In compounds whose elements have significant differences in their vapor pressures like in nitrides or carbides one component remains solid while the other evaporates:

$$AB(s) \rightarrow A(s) + B(g)$$

Both cases, congruent and noncongruent evaporation, are schematically depicted in Fig. 3.6.

Evaporating the source material by resistive heating of the crucible is the most commonly used thermal evaporation technique. One important requirement of every evaporation source is that there is only an insignificant amount of vapor created by the crucible material itself. Otherwise the purity of the formed thin-film cannot be guaranteed. Typical

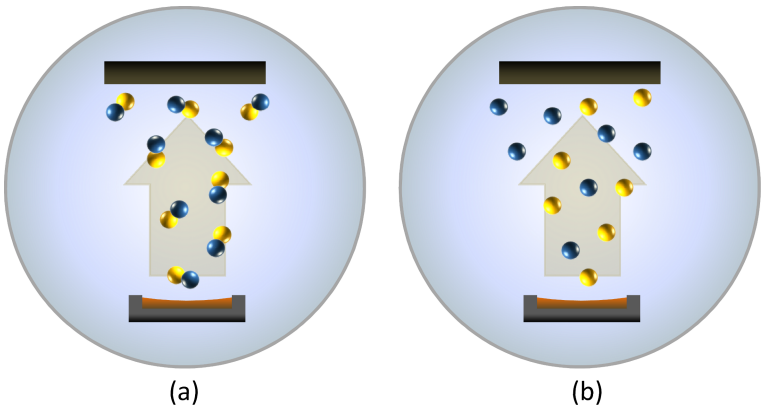

Figure 3.6: Schematic illustration of different types of thermal evaporation of compounds: (a) congruent evaporation where the compound evaporates without dissociation and (b) noncongruent evaporation where the two atomic species evaporate at different temperatures

materials for evaporation sources are tungsten, tantalum or ceramics with high melting points and low vapor pressures. Further origin for possible film contaminations are impurities in the source material to be deposited and residual gases in the deposition chamber. The former can be reduced to a minimum by outgassing of the sources, the latter is prevented by high vacuum conditions in the evaporation system.

A somehow special case of thermal evaporation is the important and powerful technique of molecular beam epitaxy (MBE) which will be treated in the following section.

3.2.2 Molecular Beam Epitaxy

As mentioned before molecular beam epitaxy (MBE) can be seen as a more sophisticated type of thermal evaporation. The major difference between those two techniques is the vacuum level where the film deposition is operated at and the use of advanced effusion cells, so-called Knudsen cells. A schematic picture of a MBE deposition chamber is given in Fig. 3.7.

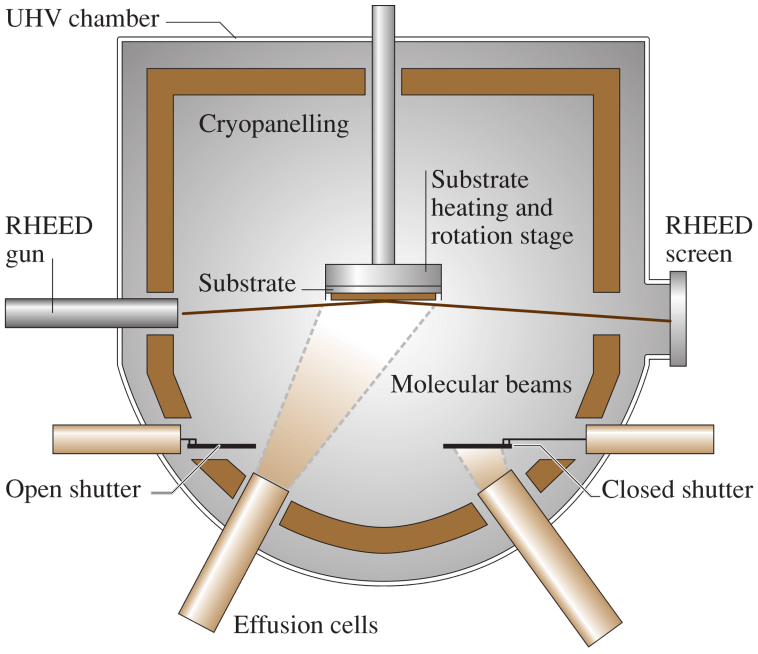

Figure 3.7: Schematic drawing of a molecular beam epitaxy (MBE) system, taken from Capper et al.[46]

While in thermal evaporation systems high vacuum conditions with pressures in the 10^{-6} mbar region are sufficient to produce high quality films, the same is not true for MBE systems. The reason for this is the reduced deposition rate in molecular beam epitaxy. Those are typically below 1000 nm/h to produce highest crystalline qualities atomic layer by atomic layer. To prevent incorporation of impurity atoms at such low growth rates ultra-high vacuum conditions with background pressures below 10^{-9} mbar are required. As already mentioned in Sec. 2.1 achieving UHV conditions is time consuming and the equipment is much more expensive. But since the advantages of molecular beam epitaxy clearly exceed those disadvantages, MBE has become one of the most important thin-film deposition techniques in the last decades. In addition, using UHV conditions makes MBE compatible with in situ analytical techniques like reflective high energy electron diffraction (RHEED) to control the monolayer growth during deposition or direct connection to other UHV analytical methods like photoelectron spectroscopies (cf. Sec. 2.1).
The requirement of precisely controlling the beam fluxes of each evaporated material led to an improvement of effusion cells. Knudsen did extensive research on molecular gas flow in the early 20th century[47]. He invented an evaporation source fulfilling the requirements of precisely controllable effusion cells with a uniform flux in forward direction. Their main difference to common effusion cells is a small opening from which the evaporant escapes. As shown in Fig. 3.7 shutters allow to stop the growth process without switching off the effusion cells itself.
One disadvantage of using Knudsen cells or any other type of solid evaporation sources in MBE systems is the problem of refilling them. Since they are located in the vacuum chamber a refilling requires breaking the vacuum. Since establishing UHV conditions is fairly time consuming there are some popular modifications of the MBE process using volatile gas sources. Those gas-source MBE (GSMBE) or metal-organic MBE (MOMBE) systems are explained later in detail in Sec. 3.4. First, it is necessary to take a closer look at chemical vapor deposition (CVD) processes since using gas sources films are deposited by chemical reactions instead of physical deposition.

3.3 Chemical Vapor Deposition

As mentioned above, external sources containing gaseous reactants that flow into the deposition chamber can be refilled easily and timesaving compared to thermal evaporation or MBE effusion cells. While evaporation and film formation in PVD techniques are

physical processes, in chemical vapor deposition (CVD) volatile gases are introduced in the deposition chamber to react there and form a solid film at a heated substrate surface. CVD has many advantages over PVD techniques. Surfaces with complex topographies can be coated without any shadowing effects since there is no requirement for line-of-sight geometry as in evaporation[44]. The deposition itself is generally more conformal compared to PVD, i.e. it covers rough surfaces in a much more uniform manner. It is able to produce high quality epitaxial films as well as amorphous layers depending on the deposition parameters and there is usually no need for very high vacuum conditions using CVD, even though this can have advantages as will be shown later in this chapter.

Chemical vapor deposition systems consist of three main parts: the gas inlet, the reaction chamber and an exhaust for maintaining a constant gas flow and removal of reaction by-products. Depending on the condition of aggregation precursors are dispensed into the reaction chamber in different ways. If the vapor is in its gaseous phase and its vapor pressure sufficiently high it can be fed directly into the system. For precursors that are in a liquid or solid state at ambient conditions an introduction into the deposition chamber is done by aid of evaporators or sublimators. Usually transport gases like H_2 are used to transport the precursor into the chamber. Especially H_2 as carrier gas can have advantageous properties on the deposited films in terms of reduction of contaminants[48]. The reaction chamber containing the substrate to be deposited can either be a hot-wall reactor where both substrate and reactor walls are heated or it can be a cold-wall reactor where only the substrate is kept at elevated temperatures. Cold-wall reactors do have the advantage over hot-wall reactors that no reactions occur at the reactor walls which form particles that can fall on the substrate and contaminate the surface[49].

In CVD processes the precursor gases flow through the reaction chamber and the substrate is placed into this gas stream. Depending on the gas velocity there are two different flow regimes: a preferred laminar flow where the gas molecules flow parallel to each other and a turbulent flow regime. Turbulent flows are unfavorable and to prevent since resulting swirls can lead to a nonuniform defect-rich thin-film. The dimensionless Reynold's Number Re is used to express the type of flow regime. For $Re < 1100$ the flow will have a laminar character while there turbulent flow regime starts at $Re > 2100$. In between there is a mixed flow type.
From theory of fluid mechanics it is known that near the sample surface a boundary layer is formed in which the gas flow velocity is reduced down to zero directly at the surface and vapor concentrations differ from those in the gas stream. Both, precursor molecules

and gaseous reaction by-products have to pass through this boundary layer by chemical diffusion processes before they can be deposited onto the substrate as shown later.

Depending on the material to be deposited there are several different general classes of reaction types used in CVD processes. Those include amongst others:

- pyrolysis: thermal decomposition of precursor molecules on a hot substrate surface, e.g. Si or metal deposition
- reduction: reduction by hydrogen gas as reducing agent, e.g. Si or metal deposition
- oxidation: precursor molecule is oxidized by O_2 as oxidizing agent to form nonvolatile oxide, e.g. SiO_2 deposition
- compound formation: formation of compound by reaction of two precursors each containing one of the compound elements, e.g. carbide or nitride formation for wear-resistant coatings

The reactions used in this thesis are all of the compound formation type which will be discussed later in Sec. 3.4 in more detail. The other reaction types are will not be treated here since they have not been used. For further details various textbooks about chemical vapor deposition are available[43;44;49] for the interested reader.

Several factors do have influences on the growth kinetics in CVD. Figure 3.8 schematically depicts the different reaction steps that are necessary to produce a thin-film of the desired compound material: In order for a film to grow, precursor molecules from the introduced vapor have in a first step (a) to travel towards the substrate. Due to the boundary layer formation step (b) involves diffusion through this layer (indicated by a yellow background in Fig.3.8) towards the substrate surface. Reaching it, the molecules might be adsorbed (cf. Sec. 3.1) if they find a surface site which is not already occupied by other precursor molecules in step (c). Step (d) involves the chemical reaction of the adsorbed precursor molecule. There are two possible reaction partners to form a compound with, either one other absorbed molecule on the substrate surface or one which already diffused through the boundary layer but has not been adsorbed yet. Since chemical reactions require the breaking of intramolecular bonds those reactions are likely to occur just at the heated substrate where the required activation energy is supplied in the form of heat and catalytic activity. At the same time chemical reactions between the precursor molecules in the main

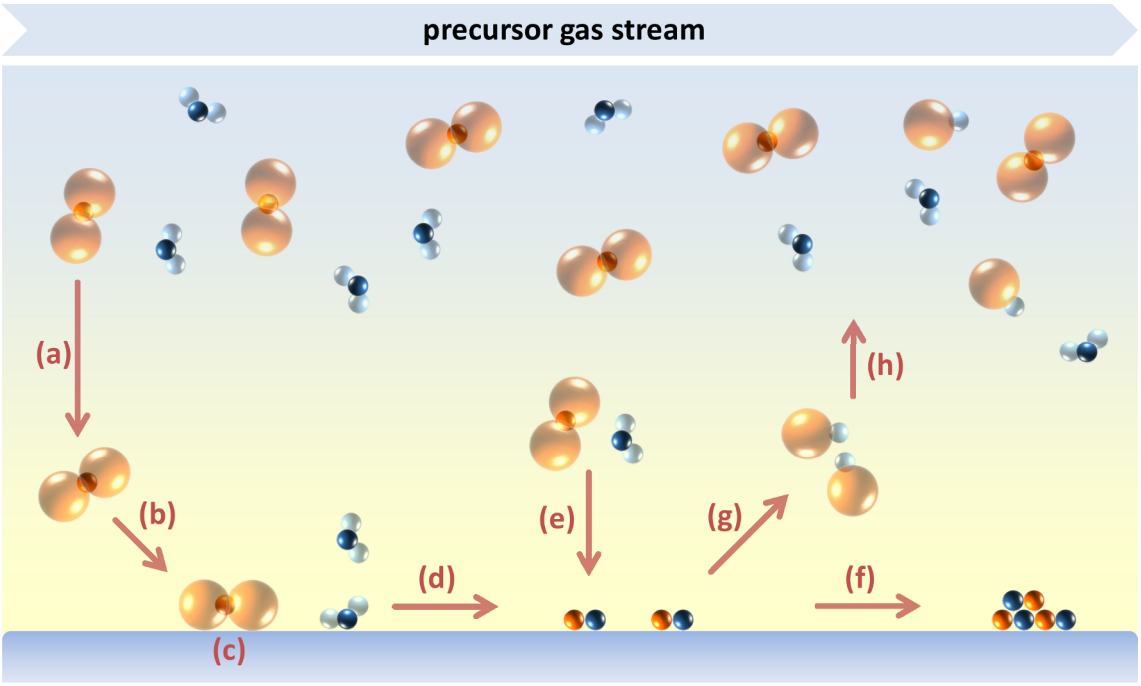

Figure 3.8: Primary atomic processes during chemical vapor deposition: (a) transport to the substrate, (b) diffusion through boundary layer, (c) adsorption, (d) chemical reaction, (e) deposition directly from the gas phase, (f) nucleation and film formation, (g) diffusion of reaction by-products through boundary layer, (h) incorporation of by-products into gas stream

vapor stream are unlikely to happen. This is not necessarily true for precursor molecules that are in the boundary layer at the closer vicinity to the heated surface. Those reactants may gain enough thermal energy to react with each other and deposit undesired weakly bound material onto the surface as illustrated in step (e). In step (f) the atoms have nucleated and the film is started to form. Depending on the substrate temperature and the deposition rate, layers with different qualities are possible to grow. If the deposition rate is low, less nuclei are formed on the surface and the film will show good structural qualities. At higher deposition rates, the atoms tend to cluster which results in polycrystalline or even amorphous films. In addition, steps (g) and (h) in Fig. 3.8 show the removal of gaseous reaction by-products from the surface by diffusion through the boundary layer and incorporation into the precursor gas stream.

To improve the film quality, several modifications of the standard CVD process have been developed. Low-pressure CVD (LPCVD) distinguishes from conventional CVD by reducing the pressure from atmospheric to pressures around 1 mbar [43]. Advantages are higher deposition rates, improved film thickness uniformities and less defects in the deposited

films. Another modification is the plasma-enhanced CVD (PECVD) where the pressures are reduced as in case of LPCVD but in addition a glow discharge is initiated in the chamber. In this plasma the precursor molecules will decompose and therefore the substrate temperatures can be significantly lowered. In case of metal-organic CVD (MOCVD) as a third variant of CVD, no changes in the setup or pressure region are carried out. In contrast to conventional CVD at least one of the precursors has to be a metal-organic volatile compound as the name already implies. Usually, H_2 or N_2 are used as carrier gas for the precursor transport. MOCVD has become an important deposition method because of its ability to grow high quality epitaxial films especially for the production of III-V semiconductors. Hence, the notation metal-organic vapor phase epitaxy (MOVPE) is also quite common in use.

3.4 Metal-Organic Molecular Beam Epitaxy

Actually related to chemical vapor deposition but being treated in a separate section due to its hybrid character between metal-organic chemical vapor deposition and molecular beam epitaxy is metal-organic molecular beam epitaxy (MOMBE). In this technique the particular advantages of metal-organic precursors are combined with ultra-high vacuum conditions as used in MBE. The metal-organic vapor introduced into the chamber from external reservoirs is directed towards the substrate through small tubes as molecular beams. Due to the UHV conditions gas phase reactions can virtually be excluded and growth reactions are occurring almost exclusively at the substrate's surface resulting in very uniform films. MOMBE first was used to produce high quality GaAs films from trimethylgallium (TMGa) and cracked arsine to avoid morphological defects in 1985 [50]. In literature, MOMBE sometimes is also referred to as chemical beam epitaxy (CBE).

Besides the UHV conditions, the choice of the metal-organic precursor determine the resulting film properties significantly in MOMBE. There are several important characteristic features a precursor has to fulfill to be suitable to use in MOMBE growth processes. On the one hand they have to have high vapor pressures to achieve high transport rates. Usually this is the case for metal-organic compounds and therefore a carrier gas as in case of CVD is not necessary. Another requirement for precursor is the stability of the molecules at ambient temperatures. Otherwise decomposition reactions may occur and the molecule fragments may contaminate the growing layer. To prevent carbon or oxygen

incorporation into the growing films the reaction on the surface has to remove the organic ligands of the metal atoms and the reaction products have to be volatile to be effectively removed from the substrate.

An example is the MOMBE deposition of zinc oxide[21;51]. A precursor selection of diethylzinc $Zn(C_2H_5)_2$ and ultrapure water H_2O can result in very high quality epitaxial films on appropriate substrates, for instance Al_2O_3 $(1\bar{1}02)$ or SiC (0001)[51]. The base pressure of the MOMBE system included in the Integrated System (cf. 2.1) usually is in the 10^{-10} mbar range. For deposition of ZnO films diethylzinc (DEZn) with a partial pressure of $p_{\,\mathrm{DEZn}} = 2 \cdot 10^{-6}$ mbar and water with a pressure of $p_{\,\mathrm{H_2O}} = 8 \cdot 10^{-6}$ mbar are introduced to the deposition chamber by two leak valves. The temperature of the substrate is kept at a temperature of $T = 450\,^{\circ}\mathrm{C}$. On the surface, the ethyl ligands of the diethylzinc molecule react with the hydrogen of the water and form gaseous ethane C_2H_6. The remaining hydroxide is bound to the zinc atom, forming an $Zn(OH)_2$ intermediate state, until it reacts with another diethylzinc molecule, finally forming a ZnO compound.

4 Atomic Layer Deposition of ZnO

In comparison to those growth techniques presented in Chp. 3, *atomic layer deposition* (ALD) differs significantly in its growth mechanism. ALD belongs to the field of CVD techniques (cf. Sec. 3.3) but in contrast to classical CVD the precursor gases are not supplied simultaneously. Instead, two separated surface reactions are forming the compound to be deposited. It is its characteristic self-limited growth mode that allows atomic layer deposition a precise thickness control of the deposited materials in the sub-monolayer regime.

ALD has already been invented in the 1970s by Suntola et al[52]. Its been developed for depositing thin dielectric zinc sulfide (ZnS) layers for use in thin-film electroluminescent displays. Even though ALD has already been invented nearly half a century ago, it is becoming more and more important just recently because the need for ultra-thin films of high uniformity rises. For instance, the *International Technology Roadmap of Semiconductors* (ITRS) included atomic layer deposition for the production of high dielectric constant gate oxides and as Cu diffusion barriers just recently. In chalcopyrite thin-film solar cell technology, ALD is more and more applied for buffer layer deposition. Further details about buffer layers in chalcopyrite solar cells are given later in Chp. 5.

Since in the beginning of ALD the deposited films were mostly of single-crystalline epitaxial nature, the acronym ALE (*atomic layer epitaxy*) was introduced. In this work, independently on producing single- or polycrystalline films, the term ALD is used.

This chapter is structured as follows: first, the ALD process of ZnO deposition is treated in detail. Afterwards, the assembly of the UHV-ALD reactor and the process of commissioning is presented. In Sec. 4.3 the basic growth parameter for zinc oxide ALD using diethylzinc (DEZn) and water (H_2O) as precursor gases are determined and the initial growth of ALD-ZnO on hydrogen-terminated silicon is investigated in Sec. 4.5.

4.1 Basic Principles of Atomic Layer Deposition

As mentioned above, the characteristic feature of ALD is the sequential supply of reaction gases, delivering one of the components of the compound to be formed. A common ALD reaction sequence consists of four stages. First, a gaseous reactant A is introduced into the deposition chamber onto a heated substrate until the sample's surface is completely saturated. This can happen either by the precursor gas or one of its reaction products in case of a chemical reaction occurring at the surface which is usually the case. After saturation, the excess precursor gases and gaseous reaction by-products are flushed away by a non-reactive purging gas. Commonly, this is argon (Ar) as non-reactive noble gas. Afterwards, the second precursor gas (reactant B) is fed into the chamber and reacts with reactant A at the sample surface until the reaction product saturate the surface. Again, reaction products and surplus precursor gases are removed by an Ar purge. The sequence of these 4 steps is called one ALD *cycle*. Since all reactions in ALD occur at the sample's surface without any gas phase reactions, only up to one monolayer (ML) of the compound to be formed can be deposited during one cycle. This is schematically shown in Fig. 4.1 for the atomic layer deposition of a compound AB.

This unique reaction mechanism is the reason for atomic layer deposition offering a couple of advantages over other deposition techniques:

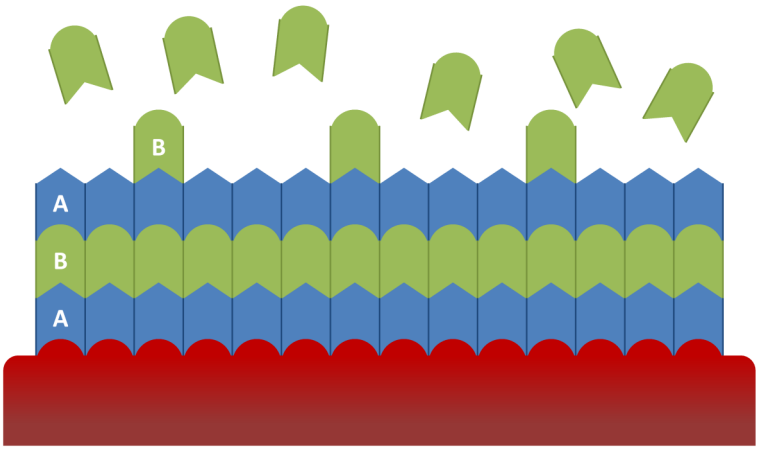

Figure 4.1: Reaction scheme of AB compound formation during atomic layer deposition. In contrast to other deposition techniques, the reactants which deliver the A and B components are not fed in at the same time but sequentially one after another. It is self-limited by saturation of the available reactive sites and the compound forms in two separated half-reactions.

deposition rate: in ALD the deposition rate is not depending on the precursor flux but on the number of cycles due to saturating the limited number of reactive surface sites. Hence, its self-limiting growth mode provides thickness control in the range of an atomic layer.
film conformity: another feature of ALD is its superior conformity on surface structures with high aspect ratios. No other deposition technique is able to coat trenches or steps as uniform as ALD does. In addition, the films are very continuous and pinhole-free over large areas and result in very sharp interfaces.
substrate temperature: right from the start, ALD was used to grow high-quality epitaxial films. In contrast to other techniques, the substrate temperatures are significantly lower because diffusion processes are less important for saturating the reaction sites. Those lower substrate temperatures also enable atomic layer deposition on substrates that would usually decompose at elevated temperatures as for instance most polymers do.

4.1.1 Surface Reactions

The surface reactions in atomic layer deposition differ significantly from other deposition techniques because of the sequential supply of the reactive precursor gases. This section will provide a detailed view on the reaction mechanisms during zinc oxide deposition using organometallic diethylzinc ($Zn(C_2H_5)_2$) as metal-precursor and water (H_2O) as oxidizing agent. Diethylzinc is highly reactive with water. Supplied simultaneously, both ethyl ligands will react with the two hydrogen atoms of the water molecule and form gaseous ethane (C_2H_6). At the same time, the remaining Zn and O atoms will form a ZnO compound:

$$Zn(C_2H_5)_2 + H_2O \rightarrow ZnO + 2\ C_2H_6\ (g) \tag{4.1}$$

This reaction is highly exothermic with a formation enthalpy of $\Delta H = -70$ kcal[53].
Since atomic layer deposition does not supply both reactants at the same time, this reaction splits into two so-called *half-reactions*. The first half-reaction in an ZnO ALD process is shown in Fig. 4.2 where a substrate surface terminated by hydroxides (-OH) is assumed. This is not necessarily true for the first deposition cycles but a proper assumption if the first complete monolayer of ZnO has formed as shown later. After introducing

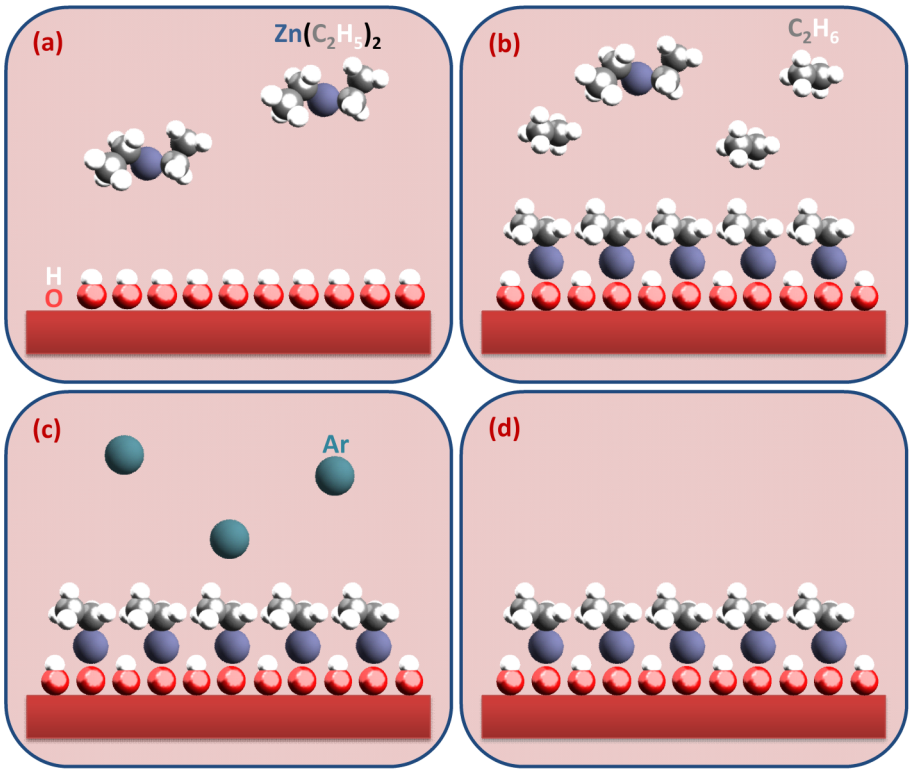

Figure 4.2: Reaction mechanism of the first ALD half-reaction using diethylzinc and water to form ZnO. (a) DEZn exposure; (b) ligand exchange; (c) Ar purge; (d) monoethylzinc saturated surface

the diethylzinc into the deposition chamber (a), the chemisorption of the molecule takes place by a ligand exchange mechanism: one of the ethyl ligands reacts with one of the the hydrogen atoms of the hydroxides located at the substrate's surface. After reacting, one ethane molecule is released as gaseous reaction by-product to the vacuum. The remaining monoethylzinc (MEZn) is bound to the surface at the left over oxygen atom. This reaction occurs until all reactive sites are saturated as shown in Fig. 4.2 (b). After complete saturation, the surplus reactant gases and reaction by-products are removed by flushing the chamber with non-reactive argon (c) to prevent further unwanted gas-phase reactions. One ends up with a surface completely saturated by monoethylzinc molecules as shown in Fig. 4.2 (d). One can express this half-reaction by Eq. 4.2, where $\|$ denotes the surface of the substrate:

$$\| - \mathrm{OH} + \mathrm{Zn(C_2H_5)_2} \rightarrow \| - \mathrm{O} - \mathrm{Zn(C_2H_5)} + \mathrm{C_2H_6(g)} \tag{4.2}$$

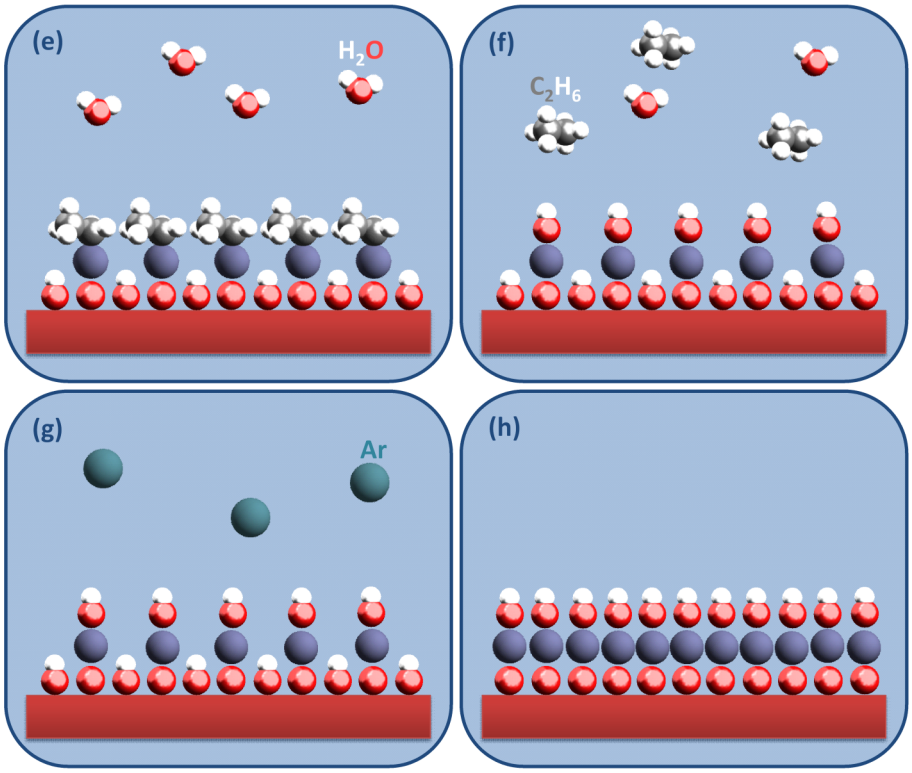

Figure 4.3: Reaction mechanism of the second ALD half-reaction using diethylzinc and water to form ZnO. (e) H_2O exposure; (f) ligand exchange; (g) Ar purge; (h) hydroxide saturated ZnO monolayer

The second half-reaction is called the *oxidizing half-reaction* and is shown in Fig. 4.3. First, the oxygen precursor is introduced into the chamber (Fig. 4.3 (e)). In case of ZnO atomic layer deposition usually ultra-pure water is used as reactant. Again, chemisorption takes place via a ligand exchange: the water reacts with the MEZn at the substrate's surface, formed during the first half-reaction. One of the hydrogen atoms removes the one ethyl ligand left, again forming ethane. The remaining hydroxide forms a chemical bond with the zinc atom on the surface as shown in Fig. 4.3 (f). Afterwards, the excess precursor gases and the ethane is removed by argon flushing (g) just like in the zinc half-reaction. Describing this half-reaction in form of a chemical reaction equation results in:

$$\| - O - Zn(C_2H_5) + H_2O \rightarrow \| - O - Zn - OH + C_2H_6 \text{ (g)} \tag{4.3}$$

Both half-reactions are irreversible chemical reactions. This is one of the important precursor requirements to achieve self-limiting conditions necessary for ALD. After the purging step, one ends up with one ZnO monolayer covered by one hydroxide monolayer (Fig. 4.3 (h)). Hence, the assumption made above, having an hydroxylated surface before starting the first half-reaction, can considered being true after the initial complete ZnO monolayer was formed. What happens during the initial growth of zinc oxide is also investigated in this work and shown later in Sec. 4.5. Usually, the deposition of one monolayer is not achieved after one ALD cycle but requires several deposition steps. This is treated in detail in the following section. Since its self-limiting growth is one of the most important features of ALD, we will take a closer look at the surface saturation behavior during precursor exposure.

4.1.2 Saturation

The self-limiting characteristic of ALD is most important to control the thickness of the deposited films. Since chemical reactions only occur between the precursor molecules and reactive surface sites and not among the precursor molecules themselves, there is only a finite number of surface sites available to react as shown schematically in Fig. 4.1. If all reactive sites are occupied by reaction products, no further molecules can be adsorbed and the surface is saturated. Hence, only one monolayer of the adsorbate is accepted by the surface. The number of adsorbed precursor molecules does not only depend on the number of reactive sites but also on the size of the chemisorbed molecule. Fig. 4.2 (d) shows how the size of the adsorbed precursor ethyl ligands cause steric hindrance so that not all reactive sites on the surface can be saturated in one ALD cycle. Even if in literature often it is stated that one ALD cycle deposits one monolayer of material, it is obvious that those steric hindrance effects effectively limit the maximum deposition of material per ALD cycle to some value below one complete monolayer.

One requirement for complete saturation in atomic layer deposition is a sufficiently long exposure time of the surface by the particular precursor gases. Fig. 4.4 plots the surface coverage against the exposure time. In the beginning, the surface coverage increases rapidly, until a maximum is reached. How long it takes until the complete surface is saturated depends on the pressure of the precursor gas and the adsorption rate [55]. Ideally, the reaction is as fast as possible to minimize the exposure times to keep the contamination

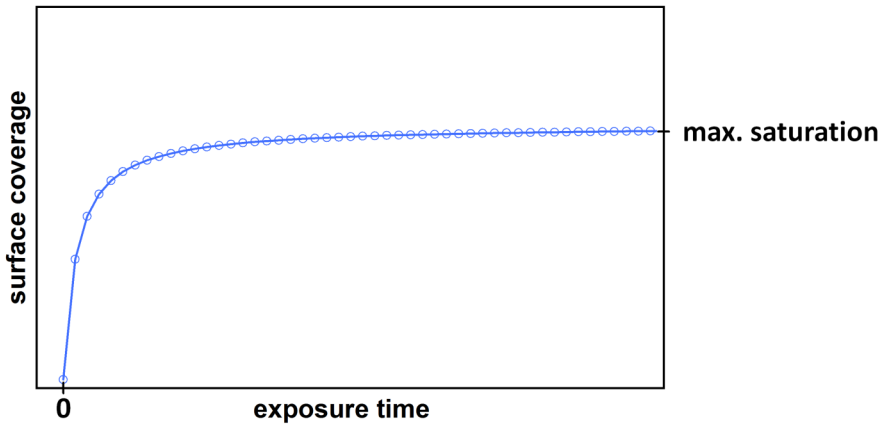

Figure 4.4: Surface coverage vs. duration of precursor exposure according to Ritala and Leskelä [54]. If sufficient exposure times are chosen the surface is completely saturated. The maximum saturation depends on both, reactive surface sites and steric hindrance effects of the precursor molecules.

level in the deposition chamber as low as possible. If the exposure times are chosen too short, thickness variations can occur in the films due to the incomplete surface coverage.

During Ar purge, the surface coverage should remain constant, which is usually true since the chemisorbed surface species are sufficiently stable. If the Ar purging times are not long enough for sufficiently removing all residual precursor gases and reaction products, gas-phase reactions can occur during exposure of the next reactant. Those gas-phase reactions would lead to an unwanted CVD-like growth which results in growth rates larger than the self-limited ALD growth. Therefore, it is important to carefully pay attention to the particular exposure and purging times when start running an ALD reactor. One ends up with a ALD sequence scheme as shown at the top of Fig. 4.5.

In addition to the exposure and the purging steps, there is an additional pumping stage after each Ar flush. This step is not present in standard ALD reactors that operate under ambient pressures. In contrast to those reactors, the one designed and assembled in this work is an UHV-compatible ALD reactor as shown later in Sec. 4.2. Since during exposure and purging the pressure rises significantly in the chamber, a pumping step was added to decrease the total pressure of the system at least down to high vacuum conditions after each half-reaction. The pressure evolution in the deposition chamber is shown in the lower part of Fig. 4.5.

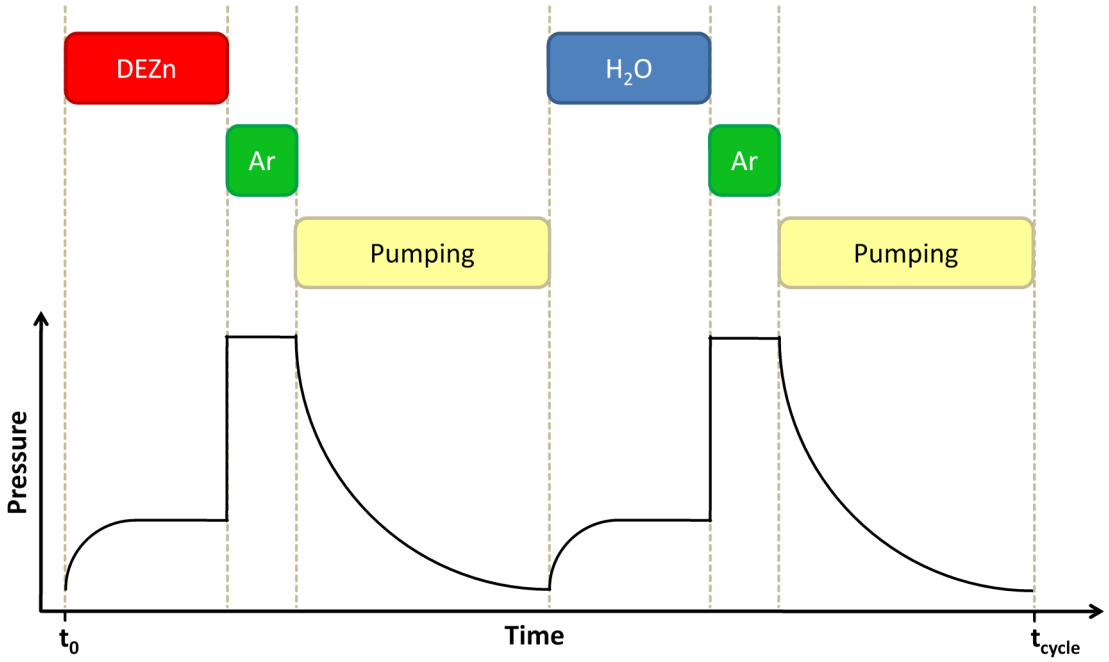

Figure 4.5: (top) ALD pulse scheme of the UHV-ALD reactor assembled for this work; (bottom) pressure evolution during one complete ALD cycle.

4.1.3 Temperature Dependence

Since all reactions in an ALD process are surface-controlled, there are not many parameters having major influences on the deposition. Besides the exposure and purging times discussed above the most important parameter is the substrate's temperature during growth. The additional energy that is supplied in form of heat is necessary to initiate the ligand exchange to chemisorb the precursor molecule at the surface[56]. Hence, atomic layer deposition process is also referred to as *thermal ALD*[53]. The temperature regime where the ALD process fulfills the requirement of self-terminating chemical reactions is termed the *ALD window*[55]. In this temperature range, a constant amount of material is deposited during one ALD cycle, the so-called *growth-per-cycle* or *GPC*, due to complete saturation of all surface sites. Usually, the ALD window spreads over a wider temperature range since minor temperature changes do not have a significant influence on the adsorption behavior of the precursor molecules.

Fig. 4.6 shows all typical temperature dependencies of the GPC on temperature. In the middle, the ALD window regime of constant self-limited ALD growth is present. The center of this temperature range is the preferred substrate temperature since small

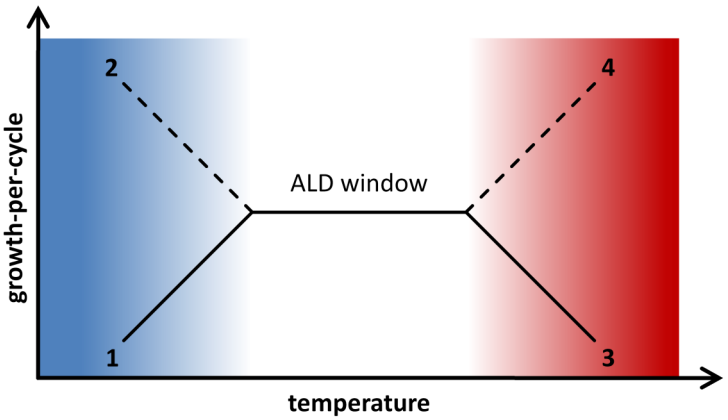

Figure 4.6: Temperature dependence of the growth-per-cycle (GPC) according to Suntola[56]. The temperature region where the characteristic self-limited growth keeps the GPC constant is referred to as ALD window.

temperature variations do not affect the deposition rate.

If the substrate's temperature is too low, the energy supplied to the reactants is smaller than the activation energy to have a catalytic effect and therefore no chemical reaction occurs between surface and precursor molecule. If the temperature exceeds the activation energy, the reactions might still be too slow to saturate the surface completely within the exposition time. The growth-per-cycle decreases with respect to the ALD window as indicated by branch (1) in Fig. 4.6. This behavior is most commonly investigated in thermal ALD processes. Nevertheless, a lower substrate temperature can also show the effect of an increase in growth rate as indicated by the dashed line of branch (2). In this case, the lower temperature leads to condensation of precursor molecules or reaction products on top of the surface. This results in lower quality films since the deposition process does not base on the characteristic self-limiting ALD properties.

On the high temperature side, when temperature exceeds the ideal ALD window regime, the growth rate usually decreases (3). In this case, the adsorbed precursor molecules desorb, leaving behind unsaturated surface sites where no reaction partner is present during the subsequent precursor exposition (cf. Fig. 4.1). In contrast, the GPC might also increase at elevated temperatures as indicated by branch (4) in Fig. 4.6. This happens in case of an undesired precursor decomposition which then condenses at the formed monolayer[56].

The ideal growth-per-cycle dependence on substrate temperature is indicated by the solid lines in Fig. 4.6.

4.1.4 Deposition Rate

A theoretical model developed by Puurunen[57] relates the amount of material deposited in one ALD cycle under ideal growth conditions, i.e. complete surface saturation in the ALD window temperature range, on either size effects of the adsorbed precursor molecules (steric hindrance of the ligands) or the number of reactive surface sites. Considering the molecule size, in case of ZnO deposition the number of reactive hydroxide surface sites can be considered much higher than the number of adsorbed monoethylzinc molecules. Hence, the growth-per-cycle is mainly limited by steric hindrance effects of the ethyl ligands.
Since the original substrate surface and the deposited film usually show different chemical compositions, the GPC is also expected to vary during initial atomic layer deposition. The formation of the first monolayer can take several ALD cycles resulting in a reduced growth-per-cycle. After the initial monolayer completed, the growth rate settles to the constant value determinable from the ALD window in Fig. 4.6.

After introducing of the atomic layer deposition process, the following section will concentrate on the setup of the ZnO ALD reactor and the determination of its ideal deposition parameters.

4.2 Reactor Design and Commissioning

Since its invention, a couple of different ALD reactor types have been developed. The most commonly used reactor type is the so-called *traveling-wave reactor* where the precursor is transported towards the sample by a continuous flowing inert carrier gas. The first commercially available ALD reactor was the F-120 by Microchemicals Ltd. Nowadays, further companies like Cambridge NanoTech or Picosun (founded by Tuomo Suntola, the inventor of this technique), offer ALD reactors.
As in CVD reactors, distinctions are made between hot and cold wall ALD reactors. Since their advantages and disadvantages are identically to those in CVD reactors, they are not repeated here. More details are found either in Sec. 3.3 or in the reviews of Ritala and Leskelä[54] or George[53].
In addition to thermal ALD reactors, there are also plasma-enhanced ALD (PE-ALD) reactors in use. As in plasma-enhanced CVD, those reactors are using a plasma to induce chemical reactions that would not be possible just using thermal energy[53]. An advantage

of PE-ALD is the possibility of reducing the substrate temperature without negative influences on the film quality. This might be important using substrates that decompose at higher temperatures like polymer substrates. On the other hand, the self-limiting reactions are best fulfilled by thermal ALD, since in PE-ALD reactant decomposition can cause problems with conformity[55].
In this work, a thermal ALD reactor for zinc oxide deposition has been designed. To allow in situ growth and analysis of the grown films, the reactor is compatible to ultra-high vacuum conditions and attached to the Integrated System (see Sec. 2.1).

4.2.1 UHV-ALD Reactor

Figure 4.7 shows schematically the setup of the UHV-compatible cold-wall ZnO-ALD reactor build up in this work. Its key components are pneumatic *Swagelok Atomic Layer Deposition Diaphragm Valves* which are additionally equiped with solenoid pilot valve assemblies. These valves allow to achieve high-speed valve opening and closing times of up to 5 ms. Each precursor and purging gas requires one ALD valve to control its intake into the deposition chamber. Hence, 3 ALD valves are the minimum requirement for the deposition of a compound formed by the reaction of two precursor gases separated by one purging gas.

The ALD valves run in *normally closed* operation, i.e. they just open if they get a signal supplied by an *Advantech USB-4761 8 channel relay* control unit. This control unit translates the commands of a software that has been written to actuate the ALD valves into opening signals.
As mentioned above, this ALD reactor is attached to the Integrated System and operated under ultra-high vacuum (UHV) conditions to allow in situ growth and analysis experiments. Hence, a turbo molecular pump and a rotary vane pump are necessary to achieve those low pressures. The base pressure in this ALD system is typically in the range of $5 \cdot 10^{-9}$ mbar. Not reaching lower pressures is mainly caused by residues of the water used as oxygen precursor. Not in operation, the deposition chamber pressure is determined by an ionization gauge. Running the atomic layer deposition process, the pressure can shortly rise into the millibar region, during the purging steps. Since such pressure fluctuations would destroy the hot filament of the ionization gauge, the pressure during operation is measured by the Pirani gauge of a Balzers full range vacuum gauge.

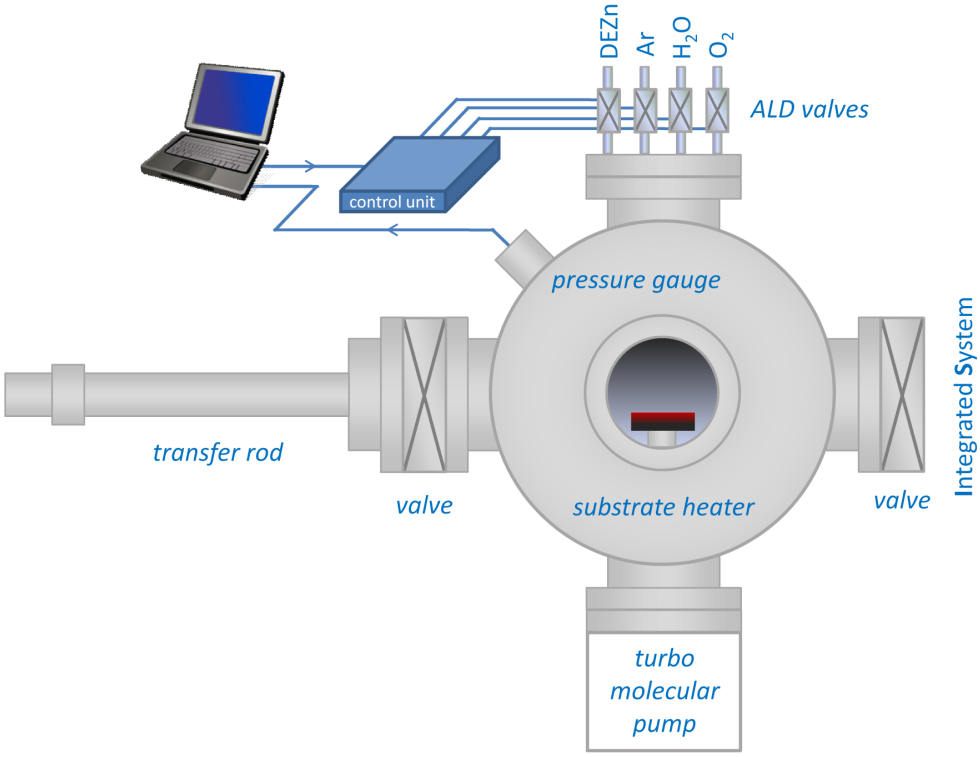

Figure 4.7: Sketch of the UHV-compatible ZnO-ALD reactor build up for this work. The key components are discussed in the text.

One advantage of those Balzers pressure gauges is the possibility of constantly logging the pressure in the deposition chamber. This can be useful to control process parameters like valve opening times. The lower pressure limit of the Pirani is about $2 \cdot 10^{-2}$ mbar and therefore still sufficient to measure the pressures in the deposition chamber during precursor exposure.

One crucial part of the ALD reactor is the sample heater. In the beginning, a coiled tungsten wire was used to heat the sample. This attempt was not very successful because either the shock pressure during purge or deposited ZnO on the tungsten wire led to failure of the heater after a couple of weeks of operation. This problem was solved by using a Boralectric heating element, which are build up of a graphite conductor surrounded by a boron nitride ceramic. Those heating elements have high thermal shock resistance and are inert to corrosive gases. Figure 4.8 shows the power input characteristics for different temperatures in a regime interesting for atomic layer deposition. The substrate temperature is regulated automatically using a Eurotherm 815s PID controller. The temperature is raised by 15°C/min until the final temperature is reached to prevent thermal stress in

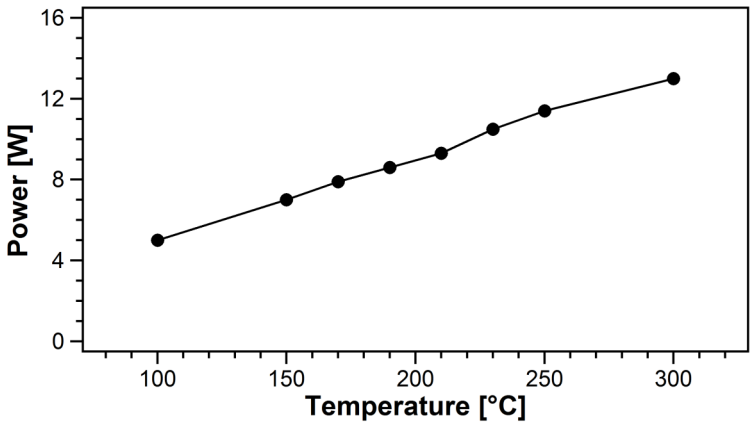

Figure 4.8: Power consumption characteristics of the boron nitride / graphite Boralectric heater in a temperature regime relevant for successful ZnO-ALD. In the required temperature regime between $100 - 300\,^{\circ}\mathrm{C}$ the power consumption shows a linear behavior.

the samples. The same applies for cooling down the samples after the zinc oxide has been deposited.

4.2.2 Precursor Materials

As described in Sec. 4.1, two precursor gases and one purging gas is required for successful ALD of zinc oxide. Argon is chosen as purging gas because of its inertness and its availability at the Integrated System. The argon pressure in the gas supply is about $1.5 - 2$ bar. Setting up lower pressures could lead to diffusion of impurities from the environment into the gas supply system. Because such high pressures would lead to a shut-down or even a damaging of the turbo molecular pump, a short purging time of 25 ms was chosen. While flushing the chamber, the pressure reaches values of around 1 mbar but decreases very quickly after the purge.

Organometallic diethylzinc (DEZn) supplied by Sigma-Aldrich is chosen as the zinc precursor for the ZnO deposition. The ALD sources consist of a custom made two-branched glass tube equipped with a CF-flange and an all metal angle valve for UHV-compatibility. Diethylzinc is liquid at room temperature and very reactive with oxygen. Therefore, filling the source had to be carried out in a glove box under argon atmosphere.
The standard oxygen precursor for ZnO ALD is water. A source identical in construction with the DEZn source is filled with ultra-pure water of highest purity. Additionally, pure

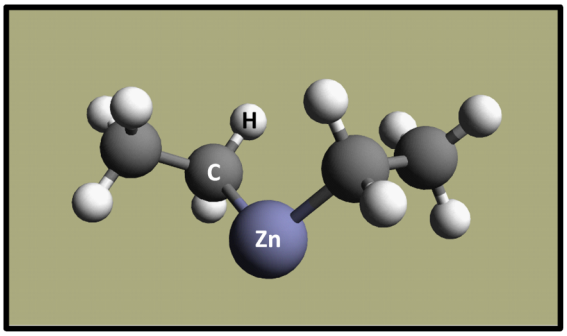

Figure 4.9: Organometallic diethylzinc ($Zn(C_2H_5)_2$) molecule being composed of one zinc atom and two ethyl (C_2H_5) ligands.

O_2 can be used as oxygen precursor as shown later in Chp. 6. The oxygen is provided by a 1 l O_2 lecture bottle (99.998 vol %) controlled by an additional ALD valve.

To control the vapor pressure of the liquid precursors DEZn and water and to prevent thermal degradation of the diethylzinc, both sources can be cooled independent of each other using Peltier elements. Therefore, each source is equipped with a thermocouple and Eurotherm 815s PID controllers to keep the temperature of each source constant. One further advantage of the cooled DEZn source is the possibility of additional cleaning of the liquid precursor by sublimation from the uncooled branch of the source into the cooled one to minimize impurities.

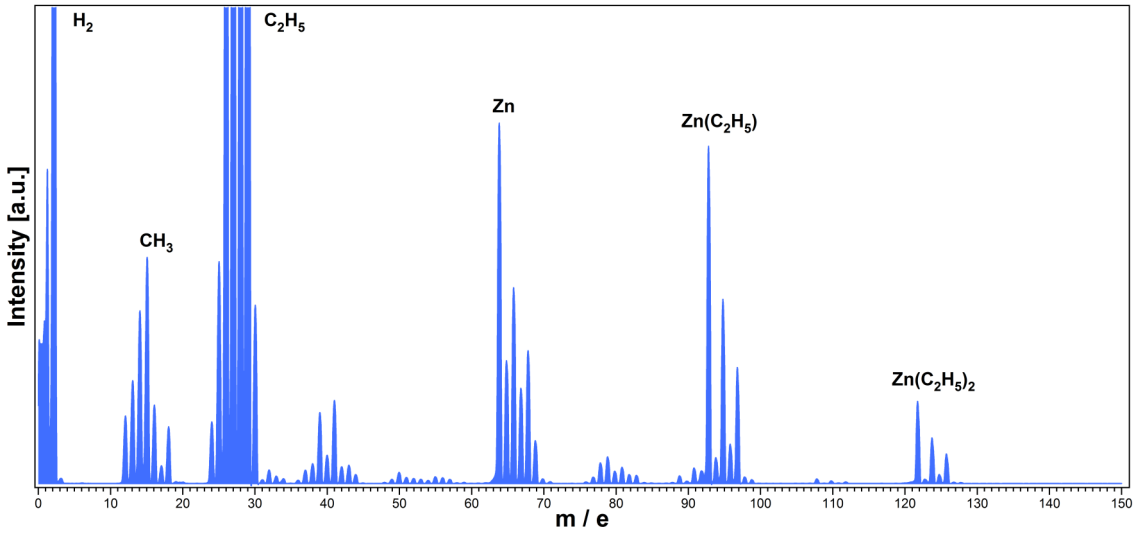

Figure 4.10: Mass spectrum of diethylzinc fed into the atomic layer deposition chamber. Besides the dominant peaks resulting from fragments of the molecule, no contaminations of the DEZn are observable.

Fig. 4.10 shows a mass spectrum of room temperature DEZn during introduction into the deposition chamber. The spectrum has been recorded with a quadrupole mass spectrometer. According to Kuniya et al. the peaks arising around 122 m/e correspond to DEZn[58]. Additional peak regions arise due to decomposition of the diethylzinc in the mass spectrometer ion source into $Zn(C_2H_5)^+$ (93 m/e) and Zn (64 m/e) mainly by losing their ethyl ligands (29 m/e). Even though gaining information from the mass spectra about the DEZn is not easy it gives an idea about the purity in the system. For instance, the amount of water (18 m/e) or hydroxides (17 m/e) is very low. Other contaminants are not identified in the mass spectrum.

To prevent decomposition of the precursor, the sources are cooled as mentioned above. At the same time the vapor pressure has to be sufficiently high to achieve complete saturation on the surface in an adequate time scale. To get an idea about the temperature dependence of the vapor pressure, it has been calculated using the *Antoine equation*:

$$\log p = A + \frac{B}{(T[\mathrm{K}] + C)} \text{ [Pa]} \tag{4.4}$$

A,B and C are parameter that can be experimentally determined[59], while T is the absolute temperature. An excellent online database is the NIST Chemistry WebBook[60] providing a huge selection of data for different materials. For diethylzinc, Stull determined the following values[61] being valid in the temperature regime of interest:

$A = 4.41445$, $B = 1571.638$, $C = -34.978$ between $T = 250.7 - 391.0$ K

Bridgeman and Aldrich determined the Antoine equation parameters for water[62]. There, the parameters vary in the range of interest what has to be taken into account. Those parameters are:

$A = 5.40221$, $B = 1838.675$, $C = -31.737$ between $T = 273 - 303$ K
$A = 5.20389$, $B = 1733.926$, $C = -39.485$ between $T = 304 - 333$ K

The vapor pressures have been calculated in a temperature regime between -20°C and 60°C for diethylzinc and water, respectively. The results are plotted in Fig. 4.11. Both curves intersect at 8°C having a vapor pressure of 10.72 mbar. Hence, 8°C has been chosen to be the optimal temperature the sources are kept at.

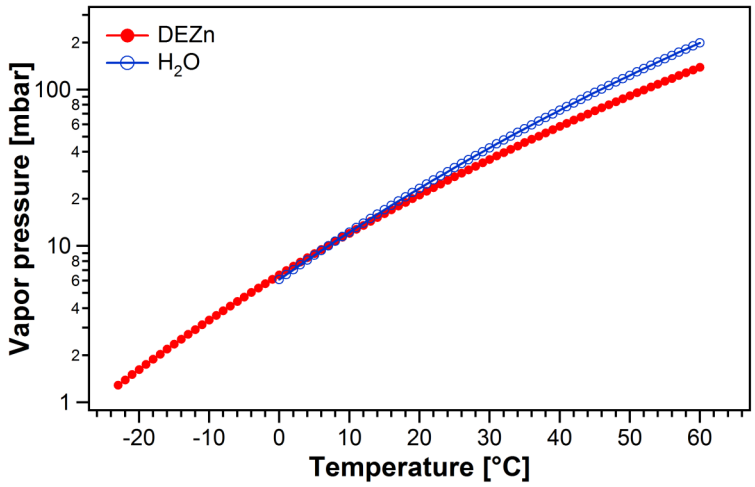

Figure 4.11: Vapor pressures of diethylzinc and water calculated by the Antoin equation (Eq. 4.4). At 8 °C both vapor pressures equal 10.72 mbar.

There are several zinc precursor materials available to deposit zinc oxide films by ALD or CVD methods. Amongst others, ZnO was successfully produced using $ZnCl_2$ [63], organometallic zinc acetate ($Zn(CH_3COO)_2$) [64] or dimethylzinc (DMZn, $Zn(CH_3)_2$) [65]. Ye et al. compared the structural properties of MOCVD deposited ZnO films using both, diethylzinc and dimethylzinc as zinc precursor, respectively [65]. Both films showed preferential growth orientation along the c-axis as X-ray diffraction experiments revealed. In contrast to DEZn-grown films, the XRD peaks of the films deposited with DMZn exhibit a larger peak widths. This indicates an improved structural quality of films deposited with DEZn. In addition, Raman spectroscopy of DEZn-grown ZnO do not show any phonon modes besides those of ZnO. In contrast, DMZn-grown ZnO films show additional phonon modes assigned to carbon and hydrogen content in the zinc oxide. This clearly indicates a much higher chemical and structural film quality using diethylzinc as zinc precursor. This, and the matter of fact that DEZn was already successfully used for MOMBE ZnO deposition in our group [21;51], made the decision for diethylzinc as zinc precursor in this ALD reactor.

4.2.3 ALD Valve Response

In ALD, surface saturation is achieved very fast and hence, the ALD valves have to have reliable response times in the millisecond range. In order to check the valve response on the opening signal of the control unit, each ALD valve is additionally equipped with an

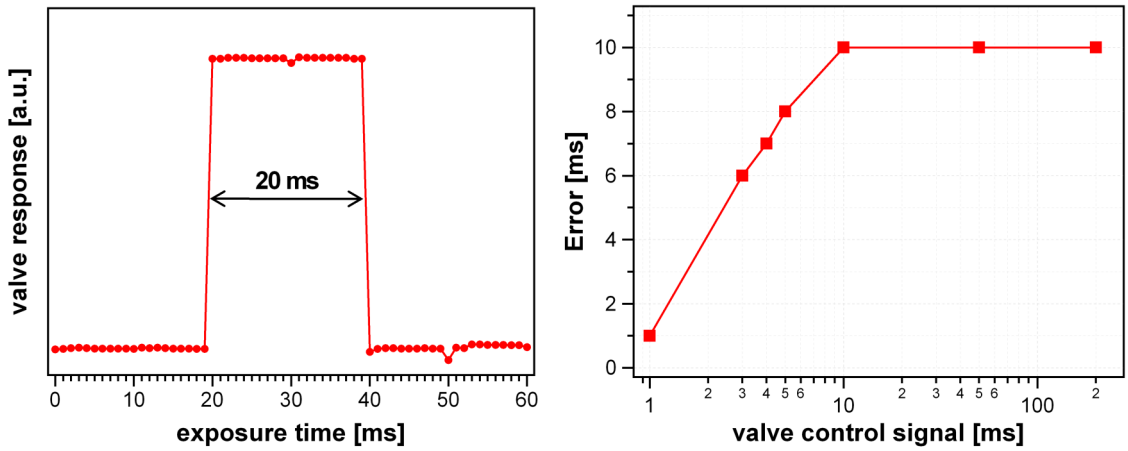

Figure 4.12: (left) Actuator-position sensor response signal for a valve opening signal of 10 ms; (right) valve specific delay of response time for the DEZn valve.

electronic actuator-position sensor, transmitting a response signal to a data acquisition unit. In addition to the opening and closing times the manufacturer specified with 5 ms respectively, a significant delay in valve response has been found. On the left hand side of Fig. 4.12 the response signal of an ALD valve is presented. The control unit delivered a 10 ms opening signal whereas the valve actuator-position sensor gave notice of a valve opening of 20 ms.

For deeper insight, the valve response times have been determined with respect to the input signal of the control unit. As shown at the right part of Fig. 4.12, at very short exposure times, the discrepancy between both signals rises until a maximum error of 10 ms is reached. For exposure times longer than 10 ms, the error remains constant. Hence, 11 ms has been chosen the minimum exposure time for this particular valve, since the error can easily be corrected by the ALD control software.
This response characteristic has been determined for each of the ALD valves, resulting in minimum exposure times of 10 ms for the DEZn valve as just shown, 12 ms for the H_2O and O_2 valves, respectively and 13 ms for the Ar valve.

Fig. 4.13 shows the pressure evaluation during one typical ALD cycle as shown later in Sec.4.3. The two prominent features in the upper part arise from the argon purge. The maximum pressure usually reaches values of $1-2$ mbar and it takes about 5 s until the Pirani detection limit of $2 \cdot 10^{-2}$ mbar is reached. Due to this pressure impulse, an additional pumping step of 20 s has been implemented after the purging step for two reasons: on the one hand, at least high-vacuum conditions are desired during precursor exposure to prevent incorporation of impurities into the deposited film. On the other hand,

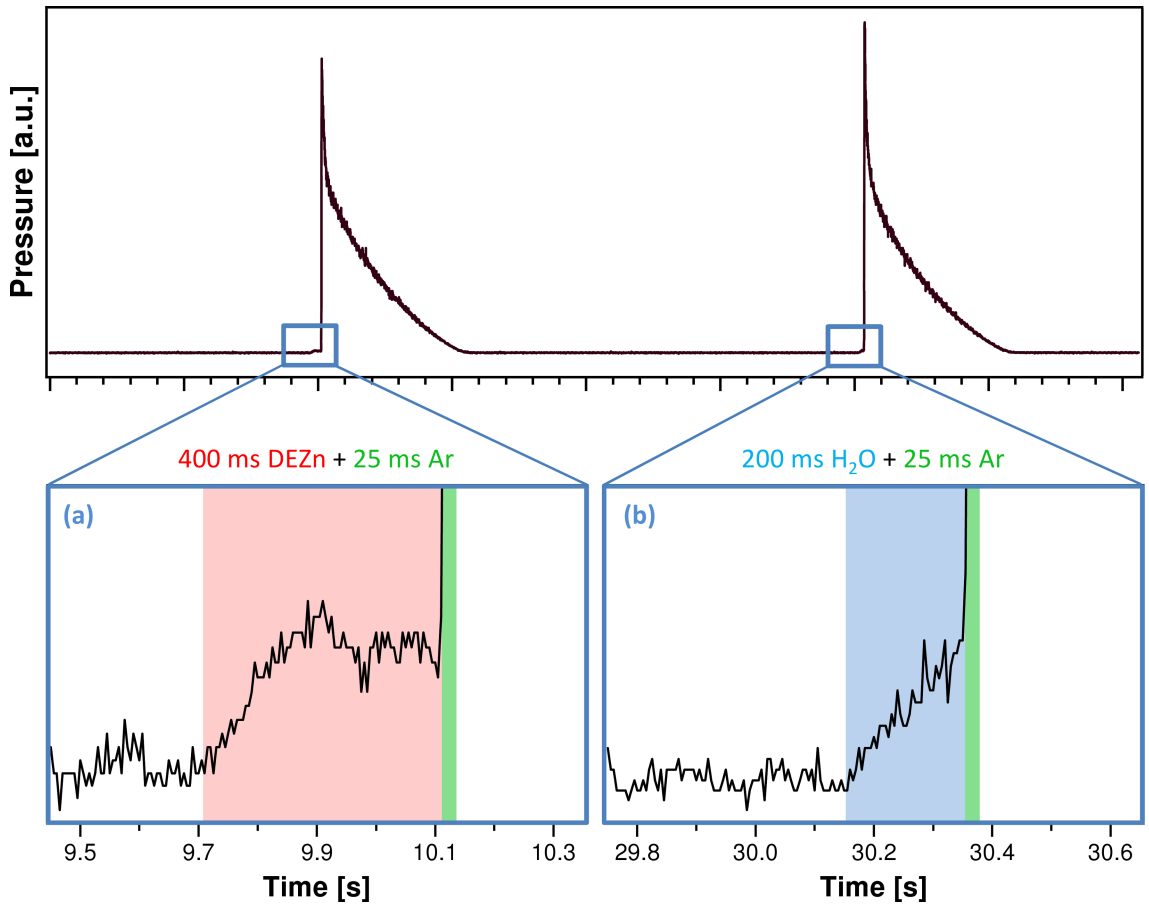

Figure 4.13: (top) Pressure evolution in the reactor chamber during one ALD cycle; (a) 400 ms DEZn exposure (red) followed by 25 ms Ar purge (green); (b) 200 ms H_2O exposure (blue) followed by 25 ms Ar purge.

the turbo molecular pump would shut-down due to those high pressures if no additional pumping step is performed.

Taking a closer look, it is even possible to check the pressure rising in the chamber during precursor exposure as shown in Fig. 4.13 (a) for 400 ms DEZn and 200 ms H_2O followed by 25 ms Ar flush. The length of the valve control signal for DEZn exposure is indicated by the red background in (a), whereas the signal for water exposure is indicated by a blue background. Especially in case of DEZn one can nicely see the pressure rising until a constant value of about $1.3 \cdot 10^{-1}$ mbar is reached.

Integrating the area of the pressure peaks can help controlling the reproducibility of the ALD reactor: a constant precursor intake at each ALD cycle is required for saturation of the sample surface and at the same time one can easily check whether the precursor sources have to be refilled.

4.3 Growth Parameters for ZnO-ALD

After the ALD reactor has successfully started operation, the growth parameters for reproducible ZnO atomic layer deposition have been determined as shown in this section. Furthermore, the chemical and structural properties of the deposited ZnO films are characterized.
As already mentioned in the Sec. 4.1, the basic process parameters for ideal self-limiting atomic layer deposition are the exposure times of the precursors to completely saturate the surface and the substrate's temperature. To determine those parameters for ALD of ZnO using diethylzinc and water as precursor materials, well-defined substrates have to be used to prevent substrate-induced effects on the growth rate of the ZnO.

4.3.1 Substrate Preparation

Polished silicon in a (111)-orientation was chosen to be used as substrate material because clean planar surfaces can be achieved relatively easily. To remove the thin natural oxide layer on the silicon surface, the substrates are prepared in a wet-chemical process directly before introduction into the Integrated System. Since the symmetry of the bulk crystal is broken at the surface, the bonding situation of the surface atoms differs from those in the bulk. This results in dangling bonds of the atoms located at the surface illustrated by the red atoms in Fig. 4.14 (a). In addition, reconstruction processes of the atoms occur at the surface to minimize the energetic situation of the system. The wet-chemical preparation on the one hand removes the surface oxides but at the same time saturates the dangling bonds by hydrogen atoms. This results in a stable, hydrogen-terminated Si(111)-H substrate surface, preventing an immediate re-oxidation of the silicon during transport to the Integrated System. Fig. 4.14 (b) presents the LEED pattern of one of the prepared Si(111)-H substrates, showing an unreconstructed 1x1 surface structure.

The wet-chemical sample preparation process starts with degreasing the silicon successively in an acetone and ethanol ultrasonic bath at 40 °C. Afterwards, possible solvent residues are removed by rinsing with ultrapure water. To obtain clean surfaces, a thick oxide layer is formed containing impurity atoms located at the silicon surface. This is achieved by treating the substrates in a boiling solution of 50 % sulfuric acid (H_2SO_4) and 50 % hydrogen peroxide (H_2O_2) for 10 min at 80 °C. After rinsing in ultrapure water,

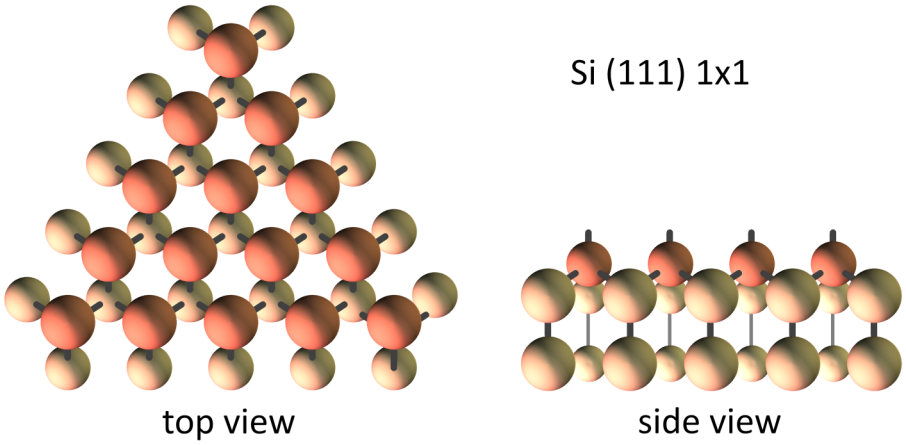

(a)

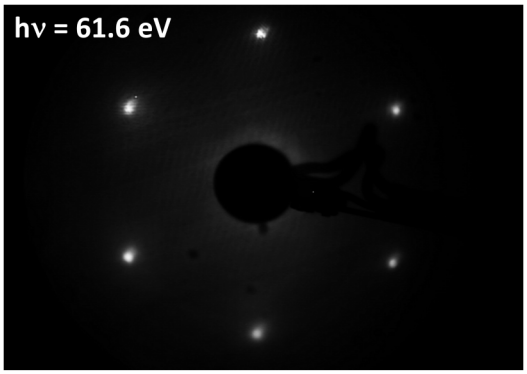

(b)

Figure 4.14: (a) crystal structure of Si(111) 1x1, atoms with unsaturated dangling bonds are shown in red; (b) LEED pattern of a hydrogen-terminated Si(111) 1x1 with hν = 61.6 eV

the oxide layer (and all impurities within) is removed in an ammonium fluoride (NH_4F) bath (40 %) at room temperature. At the same time the NH_4F removes the silicon oxide, it terminates the dangling bonds at the substrate's surface with hydrogen resulting in a clean Si(111)-H passivated surface. This hydrogen termination is sufficiently stable to prevent an oxidation of the surface during dry blowing with nitrogen, mounting the substrate on an sample holder and transferring it into the UHV system. Further details of the wet-chemical preparation process are described elsewhere[66].

After transfer into the Integrated System, the substrate is characterized by means of photoelectron spectroscopy for two reasons: first to make sure the cleanliness of the prepared surface and to determine the intensity of the Si 2p photoemission peak prior to

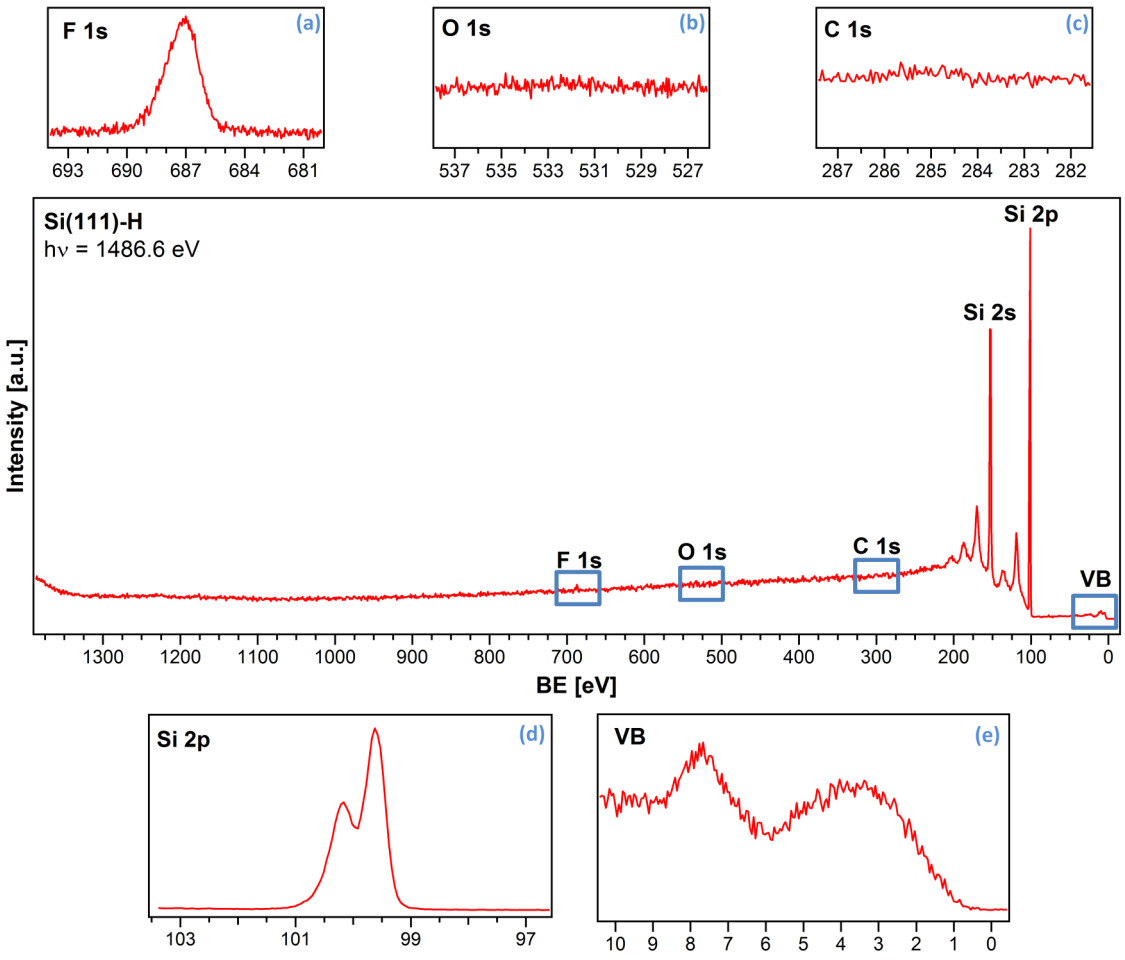

Figure 4.15: X-ray photoemission survey spectrum of Si(111)-H and the corresponding detail spectra of: (a) F 1s, showing small amounts of fluorine due to NH_4F treatment; (b) O 1s; (c) C 1s; (d) Si 2p; (e) valence band

atomic layer deposition. This peak is used to calculate the ZnO thickness after ALD by attenuation of the overlayer as described earlier in Sec. 2.2.1. The Si 2p spectrum shown in Fig. 4.15 (e) also demonstrates the spin-orbit splitting, having an energy difference of about 0.8 eV.

Figure 4.15 shows the survey spectrum of a Si(111)-H substrate prepared by the wet-chemical process described above. The insets show detail spectra of possible surface contaminants: fluorine (a), oxygen (b), and carbon (c). There are only very small amounts of oxygen and carbon present at the silicon surface. Hence, we neglect any influences of those traces on the initial growth of the ZnO.
As shown in Fig. 4.15 (a), a small amount of fluorine is present at the surface originating

from the ammonium fluoride treatment. Annealing the sample to 150 °C leads to complete removal of the fluorine.

4.3.2 Surface Saturation and ALD Window using DEZn and H_2O

First, the necessary exposure times of the two precursor materials diethylzinc and water had to be determined. This is crucial to achieve complete surface saturation and hence self-limited atomic deposition as mentioned earlier. The easiest method to make sure that the precursor exposure length is sufficient to saturate the surface is to determine the ZnO deposition per ALD cycle. This growth-per-cycle (GPC) will saturate at a maximum when the substrate is entirely covered with one monolayer of the precursor. To exclude effects of the second precursor on the GPC, an exposure time is chosen that definitely saturates the whole substrate.

The growth-per-cycle does not only depend on the amount of material that is provided during an ALD cycle but can also be affected by the number of reactive surface sites of the topmost atomic layer[57]. Since number and type of the reactive surface sites will differ between the pure Si(111)-H surface and ZnO, the GPC is expected to change during initial growth of the first completed ZnO monolayer. To avoid those surface effects, a very

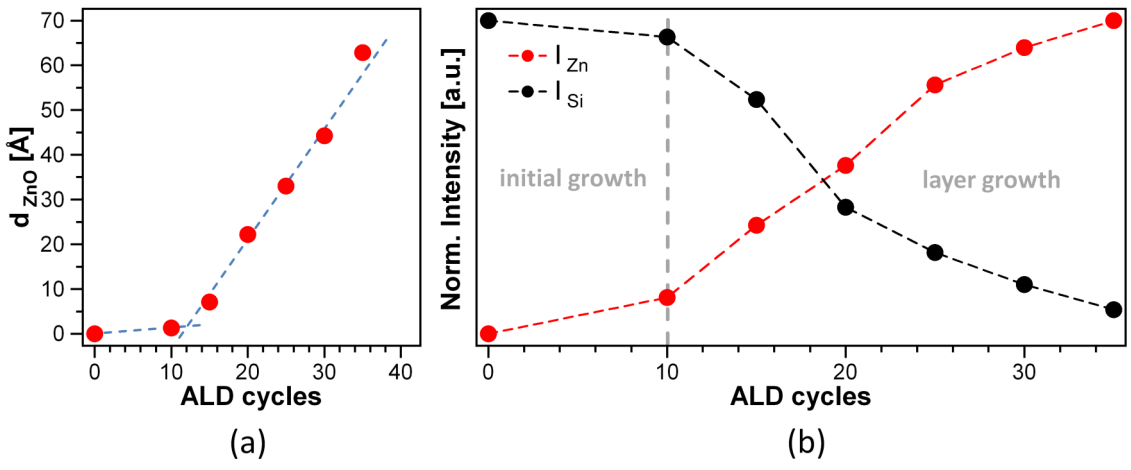

Figure 4.16: (a) GPC dependence on initial ZnO monolayer formation; (b) Normalized peak intensities plotted against ALD cycle. During the first approx. 10 ALD cycles the first ZnO monolayer is formed. Afterwards ideal layer-by-layer growth is achieved (cf. Fig 3.4).

thin layer of about 1 nm ZnO has been deposited prior to the actual experiment. This excludes any nucleation effects on the growth rate. As can be seen from Fig. 4.16 (a) it takes about 10 ALD cycles to complete the first ZnO monolayer. Comparing Fig. 4.16 (b) and Fig. 3.4 indicates that after the first monolayer has formed, an ideal layer-by-layer growth is achieved as expected in atomic layer deposition. The thickness of the initial ZnO layer still allows Si 2p photoelectrons of the substrate to travel through the overlayer without much attenuation. After characterization with XPS, five additional ALD cycles were grown and the film thickness has been determined by the attenuation of the Si 2p photoelectrons (cf. Sec.2.2.1). The GPC is simply the gain in film thickness divided by the number of ALD cycles deposited. Photoemission spectra of the involved elements are presented in Fig. 4.17. The left spectra show the Si 2p photoemission lines being attenuated by the ZnO overlayer. The spectra in the middle and at the right hand side show the rise of the Zn $2p_{3/2}$ and the O 1s photoemission, respectively. The O 1s peak consists of two separate photoemission peaks chemically shifted by approximately 1.5 eV. Detailed analysis of this second component will be the focus of Sec. 6.3.

The results of the surface saturation experiments are shown in Fig. 4.18. In case of DEZn saturation, a H_2O exposure time of 200 ms was selected to be sufficient to saturate all monoethylzinc surface adsorbates. All experiments were carried out at 210 °C.
An exposure time of diethylzinc of 400 ms has been determined to be sufficient to achieve

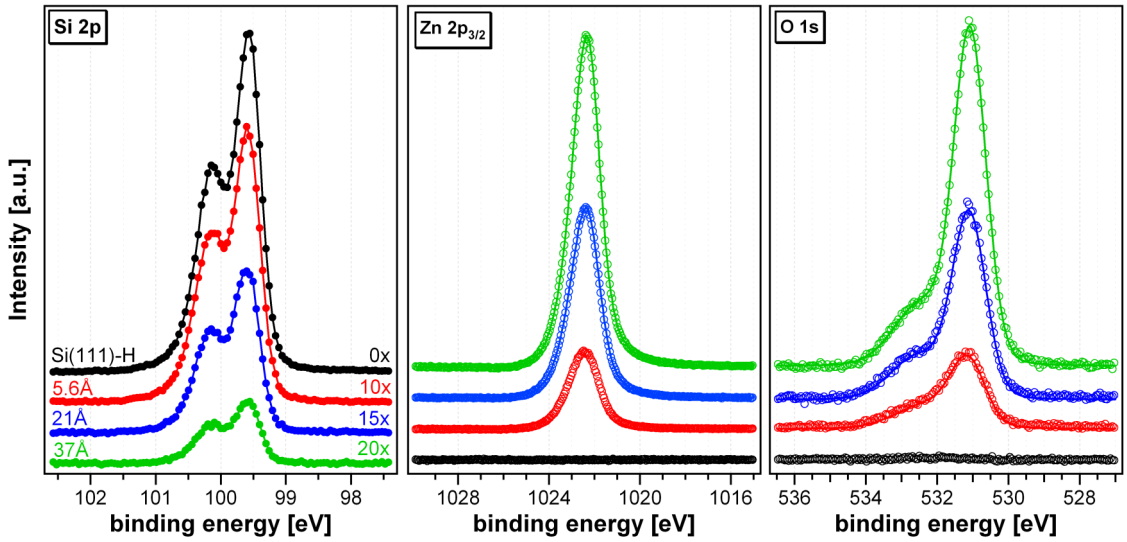

Figure 4.17: X-ray photoemission spectra of Si 2p, Zn $2p_{3/2}$ and O 1s. All spectra are excited by Al Kα radiation of 1486.7 eV. The attenuation of the silicon signal contains information about the ZnO overlayer thickness.

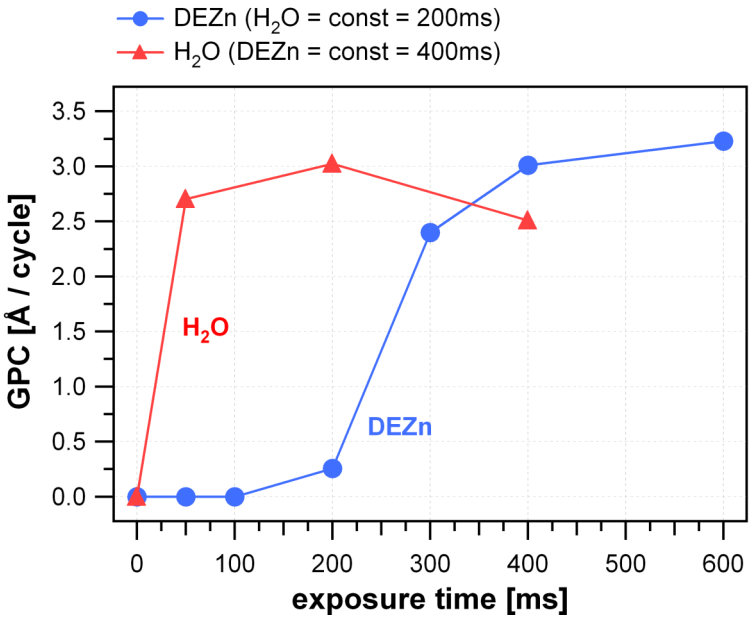

Figure 4.18: Growth-per-Cycle (GPC) dependence over precursor exposure of diethylzinc and water. At exposure times of 400 ms in case of DEZn and 50 ms in case of H_2O, the surface is completely saturated, indicated by the constant deposition rate of about 3.0 Å/cycle.

total saturation of the substrate's surface. The amount of ZnO deposited per ALD cycle approaches about 3.0 Å/cycle. The same value is reached in case of keeping the DEZn exposure time constant at 400 ms and varying the H_2O exposure time. 50 ms H_2O exposure are already sufficient to completely react with all available surface sites. To guarantee reproducibility of the atomic layer deposition process, exposure times of 400 ms for DEZn and 200 ms in case of H_2O were chosen for all upcoming ZnO ALD cycles.

The second crucial parameter of ZnO atomic layer deposition is the temperature of the substrate. To determine the temperature range of ideal self-limiting ALD growth, a thin ZnO layer was deposited onto the Si(111)-H for the same reasons as in case of the saturation experiments. Again, five ZnO-ALD cycles were deposited afterwards and the film thickness was determined by means of XPS. These experiments have been carried out for different well-defined substrate temperatures to determine the growth-per-cycle dependence on deposition temperature. In Fig. 4.19 the GPC is plotted against deposition temperature. As in theory (see Fig. 4.6) three temperature regimes can be classified in Fig. 4.19. At low temperatures, low reaction kinetics, i.e. slow reactions of the precursor molecules with the surface species, result in a decreases GPC. With increasing temper-

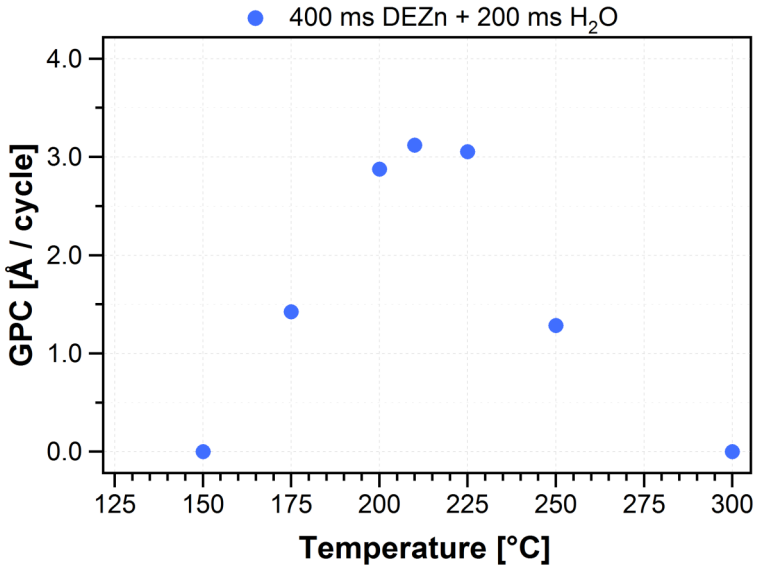

Figure 4.19: Growth-per-cycle dependence on deposition temperature. The temperature regime showing constant deposition rate and hence temperature-independent self-limiting growth is referred to as the *ALD window*.

ature, the GPC increases until it reaches a value of 3.0 Å/cycle. This point defines the beginning of the ALD window, the regime of temperature independent self-limited ALD. The ALD window using the precursor combination DEZn and water is located between 200 °C and 225 °C. Hence, 210 °C is determined as the optimal deposition temperature of this ALD reactor. At temperatures higher than 225 °C, desorption of the precursors molecules adsorbed on the surface increases, which again results in a decrease in growth rate.

To verify this growth rate, a ZnO film of 200 ALD cycles has been deposited and a cross-section scanning electron microscopy (SEM) image has been taken. Analysis of this image resulted in a film thickness of approximately 42.4 nm. In combination with the amount of deposition cycles, a growth rate of 2.1 Å/cycle has been determined. Both growth rates match to literature values of $1.9 - 2.8$ Å/cycle previously reported by other groups[14;67–71] for the ZnO atomic layer deposition using DEZn and H_2O as reactants. One has to keep in mind that both methods offer sources of error, namely imprecise film thickness determination from the SEM images and errors during data processing and IMFP calculation in case of PES. From now on, the value determined by photoelectron spectroscopy is used to express the film thickness, since it can be determined in situ and without big effort.

Assuming the zinc oxide growing in a preferred orientation along its c-axis (shown later in Sec. 4.4) results in a monolayer thickness for ZnO of 5.2 Å/cycle. Hence, a deposition rate of 3.0 Å/cycle corresponds to a growth of ≈ 60 % of an entire monolayer, limited by steric hindrance effects caused by the ethyl ligands of the DEZn. Thus, one can assume a complete ZnO monolayer to be formed each two ALD cycles.

An additional information about the ALD process can indirectly be achieved from the ALD window in Fig. 4.19: due to the existence of the self-limited growth character it is proofed that the argon purging step is sufficient to remove all residual precursor gases from the reactor and therefore prevent CVD-like deposition from the gas phase during the ALD process.

4.4 Chemical and Structural Characterization of ALD-ZnO films

After determination of the optimal growth parameter for self-limited atomic layer deposition of ZnO, chemical and structural film properties of the deposited layers are investigated. Therefore, a ZnO layer of 50 ALD cycles and an estimated film thickness of $d_{ZnO} = 15$ nm is deposited onto Si(111)-H. Since this thickness is much larger than the

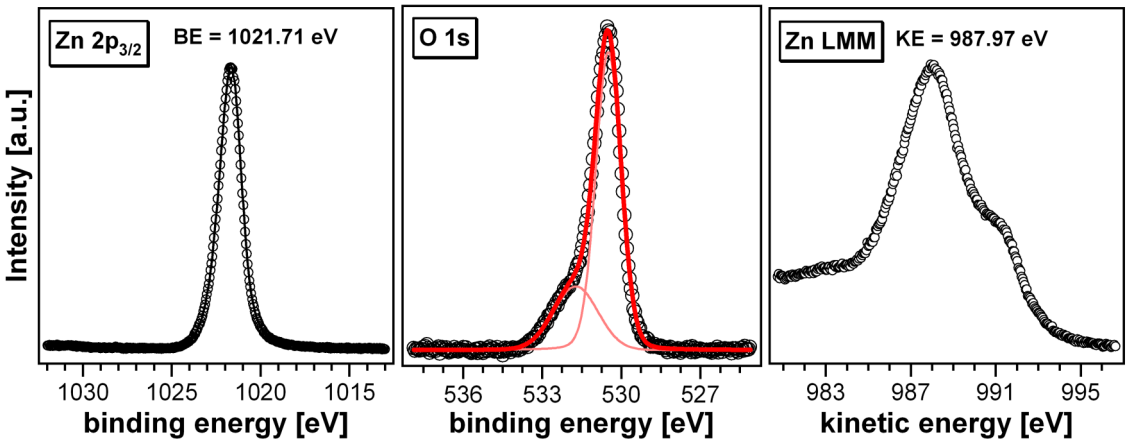

Figure 4.20: Photoemission spectra of an ALD-ZnO layer much thicker than the escape depth of the photoelectrons. All spectra are recorded using Al-Kα radiation of 1486.7 eV. Quantification of the spectra results in a [Zn]:[O] ratio of 0.97 and an zinc Auger parameter of 2009.68 eV.

escape depth of the photoelectrons, possible effects of the Si(111)-H/ZnO interface can be ruled out. Fig. 4.20 plots the photoemission spectra of the Zn $2p_{3/2}$ and O 1s photoelectrons and the Zn LMM Auger electron peak. After background removal, peak fitting results reveal a [Zn]:[O] ratio of 0.97, i.e. the ZnO layer is close to the stoichiometric composition of 1.00. At this point it is reminded that for compositional analysis the sum of both O 1s components is taken into account.

Furthermore, the Auger parameter has been calculated to investigate the chemical environment of the zinc component. Peak fitting results in a Zn $2p_{3/2}$ photoelectron binding energy of BE = 1021.71 eV. In combination with the kinetic energy of the Zn $L_3M_{4,5}M_{4,5}$ Auger electrons of KE = 987.97 eV the Zn Auger parameter results in:

$$\begin{aligned} \text{AP (Zn)} &= \text{BE (Zn } 2p_{3/2}) + \text{KE (Zn } L_3M_{4,5}M_{4,5}) \\ &= 1021.71 \text{ eV} + 987.97 \text{ eV} \\ &= 2009.68 \text{ eV} \end{aligned} \tag{4.5}$$

This Auger parameter is in excellent agreement with the zinc Auger parameter of ZnO observed previously for the MOMBE ZnO deposition[21]. Combination of the Auger parameter and the results of the composition analysis clearly reveal that the ALD reactor has the ability to deposit ZnO layers of high quality.

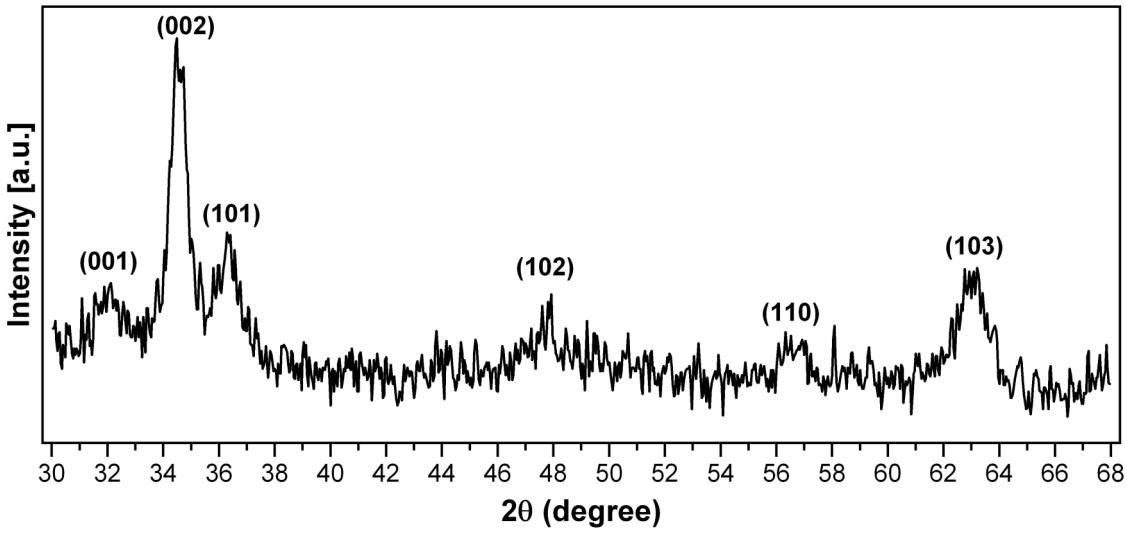

Figure 4.21: Grazing-incidence X-ray diffraction data of an approx. 50 nm thick ALD-ZnO layer. In comparison with XRD data of ZnO powders[72], a preferred orientation along the c-axis is assumed[73].

Since this work is focused mainly on the electrical and chemical properties of ZnO grown by atomic layer deposition, only brief analysis of the structural properties is presented in this work. To characterize the structural quality of the ALD-grown ZnO films, *grazing-incidence X-ray diffraction* (GI-XRD) experiments have been carried out. Using GI-XRD, the thickness of the film under investigation can be significantly smaller than in conventional X-ray diffraction experiments. Anyhow, the thickness should exceed 50 nm to get an satisfactory signal-to-noise ratio. Hence, a ZnO film of 200 ALD cycles, resulting in roughly 60 nm ZnO film thickness, has been prepared again using Si(111)-H as substrate material. The results of the GI-XRD using Cu-Kα radiation are shown in Fig. 4.21. The most prominent feature in Fig. 4.21 can be assigned to a (002) reflex[73]. Most references in XRD databases[72] usually provide structural information of statistically oriented powders without any preferred growth orientation. Nevertheless, the line positions of those powders match to those of the ALD-ZnO film presented in Fig. 4.21. This verifies the ZnO is growing in wurtzite structure, as expected. The intensity distribution of the Bragg peaks differs from those in the powders, giving an indication that the films grow along a preferred orientation. Matsubara et al. present XRD measurements of epitaxially deposited ZnO films on $LiNbO_3$ substrates. Their XRD measurements only result in one single Bragg peak related to a (002) reflection. Since the (002) peak of the ALD-ZnO films is the most prominent one, we assume those layers to grow in a preferred orientation along the c-axis.

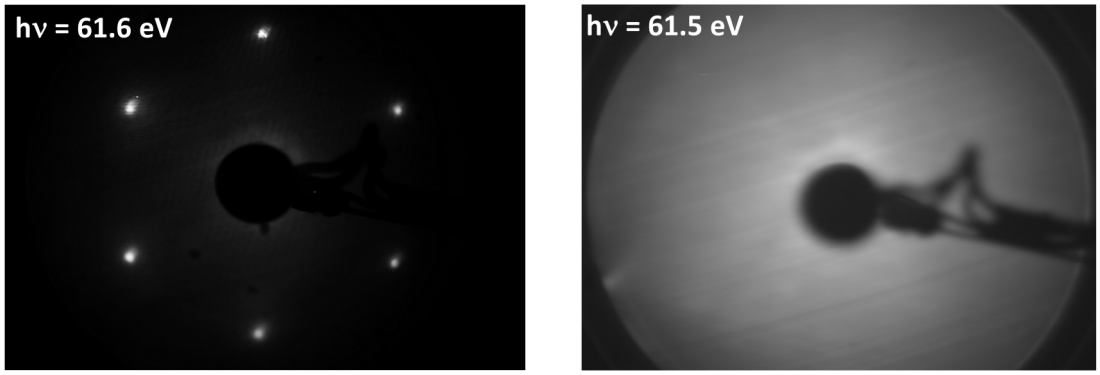

(a) (b)

Figure 4.22: (a) Low-energy electron diffraction (LEED) pattern of the clean Si(111)-H 1x1 substrate; (b) LEED spots disappear after deposition of ALD-ZnO since the lattice mismatch of the two materials avoids highly-ordered growth of the ZnO layer.

Furthermore, ALD-ZnO films have been investigated in situ by *low-energy electron diffraction* (LEED). Prior to ZnO deposition, the Si(111)-H substrate has been characterized to validate its structural quality. Fig. 4.22 (a) verifies the Si(111)-H substrate having a 1x1 surface orientation[74] without showing any superstructure spots. After 50 ALD cycles, the LEED pattern of Fig. 4.22 (b) does not show any reflexes. Instead, the background intensity has risen. Hence, even though the films grow in a preferred orientation along the c-axis as resulted from the GI-XRD measurements, the films do not show a long-range order resulting in LEED spots. This is also expected, since the lattice constants of (111)-oriented Si ($a = 3.84$ Å[74]) and ZnO along its c-axis ($a = 3.25$ Å[20]) differ significantly, resulting in lattice mismatch of 15.4%

4.5 Initial Growth of ALD ZnO on Si(111)-H

In general, films produced by atomic layer deposition are usually in the nanometer range. Hence, the interface between substrate and ZnO deposit cannot be neglected anymore. The thinner the deposited film, the more chemical or structural changes at the interface influence the electronic properties of the material and, depending on its application, the efficiency of the device. Therefore, the focus of the following section is on the initial ALD-ZnO growth on Si(111)-H substrates and the properties of its interface.

To investigate the initial growth on silicon, monolayers of zinc oxide are deposited stepwise onto the substrate. As determined in Sec. 4.3, it takes about two ALD cycles until one complete ZnO monolayer is formed. After deposition of each monolayer, the sample is characterized by means of photoelectron spectroscopies. These steps are repeated until the deposited layer thickness exceeds the escape depth of the silicon photoelectrons. Fig. 4.23 plots the photoelectron spectra of the involved elements oxygen, zinc and silicon after each deposition step.

The spectra in the front of Fig. 4.23 belong to the pure Si(111)-H substrate. The Si 2p peaks have a FWHM of about 0.5 eV and there is no indication of a surface oxide. The intensity of the Si 2p photoelectron peak is determined for calculation of the ZnO layer thickness as described above. In Sec. 4.3.2 it has already been mentioned that it takes several ALD cycles until the initial growth of ZnO on Si(111)-H starts. Therefore, in the first step 5 ALD cycles were deposited, resulting in a calculated film thickness of 0.96 Å

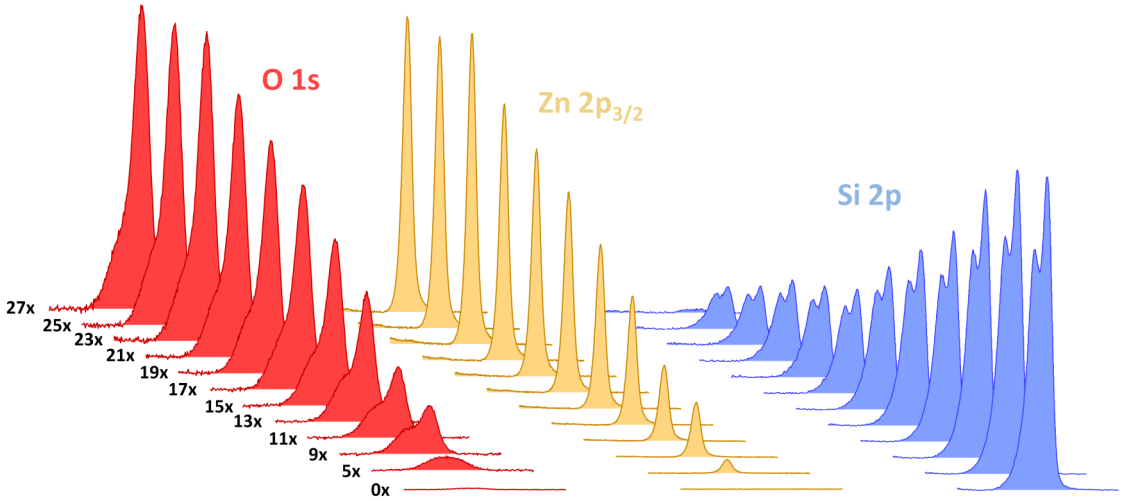

Figure 4.23: Photoemission spectra of (left) O 1s; (middle) Zn $2p_{3/2}$; (right) Si 2p during monolayer-wise atomic layer deposition of ZnO. While the substrate signal constantly decreases during deposition, both film elements rise until they reach a maximum. No oxidation of the silicon is observed during deposition of ZnO with ALD. All spectra are recorded using Al Kα radiation and background signals were removed.

corresponding to an initial surface coverage of the deposit of about 0.33 %. In step two, 4 additional ALD cycles were deposited to complete this first monolayer. Afterwards, two ALD cycles were sufficient to grow ZnO in monolayer steps. The spectra in Fig. 4.23 clearly show the attenuation of the substrate's Si 2p photoemission signal until it completely disappears after 27 x ALD. The corresponding film thickness after this deposition step is about 45 Å. At the same time, the photoemission peaks of both film elements zinc and oxygen rise until they reach a maximum. This maximum is achieved after about 23 x ALD while there is still a small silicon peak visible. This might occur due to the differences in the inelastic mean free paths (IMFP) of the contributing elements. While the Al Kα excited Si 2p photoelectrons exhibit high kinetic energies of 1388 eV resulting in an IMFP of about 30 Å, the kinetic energies of the O 1s and Zn $2p_{3/2}$ electrons are significantly lower. Their IMFPs amount to 24.2 Å and 16.9 Å, respectively, resulting in a slightly reduced information depth in comparison with Si 2p.

The resulting peak intensities of the spectra plotted in Fig. 4.23 are determined and normalized to 100 % with respect to the most intense peak of each element as shown in Fig. 4.24. To illustrate the peak intensity behavior during initial growth, the results are plotted against the number of atomic layer deposition cycles in Fig. 4.24 (a) and the ZnO

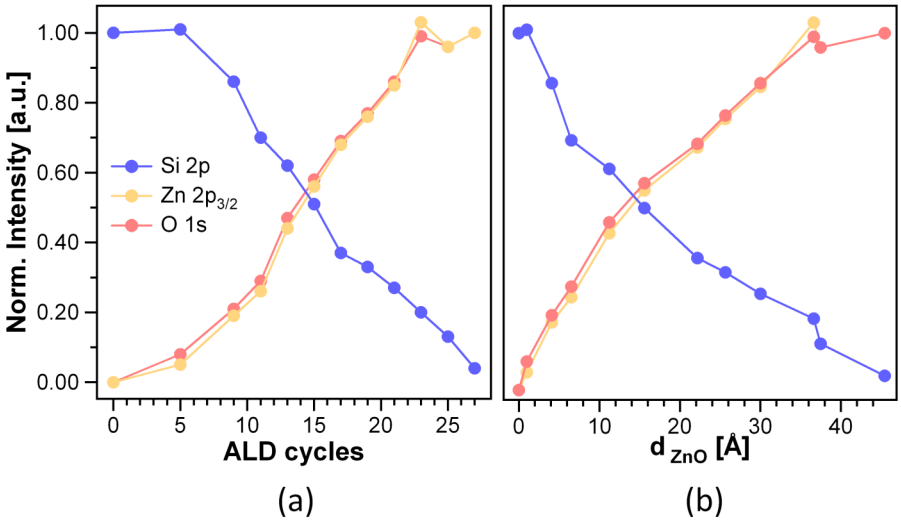

Figure 4.24: Photoemission peak intensity development of initial ZnO atomic layer deposition. Peak intensities for each element are normalized to 100 % of the maximum intensity. Peak intensities are plotted against deposition cycles (a) and ZnO overlayer thickness (b), respectively.

overlayer thickness in Fig. 4.24 (b). Both, initial ZnO monolayer formation and saturation of the zinc and oxygen signals at a maximum are clearly noticeable. The attenuation of the silicon substrate signal again matches to the expected layer-by-layer growth mode after the initial ZnO monolayer was formed.

Figure 4.25 (a) presents the regional spectrum of the Zn $2p_{3/2}$ photoemission line after the last deposition step. The black circles represent the measured data after removing the secondary electron background by a Shirley routine. Fitting the peak by a Voigt function, a convolution of a Gaussian and Lorentzian profile, ends up in the peak fit shown as a solid red line. The resulting error is illustrated by the green line. The zinc spectrum shows no indication for a second chemical component in the ZnO layer. In addition, the Zn $2p_{3/2}$ photoemission contains information about the crystalline quality during initial growth. Therefore, the peak full width at half maximum (FWHM) of the Zn $2p_{3/2}$ photoemission line was determined after each deposition step and plotted as a function of ZnO thickness in Fig. 4.25 (b).

The peak width can be taken as an indication of the order in the crystal. The broader the photoemission peak, the more disordered the film[75]. Fig. 4.25 (b) shows a significant decrease from an initial value of 1.72 eV after the first deposition step down to a constant value of 1.53 eV. This indicates an increased amount of disorder in the film at

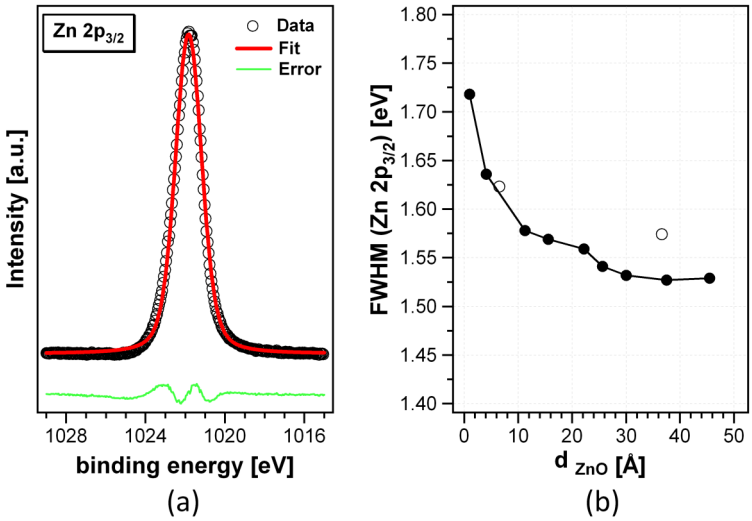

Figure 4.25: (a) Peak fitting (red line) of the Zn $2p_{3/2}$ photoemission line (black circles) revealing one single zinc component in the ZnO film; (b) FWHM dependency on deposited ZnO film thickness. The peak width is giving an indication of the disorder at particular film thicknesses.

the ZnO-Si(111) interface, while the chemical environment becomes more homogeneous with increasing film thickness. This can cause considerable effects on device efficiencies as the interface disorder may induce increased charge carrier scattering lowering their mobilities[75].

While the Zn $2p_{3/2}$ photoelectrons do not show significant changes during initial growth, the opposite is true in case of the oxygen component. As mentioned earlier, the O 1s does not only show one but two chemical components as readily identifiable in Fig. 4.23. To clarify its extensive change during initial growth, the O 1s photoemission spectra at different deposition stages are plotted in Fig. 4.26. Three different deposition steps are chosen to illustrate the O 1s behavior with increasing film thickness: a very thin, not even completed film corresponding to the first deposition step is shown in Fig. 4.26 (a). Fig. 4.26 (b) represents an intermediate thickness regime of about 4 Å, while the spectrum shown in Fig. 4.26 (c) belongs to a film thickness of 45.45 Å, where the initial ZnO growth already finished.

To identify the two different chemical components present in the crystal, the determined binding energies are compared to reference work by other groups. Dupin et al. published a study on various metal oxides, amongst others zinc oxide[76]. Almost all metal oxides show two oxygen components with the main component being O^{2-} ions bound to the

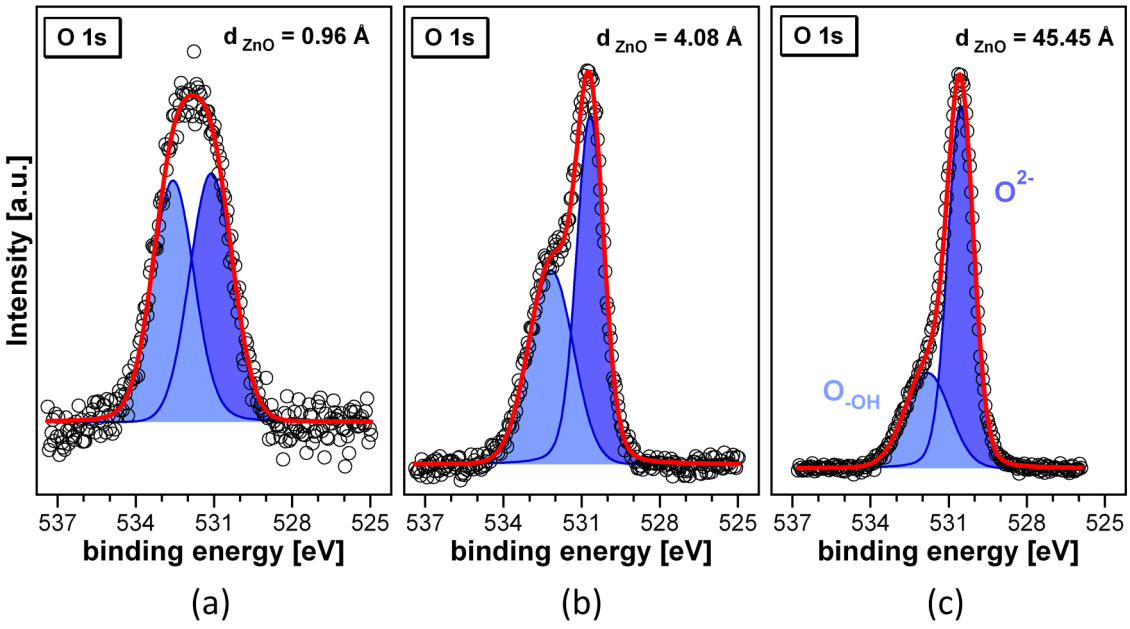

Figure 4.26: Evolution of the O 1s photoemission during initial growth. Two chemical components are observed, that are related to $[O^{2-}]$ anions forming ZnO (dark blue) and an $[O_{-OH}]$ component usually attributed being located at the surface of the ZnO (light blue).

metal ion. In case of ZnO, those O^{2-} ions that are bound to the zinc atoms have binding energies around 530.5 eV.
The second oxygen component is usually attributed to hydroxide oxygen (-OH) [76] mainly located at the surface of the ZnO film. Their O 1s electrons exhibit a chemical shift of $\Delta BE \approx 1.5$ eV. This especially fits for ZnO-ALD using H_2O as oxygen precursor, where the reaction model predicts a hydroxide terminated surface after each deposition cycle (cf. Eq. 4.3).

Hence, all three O 1s spectra were fitted with two oxygen components, as labeled in Fig. 4.26 (c). A third component related to water molecules weakly adsorbed at the surface around binding energies of 533.5 eV [77] is not observed. During formation of the first ZnO monolayer, both oxygen components show equal intensities. There is no evidence for an oxidation of the silicon. On the one hand, the formation of SiO_2 would result in a photoemission peak at 103.5 eV [78] and on the other hand, a third oxygen component would be observed in Fig. 4.26 (a) in an energy range between $532.5 - 533.2$ eV [79]. Further deposition would decrease an O 1s signal originating from SiO_2 in Fig. 4.23 (b) until it vanishes completely for thick ZnO films in Fig. 4.26 (c). This is not observed and in

combination with the absence of an Si 2p photoemission signal at 103.5 eV, an oxidization of the Si(111)-H substrate can be ruled out.
Peak fitting results show no significant change in peak width ($[O^{2-}]$ = 1.07 eV and $[O_{-OH}]$ = 1.97 eV) or an increased chemical shift between those two oxygen components (ΔBE = 1.25 eV) during initial growth. Instead, Fig. 4.23 (b) and (c) show a continuous increase of the $[O^{2-}]$ component with respect to the $[O_{-OH}]$. Plotting the $[O_{-OH}] : [O^{2-}]$ development over the corresponding film thickness shows a constant decrease of the intensity ratio. During deposition of the first ALD cycles both components are present to same amounts. After initial monolayer formation the intensity of the $[O_{-OH}]$ decreases until it settles at 40 % of the $[O^{2-}]$ intensity, as shown in Fig. 4.27 (a).

Deeper insight into the initial atomic layer deposition of ZnO on Si(111)-H is obtained by composition analysis after each deposition step. As already mentioned in Sec. 2.2.1, the total O 1s intensity is used for determination of the film composition. Hence, both oxygen components contribute to the calculated [Zn]:[O] ratio. The determined [Zn]:[O] ratio is illustrated in Fig. 4.27 (b) plotted against the calculated film thickness. Ideal stoichiometry of [Zn]:[O] = 1.00 is indicated by the dotted line. During initial monolayer formation, the film is extremely oxygen-rich with a calculated composition of [Zn] : [O] $\approx$ 0.5. After completing the first monolayer, a sudden jump is observed in the [Zn]:[O] ratio. With increasing film thickness, the excess amount of oxygen incorporated into the ZnO decreases,

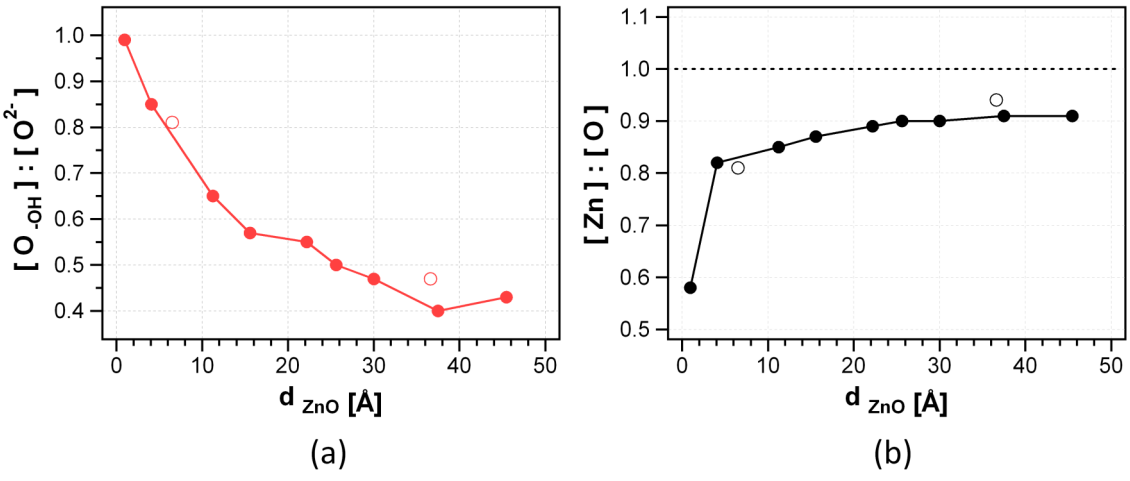

Figure 4.27: (a) Intensity ratio of the two oxygen components O^{2-} and O_{-OH} plotted against ZnO thickness; (b) Thickness dependency of the composition. The interface is highly oxygen-rich, even though no silicon oxide formation is observed.

ending up in a composition that saturates at [Zn] : [O] = 0.91. The films deposited in monolayer steps show a slight zinc deficiency, while those films deposited in one single step are close to stoichiometry as shown earlier. Since all deposition parameters were kept unchanged, there are only two possible explanations. Both are related to a removal of surface hydroxides, either by the raise in substrate temperature prior to the next atomic layer deposition step or by irradiation damage during surface analysis.

Additional information about the local chemical environment during initial deposition is obtained by analysis of the zinc Auger parameter. The Zn Auger electron spectra corresponding to each deposition step are presented in Fig. 4.28 (a). To determine the kinetic energy of the Zn $L_3M_{45}M_{45}$ peak, a single Gaussian peak has been fitted. Combination of the kinetic energy of the Auger electrons and the binding energy of the Zn $2p_{3/2}$ photoelectrons as given in Eq. 2.4 results in its modified Auger parameter. Fig. 4.28 (b) illustrates its thickness dependency during initial growth on Si(111)-H. Comparison of the determined Auger parameter with databases and values earlier reported by other groups yield information about the local chemical environment of the zinc after each ZnO atomic layer deposition step.

After five ALD cycles, i.e. at stages where the first ZnO monolayer is not yet completed, the Auger parameter amounts 2010.03 eV. The corresponding binding and kinetic energies

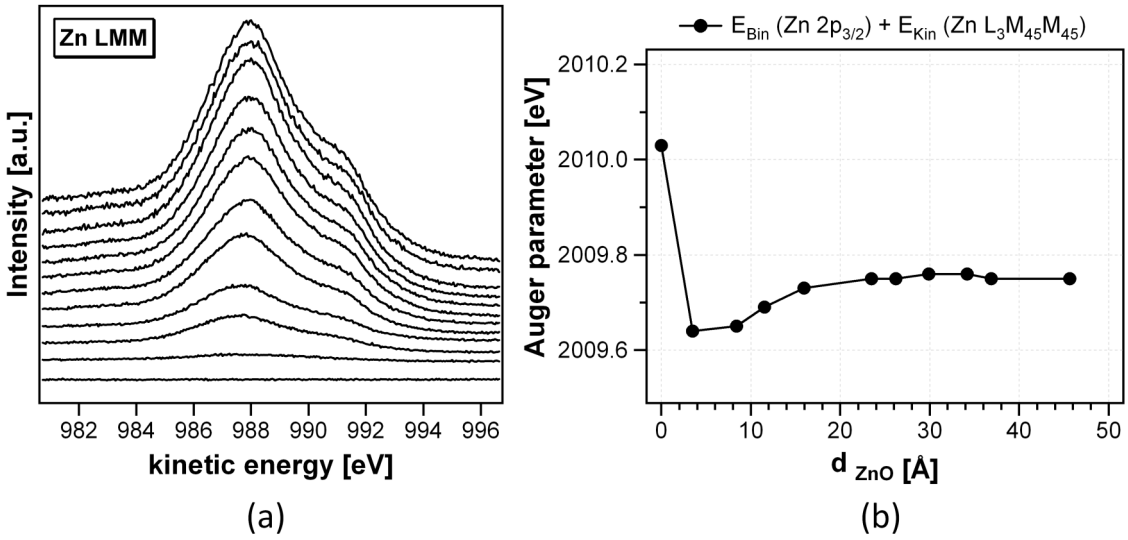

Figure 4.28: (a) Zn $L_3M_{45}M_{45}$ Auger electron spectra during initial ZnO deposition; (b) Auger parameter development with increasing film thickness.

Compound	Auger Parameter	BE (Zn $2p_{3/2}$)	KE (Zn $L_3M_{45}M_{45}$)
ZnO	2009.5 − 2011.0 eV	1021.2 − 1022.5 eV	987.7 − 988.9 eV
$Zn(OH)_2$	2009.2 eV	1022.7 eV	986.5 eV
Zn	2013.4 − 2014.4 eV	1020.8 − 1022.1 eV	991.8 − 992.5 eV

Table 4.1: Reported Zn Auger parameter[29] for different compounds potentially present during initial ZnO atomic layer deposition on Si(111)-H substrates.

are BE (Zn $2p_{3/2}$) = 1022.23 eV and KE (Zn LMM)= 987.80 eV, respectively. After completing the first monolayer, a sudden decrease to 2009.64 eV (BE = 1022.06 eV; KE = 987.58 eV) is observed, followed by a slight increase up to a film thickness of about 25 Å. Additional ZnO deposition does not affect the Auger parameter, remaining constant at 2009.75 eV (BE = 1021.83 eV; KE = 987.92 eV). Even if the results of the composition analysis suggest a formation of zinc hydroxide ($Zn(OH)_2$) at very early stages of the ZnO deposition, Auger parameter analysis disagrees. Table 4.1 summarizes all reported Zn Auger parameter values for zinc compounds possibly present at the ZnO-Si(111)-H interface. Even though there is only one reported Auger parameter available for $Zn(OH)_2$, there is a significant difference to the measured value of $\Delta AP = 0.8$ eV. The measured zinc Auger parameter rather speaks for the formation of oxygen-rich zinc oxide after completing the first deposited monolayer. The Auger parameter also indicates this initially formed monolayer to be ZnO. With increasing film thickness, the amount of surplus oxygen decreases as composition analysis pointed out. This is also observed in the development of the Auger parameter. Comparing the literature values for ZnO and $Zn(OH)_2$ reveal a decrease in Auger parameter with increasing amount of oxygen. Hence, the increase in measured Auger parameter with increasing film thickness indicates a decrease of oxygen the thicker the deposited ZnO films. This is in total agreement with the rising [Zn]:[O] ratio in this thickness region.

All individual results presented in this section help to develop a phenomenological model of the initial atomic layer deposition of ZnO on Si(111)-H. An attempt to illustrate the initial ZnO monolayer formation on Si(111)-H is made in Fig. 4.29. Before deposition of the first ALD cycle, the substrate's surface is assumed to be entirely hydrogen-terminated. However, it is obvious that this hydrogen-termination has to be removed to allow the formation of a stable bond between silicon and zinc oxide. Hence, either the diethylzinc or the water has to remove the hydrogen. For reason shown in a moment, we assume this to occur during the water exposure. Hence, as shown in the top left part of Fig. 4.29, the original hydrogen-terminated surface remains unchanged during the first DEZn exposure.

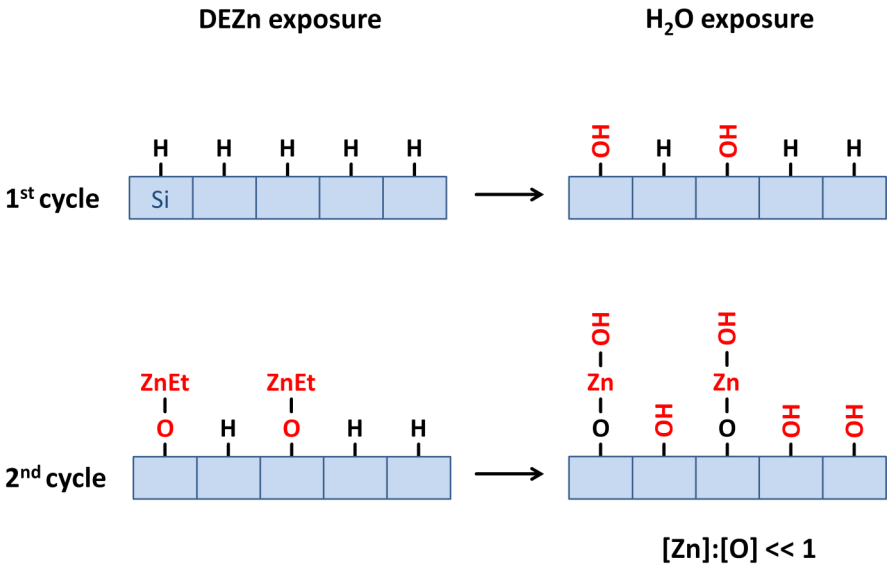

Figure 4.29: Illustration of the developed initial growth model of ZnO on Si(111)-H for the first two ALD cycle half-reactions.

There is no reactive site to bond with and all DEZn is removed by the subsequent argon purge. Afterwards, the first water pulse is introduced into the deposition chamber. However, few water molecules remove the hydrogen-termination of the silicon surface. This would end up in a hydroxylation of some silicon surface sites as shown at the top right part of Fig. 4.29.

At this stage, an investigation of the sample by means of photoelectron spectroscopy would not show big differences to the hydrogen-terminated silicon substrate. Only small amounts of oxygen might be observed if not below the detection limit of XPS.

The second ALD cycle again exposes the surface with DEZn which now finds some reactive sites in terms of surface hydroxides. As assumed in the standard model of ZnO ALD (cf. Sec. 4.1.1), one ethyl ligand will undergo a bond with the hydrogen atom forming gaseous ethane. After this half-reaction has finished, part of the surface is covered by monoethylzinc (ZnEt), while the rest is still hydrogen-terminated. This is illustrated at the bottom left of Fig. 4.29.

While the second ALD cycle is completed by exposing the substrate to water (bottom right), two different reactions do occur. At the one hand, the water removes the remaining ethyl ligand of the monoethylzinc by exchanging one hydrogen atom. On the other hand, the water will further remove hydrogen from the original Si(111)-H surface. Only for reason of illustration, a complete removal of the hydrogen-termination is assumed in the bottom right part of Fig. 4.29. After this second cycle, the entire surface is terminated

by hydroxides, as the standard model of ZnO atomic layer deposition assumes.
X-ray photoelectron spectroscopy after this cycle would show a completely different picture as after the first ALD cycle. On the one hand, the adsorbed zinc atoms would produce a photoemission peak. On the other hand, two oxygen components would be observed: one originating from the oxygen atoms bound to silicon and zinc and one originating from the hydroxides, the latter more intense than the first. Further atomic layer deposition would lead to more incorporation of $[O^{2-}]$ forming ZnO, while the amount of hydroxides will remain almost constant. This might be true if it mainly terminates the surface and only small amounts are incorporated into the crystal. This would lead to a constant decrease of the $[O_{-OH}]$:$[O^{2-}]$ ratio with increasing film thickness, until it saturates at a constant level. This is exactly what is observed in Fig. 4.27 (a).
Additionally, the model presented in Fig. 4.29 results in a very oxygen-rich initial film, observing a composition of [Zn] : [O] $\gg$ 1.00 during formation of the initial monolayer. Increasing film thickness reduces the effect of the surplus oxygen at the silicon surface, resulting in an increase of the [Zn]:[O] ratio as observed in Fig. 4.27 (b).
As mentioned above, it is assumed that the hydrogen-termination of the silicon is removed during the water exposure and not affected by the DEZn. If this would not be the case and the DEZn would remove the H-termination to form stable bonds to the silicon, the [Zn]:[O] analysis would result in a stoichiometric or even zinc-rich initial monolayer. Since this is not observed, the removal of hydrogen is assigned to the H_2O, possibly by formation of H_2 reaction products.

4.6 Summary

In this chapter, the characteristic properties of atomic layer deposition were introduced, followed by a detailed description of the design, assembly and commissioning of an UHV-compatible ALD reactor. In this work, ultra-high vacuum conditions are necessary for the in situ deposition and analysis experiments, without any modification of the material's surfaces under investigation.
Furthermore, the successful atomic layer deposition of zinc oxide has been demonstrated, using the widely-used precursor combination of diethylzinc and water as reactants. The existence of the so-called *ALD window*, i.e. a temperature-regime where the deposition rate remains constant, indicates an self-limited atomic layer deposition process. In addition, photoemission studies of the stepwise deposition of ZnO monolayers on hydrogen-

terminated silicon show ideal layer-by-layer growth of the material.
After investigation of the film properties that reveal the high quality of the ZnO grown by the ALD system, the initial growth of ZnO on Si(111)-H has been determined by in situ photoelectron spectroscopies. Analysis of the [Zn]:[O] ratio and the combined Auger parameter of the zinc component show an oxygen-rich initial growth that turns into stoichiometric ZnO during the growth of the first 3 nm. It is worth mentioning that no oxidation of the silicon substrate has been observed during the photoemission studies.
All things considered, we showed that we are able to deposit high-quality ZnO films with the accuracy of an atomic monolayer. Hence, the ALD reactor designed for this work is suitable for further experiments on the interface formation of ZnO and epitaxial $CuInSe_2$ (112), presented in the following chapter.

5 ALD-ZnO as Cd-free Buffer Layer for Chalcopyrite Solar Cells

One of the main interests in chalcopyrite solar cell research is to substitute the CdS buffer layer by a cadmium-free alternative for junction formation with the p-type chalcopyrite absorber. As extensively discussed in the introductory chapter (see Sec. 1.1.2), one of the main motivations is the toxicity of Cd, which might lead to legal regulations in different countries, such as Germany[5]. On the other hand, it is technologically advantageous to replace the chemical bath deposition (CBD) by a vacuum deposition process, resulting in a continuous in-line vacuum production of the solar cell device.
Various materials are investigated as alternative buffer layer candidates. Most promising results are achieved by In_2S_3 and Zn-based materials such as ZnS, ZnSe, or ZnO[5;10]. Often even higher efficiencies are achieved if the buffers additionally contain some oxygen, most often in terms of hydroxides. These materials were deposited by several deposition techniques besides the standard chemical bath deposition, as for instance chemical vapor deposition methods, sputtering, or atomic layer deposition. An additional advantage to the cadmium issue is their increased band gap with respect to CdS. This reduces the absorption of photons in the spectral region between $350 - 550$ nm which can result in an increase of the solar cell's efficiency. Also ZnO deposited directly on chalcopyrite absorbers showed some good results in terms of device efficiency[5;10]. Especially the role of oxygen in the buffer layer material is not well understood, yet.
While all of those studies investigated the alternative buffer materials in terms of the efficiency of the fabricated devices, our approach is focused on the chemical and electronic properties of the interface between the chalcopyrite absorber and the buffer material. To understand the fundamental properties of this contact, all our experiments are carried out on well-defined single crystalline chalcopyrite absorbers, grown in the technologically relevant (112) orientation. The (112) orientation was chosen, since it is the preferred growth orientation of polycrystalline chalcopyrites used in solar cell production.

In an earlier study of ZnO deposited by MOMBE (cf. Sec. 3.4) on $CuInS_2$ (112), it was found evidence for an intrinsically formed ZnS layer at the interface of both materials [21]. This layer might improve the alignment of the electronic bands at the interface. Similar experiments are part of the thesis of Hofmann, where the interface of MOMBE-ZnO and $CuInSe_2$ (112) is investigated [9]. As observed in the case of $CuInS_2$, the chalcopyrite anion forms an intrinsic buffer layer with the zinc atoms, forming an intrinsic ZnSe layer at the interface of the $CuInSe_2$ and the ZnO [22].
In this section, the interface formation of $CuInSe_2$ (112) and ZnO deposited by atomic layer deposition is investigated. This is motivated mainly by two reasons: first, the self-limited ALD growth mode allows controlled deposition of the ZnO in monolayer steps. In combination with in situ photoelectron spectroscopy analysis, it is the best method to determine the band alignment and to investigate the formation of intrinsic interface layers. Secondly, the significantly lower substrate temperature of the atomic layer deposition process allows to investigate the influence of the substrate temperature on the interface layer formation. While during MOMBE ZnO deposition the sample's temperature usually is 400 °C, the ideal substrate temperature during ZnO-ALD was determined being 210 °C, as shown in the previous chapter. The influence of this strongly decreased substrate temperature on the initial growth of the ZnO on $CuInSe_2$ (112) is one of the key questions of this chapter.

5.1 Epitaxial $CuInSe_2$ (112) Absorber Substrates

As mentioned above, highly-ordered epitaxial $CuInSe_2$ absorber films are used to investigate the fundamental properties of the $CuInSe_2$ | ZnO interface. All films are prepared by molecular beam epitaxy (see Sec. 3.2.2) in a deposition chamber attached to the Integrated System. This allows real in situ deposition and analysis, i.e. all experiments are carried out under ultra-high vacuum conditions without any environmental influences on the samples.
To grow epitaxial films, proper substrates with similar lattice constants are required. In case of $CuInSe_2$ in (112) orientation, GaAs (111)A (i.e. Ga-terminated) substrates are used. Before they are introduced into the Integrated System, the natural oxide is removed and the surface sulfur-terminated to prevent any contamination during transfer into the vacuum system. The procedure of GaAs preparation is described in detail elsewhere [80].
The temperature of the evaporation sources is controlled by PID controllers and set to

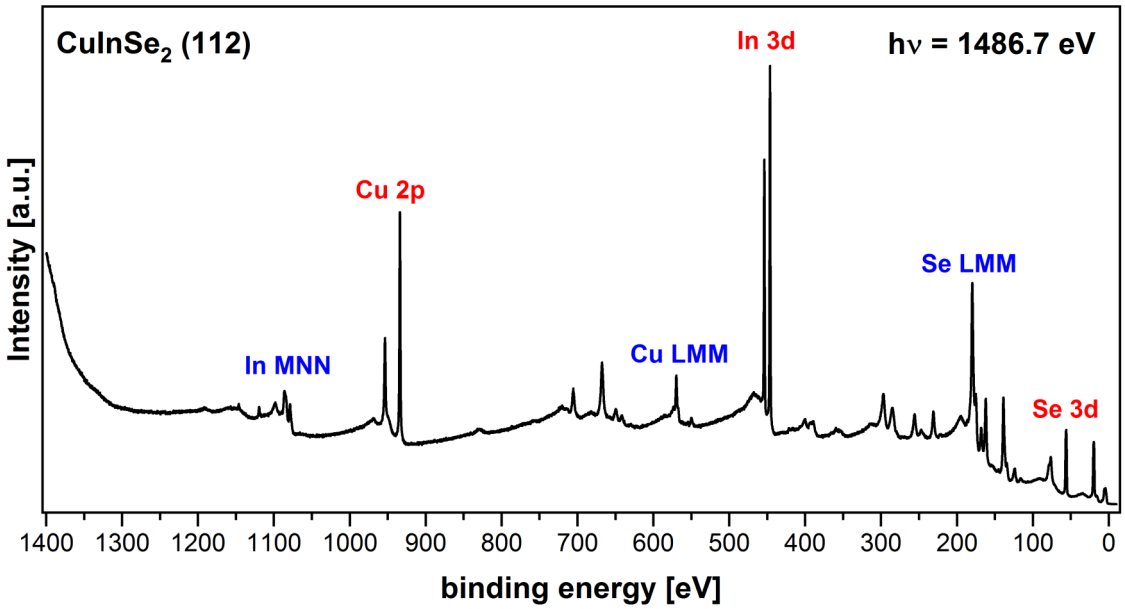

Figure 5.1: Photoemission survey spectrum of an $CuInSe_2$ (112) absorber layer epitaxially grown on GaAs (111)A. Some of the important photoemission lines of this work are labeled in red (photoelectrons) or blue (Auger electrons), respectively.

T_{Cu} = 1040 °C, T_{In} = 900 °C and T_{Se} = 210 °C, respectively. For $CuInSe_2$ deposition, the substrate temperature is raised to 525 °C under selenium atmosphere. This leads to a replacement of the sulfur surface-termination by a selenium-termination. At such high temperatures, excess Se does not stick to the surface and reevaporates immediately. After the deposition temperature is reached, the shutters of the Cu and In sources are opened simultaneously and the $CuInSe_2$ starts to grow with a rate of approx. 5 nm/min[9]. Typical absorber layer thicknesses are in the range of 100 nm to achieve relaxed layers by preventing internal stresses due to interface effects. More details, not only about the growth of the absorber films, but also their electronic structure and the formation of the Cu-poor defect compound $CuIn_3Se_5$, are investigated in detail in the thesis of Hofmann[9].

After successful deposition of the $CuInSe_2$ absorber, the sample is transferred under UHV conditions to the analysis chamber where it is characterized using photoelectron spectroscopy. A survey spectrum of one of those absorber layers is presented in Fig. 5.1 using Al Kα radiation. In comparison to Si or ZnO spectra shown in previous chapters of this work, the ternary chalcopyrite produces a more complex survey spectrum with various different photoelectron and X-ray induced Auger electron emission peaks. Therefore, the most important photoelectron peaks of the contributing elements in Fig. 5.1 are labeled in red. In particular, these are Cu 2p electrons at binding energies around 933 eV,

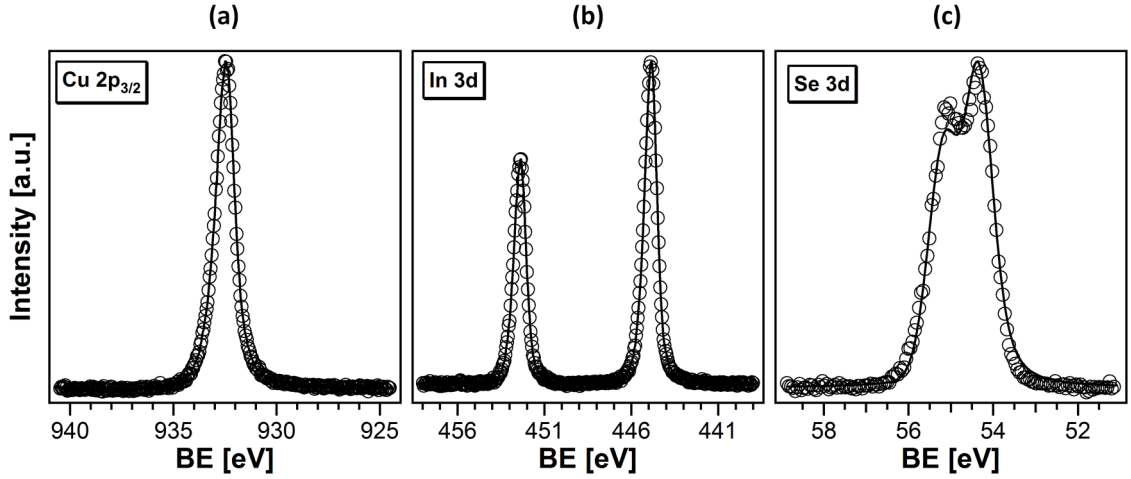

Figure 5.2: Regional XPS spectra of the most dominant photoelectron lines present in the ternary $CuInSe_2$ absorber layer. (a) Cu $2p_{3/2}$ around 933 eV; (b) In $3d_{1/2}$ at 452.5 eV and In $3d_{5/2}$ at 445 eV; (c) Se 3d. All spectra are recorded using monochromatic Al Kα radiation to excite the photoelectrons.

In 3d at 444 eV, and Se 3d having binding energies of approximately 54 eV. In addition to the photoelectron lines, there are corresponding Auger emission peaks present in the survey spectrum. In Fig. 5.1, those lines are indicated by blue labels. The regional photoelectron spectra are presented in Fig. 5.2 (a)-(c) after removal of the secondary electron background by a Shirley routine.
Analysis of the [Cu]:[In] peak intensities results in a near-stoichiometric $CuInSe_2$ surface composition of 0.98 and an anion to cation ratio of [Se]/[Cu] + [In] = 1.17. A binding energy of the Cu $2p_{3/2}$ photoelectrons of 932.78 eV has been determined. In combination with the kinetic energy of the Cu $L_3M_{45}M_{45}$ Auger electrons (916.65 eV), this results in a combined Auger parameter of α(Cu) = 1849.43 eV. According to reported literature and database values, this Auger parameter also indicates a near-stoichiometric composition of the $CuInSe_2$ absorption layer.

One further feature present in the survey spectrum should be discussed shortly. At binding energies of 1144 eV and 1117 eV there are two very small peaks observed. These can be identified as Ga $2p_{1/2}$ and Ga $2p_{3/2}$ photoelectrons, respectively[79]. If these peaks do, however, originate from the substrate, there should also be an arsenic signal contributing the spectrum in terms of two As 2p peaks being visible at 1324 eV and 1359 eV, respectively. Since this is not the case, it has to be assumed that small amounts of the gallium diffuses into the $CuInSe_2$ crystal during the deposition process.

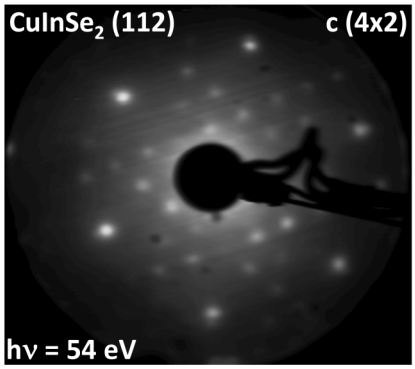

Figure 5.3: Low energy electron diffraction (LEED) pattern of one of the $CuInSe_2$ (112) absorber layers used as substrates for the CISe/ALD-ZnO interface investigation. The pattern indicates a c(4x2) surface reconstruction.

The low energy electron diffraction (LEED) pattern presented in Fig. 5.3 demonstrates the epitaxial growth of the $CuInSe_2$ on GaAs (111)A, resulting in a (112) oriented film. The dominant spots in the LEED pattern show a hexagonal zinc blende structure. Additional spots are introduced by the chalcopyrite order, in total resulting in a c(4x2) surface reconstruction LEED pattern. More on the surface structure of $CuInSe_2$ having different orientations and their dependency on the surface composition is found extensively in the work of Hofmann[9].

5.2 ALD-ZnO on $CuInSe_2$ (112) Absorber Films

After characterization of the $CuInSe_2$ absorber substrates, the investigation of the interface formation is carried out. Therefore, the ZnO is deposited in monolayer steps onto the chalcopyrite and after each deposition step its composition and electronic properties are analyzed. These experiments are primary performed in the laboratory using combined X-ray and ultraviolet photoelectron spectroscopy analysis in the Integrated System. In addition, the same growth experiments are also carried out at the BESSY synchrotron radiation facility to benefit from the increased surface sensitivity provided by the tunable excitation energy and its high energy resolution. The combination of all those experiments result in a detailed picture of the interface formation. Additionally, the combination of core level and valence band spectroscopy yields complete information about the band alignment of the two materials.

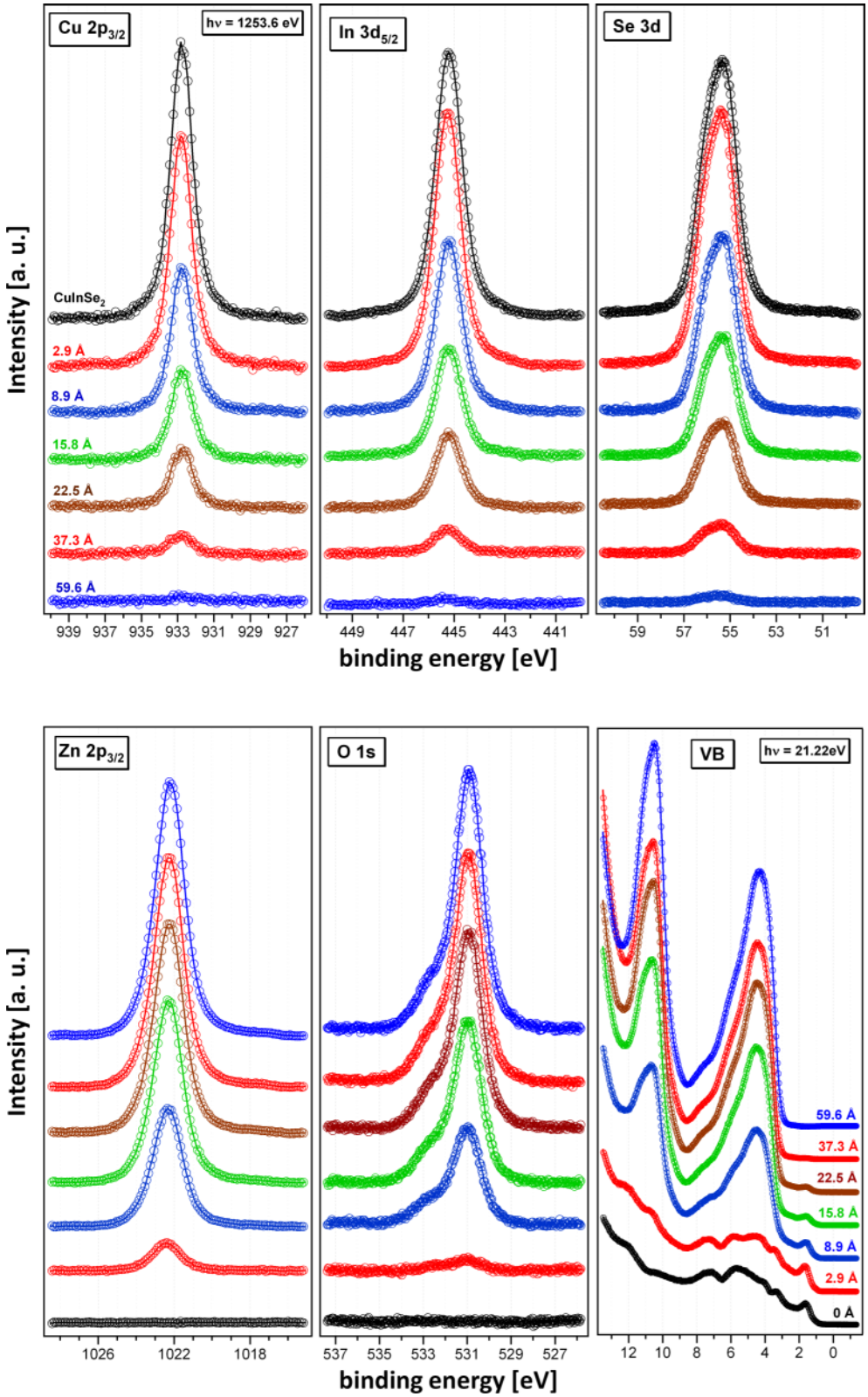

Figure 5.4: Thickness dependence of the photoemission spectra of the substrate (top), the overlayer elements, and the valence band spectra (bottom).

5.2.1 Initial Growth Characterization

The regional spectra evolution with increasing overlayer thickness is plotted in Fig. 5.4 for all contributing elements, i.e. Cu $2p_{3/2}$, In $3d_{5/2}$, Se 3d, Zn $2p_{3/2}$, and O 1s. All of those spectra were recorded using Mg Kα X-rays as excitation radiation in the laboratory. In addition to the core-level peaks of the contributing elements, the valence band spectra excited by He I radiation are also presented in Fig. 5.4.
First we will focus on the X-ray photoemission spectra. As expected, the elements of the substrate are attenuated with increasing film thickness, while the photoemission signals of the overlayer start increasing. The intensities of the photoemission lines of all five elements are plotted against the overlayer thickness in Fig. 5.5. Here, the attenuation of the Cu $2p_{3/2}$ substrate peak is used to calculate the overlayer film thickness.

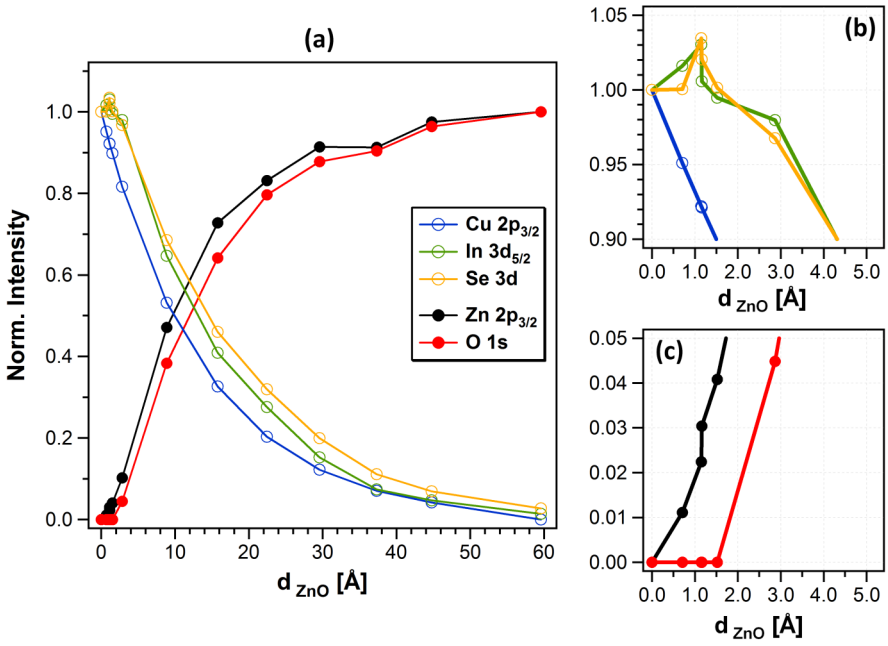

Figure 5.5: Normalized photoemission peak intensity of the contributing elements plotted against the calculated overlayer thickness, determined by the attenuation of the Cu $2p_{3/2}$ peak.

The normalized peak intensities show the characteristic behavior of ideal layer-by-layer growth, as described earlier in Sec. 3.1. Nevertheless, it is already visible in Fig. 5.5 (a) that the indium and selenium photoemission signals show a slight delay in their attenuation behavior with respect to the Cu $2p_{3/2}$. This is also illustrated by the image enlargement shown in Fig. 5.5 (b) for the initial deposition steps. While the Cu $2p_{3/2}$ is

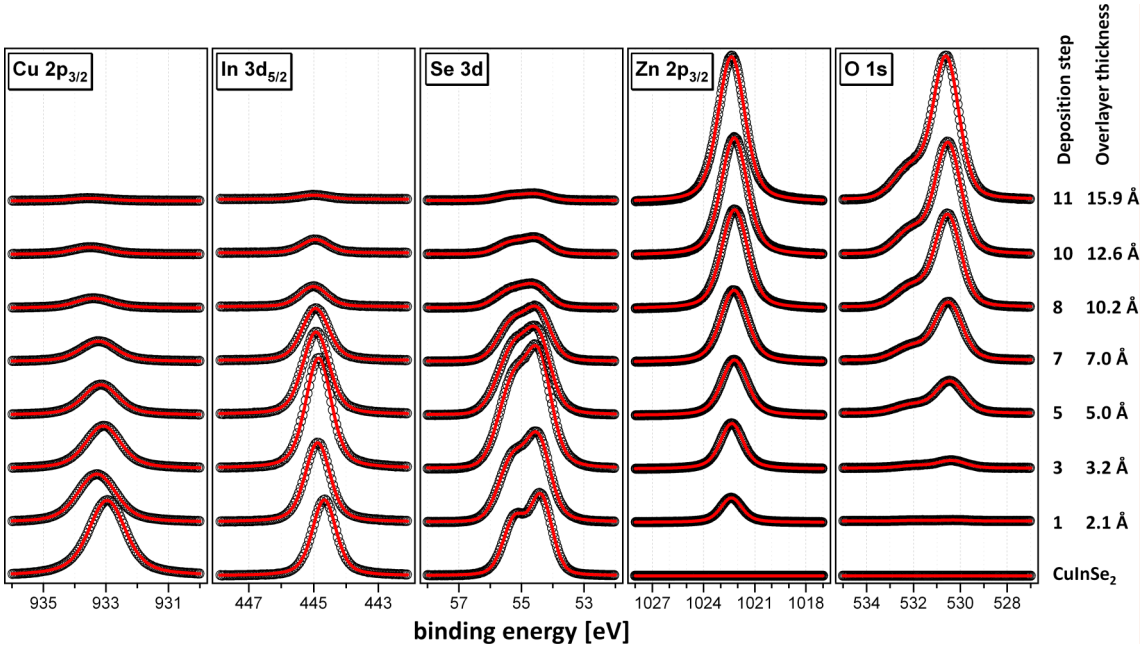

Figure 5.6: Photoemission spectra evolution with increasing overlayer thickness using synchrotron radiation to excite the photoelectrons with constant kinetic energy of KE = 130 eV to achieve higher surface sensitivity and energy resolution.

attenuated from the first deposition step on, the peak intensities of the In $3d_{5/2}$ and Se 3d even seem to increase rather than being attenuated.

A magnification of the normalized peak intensities of the ZnO overlayer during initial growth is plotted in Fig. 5.5 (b). While the zinc photoemission starts raising immediately, there is no oxygen observed at the first deposition steps. To gain deeper insight on the initial deposition behavior, same experiments were performed using synchrotron radiation at the BESSY II. There, the surface sensitivity was increased by tuning the excitation energy, that all emitted photoelectrons have the same kinetic energy of KE = 130 eV. This has basically the advantage of equal inelastic mean free paths (IMFP) for all elements, which is resulting in better comparability of the particular elements, since all photoelectrons are created within the same depth region of the material under investigation. To avoid the time consuming UHV transfer using the transfer box, the ALD reactor was directly attached to the SoLiAS analysis system. This allows much faster in situ analysis of the deposition experiments. In analogy to the experiments performed in the laboratory, the ZnO was deposited in monolayer steps onto the chalcopyrite absorber. Fig. 5.6 presents the regional spectra of the contributing elements after normalization (cf. Sec. 2.2.3) and removal of the secondary electron background.

Even though the experiments performed at the synchrotron radiation facility show comparable spectral characteristics, there are some differences discussed in detail in the following. First, the photoemission peaks of the substrate elements Cu, In and Se show an enhanced shift in their binding energies after deposition of the first monolayer with respect to the experiments in the laboratory. Since the magnitude of the shift is similar for all three elements, we can assign this shift to a band bending at the interface, rather than a chemical shift in the substrate.
As already indicated by the laboratory experiments, the attenuation of the indium and selenium show a different attenuation characteristics than the copper signal. This behavior has already been observed in experiments performed by Andres et al. for the MOMBE ZnO deposition on $CuInS_2$ (112). A delay in the initial deposition of oxygen was observed, while at the same time the sulfur photoemission intensity did not decrease immediately. This led to the conclusion of the formation of a ZnS interfacial layer between the $CuInS_2$ absorber and the zinc oxide[21]. A similar behavior was observed just recently for MOMBE ZnO deposition on $CuInSe_2$ (112) by Hofmann[9;22], where a ZnSe interfacial layer was identified, having a thickness of about 2 nm.

Initial Growth - Influence on Substrate's Elements

In contrast to MOMBE deposition, where the Cu and In signals were both attenuated during the formation of the ZnSe layer, this is not observed in case of atomic layer deposition. In fact, only the Cu $2p_{3/2}$ is attenuated, while the indium even appears to increase during initial growth. The enhanced surface sensitivity of the SR-PES experiments can help identifying the interface formation in more detail. Therefore, the photoemission peak intensities are normalized to 1 and plotted over the calculated overlayer thickness. The resulting graph is shown in Fig. 5.7. The most obvious feature is the strong increase in peak intensity for the In $3d_{3/2}$ and the Se 3d photoelectrons during the initial deposition steps. They both reach a maximum in intensity after about 0.4 nm of roughly 150 % (In) and 170 % (Se), respectively. Even though the inaccuracies in data quantification using synchrotron radiation is increased (see Sec. 2.2.3), an error of such high magnitude can be excluded, particularly since the Cu 2p photoelectron line shows ideal attenuation behavior (blue line).

Further analysis of the substrate's photo emission during initial ZnO deposition does not show a significant chemical shift or change in Auger parameter. Hence, it is difficult to

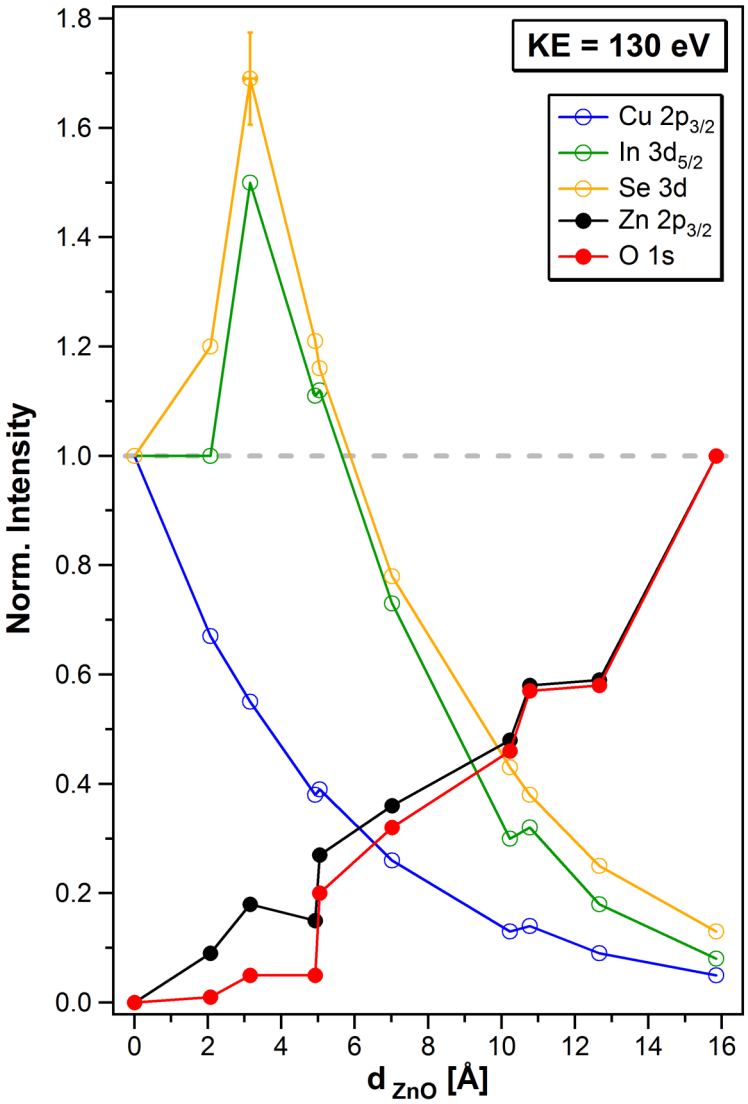

Figure 5.7: Normalized photoemission intensities during ALD-ZnO deposition investigated with synchrotron radiation at constant kinetic energies of KE = 130 eV. Due to the increased surface sensitivity, effects at the surface are pronounces with respect to the XPS investigation in the laboratory. It is observed, that the intensities of both, the selenium and the indium increase during initial growth. This is in contrast to the MOMBE deposited ZnO of earlier studies, where only the Se signal was influenced by the ZnSe formation.

draw conclusions about the local chemical environment of the elements directly from the photoemission peaks. Annealing experiments of the ZnO layer after finishing the initial growth experiments can give some indication of the mobility of the particular elements. The corresponding photoemission spectra before and after annealing the sample at 400 °C for 30 min are presented in Fig. 5.8.

While there is no indication for an intensity change of the Cu $2p_{3/2}$ or Se 3d photoelectrons, the indium signal shows a significant increase in intensity. This suggests that the indium atoms are mobile and diffuse into the ZnO film. A decrease in ZnO overlayer thickness by the annealing process can be ruled out, since this would result in a simultaneous increase of the copper and selenium photoemission peaks as well.

Compared to the XPS results shown in Fig. 5.5, the zinc and oxygen peak development shows a more linear behavior. It is also observed that the oxygen peak is significantly reduced with respect to the Zn 2p photoelectrons. But in contrast to the experiments performed by Andres and Hofmann, an oxygen photoemission peak is arising already in the early deposition stages. As usual, the O 1s peak shows two components: one at lower binding energies assigned to $[O^{2-}]$ lattice oxygen and the characteristic surface hydroxide oxygen peak at the high binding energy side. A selection of the corresponding O 1s photoemission spectra are presented in Fig. 5.9.

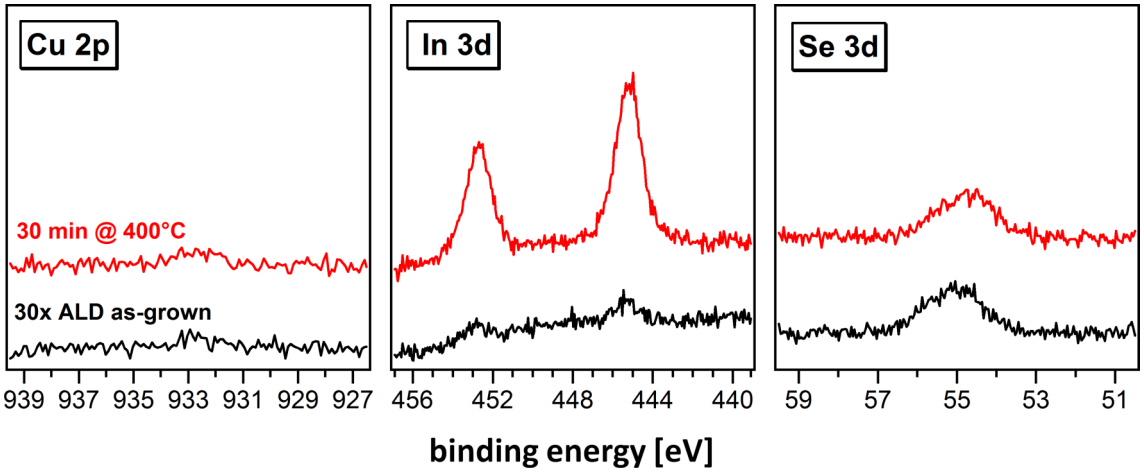

Figure 5.8: Photoemission spectra before (black) and after annealing (red) of a ALD-ZnO film on $CuInSe_2$ in the thickness range of the photoelectron information depth of the substrate. Annealing for one hour at 400 °C shows an increase in photoemission intensity of the indium signal, indicating an indium diffusion into the ZnO overlayer.

Overlayer Growth - Oxygen Component

Compositional analysis of the overlayer in terms of the [Zn]:[O] ratio is presented in Fig. 5.10 (a). Even though an oxygen peak arises from the very beginning on, the initial overlayer is extremely zinc-rich with a [Zn]:[O] ratio exceeding 7.6. With increasing film thickness, the ratio drops rapidly, resulting in stoichiometric zinc oxide after about 5 Å corresponding to one ZnO monolayer.

Comparing the two oxygen components presented in Fig. 5.9 show an increased amount of hydroxides at the surface during initial ZnO-ALD. The ratios of the two particular oxygen components over the film thickness are plotted in Fig. 5.10 (b). The increased amount of hydroxides during initial atomic layer deposition has already been observed earlier in Chp. 4 for the ZnO deposition on Si(111)-H. In contrast, the amount of hydroxides strongly exceed the amount of lattice oxygen, resulting in a $[O_{-OH}]$:$[O^{2-}]$ ratio of 1.8, while for ZnO-ALD on Si(111)-H the $[O_{-OH}]$:$[O^{2-}]$ ratio for initial growth was almost 1:1. Hence, in combination with the results of the composition analysis, there is no indication of ZnO formation from the very first deposition step on. The present oxygen is most likely

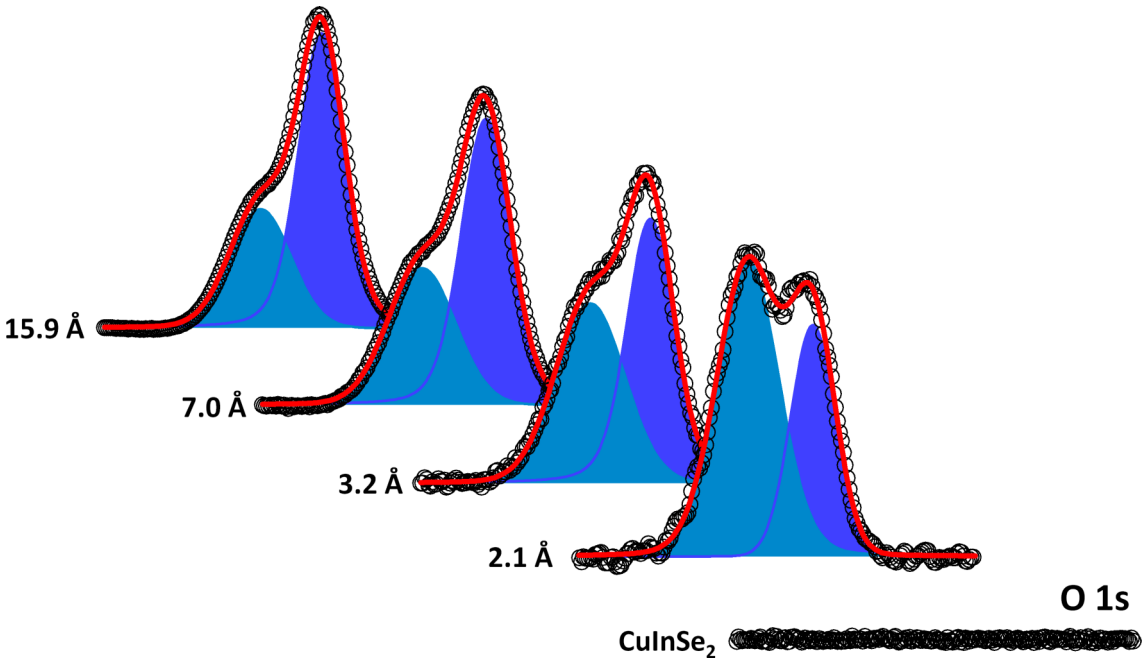

Figure 5.9: O 1s spectra evolution during initial ZnO atomic layer deposition on $CuInSe_2$. While for ZnO MOMBE on $CuInSe_2$ there was no oxygen visible during initial growth, this is not the case for the ALD process.

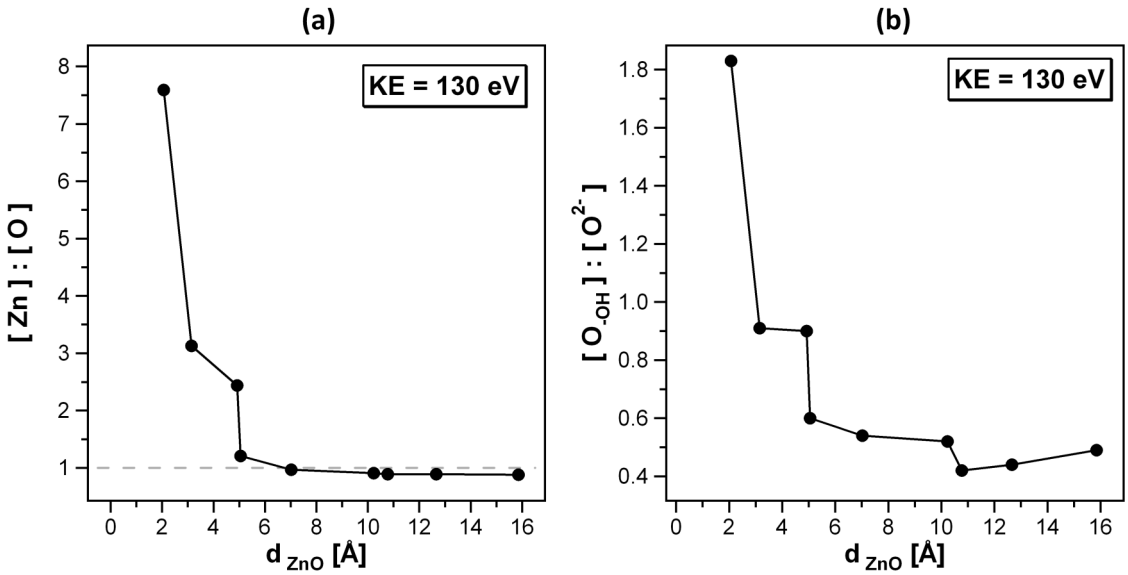

Figure 5.10: (a) Composition analysis of the overlayer plotted against its thickness. Even though there is a weak oxygen signal, the film is strongly zinc-rich before it becomes stoichiometric for thicker layers. (b) Intensity ratio of the two oxygen components observed in the O 1s spectra. In contrast to the ZnO atomic layer deposition on silicon substrates, the amount of hydroxides during initial growth is increased with respect to the lattice oxygen.

originating from hydroxides attached to the surface after the water pulse of the second ALD half-reaction.

Overlayer Growth - Zinc Component

The major difference of the ZnO |$CuInSe_2$ interface achieved by ALD and MOMBE observed so far is found in the significantly decreased interface layer thickness to 5 Å and the presence of a considerable amount of indium (cf. Fig. 5.7) besides the zinc and selenium component in the initially formed monolayer.
A powerful tool to identify the local chemical environment of an element in the compound under investigation is the combined Auger parameter α. The inset in Fig. 5.11 (a) shows no observable change in the Auger parameter for Cu and In. For technical reasons, the experiments had to be performed using Mg Kα radiation and the Auger parameter could not be determined for selenium. Hence, the Auger parameter of the zinc component is used trying to identify the interfacial layer between absorber and ALD-ZnO. Its thickness

dependence is plotted in Fig. 5.11 (a) for the laboratory experiments, while Fig. 5.11 (b) represents the experiments with more surface sensitive synchrotron radiation. In both cases, an initial zinc Auger parameter of 2011.8 eV is determined. After 5 Å, a significant drop by about 1.8 eV is observed. At this film thickness, stoichiometric ZnO is observed in the compositional analysis and therefore supports the assumption of the formation of an interface layer having that particular thickness of 5 Å. At higher film thicknesses, the Auger parameter clearly reveals ZnO formation with an Auger parameter around 2010 eV.

The results so far do not indicate a ZnSe formation similar to the situation in the MOMBE process. The additional presence of indium during initial growth gives an indication for a different chemical situation at the interface of $CuInSe_2$ and ALD-ZnO. Trying to identify this boundary layer, possible reference materials were prepared and their Auger parameters were determined using the same analytic setup, respectively. First, a ZnSe film was deposited by thermal evaporation on $CuInSe_2$ in the Integrated System. Afterwards, its Auger parameter has been determined by XPS using Al Kα radiation. The corresponding photoemission spectra are shown in Fig. 5.12 (a) and (b). The binding energy of the

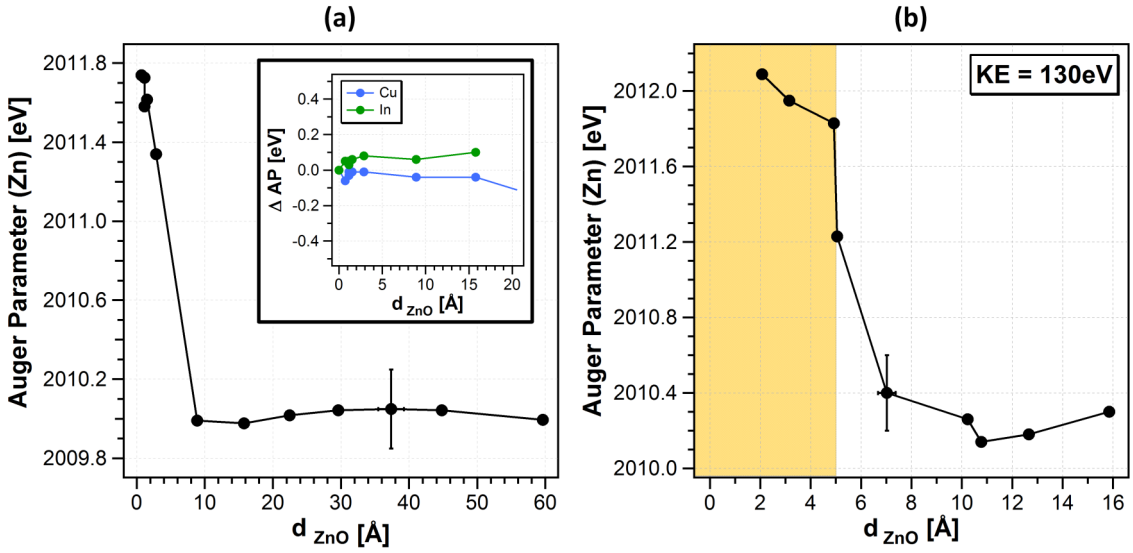

Figure 5.11: Auger parameter analysis of the zinc component with increasing film thickness. Part (a) on the left hand side shows the results of the experiments performed in the laboratory using Mg Kα radiation, while in (b) synchtrotron radiation was used for surface analysis. There is a significant drop in the Auger parameter observed, indicating the formation of an interface layer between $CuInSe_2$ and ZnO during initial ALD.

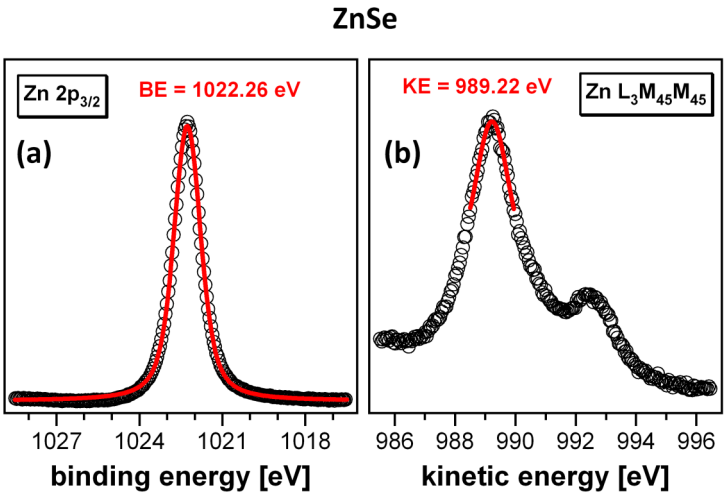

Figure 5.12: Regional photoemission spectra of the Zn $2p_{3/2}$ photoelectron and Zn LMM Auger electron lines for a ZnSe film deposited on $CuInSe_2$ to determine the combined Auger parameter as a reference to the one observed for initial ZnO-ALD on $CuInSe_2$.

Zn $2p_{3/2}$ photoelectrons amounts to 1022.26 eV, while the Auger electrons have a kinetic energy of 989.22 eV. This ends up in a combined Auger parameter of:

$$\begin{aligned} \text{AP (ZnSe)} &= \text{BE (Zn } 2p_{3/2}\text{)} + \text{KE (Zn } L_3M_{4,5}M_{4,5}\text{)} \\ &= 1022.26 \text{ eV} + 989.22 \text{ eV} \\ &= 2011.48 \text{ eV} \pm 0.2 \text{ eV} \end{aligned} \tag{5.1}$$

Considering the error of measurement of about 0.2 eV, the zinc Auger parameter determined for ZnSe is clearly below the one determined for initial ALD-ZnO deposition on $CuInSe_2$. A ZnSe boundary layer would also not explain the significant indium signal observed at the interface. Hence, the formation of an intrinsic ZnSe buffer layer can be ruled out for ALD-ZnO deposition on chalcopyrite absorber materials.

5.2.2 Interface Formation: Intrinsic Buffer Layer

This results in an alternative interpretation of the experimental data, assuming that all elements identified at the boundary layer, i.e. zinc, indium and selenium, form the interface layer. Combining those materials, the formation of a $ZnIn_2Se_4$ (ZISe) phase seems to be

most likely. Interestingly, this material is investigated by some few groups as alternative to the CdS buffer layer in chalcopyrite solar cells[81–83]. Reports on the crystal structure of $ZnIn_2Se_4$ reveal, that it belongs to the defect chalcopyrite family, crystallizing in a tetragonal structure with the space group S_4^2. Their lattice parameters were determined being $a = 5.69$ Å and $c = 11.49$ Å[81]. Fig. 5.13 illustrates the crystal structure of $ZnIn_2Se_4$ and shows the differences to the $CuInSe_2$ chalcopyrite and its crystal structure. There are only few studies about ZISe and their physical, chemical and electronic properties. While Babu et al. demonstrated ZISe thin film growth by chemical bath deposition[81] just recently, Ohtake et al. investigated the performance of $Cu(In,Ga)Se_2$ devices with coevaporated ZISe buffer layers[82]. Their measurements showed very promising results. While the reference cells using CdS buffer layers showed efficiencies of 15.9 % (1997), the alternative ZISe buffers reached efficiencies of already 15.1 %. There are only few reported values of the band gap energy of $ZnIn_2Se_4$. Babu et al. reported values between $2.15 - 2.64$ eV, depending on the pH-value of the chemical bath. A similar value of 2.22 eV has been determined by Hendia et al.[84] for evaporated thin-films. Choe reports a considerable lower value of 1.82 eV[85]. Compared to the band gap energies of CdS (2.42 eV) or ZnO (3.37 eV), the reduced band gap is not very beneficial for high efficiency solar cells. Under these circumstances it is even more surprising that Ohtake et al. achieved such high efficiencies. One reason might be the good heterojunction formation, since the crystal structures of the ZISe defect chalcopyrite and the absorber material are very similar. In addition, the vacuum coevaporation process also might have advantages over the unfavorable chemical bath deposition process in terms of surface contamination.

To give further indications about the formation of $ZnIn_2Se_4$ at the interface of the $CuInSe_2$ absorber and the ZnO, comparison of the initial zinc Auger parameter shown in Fig. 5.11 with reported values for ZISe would be helpful. Unfortunately, there are no experimental Auger parameter data reported for $ZnIn_2Se_4$ in literature or the common databases. To have some comparable data, $ZnIn_2Se_4$ crystals were grown in cooperation with the group of Prof. Binnewies at the University of Hannover. They are able to grow ZISe bulk crystals by the *chemical vapor transport* (CVT) method using iodine as transport agent[87]. Before introducing those crystals into the vacuum system, they were glued on a sample holder. The thermal instability of the glue does not allow to heat the ZISe samples after introduction into the UHV system. To remove surface contaminants such as oxygen and carbons, the sample was sputter cleaned for 60 min using Ar^+ ions of 500 eV energy. Afterwards, the $ZnIn_2Se_4$ crystals were transfered under UHV conditions into the XPS system and analyzed. No remaining contaminations of oxygen or carbon were

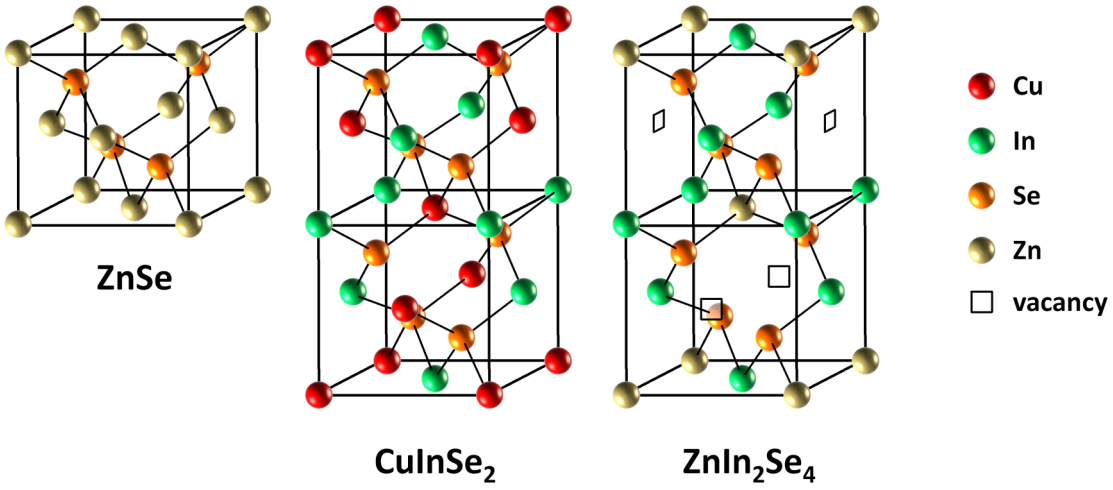

Figure 5.13: Chalcopyrite crystal structure of ZnSe, $CuInSe_2$ and the defect chalcopyrite structure of $ZnIn_2Se_4$ according to Margaritondo et al. [86]

observed. At binding energies of 630 eV a very weak additional peak was found, that can be attributed to iodine of the transport gas, implemented into the crystal during growth. For determination of the combined Auger parameter, the Zn $2p_{3/2}$ photoelectron peak and the corresponding Zn $L_3M_{45}M_{45}$ Auger electron spectrum are measured. The particular peak positions were determined after secondary electron removal by peak fitting routines described earlier in Sec. 2.2.1. The corresponding spectra are plotted in Fig. 5.14 (a) for Zn $2p_{3/2}$ and in (b) for Zn LMM, respectively.

A binding energy of BE = 1021.99 eV was determined for the Zn $2p_{3/2}$ photoelectrons. In combination with the Zn LMM Auger electrons' kinetic energy of KE = 989.73 eV, this results in a combined Auger parameter for $ZnIn_2Se_4$ of:

$$\begin{aligned} \text{AP (ZISe)} &= \text{BE (Zn } 2p_{3/2}\text{)} + \text{KE (Zn } L_3M_{4,5}M_{4,5}\text{)} \\ &= 1021.99 \text{ eV} + 989.73 \text{ eV} \\ &= 2011.72 \text{ eV} \pm 0.2 \text{ eV} \end{aligned} \tag{5.2}$$

Comparing this value with the one of the initially formed layer during ZnO-ALD deposition (2011.84 eV) can also indicate the formation of $ZnIn_2Se_4$ at the $CuInSe_2$/ZnO interface: while the zinc Auger parameter of ZnSe with a value of 2011.48 eV (cf. Eq. 5.2) is slightly lower than the one measured during initial ZnO deposition of approx. 2011.8 eV, the Auger parameter of the $ZnIn_2Se_4$ crystal fits the one determined for ZISe within the range of the measurement tolerances (±0.2 eV) of the XPS measurements.

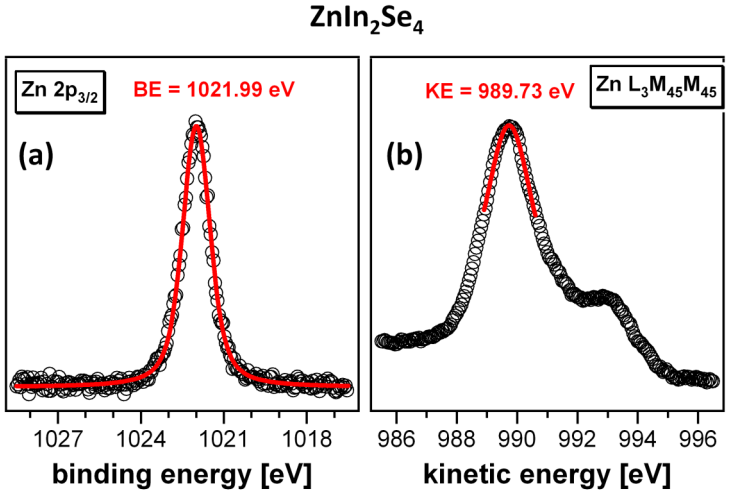

Figure 5.14: Regional photoemission spectra of the Zn $2p_{3/2}$ photoelectron and Zn LMM Auger electron lines for a $ZnIn_2Se_4$ crystal to determine their combined Auger parameters. This reference helps identifying the intrinsically formed buffer layer at the interface of $CuInSe_2$ and ZnO.

Furthermore, the Auger parameters of the indium and selenium are determined for the $CuInSe_2$ substrate, the ZnSe and $ZnIn_2Se_4$ references and for $CuInSe_2$ after the first ZnO deposition step, respectively. The resulting combined Auger parameters are summarized in Tab. 5.1. Especially the selenium Auger parameter of the ZnSe reference differs strongly from the value determined after initial ZnO deposition. Since the other values show no significant changes, this might be another indication for the presence of ZISe rather than ZnSe formed at the $CuInSe_2$|ZnO interface.

In the following, an attempt to explain the boundary layer creation is given. The main effect being responsible for the interface formation observed during ZnO-ALD is assumed to be the so-called effect of self-compensation in the chalcopyrite material. This self-compensation occurs as a reaction of doping the material and zinc is one of the typical materials known for being an n-type dopant in $CuInSe_2$ chalcopyrites by substituting the Cu sites[88]. Once zinc is deposited onto the $CuInSe_2$ surface, for instance in the form of diethylzinc, the donor atoms create electronic states in the forbidden band gap near the conduction band minimum (CBM). This results in a shift of the Fermi energy E_F towards the CBM in the uncompensated chalcopyrite[89]. In $CuInSe_2$, this shift towards the conduction band affects the defect formation energies significantly[9;90]. The chalcopyrite will form copper vacancies [V_{Cu}] as a reaction on the Fermi energy shift. The free copper [Cu^-] atoms react with the excess electrons introduced into the material by the zinc dopants and form neutral [Cu^0]. Since there is a gradient in [Cu^0] concentration, the atoms will

Compound	AP (Zn)	AP (In)	AP (Se)
$CuInSe_2$	-	852.5 eV	1360.84 eV
ZnSe	2011.48 eV	-	1360.45 eV
$ZnIn_2Se_4$	2011.72 eV	852.5 eV	1361.0 eV
$CuInSe_2$ + ZnO	**2011.8 eV**	**852.7 eV**	**1361.16 eV**

Table 5.1: Summary of all Auger parameters determined in this work. $CuInSe_2$, ZnSe and $ZnIn_2Se_4$ have been measured as references for the Auger parameter values determined for the interface layer between $CuInSe_2$ and ZnO shown in the last row.

diffuse deeper into the material, leaving behind [V_{Cu}] sites. It is not unlikely, that those vacancies are (partially) filled by the zinc atoms, resulting in a $ZnIn_2Se_4$ crystal configuration as illustrated in Fig. 5.13, as also indicated by the Auger parameter analysis. This effect would be limited to the outermost atomic layers, since further deposition of zinc on the ZISe buffer layer would not affect the chalcopyrite material underneath as intense as in case of direct deposition on the $CuInSe_2$. This, in addition with the decreased substrate temperature in the ALD process, would explain the reduced buffer layer thickness of about 5 Å compared to 20 Å in case of MOMBE ZnO deposition[9].

The reason for the different interface boundary layers achieved by the two different deposition processes, MOMBE and ALD, respectively, has to be explained by the differences in their process characteristics. As mentioned earlier, one of the main differences is the lower substrate temperature in case of atomic layer deposition of 210 °C with respect to 400 °C for MOMBE ZnO growth. In general, the higher temperature of the MOMBE process is expected have some kind of influence on the diffusion behavior of the contributing atoms. This can explain the increased buffer layer thickness of about 2 nm for MOMBE deposited ZnO with respect to 5 Å for ALD-ZnO.
The second main difference is the sequential deposition mechanism of the ALD process. This results in significantly changed growth kinetics during initial growth of the ZnO on the chalcopyrite and is most likely the reason for the $ZnIn_2Se_4$ formation instead of ZnSe as in case of MOMBE ZnO deposition.

5.3 Band Alignment of $CuInSe_2$ (112) and ALD-ZnO

The interface between the light absorbing material and the buffer layer forming the p-n junction has a crucial influence on the overall efficiency of the solar cell device. The investigation of the electronic band alignment at the junction is therefore of great interest to decide, whether a buffer layer material is applicable or not. In situ X-ray and ultraviolet photoelectron spectroscopies in combination with stepwise deposition of the junction forming material is able to determine the electronic band alignment of the two materials in contact. As shown in the previous section, a $ZnIn_2Se_4$ interface layer is formed and therefore, one has to consider two interfaces for the experimental band alignment determination: on the one hand the $CuInSe_2$ | $ZnIn_2Se_4$ interface and on the other hand the $ZnIn_2Se_4$ | ZnO interface.

Prior to the deposition of ZnO, the substrate is characterized in detail. As already introduced in Sec. 2.2.2, basic material parameters can be determined by ultraviolet photoelectron spectroscopy. According to Eq. 2.13, the work function is calculated by the position of the secondary electron cutoff energy E_{sec} and knowledge of the excitation energy, i.e. $h\nu = 21.22$ eV in case of He I excitation. For $CuInSe_2$, this results in a work function φ

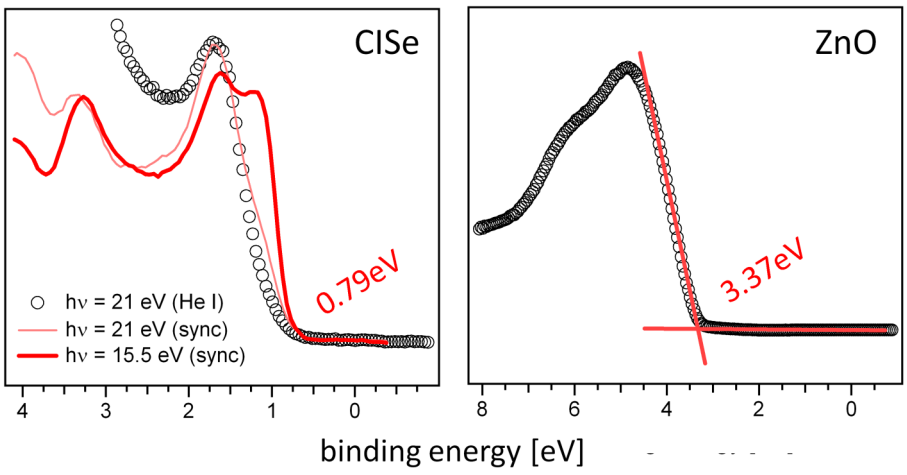

Figure 5.15: (left) determination of the true valence band maxima of the chalcopyrite by superposition of a reference spectrum recorded with synchrotron radiation of $h\nu = 15.5$ eV; (right) valence band maximum of ZnO determined by linear extrapolation.

and an ionization energy according to Eq. 2.14 of:

$$\begin{aligned}\varphi &= h\nu - E_{\text{sec}} \\ &= 21.22\ \text{eV} - 16.57\ \text{eV} \\ &= 4.65\ \text{eV}\end{aligned} \tag{5.3}$$

$$\begin{aligned}E_{\text{ion}} &= h\nu - E_{\text{sec}} + E_{\text{VBM}} \\ &= 21.22\ \text{eV} - 16.57\ \text{eV} + 0.79\ \text{eV} \\ &= 5.44\ \text{eV}\end{aligned} \tag{5.4}$$

Since the real position of the valence band maximum of $CuInSe_2$ cannot be determined directly by He I radiation (cf. thesis of Hofmann[9]) due to the overlap of different valence band states, an indirect method is applied as shown in Fig. 5.15 (a). Here, superposition of a reference spectrum recorded at the BESSY II synchtrotron facility with an excitation energy of 15 eV is used to determine the correct VBM of the chalcopyrite.
After each atomic layer deposition step, the sample is characterized by means of XPS and UPS, respectively. To determine possible band bending in the substrate or the overlayer, the binding energy changes for the contributing elements in the substrate and the overlayer are plotted against the calculated overlayer thickness in Fig. 5.16. For the substrate elements, the binding energy changes are calculated with respect to the clean substrate, while the overlayer element's energy change is given with respect to the binding energy of their first appearance in the spectra.

The band bending of the substrate is determined using only the copper and indium shifts in their particular binding energies, since their Auger parameters did not show any change of their chemical environment (cf. Fig. 5.11). The significant change of the selenium binding energy can be caused by a superposition of a possible chemical shift due to the $ZnIn_2Se_4$ formation. The initial ZnO deposition results in a band bending of $eV_b^{\text{CISe}} = 0.2\,\text{eV}$. Since the $ZnIn_2Se_4$ thickness is in the range of one monolayer, a band bending in the $ZnIn_2Se_4$ overlayer is not expected. This results in a valence band discontinuity ΔE_{VB} of the $CuInSe_2$ | $ZnIn_2Se_4$ interface of:

$$\begin{aligned}\Delta E_{\text{VB}}^{\text{CISe/ZnIn}_2\text{Se}_4} &= E_{\text{VBM}}^{\text{ZnIn}_2\text{Se}_4} - E_{\text{VBM}}^{\text{CISe}} - eV_b^{\text{CISe}} - eV_b^{\text{ZnIn}_2\text{Se}_4} \\ &= 1.8\ \text{eV} - 0.79\ \text{eV} - 0.2\ \text{eV} - 0.0\ \text{eV} \\ &= 0.81\ \text{eV}\end{aligned} \tag{5.5}$$

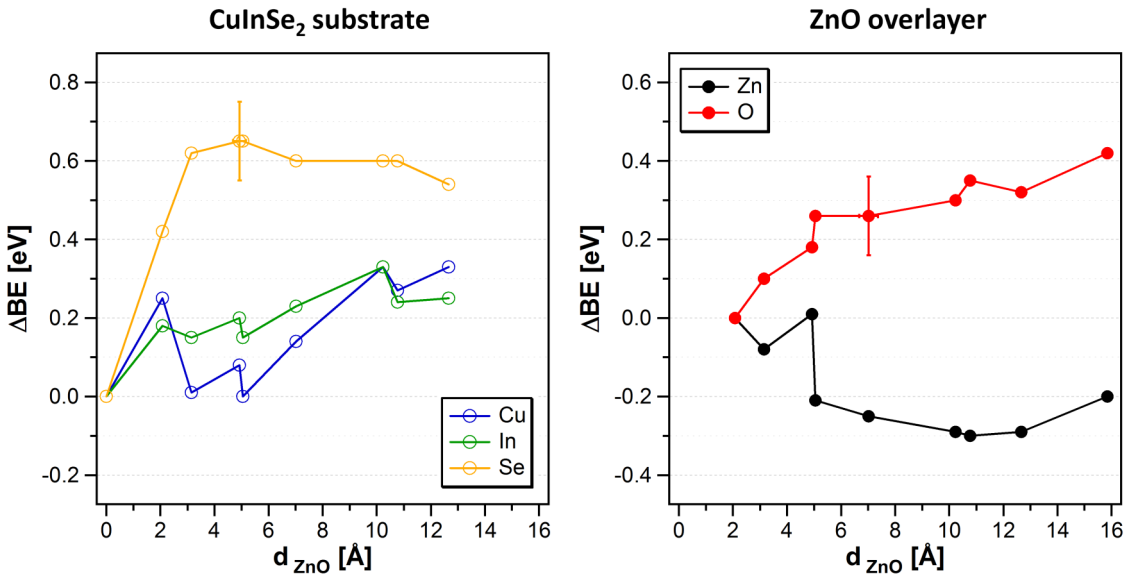

Figure 5.16: Evolution of the relative binding energies of the substrate (left) and the overlayer (right) with increasing overlayer thickness.

$E_{\mathrm{VBM}}^{\mathrm{ZnIn_2Se_4}}$ was not determined directly from the initial growth experiments, but indirectly using information gained by PES measurements of a $ZnIn_2Se_4$ bulk crystal. Since there is no abrupt interface between $CuInSe_2$ and $ZnIn_2Se_4$, the VBM is determined indirectly by the binding energy of the Zn 3d photoemission peak, which is located 9.5 eV below the valence band maximum of $ZnIn_2Se_4$. The determination of the conduction band discontinuity ΔE_{CB} is not possible for two reasons. On the one hand there is no reliable band gap energy reported for $ZnIn_2Se_4$. The few ones found in literature differ significantly among each other and are not reliable. On the other hand, even if the band gap energy is known, a film in the thickness regime of one monolayer might not match the reported band gap values of bulk $ZnIn_2Se_4$ crystals.
Instead, the surface dipole between the $CuInSe_2$ and the $ZnIn_2Se_4$ interface layer can be observed and calculated by the difference of the ionization energies of the two materials and the valence band offset:

$$\begin{aligned} eD^{\mathrm{CISe/ZISe}} &= E_{\mathrm{ion}}^{\mathrm{CISe}} - E_{\mathrm{ion}}^{\mathrm{ZISe}} + \Delta E_{\mathrm{VB}}^{\mathrm{CISe/ZISe}} \\ &= 5.44\ \mathrm{eV} - 6.48\ \mathrm{eV} + 0.81\ \mathrm{eV} \\ &= -0.23\ \mathrm{eV} \end{aligned} \tag{5.6}$$

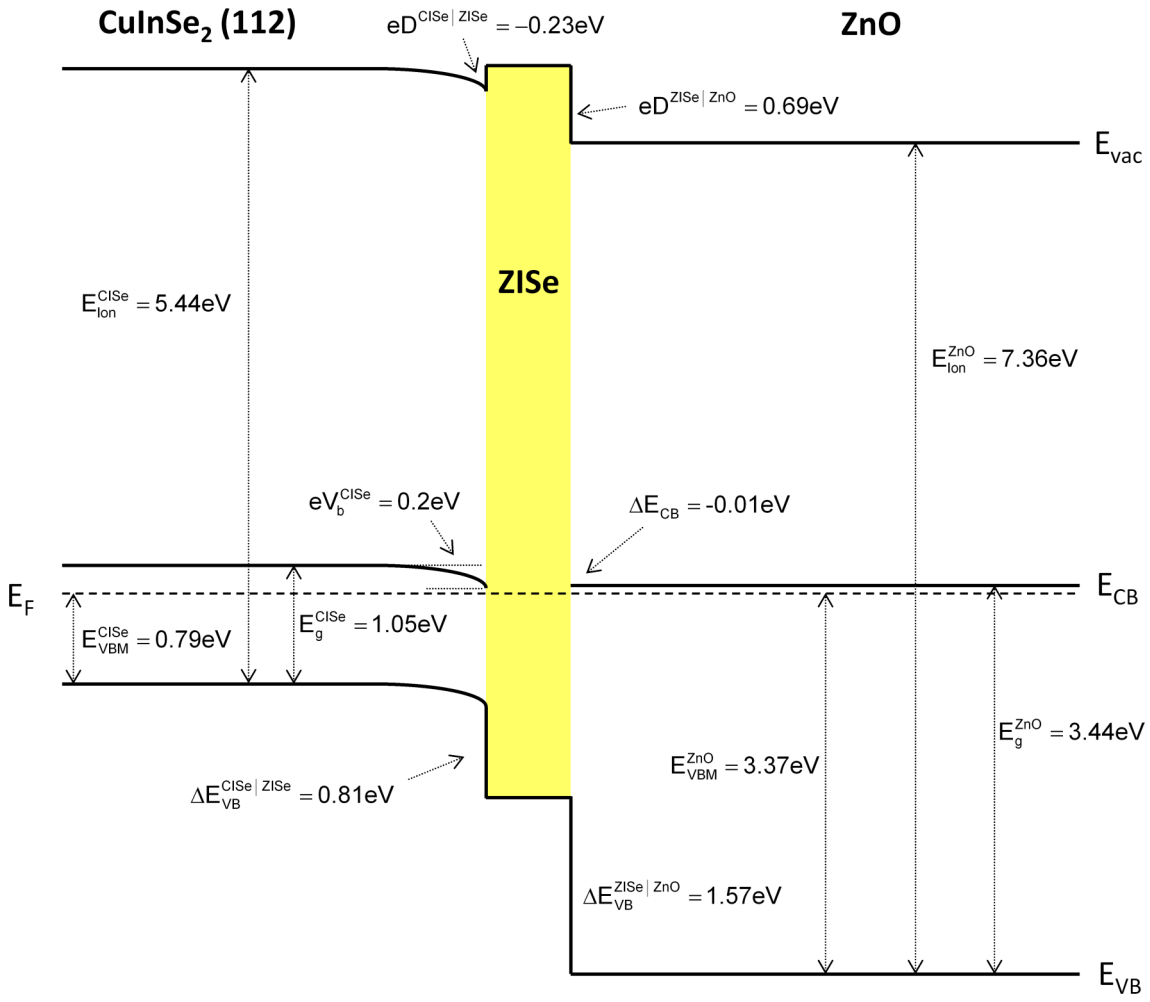

Figure 5.17: Band diagram of the $CuInSe_2$ - ALD-ZnO system with intrinsically formed $ZnIn_2Se_4$ of one monolayer in thickness.

As expected, the interface dipole is quite small, since both materials contain the same anions and have similar crystal structures.
To complete the band alignment, same anaylsis is performed for the $ZnIn_2Se_4$ | ZnO interface. The valence band maximum of ZnO was determined by linear extrapolation of the valence band edge, shown in Fig. 5.15 (b). This results in an ionization energy of the ZnO of:

$$\begin{aligned} E_{\text{ion}} &= h\nu - E_{\text{sec}} + E_{\text{VBM}} \\ &= 21.22\ \text{eV} - 17.23\ \text{eV} + 3.37\ \text{eV} \\ &= 7.36\ \text{eV} \end{aligned} \tag{5.7}$$

The binding energy change of the overlayer is plotted in Fig. 5.16. Determination of a band bending from the zinc photoelectrons is not very reliable, since they are expected to undergo a chemical shift due to the $ZnIn_2Se_4$ and ZnO formation. Hence, the O 1s photoemission peak was used to investigate a possible band bending. Indeed, there is a binding energy shift observed in Fig. 5.16, but its magnitude corresponds to the one observed in the substrate, resulting in no additional band bending in the ZnO film. Now, the valence band discontinuity of the $ZnIn_2Se_4$ | ZnO interface can be calculated:

$$\begin{aligned} \Delta E_{\text{VB}}^{\text{ZISe/ZnO}} &= E_{\text{VBM}}^{\text{ZnO}} - E_{\text{VBM}}^{\text{ZISe}} - eV_b^{\text{ZISe}} - eV_b^{\text{ZnO}} \\ &= 3.37\ \text{eV} - 1.8\ \text{eV} - 0.0\ \text{eV} - 0.0\ \text{eV} \\ &= 1.57\ \text{eV} \end{aligned} \tag{5.8}$$

The surface dipole at the $ZnIn_2Se_4$ | ZnO interface is expected to be significantly larger than at the $CuInSe_2$ | $ZnIn_2Se_4$ interface. One reason is the replacement of the selenium by more electronegative oxygen anions[9]. In addition, the interface of the chalcopyrite and the ZnSe is expected to have a high structural quality. The same is not necessarily true for the ZnO on ZnSe, since their crystal structures differ significantly. This results in a surface dipole between ZnSe and ZnO of:

$$\begin{aligned} eD^{\text{ZISe/ZnO}} &= E_{\text{ion}}^{\text{ZISe}} - E_{\text{ion}}^{\text{ZnO}} + \Delta E_{\text{VB}}^{\text{ZISe/ZnO}} \\ &= 6.48\ \text{eV} - 7.36\ \text{eV} + 1.57\ \text{eV} \\ &= 0.69\ \text{eV} \end{aligned} \tag{5.9}$$

Even though the determination of the conduction band position in the ZnSe interface layer is not possible, a comparison of the conduction band position of the ZnO with respect to the $CuInSe_2$ might give some information, if direct ALD-ZnO deposition on chalcopyrite absorbers can be beneficial for the solar cell performance, or not.
Combination of the valence band maxima of both materials and the observed band bending in the absorber gives a valence band offset of $\Delta E_{\mathrm{VB}}^{\mathrm{CISe/ZnO}} = 2.38$ eV. The conduction band offset can only be determined indirectly according to:

$$\begin{aligned} \Delta E_{\mathrm{CB}}^{\mathrm{CISe/ZnO}} &= E_g^{\mathrm{CISe}} - E_g^{\mathrm{ZnO}} + \Delta E_{\mathrm{VB}}^{\mathrm{CISe/ZnO}} \\ &= 1.05\ \mathrm{eV} - 3.44\ \mathrm{eV} + 2.38\ \mathrm{eV} \\ &= -0.01\ \mathrm{eV} \end{aligned} \tag{5.10}$$

Finally, this ends up in a complete band alignment of the $CuInSe_2/ZnIn_2Se_4/ZnO$ system as illustrated in Fig. 5.17. A negative spike in the conduction band is believed not to have very beneficial effects on the solar cell efficiency. A negative conduction band offset can lead to enhanced recombination of the electrons in the conduction band, which in turn reduces the open circuit voltage of the device. Hence, a small positive spike in the conduction band up to 0.4 eV is believed to be beneficial for the solar cell performance[15;17]. Nevertheless, the calculation of the conduction band offset of $\Delta E_{\mathrm{CB}}^{\mathrm{CISe/ZnO}} = -0.01$ eV can be subject to significant errors and is not necessarily true. On the one hand, we assume the band gap of the films in contact being equal to their bulk values. This is not necessarily true, since the band gap can vary at the surface of the material[6].
On the other hand, the interfacial $ZnIn_2Se_4$ layer will cause additional conduction band offsets at the CISe/ZISe and the ZISe/ZnO interfaces. Due to the wide scattering of reported band gap values for $ZnIn_2Se_4$ and its thickness in the monolayer range, a prediction of the band gap at such small layer thicknesses would be merely speculative.
It should be mentioned that the presence of hydroxides in the $ZnIn_2Se_4$ buffer layer was not considered in the band alignment. There might be a significant influence of the hydroxide oxygen on the band offsets at the $CuInSe_2$|ZISe interface. There are basically two issues that complicate the band alignment determination considering hydroxides in the interface layer: on the one hand it is not totally clear whether the hydroxide is incorporated in a $ZnIn_2Se_4$ matrix or just located at the ZISe surface. On the other hand, a closer investigation would require the deposition of a reference film having the same composition as the intrinsically formed interface layer. Hence, the presence of the oxygen in the ZISe buffer was neglected in this study.

5.4 Summary

In this chapter, a detailed investigation of direct ZnO atomic layer deposition on epitaxial $CuInSe_2$ (112) chalcopyrite absorber materials was presented. In contrast to ZnO deposited on epitaxial $CuInSe_2$ by a MOMBE process, where an intrinsic ZnSe layer formed, this is not observed for the ALD process. In the following, the results of this chapter are summarized shortly:

interface formation: While previous photoemission studies of MOMBE ZnO on epitaxial chalcopyrite layers revealed a ZnSe phase formed at the interface, using the ALD process a very thin $ZnIn_2Se_4$ intrinsic buffer layer was observed. The formation mechanism is believed to be induced by self-compensation effects on doping the chalcopyrite. Self-compensation results in the formation of copper vacancies and a copper diffusion away from the surface. X-ray and synchtrotron-radiation photoelectron spectroscopy indicate the formation of $ZnIn_2Se_4$, while the copper photoemission rapidly decreases. Besides the significantly reduced deposition temperature of the ALD process, the formation of $ZnIn_2Se_4$ can result from the different growth kinetics of the sequential growth mode in ALD.

boundary layer thickness: While the MOMBE deposition of ZnO on $CuInSe_2$ resulted in a buffer layer thickness around 2 nm, the $ZnIn_2Se_4$ film formed during ALD-ZnO deposition is at maximum one monolayer (0.5 nm) thick. This reduced thickness can be explained by the significantly lower deposition temperature of the substrate during atomic layer deposition, resulting in lower diffusivity of the atoms during interface formation.

oxygen-contribution: Another difference observed in the interface formation is the presence of oxygen from the initial atomic layer deposition step on. In contrast, MOMBE results showed a completely oxygen-free ZnSe boundary layer. The additional oxygen content in the buffer layer might be explained by the different growth kinetics of the ALD process. While in MOMBE both precursor materials, diethylzinc and water, are introduced simultaneously into the growth chamber, only one precursor is provided by the sequential deposition mode of ALD. This leads to incorporation of small amounts of oxygen into the buffer layer. Photoemission studies identified the oxygen component originating mainly from hydroxide oxygen. This is a quite interesting result, since several studies indicated, that buffer layers containing hydroxide components reach promising efficiencies of the solar cell devices, such as Zn(OH,Se), Zn(OH,S) or In(OH,S) [5;10;11;16;91].

electronic band line-up: Furthermore, we have shown that the ability of stepwise deposition and in situ analysis is not only a very powerful method to investigate the boundary layer formation of the $CuInSe_2$/ZnO system, but can also give a detailed picture of the electronic band line-up at the interface. The intrinsic formation of a $ZnIn_2Se_4$ (ZISe) buffer layer results in a more complex band alignment, since there is not only one $CuInSe_2$/ZnO interface, but two interfaces $CuInSe_2$/ZISe and ZISe/ZnO have to be taken into account. The experimentally determined band line-up at the CISe/ZISe interface shows a valence band offset of 0.8 eV and an induced band bending of about 0.2 eV. As expected from the similarity of the two materials, only a small surface dipole was observed. At the ZISe/ZnO interface, the dipole was significantly enhanced due to the more electronegative oxygen in the ZnO and the more imperfect interface quality. While a valence band offset of 1.57 eV was determined, the thickness of the ZISe buffer of only one monolayer does not allow to draw conclusions about the conduction band behavior of the $CuInSe_2$/$ZnIn_2Se_4$/ZnO system.

indium diffusion: annealing experiments indicate a significant diffusivity of the indium into the ZnO overlayer. The same behavior has already been observed in the MOMBE ZnO deposition experiments by Hofmann[9]. Reported experiments with different types of alternative buffer layers indicated, that indium-containing films often yield highest device efficiencies. According to Rockett, this can result from interdiffusion of the indium. This interdiffusion can reduce interfacial defects, which would lower interface recombination of the electrons and can also lead to a grading of the junction, reducing the effects of possible band offsets[5]. Hence, the presence of mobile indium found can have beneficial effects on the properties of the electronic junction.

6 Water-free ZnO ALD

Probably the most challenging task in the field of ZnO research is to achieve reproducible p-type doping. As already mentioned earlier, hydrogen impurities in the crystal play a crucial role since they are able to compensate the effects of the p-dopants (such as nitrogen) incorporated into the crystal at an oxygen site[92]. More on the role of hydrogen in ZnO is reported in detail in the work of van der Walle[93] or Nickel et al[94–97].
In conventional atomic layer deposition of ZnO, water is used as the oxygen precursor that can act as a possible hydrogen source, since during its reaction with diethylzinc, a hydroxide is formed in an intermediate reaction state. Hence, a new ALD process having an alternative oxygen precursor than water, producing films of same structural, chemical and electrical quality would be advantageous for ZnO ALD.
There are only few reports on alternative oxygen precursors used in ZnO atomic layer deposition. Most of those techniques use either an ozone (O_3)[68] or an O_2 plasma[69]. This might be advantageous in terms of lowering the substrate's temperature during deposition, but it usually results in lower quality ZnO compared to thermal-ALD. There are several reports about successful ZnO atomic layer deposition using $ZnCl_2$ as metal precursor[55;98]. These groups used molecular oxygen (O_2) as oxidizing agent. There is one only study on ZnO atomic layer deposition using organometallic diethylzinc and O_2 by Park et al[70]. They report a very low growth per cycle of 0.36 Å, not indicating real atomic layer deposition characteristics.
In the following chapter, the first successful study of a new water-free atomic layer deposition process will be presented. Zinc oxide films are deposited using a precursor combination of metal-organic diethylzinc and O_2 as the oxygen source. The initial growth on Si(111)-H substrates is investigated and compared to the standard ALD process using water as oxidizing agent. A comparison of the two different ZnO films will yield information about the reaction mechanism of the new water-free ALD process and the chemical and electronic properties of the ZnO films achieved.

6.1 Growth Parameters for ZnO-ALD using O_2 precursor

As previously mentioned in Sec. 4.2, molecular O_2 is provided by a 1 l lecture bottle having an initial pressure of 10 bar. It is connected to an additional ALD diaphragm valve by UHV-compatible tubing. Hence, the ALD reactor is capable to deposit ALD-ZnO by use of two different oxygen precursors: water and molecular oxygen, respectively. To differentiate between both precursors, the terms H_2O-ALD and O_2-ALD are used from now on, depending on what oxidizing agent has been used.
Compared to using water as oxygen precursor, the pressure in the deposition chamber during O_2 exposure is significantly higher. To prevent an automatic shut down or even damage of the turbo molecular pump, the shortest operable valve opening time is chosen for O_2 exposure. As already discussed in Sec. 4.2.3, the error in response time of the valve used for O_2 control is 12 ms. Hence, 13 ms is the shortest possible exposure time for this valve, resulting in a maximum pressure of 1 mbar in the deposition chamber during oxygen exposure. Because of those high pressures, a complete surface saturation is expected even after this short exposure times. Since no modifications are made with respect to the DEZn exposure, its saturation behavior as presented in Fig. 4.18 will remain the same.
To determine the ideal substrate temperature for O_2-ALD, the same procedure as in Sec. 4.3.2 for H_2O-ALD was carried out. Hydrogen-terminated Si(111) is selected as substrate material to achieve comparableness to H_2O-ALD. As described in Chp. 4, a thin ZnO film was deposited onto the Si(111)-H to rule out effects of initial monolayer formation on the growth-per-cycle. Afterwards, five ALD cycles were deposited and the growth rate was measured by X-ray photoelectron spectroscopy. The temperature range in which the growth-per-cycle has been determined started at 150 °C and was increased in steps of 20 °C. The resulting growth rates per ALD cycle are plotted as red triangles against the substrate's temperature in Fig. 6.1. For ease of comparison, the temperature dependence using water as oxygen precursor is also plotted.
First of all, the presence of a temperature region with the typical temperature-independent GPC in Fig. 6.1 between $185 - 210$ °C validates the existence of self-limiting atomic layer deposition. It is the first successful study of ZnO atomic layer deposition using the precursor combination diethylzinc and O_2. The O_2-ALD window is, compared to the one observed in H_2O-ALD, just slightly shifted by 15 °C towards lower substrate temperatures. Hence, a substrate temperature of 200 °C is ideal for successful O_2-ALD.
The most prominent difference between both precursor combinations is found in the deposition rate per ALD cycle. For H_2O-ALD the GPC is 3.0 Å corresponding to roughly

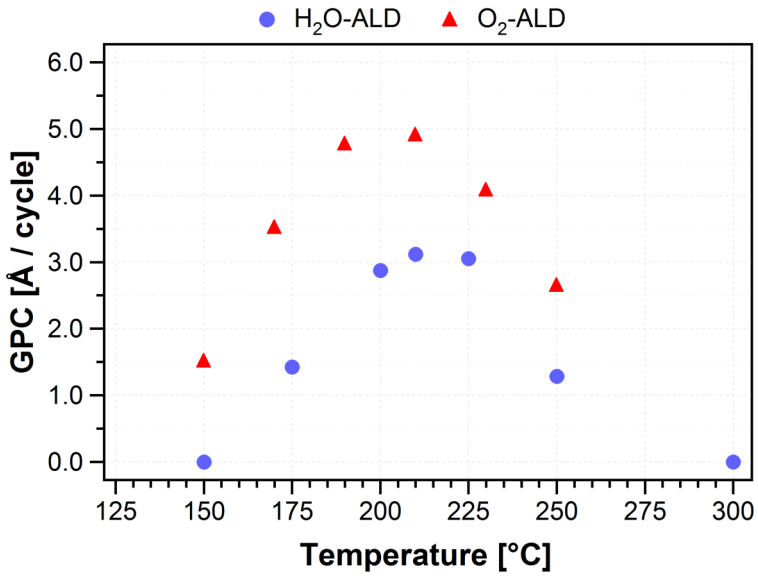

Figure 6.1: Growth-per-cycle (GPC) dependence on deposition temperature of the ZnO-ALD using DEZn and molecular oxygen (O_2). The characteristic ALD window indicates self-limited ideal growth behavior. The increase in deposition rate is the result of a different reaction mechanism, not limited by steric hindrance effects of the ethyl-ligands.

60 % of one complete ZnO monolayer in preferred (0001) orientation, whereas using O_2 as oxidizing agent the deposition rate per ALD cycle is increased significantly. In comparison to H_2O-ALD, the GPC in O_2-ALD increases by a factor of more than 1.5 reaching a value of 5.0 Å. Accordingly, each ALD cycle almost one entire ZnO monolayer is formed using O_2 as oxidizing agent.

While the GPC was limited due to steric hindrance effects of the ethyl ligands of the diethylzinc in case of H_2O-ALD, this effect is obviously not observed in O_2-ALD. It is rather a complete removal of both ethyl ligands during DEZn exposure that leads to the strong increase in growth rate. Furthermore, the chemical reactions at the surface are expected to be much more complicated as compared to reaction 4.2 and 4.3, due to the absence of hydroxides in the reaction channel. As a result, the formation of ethane by a ligand exchange mechanism as in case of reaction 4.2 is most likely not going to occur. Instead, other reaction products than ethane have to form. Further analysis to identify possible reaction mechanisms is made in the following sections.

6.2 Initial Growth of O_2-ALD ZnO on Si(111)-H

After successful water-free atomic layer deposition has been demonstrated in the previous section, the aim of the following one is to gain insight into the initial growth of ZnO deposited by O_2-ALD. To compare the O_2-ALD ZnO with the results of initial ZnO ALD using H_2O as oxidizing agent, ZnO layers are deposited monolayer-wise on Si(111)-H substrates and characterized in situ by XPS, as described earlier in Sec. 4.5. The photoemission spectra of the involved elements Si, Zn and O are presented in Fig. 6.2.

As expected, the substrate's signal is attenuated after each deposition step and disappears completely when the film thickness exceeds the information depth of the photoelectrons. At the same time, both film elements rise until their intensities reach a maximum. The normalized intensities of the particular peaks are plotted in Fig. 6.3. As in case of H_2O-ALD, the observed attenuation and increase behavior demonstrate ideal ZnO layer-by-layer growth also in case of O_2-ALD. Comparing the peak intensity evolution with Fig. 4.24, shows no major differences. Only the initial growth of the first ZnO monolayer seems to complete sooner in case of O_2-ALD. Furthermore, it seems to take longer until the substrate's photoemission signal is completely attenuated. However, especially for film thicknesses in the range of the information depth, small intensity variations of the substrate's photoemission signals will have a large influence on the calculated film thick-

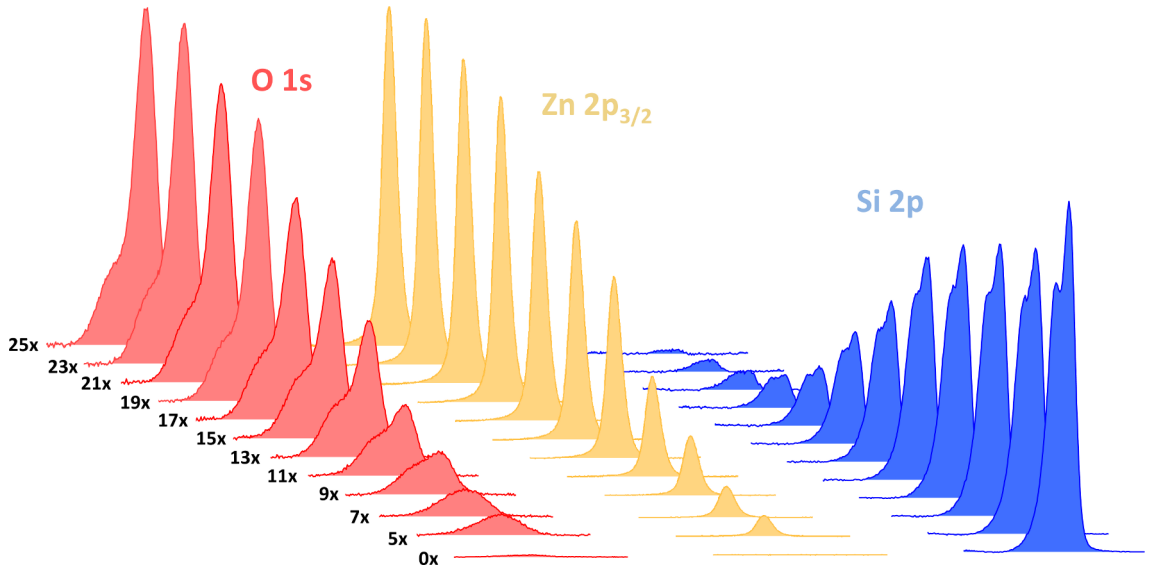

Figure 6.2: X-ray photoelectron spectra of initial ZnO growth using O_2 as oxygen precursor. Al Kα radiation is used to excite the photoelectrons.

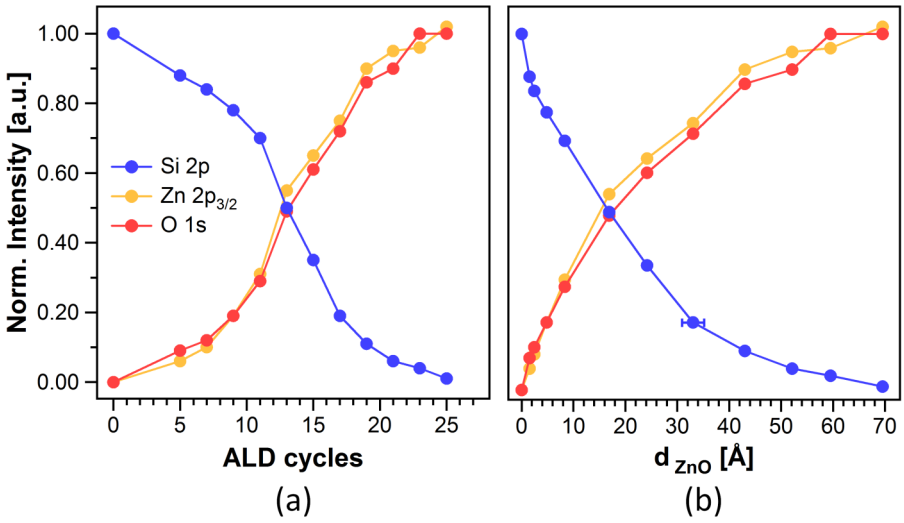

Figure 6.3: Normalized photoemission intensities of Si, Zn and O during initial ALD of ZnO using O_2 as oxygen precursor. To gain insight into the growth behavior, the intensities are plotted over (a) the number of ALD cycles and (b) the corresponding ZnO film thickness.

ness. This results in an increased standard deviation of the calculated film thickness for film thicknesses in the range of the sampling depth. Anyway, comparing the measured attenuation behaviors of both O_2-ALD and H_2O-ALD with the expected PES characteristics during layer-by-layer growth (cf. Fig. 3.4) results in a more ideal attenuation behavior for O_2-ALD.

Peak fitting results of the Zn $2p_{3/2}$ photoemission line are shown in Fig. 6.4 (a). As for H_2O-ALD, no additional chemical component can be identified. The resulting peak width are plotted over the film thickness in Fig. 6.4 (b). For ease of comparison, the H_2O-ALD results presented in Chp. 4 are also shown.

At first glance, there are no significant differences between both films. The one grown by the standard ALD process seems to show slightly increased peak width during the first deposition step but that can be assigned to the smaller film thickness of only 0.96 Å compared to 1.55 Å in case of O_2-ALD. At later deposition steps, the peak width of the Zn $2p_{3/2}$ photoemission line converges to 1.5 eV while in case of H_2O-ALD only 1.55 eV is achieved. Hence, the disorder in the films seems to be slightly reduced using O_2 as the oxidant. There are no significant differences observed in the zinc component of the film compared to H_2O-ALD ZnO. More interesting are possible differences in the oxygen components of the ZnO grown by O_2-ALD with respect to those grown under standard conditions.

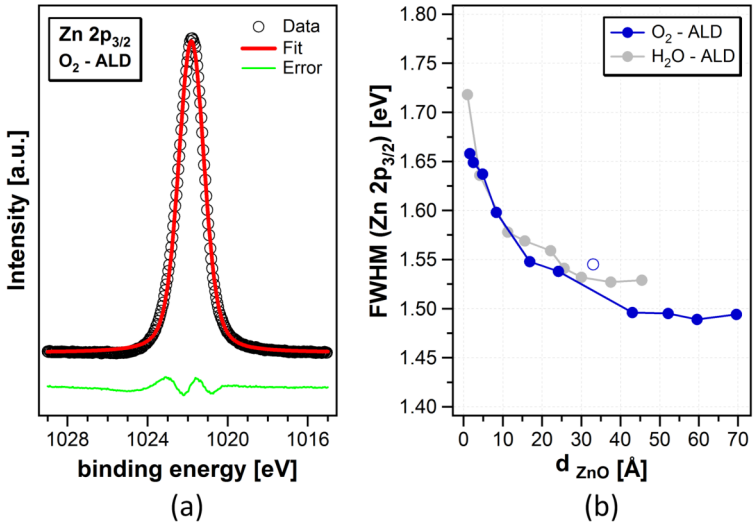

Figure 6.4: (a) Zn $2p_{3/2}$ photoemission spectrum and associated peak fitting; (b) evolution of the Zn $2p_{3/2}$ peak width during initial ZnO growth in an O_2-ALD process.

Fig. 6.5 is illustrating the development of the O 1s during initial O_2-ALD of ZnO on Si(111)-H. Therefore, three photoemission spectra and their corresponding peak fits are presented as in case of H_2O-ALD in Chp. 4, representing three different stages of ZnO ALD. Part (a) shows the resulting O 1s photoemission after the first deposition step. The calculated film thickness of 1.55 Å indicates a very thin and not yet closed ZnO layer. Again, as in case of H_2O-ALD, there are two different oxygen components observed. The one at a binding energy of BE = 530.5 eV is again assigned to $[O^{2-}]$. In contrast to H_2O-ALD, where the second component originates from hydroxides, the reaction mechanism of O_2-ALD is unknown. Until the chemical origin of the second oxygen component in O_2-ALD is identified and investigated in more detail later in this work, it is referred to as the negatively charged $[O^{-}]$ component. Peak fitting results in a somewhat increased peak width of both components. While the $[O^{2-}]$ species of H_2O-ALD grown ZnO had a FWHM of 1.07 eV, using an O_2 precursor shows a peak width of 1.12 eV. The same arises for the $[O^{-}]$ species that exhibit a FWHM of 2.08 eV compared to 1.97 eV of the hydroxide peak using water as oxidizing agent.

With increasing film thickness, those values do not change significantly. Instead, the intensity of the $[O^{2-}]$ rises with respect to the second oxygen component. The development of the $[O^{-}] : [O^{2-}]$ with increasing film thickness is plotted in Fig. 6.6 (a). At early stages of ZnO deposition, the $[O^{-}]$ component actually exceeds the $[O^{2-}]$ resulting in a ratio of $[O^{-}] : [O^{2-}] \approx 1.46$, while in case of H_2O precursor a value around 1.0 was determined.

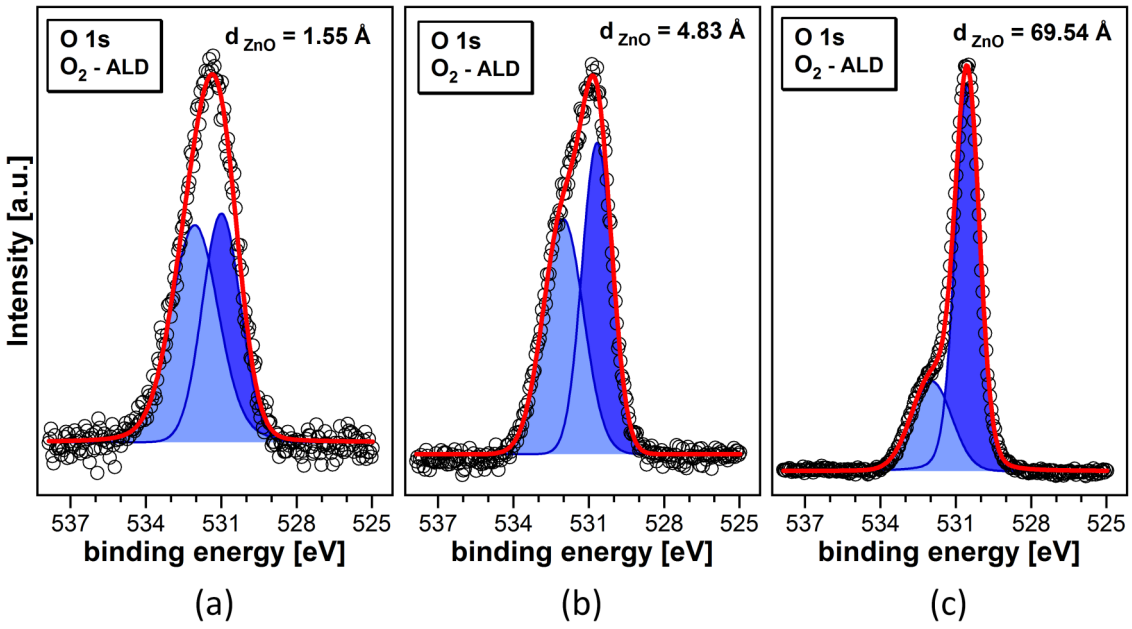

Figure 6.5: O 1s photoemission spectra at three different deposition stages: (a) a very thin O_2-ALD ZnO layer; (b) after the first monolayer has been completed; (c) at film thicknesses larger than the information depth of the photoelectrons.

The thicker the film, the more the ratio between both oxygen species decreases, approaching $[O^-] : [O^{2-}] \approx 0.36$ which is almost the same value than in H_2O-ALD zinc oxide. A closer investigation of the oxygen in the films produced by both H_2O- and O_2-ALD and their behavior on annealing is presented later in Sec. 6.3.

At first, characterization of the initial O_2 precursor ZnO atomic layer deposition is to be brought to an end. Therefore, the [Zn] : [O] ratio is determined and compared to the initial growth of H_2O-ALD. The results of both ZnO layers are shown in Fig. 6.6 (b). While the [Zn] : [O] ratio during deposition of the first 5 Å (i.e. the first ZnO monolayer) is identical for both precursors, a constant composition of $[Zn] : [O] \approx 0.94$ is already achieved after deposition of roughly 1 nm ZnO using O_2-ALD. This is almost a factor three earlier than in case of H_2O-ALD. The resulting film ends up with an overall oxygen-rich composition. If this is also affected by the interruption after each monolayer deposition step and the subsequent photoelectron spectroscopy, as discussed in Chp. 4, is clarified in the next section. There, ZnO films thicker than the information depth of the photoelectrons are characterized to gain more information about the oxygen component.

Analysis of the combined Auger parameter completes the comparison of initial growth behavior of O_2-ALD and H_2O-ALD. Therefore, the kinetic energies of the Zn $L_3M_{45}M_{45}$

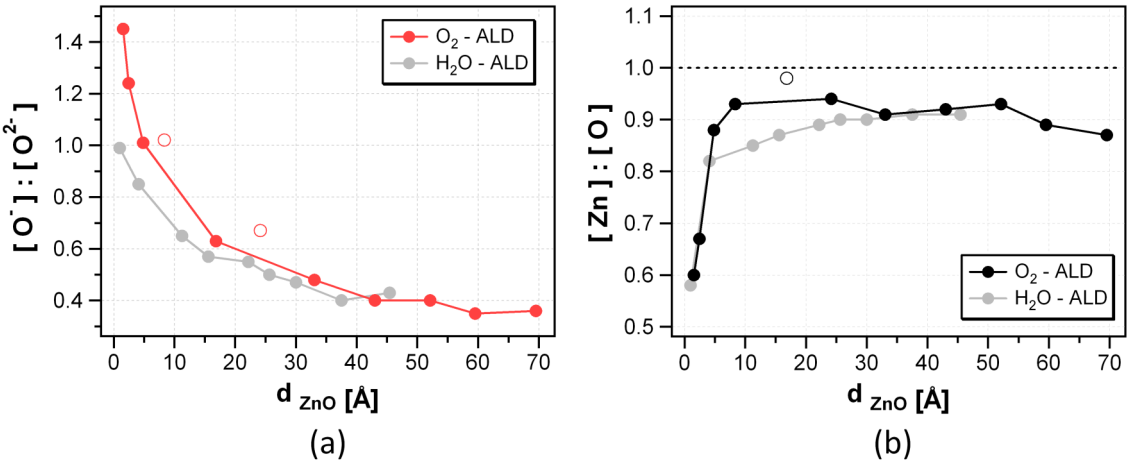

Figure 6.6: (a) $[O^-] : [O^{2-}]$ ratio of the initial growth of ALD-ZnO using molecular oxygen (O_2) as oxidizing agent; (b) [Zn] : [O] ratio plotted over the ZnO thickness.

have been fitted with the same method as described earlier in Sec.4.5. The corresponding spectra of the X-ray induced Auger electrons are shown in Fig. 6.7 (a), while the combined Auger parameter of the Zn $L_3M_{45}M_{45}$ and the Zn $2p_{3/2}$ photoelectrons is plotted against the ZnO thickness in Fig. 6.7 (b). The Auger parameter of the initially formed partial monolayer is determined to be 2009.78 eV. At first sight this value seems to be more than 0.2 eV lower than in case of H_2O-ALD. Taking into account that in case of O_2-ALD the average film thickness of the initially formed layer is slightly higher than the H_2O-ALD

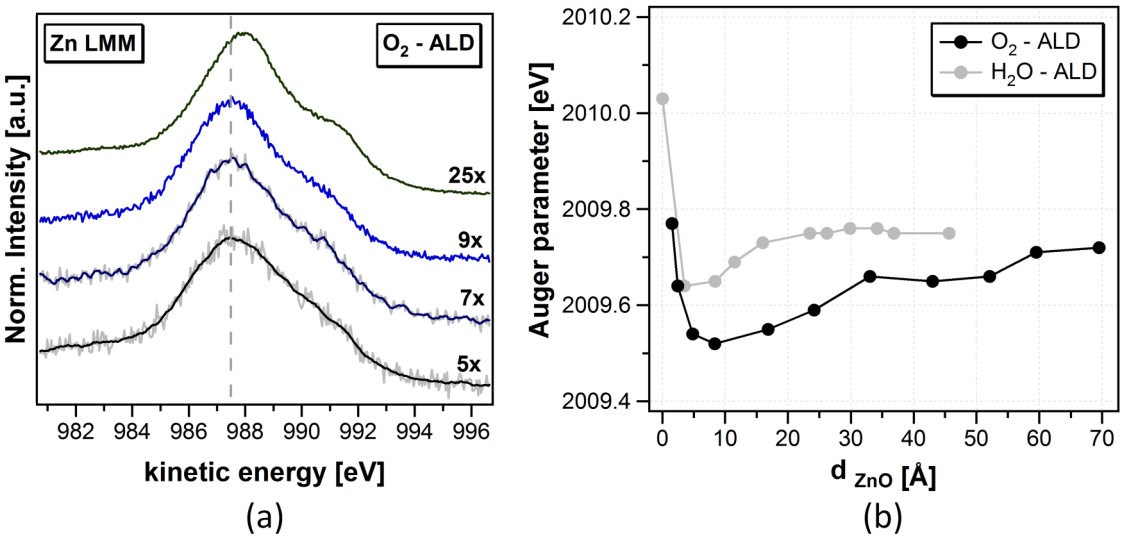

Figure 6.7: (a) Zn LMM Auger electron spectra after each monolayer deposition step and (b) the resulting combined Auger parameter with respect to the film thickness.

layer, comparison of the Auger parameter results in no significant changes during initial growth. After formation of the first ZnO monolayer, the Auger parameter exhibits a minimum value of 2009.5 eV and increases afterwards constantly until it settles at a value of 2009.7 eV, as in case of H_2O-ALD. In general, the Auger parameter vs. film thickness dependency shows the same characteristic behavior for both oxidizing precursors. While in case of water-ALD the increase of the Auger parameter was attributed to the reduced amount of oxygen in the films, this does not apply for the use of molecular oxygen as precursor. As shown earlier, the final [Zn] : [O] ratio was already reached shortly after formation of the initial ZnO monolayer.

6.3 H_2O-ALD vs. O_2-ALD ZnO

As shown in the previous section, the initial growth of O_2-ALD showed no significant differences in growth behavior compared to standard ZnO-ALD. Nevertheless, there were indications that the PES analysis after each monolayer deposition influenced the film growth. Hence, the following section focuses on the investigation and comparison of ZnO films that are on the one hand thicker than the escape depth of the photoelectrons and on the other hand were deposited in one single deposition step. Therefore, two ZnO films of roughly the same film thickness are deposited onto Si(111)-H, 50 cycles in case of H_2O-ALD and 30 ALD cycles using molecular oxygen as precursor. According to the growth-per-cycle determined, the resulting thicknesses of both films should be $d_{ZnO} \approx 15$ nm. Photoelectron spectra of the H_2O-ALD ZnO film have already been shown in Fig. 4.20 of Sec. 4.4. The corresponding photoemission spectra of the O_2 zinc oxide are shown in Fig. 6.8 for the Zn $2p_{3/2}$ (left) and O 1s (middle) photoelectrons and the Zn $L_3M_{45}M_{45}$ Auger electrons (right), respectively.

As already pointed out in the previous section, there is only one zinc component present during initial growth of ZnO. As expected, the same is true for thick ZnO layers deposited in one single step and only one Zn component is observed at 1021.89 eV in the Zn $2p_{3/2}$ photoelectron spectrum of Fig. 6.8, being shifted by 0.2 eV towards higher binding energies.
As in case of H_2O-ALD, the oxygen 1s photoelectrons show one additional component at the high binding energy side of the $[O^{2-}]$ peak. As mentioned earlier, the second component cannot be attributed to a surface hydroxide, since no water is present in the

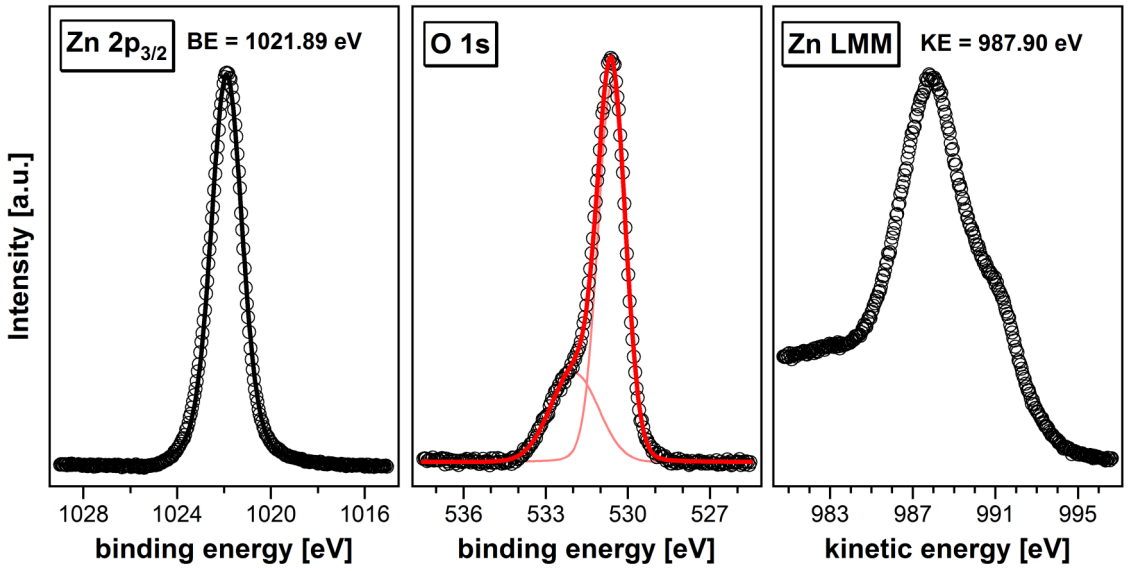

Figure 6.8: Regional spectra of a 15 nm O_2-ALD ZnO film. As in case of water-ALD, the Zn $2p_{3/2}$ photoemission peak contains no additional components. The O 1s consists of two chemically shifted peaks. In contrast to H_2O-ALD, the second component at the high binding energy side cannot originate from surface hydroxides due to the absence of water. The Zn LMM Auger peak is only slightly shifted and the combined Auger parameter is close to the value determined for H_2O-ALD.

ALD process using O_2 as an alternative oxygen precursor. Detailed analysis of the second oxygen component using synchrotron radiation and their behavior on annealing is given at the end of this section.

As shown in Fig. 6.8, the Zn $L_3M_{45}M_{45}$ Auger electron peak is located at 987.90 eV. Compared to the H_2O-grown film this value is shifted by 0.1 eV to lower kinetic energies. Hence, combining the photoelectron's binding energy and the kinetic energy of the corresponding Auger electrons of the zinc component in the O_2-ZnO layer results in a combined Auger parameter of:

$$\begin{aligned} \text{AP (Zn)} &= \text{BE (Zn } 2p_{3/2}) + \text{KE (Zn } L_3M_{4,5}M_{4,5}) \\ &= 1021.89 \text{ eV} + 987.90 \text{ eV} \\ &= 2009.79 \text{ eV} \end{aligned} \tag{6.1}$$

This is almost the same value as in case of using water as oxidizing agent (2009.68 eV) and therefore the local chemical environment of the Zn can be expected being the same for both oxygen precursors.

6.3.1 Electronic Structure and Reaction Mechanism

The capability of using a semiconductor material for certain applications is depending on its electronic structure[20]. Ultraviolet photoelectron spectroscopy (UPS) is usually applied to investigate the valence band states of semiconductor materials giving insight into the electronic properties of a certain material. As mentioned earlier in Sec. 2.2.2, in UPS photons with an energy of 21.21 eV obtained by a He discharge lamp are used to excite the photoelectrons. Due to the low energy of the photons, only electrons located in the valence band contribute to the photoemission spectrum.

Fig. 6.9 presents the valence band spectra of ZnO as-grown by atomic layer deposition using both H_2O (black line) and molecular oxygen (red line) as oxygen precursors, re-

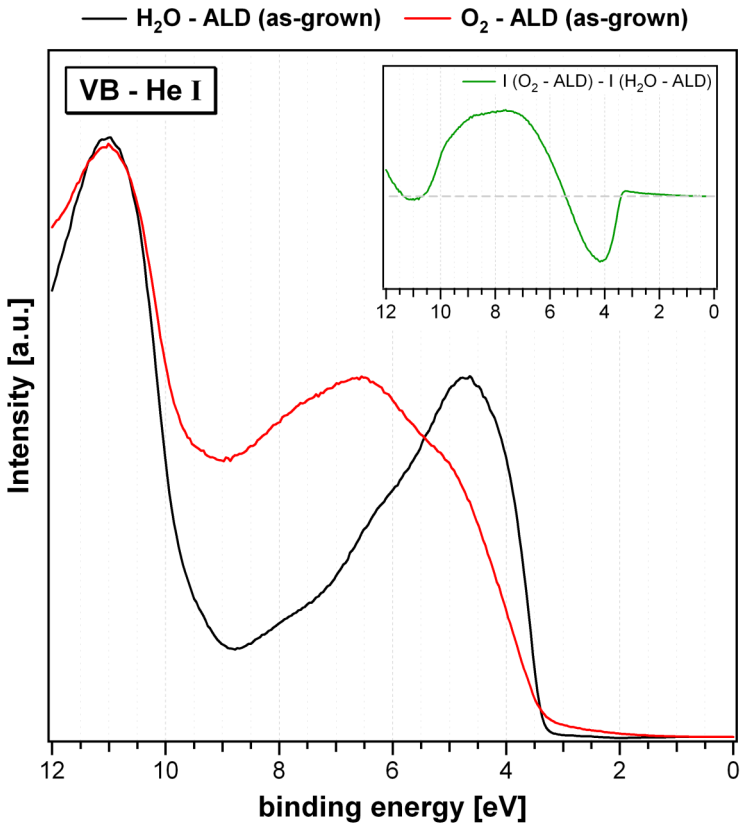

Figure 6.9: Valence band spectra of ALD ZnO deposited with both, H_2O (black line) and molecular oxygen (red line) as oxygen precursor. All spectra were recorded using He I radiation of $h\nu = 21.22$ eV. The difference spectra of both precursor combinations is illustrated in the inset. The broad feature between $6 - 10$ eV in the O_2-ALD process is likely to arise due to adsorbed hydrocarbon reaction by-products of the DEZn + O_2 reaction.

spectively. Both spectra show significant differences in their valence band structure. In case of H_2O-ALD, the valence band maximum (VBM) was determined to be located at VBM = 3.37 eV with respect to the Fermi energy (at BE = 0 eV). There are a couple of features visible that are discussed shortly. The prominent feature at a binding energy of 11.0 eV arises from Zn 3d photoelectrons[99–102]. According to Powell et al., the Zn 3d core-electrons are always located at 7.5 eV below the VBM[20]. Relating the Zn 3d binding energy to the valence band maximum, a binding energy value of 7.52 eV is determined for H_2O-ALD, which is in perfect agreement with the value reported by Powell et al. The features in the energy region between the Zn 3d peak and the valence band maximum contribute from O 2p states around 4.5 eV and from Zn 4s - O 2p mixed states around 7.9 eV with respect to the Fermi level[99–101].
The valence band spectrum of the ZnO film deposited using an O_2 precursor clearly differs in its appearance with respect to the standard precursor. While the position and intensity of the Zn 3d peak does not show any changes, the O 2p states are significantly attenuated and an additional broad feature appears 8 eV below the Fermi level. To illustrate the differences between both spectra more clearly, the inset in Fig. 6.9 shows the difference spectrum of both valence bands. The broad feature between binding energies of $6 - 10$ eV seems to consist of at least three components. Since only diethylzinc and molecular oxygen are present during the deposition, additional peaks in the valence band difference spectrum can only originate either from carbon compounds or the oxygen adsorbed at the surface itself. An UPS study of different carbon containing molecules done by Bournel et al. indicate that different carbon compounds generate features in this energy region[103]. On the other hand, a study of point defects on non-polar ZnO($10\bar{1}0$) by Göpel et al. attributes two broad features at 4 eV and 6 eV below the VBM (i.e. 7.5 eV and 9.5 eV below E_F, respectively) to the 2 p levels of adsorbed O_2^-[104]. Thus, the UPS results can not clearly identify the origin of the additional peaks in the valence band spectrum.

In case of carbon species being present, they should also be visible in the X-ray photoelectron spectra by emission of C 1s photoelectrons. Fig. 6.10 plots the regional photoemission spectra of C 1s of both ALD-ZnO layers. Spectrum (a) at the left hand side of Fig. 6.10 corresponds to the ZnO film deposited using H_2O as oxygen precursor. No indication of carbon adsorbates is found in the spectrum. This is consistent with the UPS spectrum given in Fig. 6.9, where also no spectral features of carbon were identified. These results reveal the purity of the ALD-ZnO layers using water as precursor and indicates that the ligand exchange reaction mechanism during water exposure completely removes the remaining ethyl groups of the monoethylzinc.

A completely different situation is present in the case of using O_2 precursor gas. Fig. 6.10 (b) plots the C 1s photoemission spectrum of the O_2-ALD ZnO film. In contrast to H_2O-ALD, at least two separated peaks are observed. There might be a third component present, indicated by a weak shoulder appearing at 287 eV. Unfortunately, the signal-to-noise ratio is pretty low due to the low amount of carbon at the surface, so that quantification of the results is difficult. To yield better results, the sample has been transferred under UHV conditions to the U49/2 PGM-2 beamline of the BESSY II synchrotron source. The tunable excitation energy ($85 - 1890$ eV) allows very surface sensitive photoelectron spectroscopy since the information depth is directly dependent on the excitation energy of the incident light (cf. Chp. 2).
The C 1s spectrum shown in Fig. 6.11 was recorded using an excitation energy of $h\nu = 415$ eV, resulting in a kinetic energy of the excited photoelectrons of KE = 130 eV. At this kinetic energy, the inelastic mean free path of the photoelectrons is about 9.2 Å, i.e. surface sensitive to the topmost atomic layers. The spectrum shows the same two photoemission lines observed in Fig. 6.10 (b) and no indication for a third component, which might be located deeper in the material and not contributing to the spectra due to the increased surface sensitivity. After background removal, both peaks were fitted by

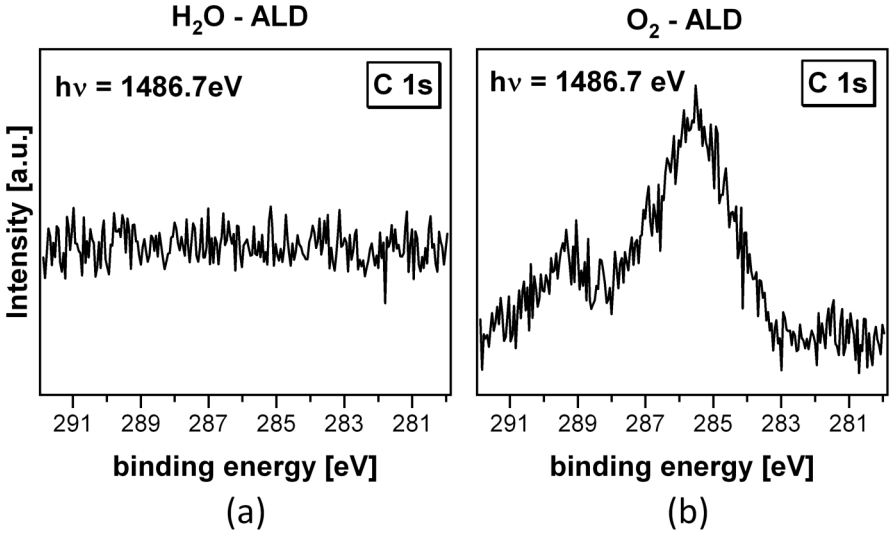

Figure 6.10: (a) Carbon 1s photoelectron spectra recorded with Al Kα radiation. The H_2O-ZnO in spectrum (a) is not showing any carbon surface contamination, indicating the complete reaction between DEZn and water into ZnO and ethane. In contrast, there is a considerable amount of carbon in case of O_2-ALD shown in (b), which indicates a more complex reaction between DEZn and O_2 with unwanted reaction by-products adsorbed at the surface.

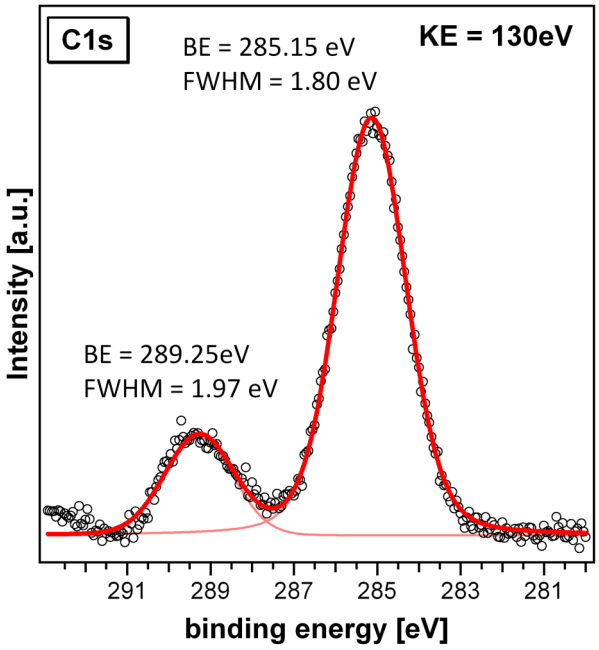

Figure 6.11: O_2-ALD ZnO C 1s spectrum recorded at the BESSY II synchrotron radiation source with an excitation energy of $h\nu = 415$ eV resulting in a kinetic energy of the C 1s electrons of KE = 130 eV. Two different carbon states are clearly identified. The peak at lower binding energies is attributed to some kind of hydrocarbons, while the higher binding energy peak's origin is a carbon in a carboxylic environment.

Voigt functions, respectively. The binding energy of the more intense peak was determined to be BE = 285.25 eV. With a peak width of FWHM = 1.8 eV the peak consist only of one single carbon component.

The second peak observed is chemically shifted by 4.1 eV to higher binding energies, indicating a very different bonding situation of the carbon atom. Its binding energy results in BE = 289.35 eV and a peak width of FWHM $\approx$ 2.0 eV. An intensity ratio between both carbon species of 4.6 was calculated.
To identify the two carbon components, the results of the ultraviolet photoelectron spectroscopy and the synchrotron radiation photoelectron spectroscopy of the C 1s peak have to be compared with studies reported by other groups. Identification of the carbon species would help to determine the chemical reaction during the atomic layer deposition. Even though there are no reports in literature that deal with the electronic structure of ZnO grown using DEZn and molecular oxygen precursors, there are various studies on the adsorption behavior of gaseous molecules on surfaces.

Reaction product	Structure	Formula	Source
ethoxyethylzinc	Et - Zn - O - Et	$C_2H_5OZnC_2H_5$	[108;109]
diethoxyzinc (DEOZn)	Et - O - Zn - O - Et	$Zn(OC_2H_5)_2$	[108;109]
ethylethylperoxyzinc	Et - Zn - O - O - Et	$C_2H_5ZnOOC_2H_5$	[108;110]

Table 6.1: Summary of reaction products during oxidation of diethylzinc (Et-Zn-Et) reported by other groups.

The diethylzinc ($Zn(C_2H_5)_2$) precursor is the only possible carbon source during the ZnO forming reaction. In their XPS study of the adsorbed state of DEZn on ZnO ($000\bar{1}$), Vohs and Barteau determined a broad C 1s peak located at a binding energy of 284.2 eV[105]. Due to its peak width of FWHM = 2.7 eV, and the different bonding situation of the two carbon atoms in the molecule they considered this peak being a convolution of two peaks of FWHM = 1.7 eV, each. They determined the binding energy of the carbon atom bound to the zinc being located at 283.4 eV, while the methyl group carbon (-CH_3) is located at BE = 284.6 eV. A similar value was reported by Klivényi et al. for DEZn adsorption at low temperatures on rhodium[106]. They determined a broad C 1s peak at 284.4 eV for high DEZn exposures. These results do not match to our measured values leading to the conclusion that the origin of the C 1s peak neither is adsorbed diethylzinc nor its ethyl ligands. Even if the binding energy difference is not differing significantly, the peak width and the absence of a second component rule out DEZn or an ethyl group being the source of carbon contamination. Atomic carbon with a reported binding energy of 284.3 eV[105] can also be excluded due to the significant difference in binding energy.
It is also unlikely that the carbon originates from thermal dissociation of the DEZn molecule at the substrate's surface. On the one hand, the initial dissociation of DEZn is reported to start at temperatures above 300 °C[107;108]. On the other hand, the deposition temperature of O_2-ALD and H_2O-ALD differs only by 10 °C. If the DEZn would dissociate, a C 1s photoemission peak would have been observed in case of water-ALD, too.
Hence, the carbon has to be a by-product of the reaction between $Zn(C_2H_5)_2$ and O_2. There are only few studies on the oxidation of diethylzinc[108–110] and most of them are theoretical works. All of these studies report that one or even two oxygen atoms are inserted between the zinc atom and the ethyl ligand. Depending on the number and position the oxygen atom(s) are inserted, this results in the following reaction products, summarized in Tab. 6.1.

In the first case, one oxygen atom is inserted between the zinc and one ethyl group. The resulting molecule is an ethoxyethylzinc (Et-Zn-O-Et) compound. The second case can be seen as an oxidation of this ethoxyethylzinc by inserting an additional oxygen atom between the other ethyl ligand and the zinc atom. This results in a diethoxyzinc (DEOZn). According to Maejima et al., this compound is stable up to temperatures of 300 °C after it dissociates into C_2H_5OZnOH and ethylene (C_2H_4)[108]. The third reported reaction product is an ethylethylperoxyzinc compound, where both oxygen atoms are located between the zinc and one of the ethyl ligands (Et-Zn-O-O-Et).
There are no photoelectron spectroscopic studies available for those reaction products. Anyhow, Verhoeven et al. investigated the interaction of different hydrocarbons[111]. There, they investigated the chemical shift of C 1s photoelectrons depending on their bonding partner. Hydrocarbons like C_2H_4, C_2H_6 or $\bullet C_2H_5$ appear at binding energies of about 285 eV. This is quite the same binding energy as observed at the intense C 1s photoemission line in case of the O_2-ALD grown ZnO layers and therefore we attribute this peak to some type of hydrocarbons. Verhoeven also states, that if one of the carbon atoms of a hydrocarbon molecule forms a single covalent bond with an oxygen atom, its binding energy shifts about $\Delta BE \approx 1.5\,eV$[111]. This situation is present in all three possible reaction products after DEZn oxidation. Hence, a C 1s signal at approximately 286.6 eV would be present in Fig. 6.11 if residuals of oxidized DEZn are present at the surface. This additional peak is not observed and so we exclude the presence of one of the reaction products summarized in Tab. 6.1 at the ZnO surface.
If an oxygen atom reacts with an hydrocarbon in a way that a double bond is formed, the resulting chemical shift is approximately $\Delta BE \approx 3.0\,eV$. Such a peak is also not present in Fig. 6.11. The third bonding type Verhoeven investigated is the formation of a carboxyl (-COOH) compound, where three covalent bonds are formed between C and the two O atoms. This configuration will shift the binding energy of the carbon atom by $4 - 4.5$ eV, which is in very good agreement with the observed binding energy shift of 4.1 eV determined for the second carbon component. Another XPS study of Dilks about peroxy features at polymer surfaces oxidized by O_2 also attributes high binding energy C 1s components at 289.1 eV to carbon in a carboxylic environment[112]. Unfortunately, combined XPS, UPS and SR-PES investigation cannot clearly identify the exact origin of the carbon components due to the absence of information about hydrogen atoms in the spectra. Nevertheless, photoelectron spectroscopy results help to narrow down the possible carbon configurations: We suggest the more intense carbon component being attributed to some kind of hydrocarbons. These can be fragments of the ethyl ligand like

a methyl radical (-CH_3) for instance, or a reaction product like ethylene (C_2H_4)[113]. The high binding energy component is most likely arising due to the presence of a carbon in a carboxylic environment, i.e. bond to two oxygen atoms for instance a carboxyl-radical (O=C-OH)[111] or carbon in a perester functionality (O=C-OO)[112]. These results indicate a much more complicated reaction mechanism at the surface during O_2-ALD with respect to H_2O-ALD.
All of the carbon species suggested above as possible products of the ALD process should be loosely bound to the surface. Hence, it is expected that they are easily removed by an heat treatment of the deposited ZnO films. Therefore, both films were annealed under UHV conditions for 60 min at 400 °C. A complete removal of any carbon species should have a significant influence on the valence band structure of the annealed ZnO. For comparison, Fig. 6.12 shows both, the as-grown and annealed ultraviolet photoemission spectra for H_2O- and O_2-ALD, respectively.

All spectra are normalized to the Zn 3d photoemission peak located at approximately BE = 11 eV. The valence band spectra of the ZnO films deposited using water as oxygen precursor are shown in the upper part of Fig. 6.12. It shows two noticeable changes of the photoemission features between the as-grown ZnO (top left) and after annealing (top right). First, the intensity of the Zn 3d peak increased strongly with respect to the oxygen induced peaks close to the valence band edge. The valence band edge itself shifted from 3.37 eV to 3.18 eV after annealing. This is almost the same value determined for annealed O_2-ALD, which has been determined being located 3.23 eV below the VBM as shown in the lower right part of Fig. 6.12.
The annealed valence band spectrum of O_2-ALD shows significant changes compared with the film without heat treatment. All additional peaks vanished and the valence band shows the same structural features as the H_2O-ZnO. This is attributed to the removal of adsorbed carbon species by the annealing process as discussed above. Both annealed ZnO films show similar valence band characteristics. Only the intensity of the O 2p electrons at BE $\approx$ 4.5 eV is more pronounced. This could indicate a higher amount of oxygen at the surface of the O_2-ALD ZnO.

6.3.2 Annealing Behavior of the Oxygen Component

Due to the absence of hydroxides and the different reaction mechanism it was not expected that the two oxygen components of both films look quite similar (cf. Fig. 6.8 and Fig. 4.20)

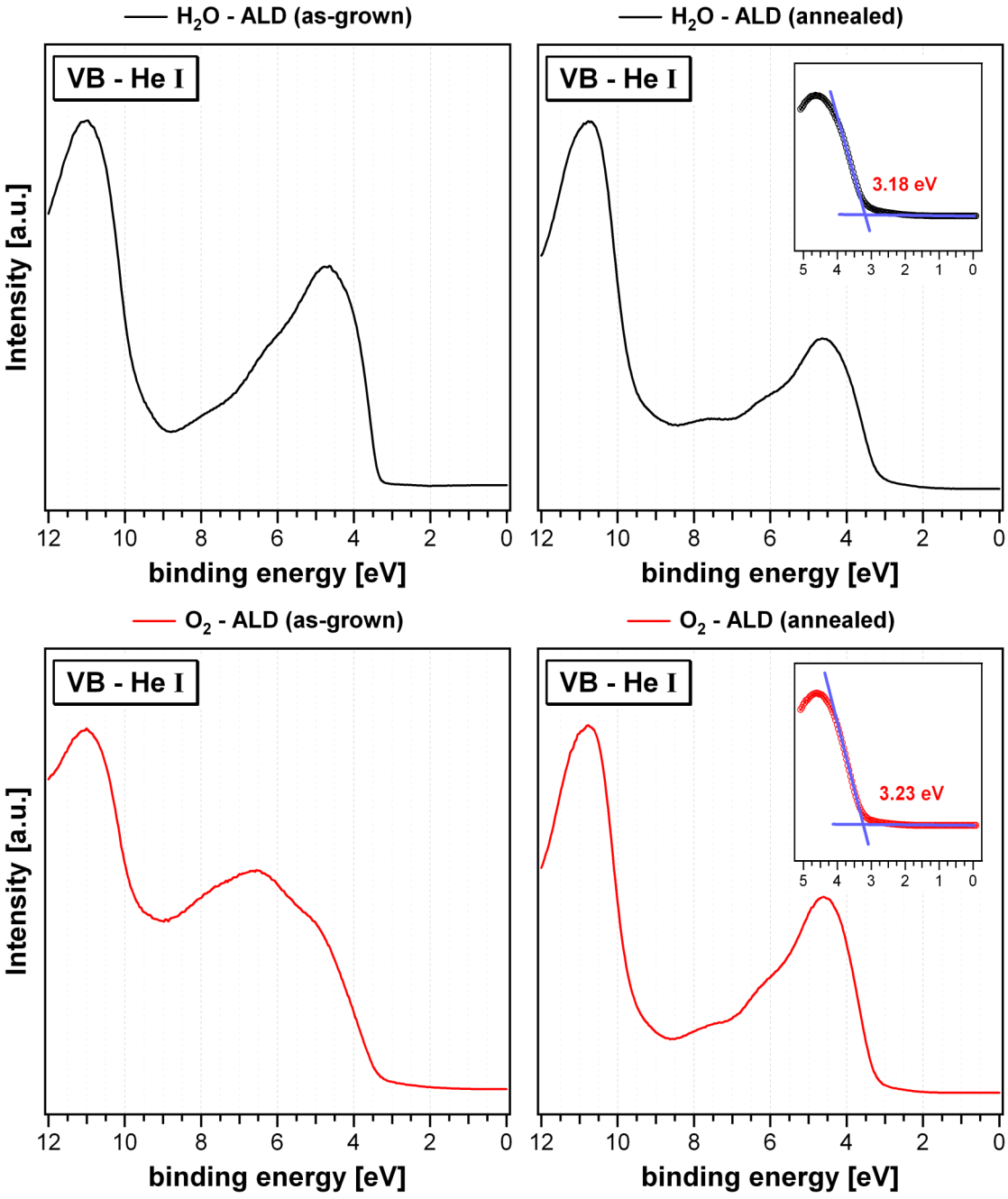

Figure 6.12: He I valence band spectra of H_2O-ALD (top) and O_2-ALD ZnO (bottom) both, before (left) and after annealing (right). Significant changes are observed in the annealed O_2-ZnO valence band spectrum, indicating the removal of adsorbed carbon compounds from the surface.

at first sight. Especially the second component that is usually attributed to surface hydroxides in case of H_2O-ALD is unlikely to have the same origin in case of O_2-ZnO. Hence, the following part of this section concentrates on the oxygen component in the particular zinc oxide films, their differences and similarities. The effects of annealing on the valence band structures was shown just recently. In Fig. 6.13 the influence of heating the sample on the O 1s photoemission signal is presented. The top left picture represents the ALD-ZnO film as deposited using H_2O as oxidizing agent. Two peaks are fitted after a Shirley background removal of the scattered electrons. The more intense one attributed to $[O^{2-}]$ forming the ZnO compound is located at BE = 530.49 eV and exhibits a peak width of FWHM = 1.07 eV. The second component, attributed to surface hydroxides $[O_{-OH}]$, is chemically shifted by ΔBE = 1.24 eV to a higher binding energy of BE = 531.73 eV. The $[O_{-OH}]$ peak width is increased with respect to the $[O^{2-}]$, resulting in a FWHM of 1.97 eV. After annealing the sample for 60 min at 400 °C, there are no big changes observed in the peak binding energies. The $[O^{2-}]$ peak position has been determined being located at BE = 530.42 eV. The difference in binding energy was kept constant at ΔBE = 1.24 eV during the fitting routine. While the peak width of the $[O^{2-}]$ photoelectrons remain constant at FWHM = 1.07 eV, the $[O_{-OH}]$ peak FWHM decreases a little, resulting in a value of FWHM = 1.86 eV after annealing. The corresponding O 1s spectrum of the annealed film is plotted at the upper right corner of Fig. 6.13. A $[O_{-OH}] : [O^{2-}]$ intensity ratio of the as-grown film of 0.36 has been calculated, i.e. the hydroxide bound oxygen amounts to 26 % of the total oxygen in the H_2O-ZnO. After annealing, the total amount of hydroxide oxygen decreases, resulting in a reduced $[O_{-OH}] : [O^{2-}]$ ratio of 0.20 (i.e. 16 % of the total oxygen).

Almost the same behavior is observed for the O_2 precursor deposited zinc oxide. The corresponding O 1s photoemission spectrum of the as-grown ZnO is shown in Fig. 6.13 (c). Initially, an oxygen ratio of $[O^-] : [O^{2-}] = 0.35$ is determined, which is almost the same amount of $[O^-]$ oxygen than in the H_2O-grown ZnO samples. After heating to 400 °C, the high binding energy oxygen component is reduced by the same amount than in case of H_2O-ALD, resulting in a $[O^-] : [O^{2-}]$ ratio of 0.20.
The peak positions and their particular widths of both oxygen components are also determined for the as-grown and annealed O_2-ZnO film. The intense $[O^{2-}]$ 1s photoelectrons have a binding energy of BE = 530.61 eV, which is almost equal to the H_2O-ALD $[O^{2-}]$ photoelectrons. In contrast, the peak is noticeable broader, having a peak width of FWHM = 1.12 eV. In addition, the chemical shift of the $[O^-]$ component is more pronounced in case of O_2-ALD. Its binding energy has been determined being 532.07 eV,

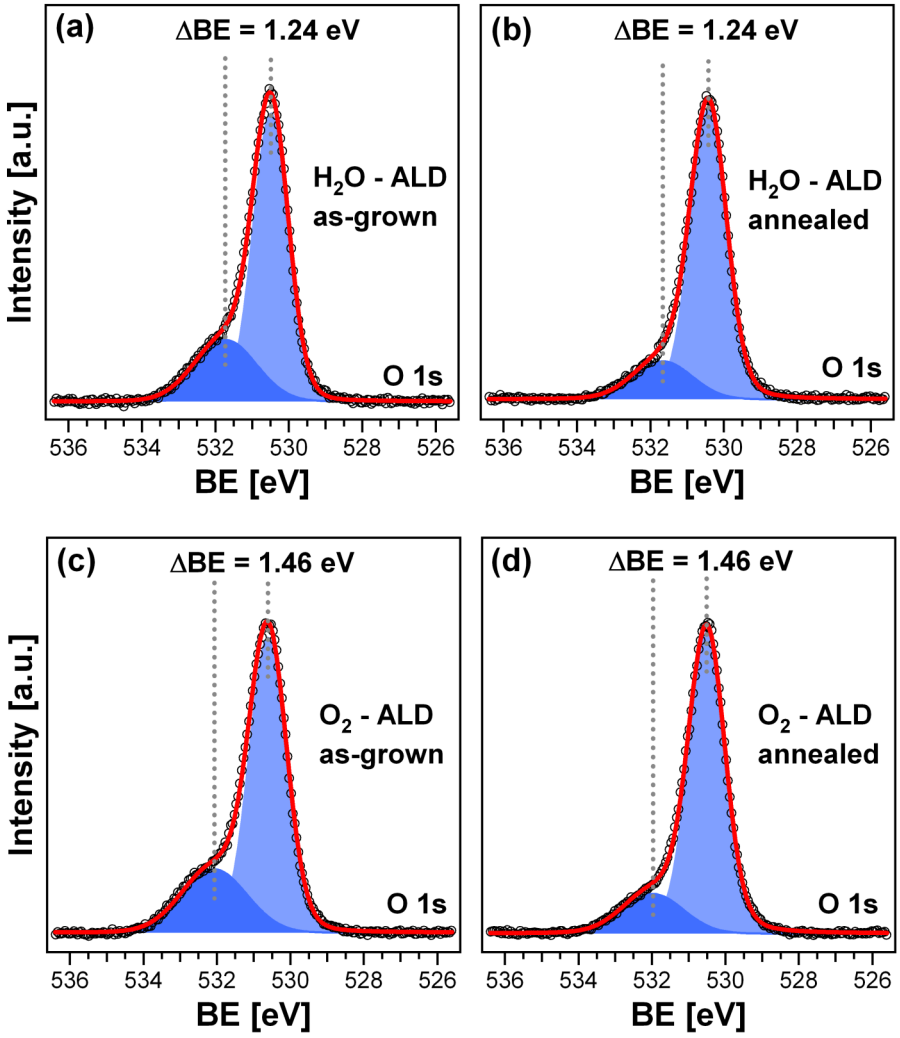

Figure 6.13: O 1s regional photoemission spectra of ALD-ZnO using both oxygen precursors and their dependence on annealing. (a) H_2O-ALD, as-grown; (b) H_2O-ALD, annealed to 400°; (c) O_2-ALD, as-grown; (d) O_2-ALD, annealed to 400°. All spectra are recorded using monochromized Al Kα radiation.

resulting in a chemical shift of ΔBE = 1.46 eV. After annealing, the $[O^{2-}]$ decreases to 1.05 eV, a value similar to the one of $[O^{2-}]$ in H_2O-ZnO. Both fitted peaks of the annealed O_2-ZnO O 1s photoemission line are shown in the lower right part of Fig. 6.13. After the annealing step, the chemical shift of both oxygen species remains constant at ΔBE = 1.46 eV. The different chemical shift of the high binding energy oxygen component in O_2-ALD and H_2O-ALD indicates a different chemical state of the $[O^-]$ oxygen in comparison with $[O_{-OH}]$. Hence, the $[O^-]$ obviously is not originating from hydroxides as reaction products of the DEZn + O_2 reaction.

In case of not being a reaction product of the DEZn + O_2 reaction, this oxygen component is likely to originate from a defect in the ZnO crystal structure. There are several studies about native defects in zinc oxide and their formation energies in literature[114–117]. Erhart et al. reported about oxygen interstitial defects where two oxygen atoms occupy one regular lattice site in a dumbbell configuration[114;117] as shown schematically in Fig. 6.14. For oxygen-rich growth conditions the $[O_2^{2-}]$ dumbbell defects have the lowest formation enthalpies of all intrinsic point defects[117]. Due to the sequential growth mode of atomic layer deposition, the growth conditions during the oxidizing half-reaction can be regarded as very oxygen-rich growth conditions. Therefore, the formation of $[O_2^{2-}]$ dumbbell defects is very likely and they should be present in significant amounts in O_2-ALD ZnO films. Its singly negative charge per atom is comparable to the bonding conditions of hydroxide oxygen in case of H_2O-ALD. Therefore it is expected that the $[O_2^{2-}]$ dumbbell oxygen also exhibits a comparable chemical shift towards higher binding energies and we can attribute the high binding energy peak in case of O_2-ALD to $[O_2^{2-}]$ dumbbell oxygen.

6.3.3 Non-destructive Photoemission Depth-Profiling

The oxygen components of both films show a similar behavior on annealing, as described earlier in this section. For H_2O-ALD, the decrease of the $[O_{-OH}]$ photoemission signal can be attributed to a removal of hydroxides from the surface of the ZnO film. If all hydroxides are located at the surface or if there is also a bulk hydroxide component will be investigated in the following. The same question arises for the $[O_2^{2-}]$ dumbbell oxygen in case of O_2-ALD. To answer these questions, non-destructive depth profiling

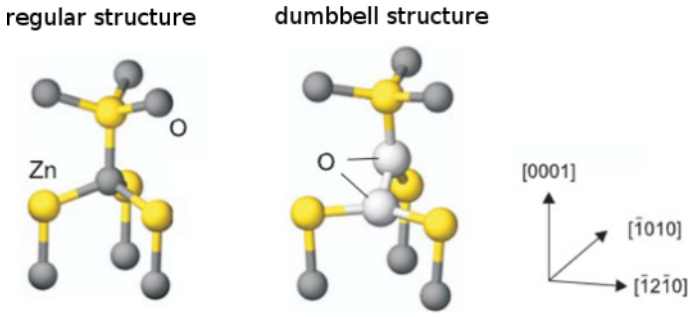

Figure 6.14: Illustration of the ideal wurtzite structure of ZnO (left) and the O_2^{2-} interstitial dumbbell defect (right). The picture has been taken from Erhart et al.[114]

using photoelectron spectroscopy is applied. Even though all photoelectron spectroscopy techniques are very surface sensitive, it is possible to decrease the information depth of the photoelectrons in two ways: Either, one tilts the surface under investigation to decrease the effective escape depth of the photoelectrons (referred to as *angle-resolved photoelectron spectroscopy* (AR-PES)). One other possibility is to change the excitation energy of the X-rays and therefore the kinetic energy of the emitted photoelectrons. This requires a tunable X-ray source and therefore a synchrotron radiation facility. Further information about depth profiling was discussed earlier in Chp. 2. In the following, both techniques are primary used to do a depth profiling of the oxygen in both ZnO films, respectively. This will help to identify if surplus oxygen is located at the surface or constantly distributed into the crystal for both oxygen precursors.

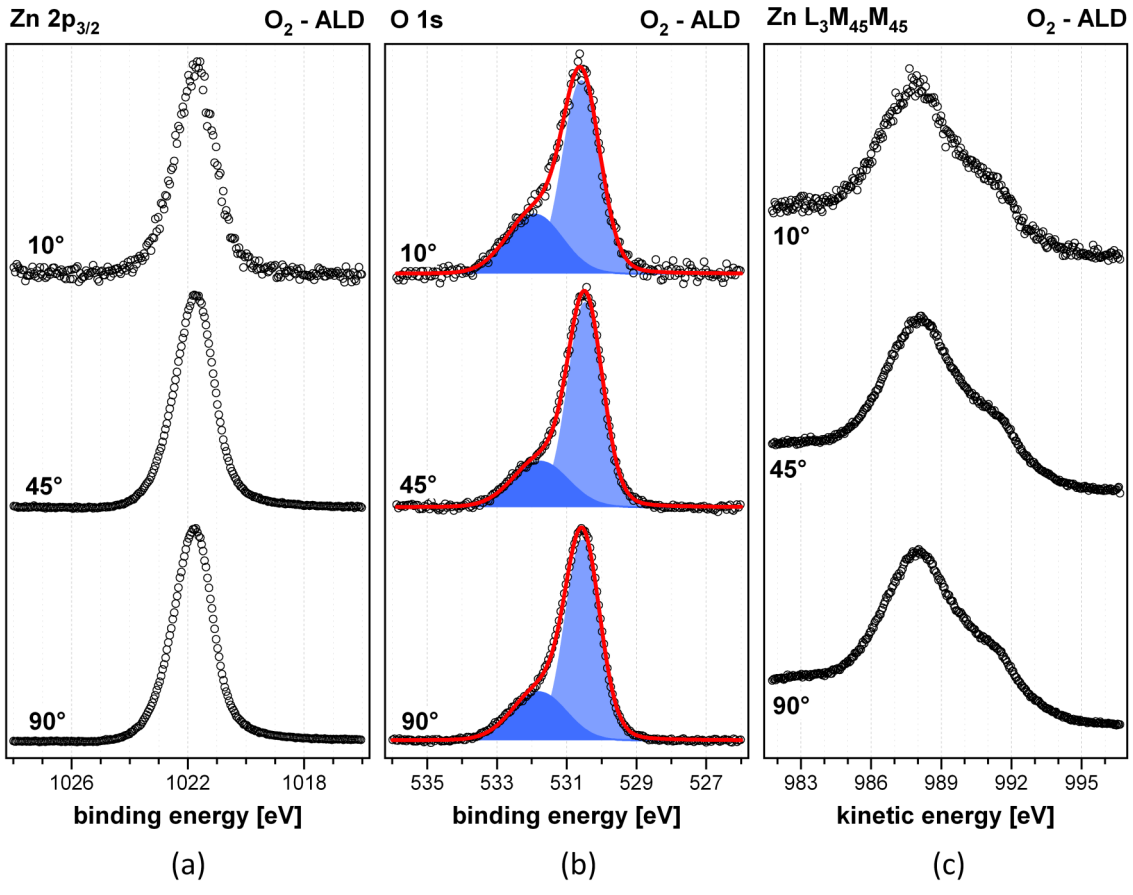

Figure 6.15: Angle-dependent X-ray photoemission spectra of ALD-ZnO using O_2 precursor. Shown are the Zn $2p_{3/2}$, O 1s and Zn LMM photoemission spectra for three exemplary exit angles. The exit angle is denoted with respect to the film's surface.

After deposition, an angular-resolved depth profile of the two as-grown ZnO films was recorded using monochromized Al Kα radiation and tilting the sample in the laboratory. The left part of Fig. 6.15 plots the Zn $2p_{3/2}$ at different exit angles, with respect to the surface. Here, 90° characterizes the emission of photoelectrons normal to the substrate's surface, while 10° describes a grazing exit angle resulting in a very surface sensitive information depth. Fig. 6.15 only plots the spectra of three different emission angles to illustrate the general behavior of the photoemission peaks. For detailed characterization of the ZnO films, the exit angle of the photoelectrons was varied in steps of 10° in the range between 90° - 50°. Afterwards, in a range between 45° - 10° spectra were recorded every 5° because of the increased influence of the emission angle on the information depth. The effective information depth of the photoelectrons entering the spectrometer depends on the emission angle, the excitation energy and the binding energy of the photoelectrons. For Al Kα excited Zn $2p_{3/2}$ photoelectrons, the effective information depth is in a range between 16.9 Å for an exit angle of 90° with respect to the surface and 2.9 Å for very flat angles of 10°.

Due to the drop in the photoemission intensities at small exit angles all spectra in Fig. 6.15 were normalized to 1 for ease of comparability. The Zn $2p_{3/2}$ photoemission spectra do not show any binding energy dependence on the exit angle. Besides the Zn $2p_{3/2}$, also the O 1s photoelectrons were recorded as shown in the middle of Fig. 6.15 for three exemplary exit angles. Its lower binding energy of about 530 eV leads to a slightly increased information depth with respect to the Zn 2p photoelectrons. This results in an effective information depth between $24.3 - 4.2$ Å for O 1s photoelectrons. In addition to the Zn 2p and O 1s photoelectrons, the Zn $L_3M_{45}M_{45}$ Auger electron peak was measured to determine the depth dependence of the combined Auger parameter of the zinc component.

The spectra shown in Fig. 6.15 originate from a ZnO film using molecular oxygen as precursor gas. The same experiments described above were also done for H_2O-ALD deposited ZnO. Quantification of the measured spectra results in depth profiles of the composition, contains information about the distribution of the two oxygen components present in the ZnO crystal, and shows the depth dependence of the Auger parameter of the zinc component. Fig. 6.16 plots all results for both oxygen precursors and is now discussed in detail. Fig. 6.16 (a) shows the [Zn]:[O] composition over the effective information depth of the photoelectrons before they undergo an inelastic scattering event. The results for H_2O-ALD are illustrated by the red markers, whereas the blue ones stand for the O_2-ALD ZnO film. In case of H_2O-ALD, the composition remains constant at a [Zn]:[O] ratio around a

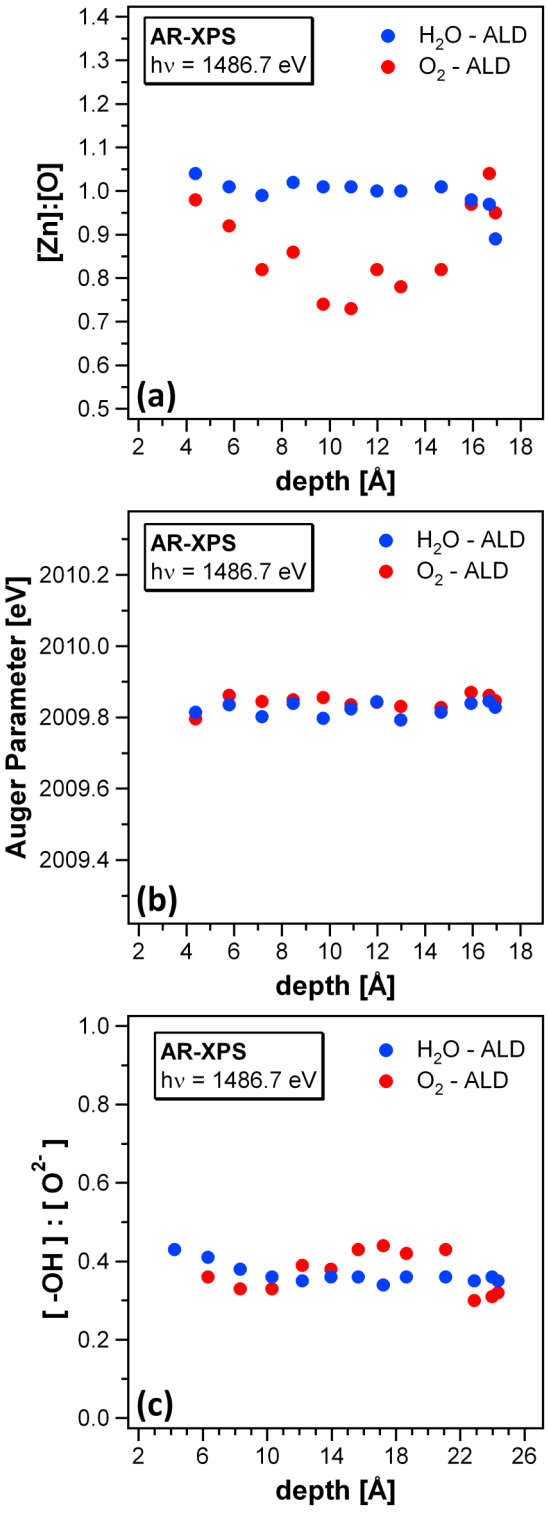

Figure 6.16: Results of angle-resolved XPS investigation of H_2O-ALD ZnO (blue) and O_2-ALD ZnO (red). Reducing the exit angle of the photoelectrons with respect to the detector increases the surface sensitivity of the measurements.

stoichiometric value of 1.0 over a wide range. Only directly at the surface the composition seems to increase slightly, resulting in zinc-rich conditions. The opposite is the case for photoemission normal to the surface, where the [Zn]:[O] ratio suddenly drops to a value around 0.90. If this decrease originates from oxygen-rich conditions deeper in the material or is due to inaccuracy of the measurement and quantification process is not clear at this moment.
The composition depth profile of the O_2-ALD grown sample yields even more unclear results. The composition at the surface and deep in the film seems to be oxygen-rich, while in between the composition drops to a value of [Zn]:[O] = 0.70. The scattering of the data indicates an increased error of the AR-XPS results in case of O_2-ALD and therefore, the AR-XPS analysis of the ZnO layers seem not to provide reliable depth information about the film composition.

The depth profile of the combined Auger parameter is shown in Fig. 6.16 (b). These results look much more reliable than the composition depth profile. There is only slight scattering of the data and the determined Auger parameters for both ZnO films lie on top of each other at a value of 2009.8 eV. This value is exactly the one determined earlier for both precursor combinations. It does not show any depth dependence and that is why it is expected that the local chemical environment of the zinc component of the ZnO film does not change strongly, but remains constant in the depth region under investigation.
Fig. 6.16 (c) shows the results of the O 1s analysis. There, the ratio of the high binding energy component (i.e. $[O_2^{2-}]$ in case of O_2-ALD and $[O_{-OH}]$ for H_2O-ALD) and the $[O^{2-}]$ oxygen is plotted against the information depth. In case of water as oxygen precursor, the amount of hydroxides deeper in the ZnO crystal is about 35 % of the $[O^{2-}]$ component. This corresponds to 26 % of the total amount of oxygen in the zinc oxide layer, as shown earlier. Closer to the surface, a constant increase of the amount of hydroxides is observed, reaching a level of 45 % with respect to the $[O^{2-}]$ oxygen and accordingly 30 % of the total amount of oxygen in the ZnO. This is just a statistical value, but indicates the tendency of hydroxides being located more at the surface than in the bulk of the ZnO. In case of O_2-ALD the scattering of the data is increased with respect to the H_2O-ALD data. Photoelectrons emitted from deeper regions of the ZnO (exit angles between $90 - 70°$) show a similar ratio of the two oxygen components as in case of water-ALD. In contrast, the depth profile of the oxygen ratio is not as constant as the one for H_2O-ALD. Similar as in composition analysis shown above, the information content of the O_2-ALD depth profile is not very reliable.

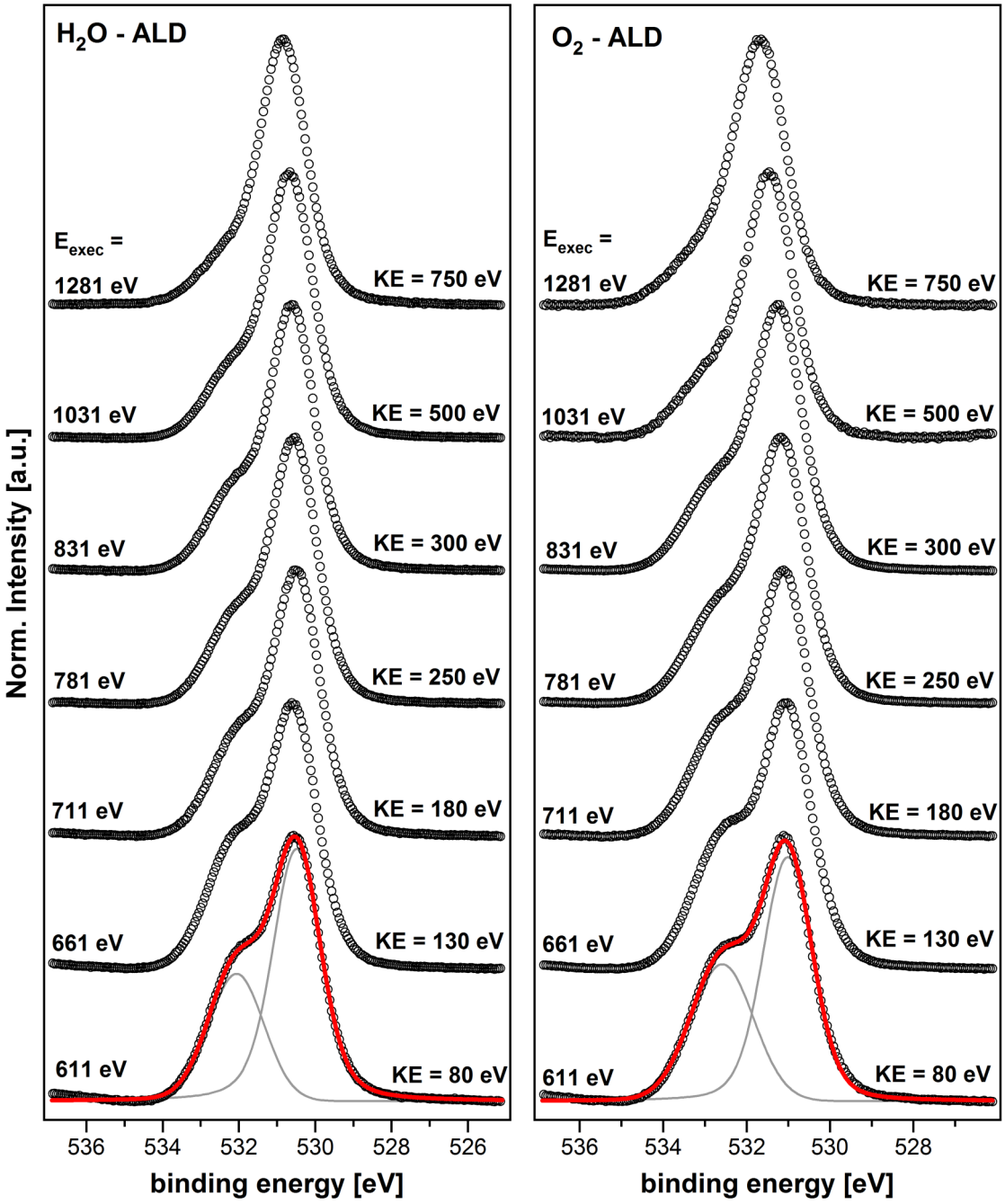

Figure 6.17: Depth-profiles of the O 1s photoelectrons of H_2O-ALD (left) and O_2-ALD (right). Changing the excitation energy results in different IMFPs of the photoelectrons and therefore containing depth information of the particular element under investigation.

From the results just presented follows that we have to proof whether this inaccuracy is caused by the sample itself or due to erroneous acquisition of the data during the measurements. Therefore, the same samples investigated in the laboratory were transferred under ultra-high vacuum conditions to the U49/2-PGM2 beamline of the BESSY II synchrotron radiation facility. Using synchrotron radiation it is possible to acquire depth profiling in two different ways. One the one hand, the analytic system allows to do angle-dependent measurements using constant excitation energy as in case of AR-XPS measurements at the Integrated System. Its advantage over Al Kα radiation used in the laboratory is the possibility of choosing a constant kinetic energy of each element's photoelectrons by choosing different excitation energies. Having same kinetic energies, the inelastic mean free path is the same for all photoelectrons, independent on their binding energies. Thus, all photoelectrons detected are created at same depths and hence are better to compare with each other.

The second possibility of recording a depth profile using synchrotron radiation is to vary the excitation energy at normal emission from the surface. Thus, the information depth where photoelectrons are emitted from is changed resulting in depth profiles of the particular elements. To distinguish between those two synchrotron-based depth profiling methods, the term *angle-resolved photoelectron spectroscopy* (AR-PES) depth profiling is used in case of changing the exit angle of the detected photoelectrons. In contrary, if the kinetic energy of the photoelectrons is varied under normal emission with respect to the surface, we use the general term *synchrotron-radiation photoelectron spectroscopy* (SR-PES) depth profiling.

Fig. 6.17 shows such a series of O 1s spectra recorded by SR-PES, varying the kinetic energy of the emitted photoelectrons between 80 and 750 eV. On the left, the spectra of H_2O-ZnO are presented, while the spectra on the right show an O_2-ALD ZnO film. The energy range is limited by two factors. For high kinetic energies, the signal intensity drops significantly due to the reduced photoionization cross-section at high excitation energies. In addition, the maximum excitation energy of the U49/2-PGM2 beamline is limited to 1890 eV. Hence, 750 eV is the highest kinetic energy that can be achieved for Zn $2p_{3/2}$ with its binding energy of about 1021 eV. The excitation of lower kinetic energy electrons is not limited by the beamline, but by the increasing amount of secondary electron background for such low kinetic energies. At kinetic energies below 80 eV, a background removal of the secondary electrons just using a Shirley routine is not sufficient and therefore 80 eV is chosen as the lower limit for the depth profiling experiments. In terms of inelastic

mean free paths, the depth information can be varied between 21.5 Å and 7.8 Å using this method. The maximum intensity of the $[O^{2-}]$ peak of the spectra plotted in Fig. 6.17 is normalized to 1. Two peaks are fitted, related to $[O^{2-}]$ and either $[O_{-OH}]$ or $[O_2^{2-}]$, as demonstrated for the 80 eV photoemission spectrum in Fig. 6.17.
To reduce the surface sensitivity even more, AR-PES depth profiling at the same samples was carried out. A kinetic photoelectron energy of 200 eV was chosen. At the one hand, at this energy there are no Auger features overlapping the photoemission peak. On the other hand, the secondary electron background is still removable by using a Shirley routine. The smallest achievable exit angle of the photoelectrons was 15° with respect to the electron detector. This results in information depths of 11.4 Å at normal emission and decreases down to 2.9 Å for flat angles.

The evaluation of the O 1s depth-profiling in terms of the $[O^{-}] : [O^{2-}]$ ratio is presented in Fig. 6.18. Here, the results for both synchrotron-based depth profiling methods are combined. The left column of Fig. 6.18 presents the more surface sensitive AR-PES results for both oxidizing agents. In addition, the right column illustrates the SR-PES depth profiles containing information from deeper regions of the material.
The upper part of Fig. 6.18 presents the standard ZnO-ALD layers using water as oxygen precursor, while the O_2-ALD ZnO film is shown on the lower part. The filled circles indicate the data of the as-grown ZnO samples and are discussed first for the case of H_2O-ALD. The corresponding depth-profiles of the $[O_{-OH}] : [O^{2-}]$ ratio are plotted in Fig. 6.18 (a) and (b), respectively. The AR-PES results show a very constant distribution of the $[O_{-OH}]$ in a region directly at the surface. Here, the number of hydroxides amount to 60 % of the $[O^{2-}]$ oxygen corresponding to 38 % of the total amount of oxygen in the ZnO. At a depth of about 11 Å the amount of $[O_{-OH}]$ starts decreasing constantly with respect to the $[O^{2-}]$ oxygen component as the data of Fig. 6.18 (b) show. The kink visible in the $[O_{-OH}] : [O^{2-}]$ AR-PES depth profile at approximately 11 Å is also observed for the depth profile using the SR-PES method. This is giving an indication that the two methods are providing reliable and consistent results of the material under investigation.
The open circles in Fig. 6.18 represent the same samples after an annealing for one hour at approximately 500 °C. As expected, the amount of hydroxides at the surface is reduced significantly by 20 % with respect to the $[O^{2-}]$ component. Interestingly, deeper in the material (starting around 14 Å) the amount of hydroxides is not reduced but remains constant at the level before annealing. This indicates, that only the hydroxides located directly at the surface are removed, but those buried deeper in the material are not subject to any changes.

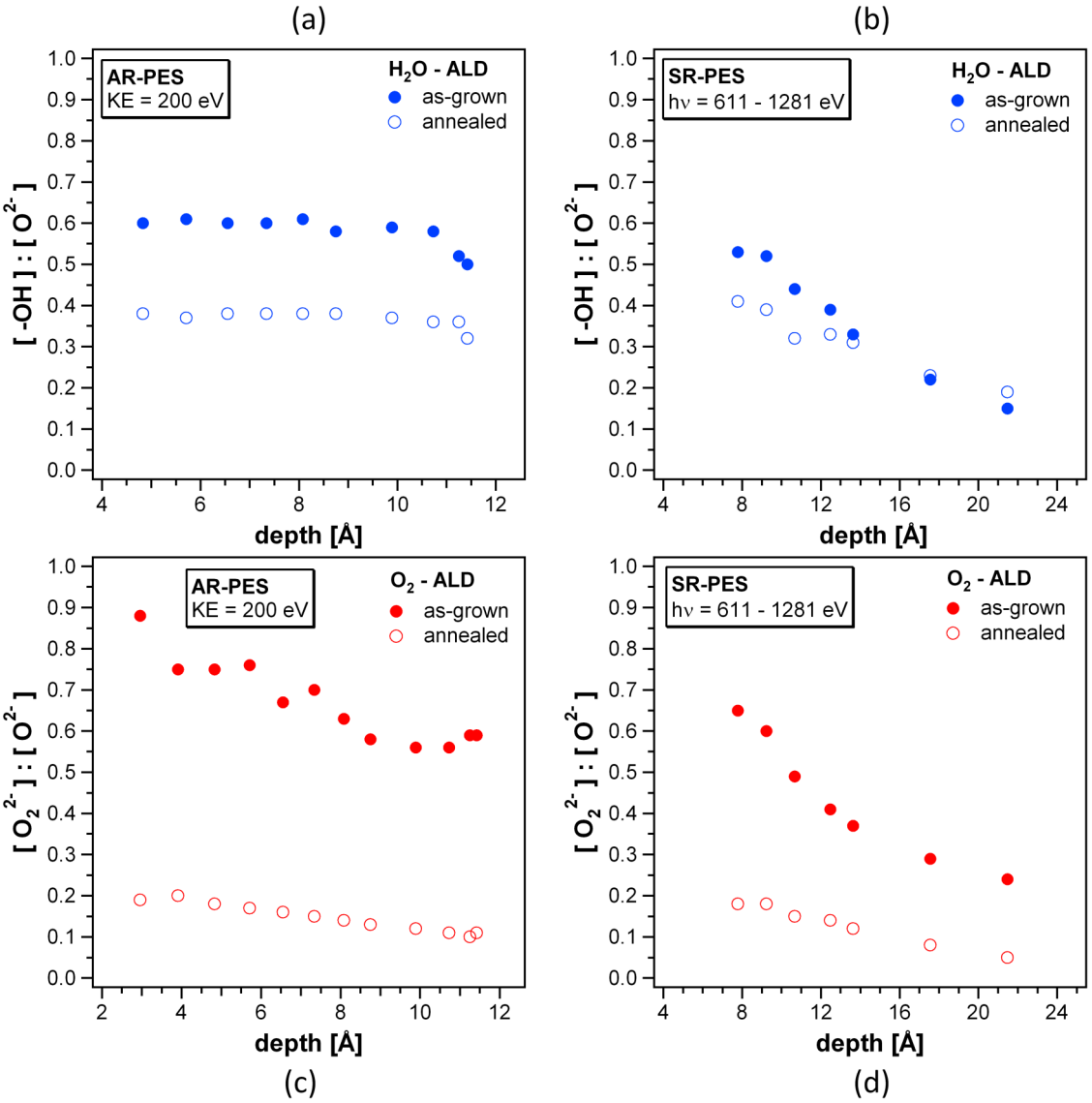

Figure 6.18: Depth-profiling results of the O 1s of H_2O-ZnO and O_2-ZnO investigated by synchrotron radiation before and after annealing the samples. Using different depth-profiling methods, information from different depth-regions can be investigated.

The depth profiling results of the O_2-ALD ZnO show a different picture of the $[O_2^{2-}]$:$[O^{2-}]$ ratio, presented in Fig. 6.18 (c) and (d). In contrast to H_2O-ALD, where a constant amount of hydroxides is distributed over the first atomic layers, the number of $[O_2^{2-}]$ dumbbell oxygen is strongly increased. While the number of hydroxides in the H_2O-ZnO account for approx. 38 % of the total amount of oxygen in the ZnO, almost every second oxygen species at the surface of O_2-ALD ZnO belongs to dumbbell oxygen. Instead

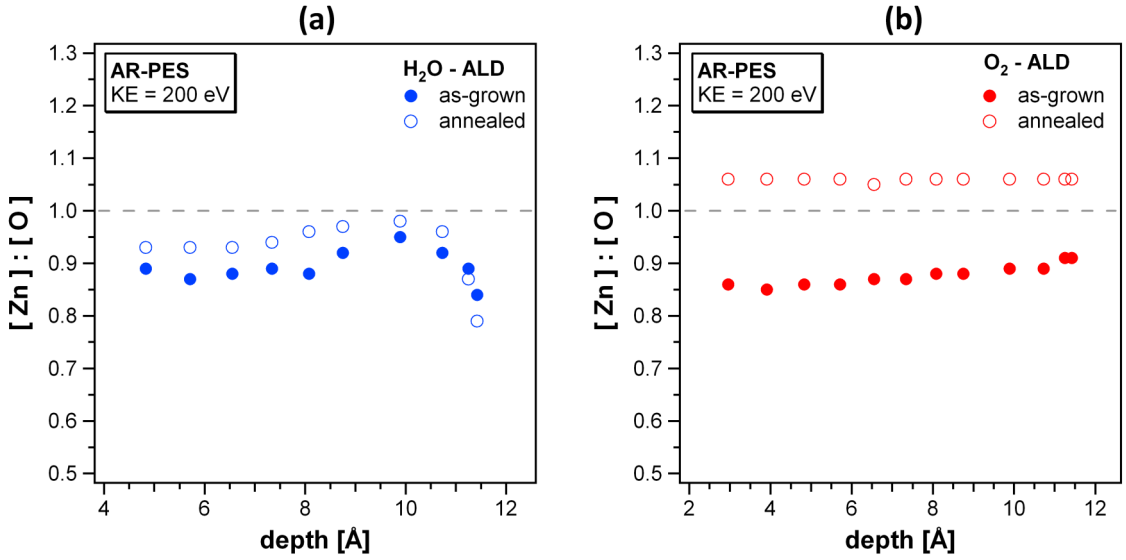

Figure 6.19: Depth-profile of the two ALD-ZnO films using different oxygen precursors. (a) presents the depth-dependent [Zn]:[O] ratio of the as-grown and annealed H_2O-ALD film, respectively, while (b) illustrates the O_2-ALD ZnO layer.

of a constant distribution as in case of the hydroxides, the concentration of dumbbell oxygen constantly decreases going deeper into the material. As in case of H_2O-ZnO, an equilibrium of the $[O_2^{2-}]$ concentration with respect to the $[O^{2-}]$ is not observed.

Annealing of the sample has a clearly increased effect on the oxygen dumbbell defect as on the hydroxides. While the number of hydroxides were were decreased by 20 % with respect to the $[O^{2-}]$ component, the oxygen dumbbell defects are strongly reduced after annealing the sample for one hour at 500 °C. Furthermore, the remaining defects are distributed more uniformly into the crystal. In contrast to the hydroxide oxygen, the dumbbell defects are not only reduced at the surface but also deeper in the material, where they almost completely disappear after annealing. Hence, it is believed that during the annealing process the interstitial dumbbell oxygen is incorporated into the ZnO crystal lattice. This results in a reduced amount of dumbbell defects and indicates the formation of ideal wurtzite ZnO shown in Fig. 6.14.

In addition to the O 1s photoemission, the zinc component of the two ZnO films has been depth-profiled by the AR-PES method. This allows to determine depth-dependent composition profiles of the ZnO films. For H_2O-ZnO, the [Zn]:[O] depth-profiles for the as-deposited and the annealed film are shown in Fig. 6.19 (a), whereas the O_2-ZnO case

is illustrated in Fig. 6.19 (b). Ideal stoichiometric composition is indicated by the dashed line in both plots. Again, the data of the annealed layers are illustrated by open circles. For the as-grown H_2O-ZnO in Fig. 6.19 (a), a surface composition of 0.9 is determined, i.e. the film is slightly oxygen-rich. Deeper in the material, a considerable change of the film's composition is observed. In this region around 10 Å, the films is closer to stoichiometry, but still slightly oxygen-rich. At even deeper regions, the ZnO composition again changes to more oxygen-rich conditions. Annealing of the sample did not change its composition characteristics. As expected, the film turns more stoichiometric at the surface due to the removal of surface hydroxides. In agreement with the O 1s depth-profiling results presented in Fig. 6.18, the composition remains constant deeper in the material, also showing the characteristic compositional change deeper in the material. It is assumed that these variations in composition originate from undefined deviations during the deposition process and does not represent all ZnO films grown by atomic layer deposition using water as oxidizing agent.

The zinc oxide film deposited by O_2-ALD does not show such variations in the composition depth-profile. The as-deposited ZnO shows a comparable surface composition to the H_2O-ALD ZnO of [Zn]:[O] ≈ 0.9, slightly increasing towards a more stoichiometric composition deeper in the material. As previously shown, the interstitial oxygen is drastically reduced during annealing of the sample. Above it was assumed that the interstitial dumbbell oxygen is incorporated into the ZnO crystal. If this is the case, it should result in an observed composition close to the stoichiometric value of [Zn]:[O] = 1.00. Surprisingly, this is not the case. Fig. 6.19 (b) clearly reveals that the composition of the ZnO film even turns zinc-rich after annealing. A constant composition of [Zn]:[O] = 1.06 is determined throughout the whole information depth of the AR-PES depth profiling experiments. This might be explained by not only incorporating the oxygen in the ZnO lattice, but the complete removal of those dumbbell structures from the crystal. This would result in oxygen vacancies [V_O]. As mentioned in the beginning of this chapter, oxygen vacancies are one of those point defects that are believed to prevent p-type doping of the ZnO. This would also explain, why there was no change observed in the valence band structure of the annealed O_2-ZnO in Fig. 6.12.

6.4 Summary

In this chapter, the first successful study of a **water-free ZnO ALD process** using pure O_2 as oxidizing precursor and organo-metallic DEZn as metal-precursor has been presented. Even though Nalwa et al. stated that molecular O_2 is too inert to react with an organometallic precursor[54], it was shown that this is obviously not the case for the reaction O_2 + $Zn(C_2H_5)_2$. Instead, the typical self-limited ALD growth behavior was demonstrated. A strong **increase in growth rate** in the ALD window temperature regime that is close to one completed ZnO monolayer per ALD cycle was observed. This indicates a completely different reaction mechanism that is **not limited by steric hindrance** effects of the ethyl-ligands. Further evidence of the differences in growth mechanism is given by the appearance of two additional carbon features in the photoelectron spectra. These are attributed to hydrocarbons and carbon in a carboxylic environment, respectively.

Investigation of the **initial growth on Si(111)-H** show no significant differences between the ZnO films using H_2O and O_2 precursors. As in case of H_2O-ALD, a second feature at high binding energies of the [O^{2-}] lattice oxygen is present in the O 1s photoemission spectra. While using water as oxygen precursor the second component clearly can be attributed to hydroxide oxygen, its origin is not clear in case of O_2-ALD.

To identify the additional oxygen component, the two particular ZnO films were investigated at the synchrotron radiation facility BESSY II. Photoelectron spectroscopy in the laboratory and non-destructive depth-profiling of the as-deposited and annealing samples at the BESSY II suggest the high binding energy oxygen component originating from an **interstitial dumbbell defect** as stated by Erhart et al.[114;117]. Heat treatment of the samples not only removes the surface carbon contamination but almost completely removes the interstitial oxygen defects by incorporation into the ZnO lattice. While the H_2O-ZnO films usually are oxygen-rich, the annealed O_2-ZnO ALD films show a slightly zinc-rich composition. This, and the similarities of the valence bands indicate the presence of oxygen vacancies in case of annealed O_2-ZnO. Depth-profiling reveals that the composition is spread across the information depth observable by synchrotron radiation depth-profiling very homogeneously. Hence, the water-free ALD of ZnO can be regarded being successful producing films of the same qualities as the standard ALD films.

7 Conclusion and Outlook

Atomic layer deposition is possibly the most promising technique for alternative buffer layer deposition in chalcopyrite solar cell production. Not only its potential of depositing high-quality material films with utmost film conformity even in the monolayer thickness regime, but also the promising results in terms of solar cell efficiency shown by other research groups in the recent years.

The primary goal of this thesis was the investigation of the interface formation and characterization of the interface's electronic properties between ZnO and $CuInSe_2$, grown epitaxially in the (112) orientation. Since all experiments performed in this thesis are very surface sensitive, any surface modifications have to be prevented until the sample was characterized by photoelectron spectroscopy. Hence, all deposition and analysis experiments were performed under ultra-high vacuum conditions without exposing the samples to air. For this purpose, a UHV-compatible ALD reactor was designed, assembled and commissioned for the deposition of zinc oxide using the standard precursor combination diethylzinc and water as reactive gases. The attachment of the atomic layer deposition chamber to the integrated deposition and analysis system in the laboratory allows in situ measurements of the specimen. It has been demonstrated that the deposition system shows the characteristic self-limited film growth in a temperature regime between approximately $200 - 225$ °C, the so-called *ALD window*. In this temperature regime, a constant deposition rate of 3.0 Å per ALD cycle is observed. Characterization of stepwise deposited ZnO films clearly reveal a layer-by-layer growth mode as it is expected for atomic layer deposition. The initial growth of ZnO on hydrogen-terminated Si(111)-H substrates indicate an oxygen-rich interface formation of the ZnO films, but does not show any oxidation of the subjacent silicon. After having the thickness of a few monolayers, the [Zn]:[O] ratio shows stoichiometric composition of the zinc oxide films.

After demonstrating successful ZnO atomic layer deposition, the interface formation of ZnO and epitaxial $CuInSe_2$ (112) was investigated. Earlier studies already investigated the ZnO deposition by metal-organic molecular beam epitaxy (MOMBE) on epitaxial chalcopyrite absorbers. In contrast to ALD, the MOMBE process exposes the sample to the two precursor gases simultaneously and the deposition takes place at significantly higher substrate temperatures. Photoemission spectroscopy results indicated the formation of an intrinsically formed ZnSe interface layer between $CuInSe_2$ and ZnO. The formation mechanism is believed to be induced by self-compensation effects on doping the chalcopyrite. Self-compensation results in the formation of Cu vacancies, while the copper diffuses away from the surface at the same time. An intrinsic interface formation is also found in this study, even though some major differences are observed either due to the lower substrate's temperature or the differing growth kinetics of the ALD process. On the one hand, instead of ZnSe a $ZnIn_2Se_4$ (ZISe) layer forms at the interface of $CuInSe_2$ and ALD-ZnO. Its layer thickness is considerably reduced in case of atomic layer deposition. While in the MOMBE case the buffer layer thickness was determined being 2 nm, Auger parameter analysis of the zinc component clearly reveals a $ZnIn_2Se_4$ thickness of only 0.5 nm, i.e. the range of one monolayer. Photoelectron spectroscopy indicates a promising effect of the intrinsic ZISe buffer layer on the electronic band alignment of the $CuInSe_2|ZnIn_2Se_4|ZnO$ system for chalcopyrite thin-film solar cell devices. In addition, MOMBE results showed a completely oxygen-free ZnSe buffer layer, while during the ALD process small amounts of hydroxide are found in the boundary layer. Their incorporation into the ZISe are most likely to be explained by the sequential deposition mode of the precursor gases in atomic layer deposition. According to several other studies, buffer layers containing considerable amounts of hydroxides, such as Zn(OH,Se), Zn(OH,S) or In(OH,S), show increased solar cell efficiencies. Hence, the additional hydroxide oxygen found in the intrinsically formed buffer layer is a very interesting result of this study. Annealing experiments of ZnO deposited on $CuInSe_2$ indicated the same indium diffusivity as in case of MOMBE ZnO deposition. This indium diffusion might also have beneficial effects on the device efficiencies, since it can reduce interfacial defects and hence lower possible interface recombination of the electrons.

In the final chapter of this thesis, successful water-free atomic layer deposition using metal-organic diethylzinc and molecular oxygen (O_2) has been demonstrated for the first time. A water-free ZnO-ALD process might be able to reduce the amount of interstitial hydrogen atoms acting as donors in ZnO. Just like the standard ALD precursor combination of diethylzinc and water, water-free atomic layer deposition shows the typical self-limited de-

position rate behavior in the temperature regime known as the ALD window. In contrast, the deposited amount of material per ALD cycle is significantly increased to 5.0 Å/cycle, i.e. almost one complete ZnO monolayer per ALD cycle. While in standard ALD, steric hindrance effects of the ethyl ligands are responsible for a limitation of the growth rate, the high deposition rate in water-free ALD indicate a completely different growth mechanism. This is also emphasized by the appearance of two additional carbon features observed in photoelectron spectroscopy. Those are attributed to hydrocarbons and carbon in an carboxylic environment and can be removed almost completely by annealing the samples. While the initial growth on Si(111)-H does not show significant differences to H_2O-ALD, the origin of a second oxygen component visible in the photoemission spectra is not likely originating from hydroxides. Instead, non-destructive depth profiling and annealing experiments at the BESSY II synchrotron radiation source led to the conclusion that this additional oxygen component originates from oxygen-dumbbell defects, that are almost complete removed after annealing the samples for 1 hour at 500 °C. In contrast to H_2O-ALD, the annealed ZnO films grown by water-free ALD show a slightly zinc-rich composition and synchrotron-radiation depth profiling indicates very conformal ZnO layers. Hence, water-free ALD of ZnO using diethylzinc and molecular oxygen do not show any structural, chemical or electronic disadvantages to the standard precursor combination.

Outlook

After successful demonstration of water-free atomic layer deposition of zinc oxide in this thesis, further work on the fundamental properties of those layers are of interest. Like several other wide band gap materials, ZnO is naturally n-doped and it is very difficult to obtain an effective and reproducible p-type doping. This is mainly resulting from compensation effects of point defects such as interstitial zinc atoms or oxygen vacancies. But also intrinsic hydrogen might play a crucial role, as it acts as an donor in the zinc oxide crystal. In atomic layer deposition of ZnO, water is often used as oxygen source in the oxidizing half-reaction. Preventing the use of water, which acts as a hydrogen source, might result in reduced amounts of hydrogen in the ZnO crystal. It is recommended to investigate if this is the case in water-free ALD zinc oxide layers in future work.

Bibliography

[1] REN21. Renewables 2011 Global Status Report, 2011.

[2] Razykov, T., Ferekides, C., Morel, D., Stefanakos, E., Ullal, H. and Upadhyaya, H. Solar photovoltaic electricity: Current status and future prospects. *Solar Energy*, 85 (8), (2011), pp. 1580 – 1608. ISSN 0038-092X.

[3] ZSW Press Release 10/2011; `http://www.zsw-bw.de/fileadmin/ZSW_files/Infoportal/Presseinformationen/docs/pi11-2010-e_ZSW-Weltrekord-DS-CIGS.pdf`.

[4] Kasap, S., Koughia, C., Ruda, H. and Johanson, R. Electrical Conduction in Metals and Semiconductors. In S. Kasap and P. Capper (Editors), *Springer Handbook of Electronic and Photonic Materials*, pp. 19–45 (Springer, 2007). ISBN 978-0-387-29185-7.

[5] Rockett, A. Current status and opportunities in chalcopyrite solar cells. *Current Opinion in Solid State and Materials Science*, 14 (6), (2010), pp. 143–148. ISSN 1359-0286.

[6] Rau, U. and Schock, H.W. Cu(In,Ga)Se_2 thin-film solar cells. In T. Markvart and L. Castañer (Editors), *Solar Cells*, pp. 303–349 (Elsevier Science, Oxford, 2005).

[7] Shay, J. and Wernick, J. *Ternary chalcopyrite semiconductors: growth, electronic properties, and applications*. International series of monographs in the science of the solid state (Pergamon Press, 1975). ISBN 978-0-080-17883-7.

[8] Zhang, S.B., Wei, S.H., Zunger, A. and Katayama-Yoshida, H. Defect

physics of the $CuInSe_2$ chalcopyrite semiconductor. *Phys. Rev. B*, 57 (16), (1998), pp. 9642–9656.

[9] Hofmann, A. *Elektronische Struktur epitaktischer $CuInSe_2$-Schichten und deren Heterokontakte für die Photovoltaik*. Ph.D. thesis, Brandenburgische Technische Universität Cottbus, 2011.

[10] Hariskos, D., Spiering, S. and Powalla, M. Buffer layers in $Cu(In,Ga)Se_2$ solar cells and modules. *Thin Solid Films*, 480-481, (2005), pp. 99–109. ISSN 0040-6090.

[11] Bhattacharya, R. and Ramanathan, K. $Cu(In,Ga)Se_2$ thin film solar cells with buffer layer alternative to CdS. *Solar Energy*, 77 (6), (2004), pp. 679 – 683.

[12] King, P.D.C., Veal, T.D., Fuchs, F., Wang, C.Y., Payne, D.J., Bourlange, A., Zhang, H., Bell, G.R., Cimalla, V., Ambacher, O., Egdell, R.G., Bechstedt, F. and McConville, C.F. Band gap, electronic structure, and surface electron accumulation of cubic and rhombohedral In_2O_3. *Physical Review B*, 79 (20), (2009), p. 205211.

[13] Spiering, S., Eicke, A., Hariskos, D., Powalla, M., Naghavi, N. and Lincot, D. Large-area Cd-free CIGS solar modules with In_2S_3 buffer layer deposited by ALCVD. *Thin Solid Films*, 451-452 (0), (2004), pp. 562 – 566. ISSN 0040-6090. Proceedings of Symposium D on Thin Film and Nano-Structured Materials for Photovoltaics, of the E-MRS 2003 Spring Conference.

[14] Yousfi, E.B., Weinberger, B., Donsanti, F., Cowache, P. and Lincot, D. Atomic layer deposition of zinc oxide and indium sulfide layers for $Cu(In,Ga)Se_2$ thin-film solar cells. *Thin Solid Films*, 387 (1-2), (2001), pp. 29 – 32. ISSN 0040-6090.

[15] Platzer-Björkman, C. $Zn(O,S)$ buffer layers by atomic layer deposition in $Cu(In,Ga)Se_2$ based thin film solar cells: Band alignment and sulfur gradient. *Journal of Applied Physics*, 100 (4), (2006), p. 044506.

[16] Yousfi, E.B., Asikainen, T., Pietu, V., Cowache, P., Powalla, M. and Lincot, D. Cadmium-free buffer layers deposited by atomic later epitaxy for

copper indium diselenide solar cells. *Thin Solid Films*, 361-362, (2000), pp. 183 – 186. ISSN 0040-6090.

[17] Platzer-Björkman, C., Lu, J., Kessler, J. and Stolt, L. Interface study of $CuInSe_2$/ZnO and Cu(In,Ga)Se_2/ZnO devices using ALD ZnO buffer layers. *Thin Solid Films*, 431-432 (0), (2003), pp. 321 – 325. ISSN 0040-6090. Proceedings of Symposium B, Thin Film Chalcogenide Photovoltaic Materials, E-MRS Spring Meeting.

[18] Contreras, M.A., Egaas, B., Ramanathan, K., Hiltner, J., Swartzlander, A., Hasoon, F. and Noufi, R. Progress toward 20% efficiency in Cu(In,Ga)Se_2 polycrystalline thin-film solar cells. *Progress in Photovoltaics: Research and Applications*, 7 (4), (1999), pp. 311–316.

[19] Janotti, A. and van de Walle, C.G. Fundamentals of zinc oxide as a semiconductor. *Reports on Progress in Physics*, 72 (12), (2009), p. 126501.

[20] Özgür, U., Alivov, Y.I., Liu, C., Teke, A., Reshchikov, M.A., Dogan, S., Avrutin, V., Cho, S.J. and Morkoc, H. A comprehensive review of ZnO materials and devices. *Journal of Applied Physics*, 98 (4), 041301.

[21] Andres, S., Lehmann, C. and Pettenkofer, C. Epitaxial growth of ZnO on $CuInS_2$(112). *Thin Solid Films*, 518 (4), (2009), pp. 1032 – 1035.

[22] Hofmann, A. Surface orientation dependent band alignment for $CuInSe_2$ - ZnSe - ZnO. *Applied Physics Letters*, 98 (11), (2011), p. 113503.

[23] Rockett, A., Abou-Elfotouh, F., Albin, D., Bode, M., Ermer, J., Klenk, R., Lommasson, T., Russell, T., Tomlinson, R., Tuttle, J., Stolt, L., Walter, T. and Peterson, T. Structure and chemistry of $CuInSe_2$ for solar cell technology: current understanding and recommendations. *Thin Solid Films*, 237 (1-2), (1994), pp. 1 – 11. ISSN 0040-6090.

[24] Einstein, A. Über einen die Erzeugung und Verwandlung des Lichtes betreffenden heuristischen Gesichtspunkt. *Annalen der Physik*, 322 (6), (1905), pp. 132–148.

[25] Hüfner, S. *Photoelectron Spectroscopy - Principles and Applications* (Springer,

2003), 3rd edn.

[26] Bubert, H. and Rivière, J.C. *Surface and Thin Film Analysis* (Wiley-VCH Verlag GmbH, 2002). ISBN 978-3-527-60016-8.

[27] Ratner, B.D. and Castner, D.G. *Surface Analysis - The Principal Techniques*, chap. Electron Spectroscopy for Chemical Analysis, pp. 47–112 (John Wiley & Sons, Ltd, 2009). ISBN 978-0-470-72158-2.

[28] Alford, T., Feldman, L. and Mayer, J. X-ray Photoelectron Spectroscopy. In *Fundamentals of Nanoscale Film Analysis*, pp. 199–213 (Springer US, 2007). ISBN 978-0-387-29261-8.

[29] NIST X-ray Photoelectron Spectroscopy Database, Version 3.5 (National Institute of Standards and Technology, Gaithersburg, 2003; `http://srdata.nist.gov/xps/`.

[30] Wagner, C. and Joshi, A. The Auger Parameter, its Utility and Advantages: A Review. *Journal of Electron Spectroscopy and Related Phenomena*, 47, (1988), pp. 283 – 313. ISSN 0368-2048.

[31] Schön, G. Auger and direct electron spectra in X-ray photoelectron studies of zinc, zinc oxide, gallium and gallium oxide. *Journal of Electron Spectroscopy and Related Phenomena*, 2 (1), (1973), pp. 75 – 86. ISSN 0368-2048.

[32] UK Surface Analysis Forum, `http://www.uksaf.org/data/table.html`.

[33] Moretti, G. Auger parameter and Wagner plot in the characterization of chemical states by X-ray photoelectron spectroscopy: a review. *Journal of Electron Spectroscopy and Related Phenomena*, 95 (2-3), (1998), pp. 95 – 144. ISSN 0368-2048.

[34] Seah, M.P. and Dench, W.A. Quantitative electron spectroscopy of surfaces: A standard data base for electron inelastic mean free paths in solids. *Surface and Interface Analysis*, 1 (1), (1979), pp. 2–11. ISSN 1096-9918.

[35] Shirley, D.A. High-Resolution X-Ray Photoemission Spectrum of the Valence Bands of Gold. *Physical Review B*, 5 (12), (1972), p. 4709.

[36] Wagner, C.D., Davis, L.E., Zeller, M.V., Taylor, J.A., Raymond, R.H. and Gale, L.H. Empirical atomic sensitivity factors for quantitative analysis by electron spectroscopy for chemical analysis. *Surface and Interface Analysis*, 3 (5), (1981), pp. 211–225. ISSN 1096-9918.

[37] Jablonski, A. and Zemek, J. Overlayer thickness determination by XPS using the multiline approach. *Surface and Interface Analysis*, 41 (3), (2009), pp. 193–204.

[38] Yeh, J. and Lindau, I. Atomic subshell photoionization cross sections and asymmetry parameters: $1 \leq Z \leq 103$. *Atomic Data and Nuclear Data Tables*, 32 (1), (1985), pp. 1 – 155. ISSN 0092-640X.

[39] Hove, M., Weinberg, W. and Chan, C. *Low-energy electron diffraction: experiment, theory and surface structure determination*. Springer series in surface sciences (Springer-Verlag, 1986). ISBN 978-3-540-16262-9.

[40] Pendry, J. *Low energy electron diffraction: the theory and its application to determination of surface structure*. Techniques of physics (Academic Press, 1974). ISBN 978-0-125-50550-5.

[41] Ertl, G. and Küppers, J. *Low energy electrons and surface chemistry* (VCH, 1985). ISBN 978-3-527-26056-0.

[42] Rockett, A. *The Materials Science of Semiconductors* (Springer Publishing Company, Incorporated, 2007), 1st edn. ISBN 978-0-387-25653-5.

[43] Ohring, M. *The Materials Science of Thin Films* (Academic Press, 2002).

[44] Gould, R. Thin Films. In S. Kasap and P. Capper (Editors), *Springer Handbook of Electronic and Photonic Materials*, pp. 659–716 (Springer, 2007). ISBN 978-0-387-29185-7.

[45] Klimova, A., Ananichev, V., Arif, M. and Blinov, L. Investigation of the Saturated Vapor Pressure of Zinc, Selenium, and Zinc Selenide. *Glass Physics and Chemistry*, 31, (2005), pp. 760–762. ISSN 1087-6596.

[46] Capper, P., Irvine, S. and Joyce, T. Epitaxial Crystal Growth: Methods and

Materials. In S. Kasap and P. Capper (Editors), *Springer Handbook of Electronic and Photonic Materials*, pp. 271–301 (Springer, 2007). ISBN 978-0-387-29185-7.

[47] Knudsen, M. Die Gesetze der Molekularströmung und der inneren Reibungsströmung der Gase durch Röhren. *Annalen der Physik*, 333 (1), (1909), pp. 75–130. ISSN 1521-3889.

[48] Hampden-Smith, M.J. and Kodas, T.T. Chemical vapor deposition of metals: Part 1. An overview of CVD processes. *Chemical Vapor Deposition*, 1 (1), (1995), pp. 8–23. ISSN 1521-3862.

[49] Carlsson, J.O. and Martin, P.M. Chemical Vapor Deposition. In P.M. Martin (Editor), *Handbook of Deposition Technologies for Films and Coatings (Third Edition)*, pp. 314 – 363 (William Andrew Publishing, Boston, 2010). ISBN 978-0-815-52031-3.

[50] Putz, N., Veuhoff, E., Heinecke, H., Heyen, M., Luth, H. and Balk, P. GaAs Growth In Metal-Organic MBE. *Journal of Vacuum Science & Technology B*, 3 (2), (1985), pp. 671–673.

[51] Andres, S., Pettenkofer, C., Speck, F. and Seyller, T. Morphology and electronic properties of metal organic molecular beam epitaxy grown ZnO on hydrogen passivated 6H-SiC(0001). *Journal of Applied Physics*, 103 (10), (2008), p. 103720.

[52] US Patent No. 4,058,430, 1977.

[53] George, S.M. Atomic Layer Deposition: An Overview. *Chemical Reviews*, 110 (1), (2010), pp. 111–131. ISSN 0009-2665.

[54] Ritala, M. and Leskelä, M. *Atomic Layer Deposition* (Academic Press, Burlington, 2002). ISBN 978-0-12-512908-4.

[55] Puurunen, R.L. Surface chemistry of atomic layer deposition: A case study for the trimethylaluminum/water process. *Journal of Applied Physics*, 97 (12), 121301.

[56] Suntola, T. Atomic Layer Epitaxy. *Materials Science Reports*, 4 (5), (1989), pp.

265–312. ISSN 0920-2307.

[57] Puurunen, R. Growth Per Cycle in Atomic Layer Deposition: Real Application Examples of a Theoretical Model. *Chemical Vapor Deposition*, 9 (6), (2003), pp. 327–332. ISSN 1521-3862.

[58] Kuniya, Y., Deguchi, Y. and Ichida, M. Physicochemical properties of dimethylzinc, dimethylcadmium and diethylzinc. *Applied Organometallic Chemistry*, 5 (4), (1991), pp. 337–348. ISSN 1099-0739.

[59] Fulem, M., Ruzicka, K., Ruzicka, V., Hulicius, E., Simecek, T., Melichar, K., Pangrác, J., Rushworth, S.A. and Smith, L.M. Vapor pressure of metal organic precursors. *Journal of Crystal Growth*, 248, (2003), pp. 99 – 107.

[60] NIST Chemistry WebBook, 2011; `http://webbook.nist.gov/chemistry/`.

[61] Stull, D. Vapor Pressure of Pure Substances Organic Compounds. *Industrial & Engineering Chemistry*, 39, (1947), pp. 517–540.

[62] Bridgeman, O. and Aldrich, E. Vapor Pressure Tables for Water. *Journal of Heat Transfer*, 86, (1964), pp. 279–286.

[63] Kopalko, K., Godlewski, M., Domagala, J.Z., Lusakowska, E., Minikayev, R., Paszkowicz, W. and Szczerbakow, A. Monocrystalline ZnO Films on GaN/Al_2O_3 by Atomic Layer Epitaxy in Gas Flow. *Chemistry of Materials*, 16 (8), (2004), pp. 1447–1450.

[64] Mar, L.G., Timbrell, P.Y. and Lamb, R.N. An XPS study of zinc oxide thin film growth on copper using zinc acetate as a precursor. *Thin Solid Films*, 223 (2), (1993), pp. 341 – 347. ISSN 0040-6090.

[65] Ye, J., Gu, S., Zhu, S., Liu, S., Liu, W., Zhou, X., Hu, L., Zhang, R., Shi, Y. and Zheng, Y. Comparative study of diethylzinc and dimethylzinc for the growth of ZnO. *Journal of Crystal Growth*, 274 (3-4), (2005), pp. 489 – 494. ISSN 0022-0248.

[66] Angermann, H., Henrion, W., Rebien, M. and Röseler, A. Wet-chemical passivation and characterization of silicon interfaces for solar cell applications. *Solar Energy Materials and Solar Cells*, 83 (4), (2004), pp. 331 – 346.

[67] Guziewicz, E., Kowalik, I.A., Godlewski, M., Kopalko, K., Osinniy, V., Wojcik, A., Yatsunenko, S., Lusakowska, E., Paszkowicz, W. and Guziewicz, M. Extremely low temperature growth of ZnO by atomic layer deposition. *Journal of Applied Physics*, 103 (3), 033515.

[68] Kim, S.K., Hwang, C.S., Park, S.H.K. and Yun, S.J. Comparison between ZnO films grown by atomic layer deposition using H_2O or O_3 as oxidant. *Thin Solid Films*, 478 (1-2), (2005), pp. 103 – 108. ISSN 0040-6090.

[69] Kim, D., Kang, H., Kim, J.M. and Kim, H. The properties of plasma-enhanced atomic layer deposition (ALD) ZnO thin films and comparison with thermal ALD. *Applied Surface Science*, 257 (8), (2011), pp. 3776 – 3779. ISSN 0169-4332.

[70] Park, S.H.K. and Lee, Y.E. Controlling preferred orientation of ZnO thin films by atomic layer deposition. *Journal of Materials Science*, 39, (2004), pp. 2195–2197. ISSN 0022-2461.

[71] Yamada, A., Sang, B. and Konagai, M. Atomic layer deposition of ZnO transparent conducting oxides. *Applied Surface Science*, 112, (1997), pp. 216 – 222. ISSN 0169-4332.

[72] PCPDFWIN Database.

[73] Matsubara, K., Fons, P., Yamada, A., Watanabe, M. and Niki, S. Epitaxial growth of ZnO thin films on $LiNbO_3$ substrates. *Thin Solid Films*, 347 (1-2), (1999), pp. 238 – 240. ISSN 0040-6090.

[74] Libralesso, L., Schroeder, T., Lee, T.L. and Zegenhagen, J. Initial stages of the epitaxial growth of Pr_2O_3 on Si(111) studied by LEED and STM. *Surface Science*, 598 (1-3), (2005), pp. L347–L354. ISSN 0039-6028.

[75] Brennan, B., McDonnell, S. and Hughes, G. Photoemission studies of the

initial interface formation of ultrathin MgO dielectric layers on the Si(111) surface. *Thin Solid Films*, 518 (8), (2010), pp. 1980 – 1984.

[76] Dupin, J.C., Gonbeau, D., Vinatier, P. and Levasseur, A. Systematic XPS studies of metal oxides, hydroxides and peroxides. *Physical Chemistry Chemical Physics*, 2 (6), (2000), pp. 1319–1324.

[77] Au, C., Roberts, M. and Zhu, A. Surface hydroxylation at a Zn(0001)-O surface. *Surface Science Letters*, 115 (2), (1982), pp. L117 – L123.

[78] Meier, U. and Pettenkofer, C. Morphology of the Si-ZnO interface. *Applied Surface Science*, 252 (4), (2005), pp. 1139 – 1146. ISSN 0169-4332.

[79] Moulder, J.F., Stickle, W.F. and Sobol, P.E. *Handbook of X Ray Photoelectron Spectroscopy* (Perkin-Elmer, Physical Electronics Division, 1992). ISBN 0962702625.

[80] Ueno, K. Heteroepitaxial growth of layered transition metal dichalcogenides on sulfur-terminated GaAs{111} surfaces. *Applied Physics Letters*, 56 (4), (1990), p. 327.

[81] Babu, P., Reddy, M.V., Revathi, N. and Reddy, K.T.R. Effect of pH on the Physical Properties of $ZnIn_2Se_4$ Thin Films Grown by Chemical Bath Deposition. *Journal of Nano- and Electronic Physics*, 3 (1), (2011), pp. 85 – 91.

[82] Ohtake, Y., Okamoto, T., Yamada, A., Konagai, M. and Saito, K. Improved performance of Cu(InGa)Se_2 thin-film solar cells using evaporated Cd-free buffer layers. *Solar Energy Materials and Solar Cells*, 49 (1-4), (1997), pp. 269 – 275. ISSN 0927-0248.

[83] Sun, X., He, Y. and Feng, J. Growth and characterization of $ZnIn_2Se_4$ buffer layer on $CuInSe_2$ thin films. *Journal of Crystal Growth*, 312 (1), (2009), pp. 48 – 51. ISSN 0022-0248.

[84] Hendia, T. and Soliman, L. Optical absorption behaviour of evaporated $ZnIn_2Se_4$ thin films. *Thin Solid Films*, 261 (1-2), (1995), pp. 322 – 327. ISSN 0040-6090.

[85] Choe, S.H. Optical energy gaps of undoped and Co-doped $ZnIn_2Se_4$ single crystals. *Current Applied Physics*, 9 (1), (2009), pp. 1 – 3.

[86] Margaritondo, G., Katnani, A.D. and LÃl'vy, F. Electronic States of $CdIn_2Se_4$ and $ZnIn_2Se_4$: Role of the Cation Pseudovacancies. *Physica Status Solidi B*, 103 (2), (1981), pp. 725–731. ISSN 1521-3951.

[87] Locmelis, S., Milke, E., Binnewies, M., Gruhl, S. and Vogt, C. Chemischer Transport fester Lösungen. 18 [1] Der Chemische Transport von $ZnIn_2S_4$, $ZnIn_2Se_4$ und $ZnIn_2S_{4-x}Se_x$-Mischphasen. *Zeitschrift für Anorganische und Allgemeine Chemie*, 631 (9), (2005), pp. 1667–1674. ISSN 1521-3749.

[88] Persson, C., Zhao, Y.J., Lany, S. and Zunger, A. n-type doping of $CuInSe_2$ and $CuGaSe_2$. *Physical Review B*, 72 (3), (2005), p. 035211.

[89] Desnica, U.V. Doping limits in II-VI compounds - Challenges, problems and solutions. *Progress in Crystal Growth and Characterization of Materials*, 36 (4), (1998), pp. 291 – 357.

[90] Klein, A. Fermi-level-dependent defect formation in Cu-chalcopyrite semiconductors. *Applied Physics Letters*, 74 (16), (1999), p. 2283.

[91] Klenk, R., Klaer, J., Köble, C., Mainz, R., Merdes, S., Rodriguez-Alvarez, H., Scheer, R. and Schock, H. Development of $CuInS_2$-based solar cells and modules. *Solar Energy Materials and Solar Cells*, 95 (6), (2011), pp. 1441 – 1445. ISSN 0927-0248. Special Issue : Thin film and nanostructured solar cells.

[92] Walukiewicz, W. Defect formation and diffusion in heavily doped semiconductors. *Physical Review B*, 50 (8), (1994), pp. 5221–5225.

[93] Van de Walle, C. Hydrogen as a cause of doping in zinc oxide. *Physical Review Letters*, 85 (5), (2000), pp. 1012–1015. ISSN 0031-9007.

[94] Friedrich, F. and Nickel, N.H. Resonant Raman scattering in hydrogen and nitrogen doped ZnO. *Applied Physics Letters*, 91 (11), (2007), p. 111903.

[95] Nickel, N.H. Hydrogen migration in single crystal and polycrystalline zinc oxide.

Physical Review B, 73 (19), (2006), p. 195204.

[96] Nickel, N.H. and Brendel, K. Hydrogen density-of-states distribution in zinc oxide. *Physical Review B*, 68 (19), (2003), p. 193303.

[97] Nickel, N.H. and Fleischer, K. Hydrogen Local Vibrational Modes in Zinc Oxide. *Physical Review Letters*, 90 (19), (2003), p. 197402.

[98] Kaiya, K., Yoshii, N., Takahashi, N. and Nakamura, T. Atmospheric pressure atomic layer epitaxy of ZnO on a sapphire (0001) substrate by alternate reaction of $ZnCl_2$ and O_2. *Journal of Materials Science Letters*, 19, (2000), pp. 2089–2090. ISSN 0261-8028.

[99] Göpel, W., Pollmann, J., Ivanov, I. and Reihl, B. Angle-resolved photoemission from polar and nonpolar zinc oxide surfaces. *Physical Review B*, 26 (6), (1982), p. 3144.

[100] Girard, R.T., Tjernberg, O., Chiaia, G., Söderholm, S., Karlsson, U.O., Wigren, C., Nylén, H. and Lindau, I. Electronic structure of ZnO(0001) studied by angle-resolved photoelectron spectroscopy. *Surface Science*, 373 (2-3), (1997), pp. 409 – 417. ISSN 0039-6028.

[101] Ranke, W. Separation of the partial s- and p-densities of valence states of ZnO from UPS-measurements. *Solid State Communications*, 19 (7), (1976), pp. 685 – 688. ISSN 0038-1098.

[102] Sawada, K., Shirotori, Y., Ozawa, K., Edamoto, K. and Nakatake, M. Valence band structure of the ZnO surface studied by angle-resolved photoemission spectroscopy. *Applied Surface Science*, 237 (1-4), (2004), pp. 343 – 347. ISSN 0169-4332. Proceedings of the Seventh International Symposium on Atomically Controlled Surfaces, Interfaces and Nanostructures.

[103] Bournel, F., Laffon, C., Parent, P. and Tourillon, G. Adsorption of some substituted ethylene molecules on Pt(111) at 95 K Part 1: NEXAFS, XPS and UPS studies. *Surface Science*, 350 (1-3), (1996), pp. 60 – 78.

[104] Göpel, W., Bauer, R. and Hansson, G. Ultraviolet photoemission studies

of chemisorption and point defect formation on ZnO nonpolar surfaces. *Surface Science*, 99 (1), (1980), pp. 138 – 156. ISSN 0039-6028.

[105] Vohs, J.M. and Barteau, M.A. Photoelectron spectroscopy of diethylzinc on the polar surfaces of zinc oxide. *Journal of Electron Spectroscopy and Related Phenomena*, 49 (1), (1989), pp. 87 – 96. ISSN 0368-2048.

[106] Klivényi, G., Kovács, I. and Solymosi, F. Thermal and photo-induced dissociation of $(C_2H_5)_2Zn$ on Rh(111) surface. *Surface Science*, 442 (1), (1999), pp. 115 – 130. ISSN 0039-6028.

[107] Thiandoume, C., Sallet, V., Triboulet, R. and Gorochov, O. Decomposition kinetics of tertiarybutanol and diethylzinc used as precursor sources for the growth of ZnO. *Journal of Crystal Growth*, 311 (5), (2009), pp. 1411 – 1415. ISSN 0022-0248.

[108] Maejima, K. and Fujita, S. Chemical vapor reactions of ZnO growth by metal-organic vapor phase epitaxy. *Journal of Crystal Growth*, 293 (2), (2006), pp. 305 – 310. ISSN 0022-0248.

[109] Bamford, C.H. and Newitt, D.M. Physical and chemical properties of organometallic compounds. Part II. The oxidation of zinc alkyls. *Journal of the Chemical Society.*, 143, (1946), pp. 688–695.

[110] Thompson, H.W. and Kelland, N.S. The oxidation of diethylzinc. *Journal of the Chemical Society*, 187, (1933), pp. 756–757. ISSN 0368-1769.

[111] Verhoeven, J. and Doveren, H.V. An XPS investigation of the interaction of CH_2, C_2H_2, C_2H_4 and C_2H_6 with a barium surface. *Surface Science*, 123 (2-3), (1982), pp. 369 – 383. ISSN 0039-6028.

[112] Dilks, A. The identification of peroxy-features at polymer surfaces by ESCA. *Journal of Polymer Science: Polymer Chemistry Edition*, 19 (6), (1981), pp. 1319–1327.

[113] Ignatyev, I.S., Xie, Y., Allen, W.D. and Schaefer, H.F. Mechanism of the C_2H_5+O_2 reaction. *The Journal of Chemical Physics*, 107 (1), (1997), pp. 141–155.

[114] Erhart, P., Klein, A. and Albe, K. First-principles study of the structure and stability of oxygen defects in zinc oxide. *Physical Review B*, 72 (8), (2005), p. 085213.

[115] McCluskey, M.D. and Jokela, S.J. Defects in ZnO. *Journal of Applied Physics*, 106 (7), (2009), p. 071101.

[116] Oba, F., Nishitani, S.R., Isotani, S., Adachi, H. and Tanaka, I. Energetics of native defects in ZnO. *Journal of Applied Physics*, 90 (2), (2001), pp. 824–828.

[117] Erhart, P., Albe, K. and Klein, A. First-principles study of intrinsic point defects in ZnO: Role of band structure, volume relaxation, and finite-size effects. *Physical Review B*, 73 (20), (2006), p. 205203.

[118] Chaisitsak, S., Sugiyama, T., Yamada, A. and Konagai, M. Cu(InGa)Se_2 Thin-film Solar Cells with High Resistivity ZnO Buffer Layers Deposited by Atomic Layer Deposition. *Japanese Journal of Applied Physics*, 38, (1999), pp. 4989–4992.

[119] Föll, H. Hyperscript Semiconductor Technology; `www.tf.uni-kiel.de/matwis/amat/semitech_en/index.html`, 2011/05/29.

[120] Garcia, F. and Tomar, M. n-CdS/p-$ZnIn_2Se_4$ thin film solar cell. *Thin Solid Films*, 69 (2), (1980), pp. 137 – 139. ISSN 0040-6090.

[121] Grimm, A., Just, J., Kieven, D., Lauermann, I., Palm, J., Neisser, A., Rissom, T. and Klenk, R. Sputtered Zn(O,S) for junction formation in chalcopyrite-based thin film solar cells. *Physica Status Solidi (RRL)*, 4 (5-6), (2010), pp. 109–111. ISSN 1862-6270.

[122] Grimm, A., Klenk, R., Klaer, J., Lauermann, I., Meeder, A., Voigt, S. and Neisser, A. $CuInS_2$-based thin film solar cells with sputtered (Zn,Mg)O buffer. *Thin Solid Films*, 518 (4), (2009), pp. 1157 – 1159. ISSN 0040-6090.

[123] Hansson, G.V. and Uhrberg, R.I.G. Photoelectron Spectroscopy of Surface States on Semiconductor Surfaces. *Surface Science Reports*, 9 (5-6), (1988), pp. 197 – 292. ISSN 0167-5729.

[124] Heinecke, H. Die metallorganische Molekularstrahlepitaxie für die Erzeugung neuartiger III-V-Halbleiterstrukturen. *Vakuum in Forschung und Praxis*, 6 (1), (1994), pp. 35–41. ISSN 1522-2454.

[125] Hüfner, S., Schmidt, S. and Reinert, F. Photoelectron Spectroscopy - An Overview. *Nuclear Instruments and Methods in Physics Research Section A: Accelerators, Spectrometers, Detectors and Associated Equipment*, 547 (1), (2005), pp. 8 – 23. ISSN 0168-9002. Proceedings of the Workshop on Hard X-ray Photoelectron Spectroscopy - HAXPES.

[126] Irvine, S. Solar Cells and Photovoltaics. In S. Kasap and P. Capper (Editors), *Springer Handbook of Electronic and Photonic Materials*, pp. 1095–1106 (Springer, 2007). ISBN 978-0-387-29185-7.

[127] Khallaf, H., Chai, G., Lupan, O., Heinrich, H., Park, S., Schulte, A. and Chow, L. Investigation of chemical bath deposition of ZnO thin films using six different complexing agents. *Journal of Physics D: Applied Physics*, 42 (13), (2009), p. 135304.

[128] Konovalov, I. Material requirements for CIS solar cells. *Thin Solid Films*, 451-452 (0), (2004), pp. 413 – 419. ISSN 0040-6090. Proceedings of Symposium D on Thin Film and Nano-Structured Materials for Photovoltaics, of the E-MRS 2003 Spring Conference.

[129] Kovacs, I. and Solymosi, F. Thermal and photoinduced dissociation of ethyl iodide to yield ethyl on a palladium(100) surface. *The Journal of Physical Chemistry*, 97 (42), (1993), pp. 11056–11063.

[130] Margaritondo, G. and Franciosi, A. Synchrotron Radiation Photoemission Spectroscopy of Semiconductor Surfaces and Interfaces. *Annual Review of Materials Science*, 14 (1), (1984), pp. 67–93.

[131] Mönch, W. Electronic Properties of Semiconductor Interfaces. In S. Kasap and P. Capper (Editors), *Springer Handbook of Electronic and Photonic Materials*, pp. 147–160 (Springer, 2007). ISBN 978-0-387-29185-7.

[132] Naghavi, N., Renou, G., Bockelee, V., Donsanti, F., Genevee, P.,

Jubault, M., Guillemoles, J. and Lincot, D. Chemical deposition methods for Cd-free buffer layers in CI(G)S solar cells: Role of window layers. *Thin Solid Films*, 519 (21), (2011), pp. 7600 – 7605. ISSN 0040-6090. Proceedings of the EMRS 2010 Spring Meeting Symposium M: Thin Film Chalcogenide Photovoltaic Materials.

[133] Neumark, G., Gong, Y. and Kuskovsky, I. Doping Aspects of Zn-Based Wide-Band-Gap Semiconductors. In S. Kasap and P. Capper (Editors), *Springer Handbook of Electronic and Photonic Materials*, pp. 843–854 (Springer, 2007). ISBN 978-0-387-29185-7.

[134] Ramaiah, S. and Kodigala. Chapter 4 - Structural Properties of I-III-VI_2 Absorbers. In S.R. Kodigala (Editor), *Cu($In_{1-x}Ga_x$)Se_2 Based Thin Film Solar*, Thin Films and Nanostructures, pp. 115 – 194 (Academic Press, 2010).

[135] Ruckh, M., Schmid, D. and Schock, H.W. Photoemission studies of the ZnO/CdS interface. *Journal of Applied Physics*, 76 (10), (1994), pp. 5945–5948.

[136] Shimizu, A., Chaisitsak, S., Sugiyama, T., Yamada, A. and Konagai, M. Zinc-based buffer layer in the Cu(InGa)Se_2 thin film solar cells. *Thin Solid Films*, 361-362 (0), (2000), pp. 193 – 197. ISSN 0040-6090.

[137] Solymosi, F. Thermal stability and reactions of CH2, CH3 and C2H5 species on the metal surfaces. *Catalysis Today*, 28 (3), (1996), pp. 193 – 203. ISSN 0920-5861. Scientific Aspects of Practical Metallic Catalysts.

[138] Turner, N.H. and Schreifels, J.A. Surface Analysis: X-ray Photoelectron Spectroscopy and Auger Electron Spectroscopy. *Analytical Chemistry*, 68 (12), (1996), pp. 309–332. ISSN 0003-2700.

[139] Veuhoff, E., Pletschen, W., Balk, P. and Lüth, H. Metalorganic CVD of GaAs in a molecular beam system. *Journal of Crystal Growth*, 55 (1), (1981), pp. 30–34. ISSN 0022-0248.

[140] Wang, J. and Isshiki, M. Wide-Bandgap II-VI Semiconductors: Growth and Properties. In S. Kasap and P. Capper (Editors), *Springer Handbook of Electronic and Photonic Materials*, pp. 325–342 (Springer, 2007). ISBN 978-0-387-29185-7.

[141] Yu, K., Spicer, W., Lindau, I., Pianetta, P. and Lin, S. UPS studies of the bonding of H_2, O_2, CO, C_2H_4 and C_2H_2 on Fe and Cu. *Surface Science*, 57 (1), (1976), pp. 157 – 183. ISSN 0039-6028.

[142] Zhou, X.L., Blass, P.M., Koel, B.E. and White, J.M. Low energy electron induced chemistry: C_2H_5Cl on Ag(111). *Surface Science*, 271 (3), (1992), pp. 452 – 467. ISSN 0039-6028.

Danksagung

Zum Abschluss möchte ich mich bei allen bedanken, die in den letzten drei Jahren (und/oder davor) zu der erfolgreichen Fertigstellung dieser Dissertation beigetragen haben.

Angefangen wird bei **Prof. Dr. Christian Pettenkofer**, nicht nur dafür, dass er mir die Möglichkeit gegeben hat meine Doktorarbeit am HZB anzufertigen und damit für ein geregeltes monatliches Auskommen gesorgt hat, sondern auch für die entspannte Arbeitsatmosphäre und seine einzigartige Doktorandenbetreuung. Danke, dass du mir jederzeit mit Rat und Tat zur Seite gestanden hast, für die freien Entfaltungsmöglichkeiten und die großartigen Dienstreisen (mit Ausnahme des fränkischen *Tal des Todes*...). Neben der Physik habe sehr viel von dir für das Leben gelernt. So weiß ich beispielsweise jetzt, wie man Probleme mit kroatischen Zuhältern löst oder wo man als Vegetarier die besten Hax'n während einer DPG Tagung bekommen kann. Danke!

Bei **Prof. Dr. Bernd Rech** möchte ich mich dafür bedanken, dass er sich - obwohl von Arbeitsmangel bei dir wohl keine Rede sein kann - sofort bereit erklärt hat die universitäre Betreuung an der Technischen Universität Berlin zu übernehmen und mir damit mein lang erarbeitetes Ziel vom Dr.-Ing. ermöglicht.

Nicht nur dafür, dass er sich bereit erklärt hat als externer Gutachter dieser Arbeit zu wirken, möchte ich mich bei **Prof. Dr. Wolfgang Jäger** bedanken. Sie haben mir viel ermöglicht in den letzten Jahren und wahrscheinlich hätte ich diese Dissertation nie geschrieben, wenn Sie nicht stets soviel Interesse an Ihren (ehemaligen) Studenten zeigen würden.

Meinem Leidensgenossen in Sachen Doktorarbeit, **Dr. Andreas Hofmann**, gilt ganz besonderer Dank. Mit deinem großartigen Sinn für Humor haben die Arbeiten im Labor und im Büro sehr viel Spaß gemacht. Das wird mir fehlen, wenn es irgendwann nicht mehr so ist. Ohne dich wäre ich in den letzten drei Jahren sicherlich verrückt geworden. Oder bin ich es gerade deswegen geworden? Wie dem auch sei: Danke, Alter!

Bei **Dr. Carsten Lehmann** und **Dr. Wolfram Calvet** möchte ich mich für die vielen (nicht) wissenschaftlichen Diskussionen bedanken, die meist zum tiefergehenden Verständnis der Materie geführt haben. Eure Unterstützung am Integrierten System bzw. der SoLiAS haben am Erfolg der Experimente maßgeblich beigetragen.
Gleiches gilt für **Wolfgang Bremsteller** und **Herbert Sehnert**, deren Bastelkünste das wartungsintensive technische Equipment am Leben gehalten haben. MacGyver würde den Hut ziehen! Außerdem danke ich euch beiden für das angenehme Arbeitsklima im Büro und im Labor. Den beiden ehemaligen Arbeitsgruppenmitgliedern **Dr. Patrick Hoffmann** und **Julius Kühn** möchte ich für die anfängliche Unterstützung beim Aufbau des ALD Systems und dessen Inbetriebnahme danken.
Für die schnelle und unkomplizierte Herstellung der $ZnIn_2Se_4$ Referenzkristalle möchte ich mich bei **Prof. Dr. Michael Binnewies** und seiner Arbeitsgruppe am Institut für Anorganische Chemie der Leibniz Universität Hannover bedanken. **Carola Klimm** danke ich für die Unterstützung bei den SEM Untersuchungen meiner ZnO Schichten. Besonderer Dank gilt **Dr. Christiane Stephan** für die GI-XRD Messungen, ihr unglaubliches Wissen was alles im und rund um das HZB angeht und für die lustige Zeit abseits der Arbeit.
Für ihren Beitrag an der angenehmen Arbeitsatmosphäre danke ich des Weiteren allen restlichen und ehemaligen Mitarbeitern der Arbeitsgruppe **E-I1** (formerly known as **E-I4**, bzw. **SE6**) und den Kollegen der CISSY-Gruppe, **Dr. Iver Lauermann**, **Alexander Grimm** und **Britta Höpfner**. Besonders **Dr. Benjamin Johnson** danke ich für unsere Kaffeepausen während, und für das Bier zu vernünftiger Musik nach der Arbeit. The fiese Ämi rocks!
Danke allen **HZB Doktoranden**, mit denen ich in den letzten drei Jahren viel Spaß gehabt habe und von denen einige gute Freunde geworden sind.
Dr. Claudia Klingler danke ich für die ausführlichen Korrekturen dieser Dissertation und bei **Thomas Gaertner** bedanke ich mich für die vielen Stunden an den Kickertischen im Berliner Nachtleben, den vielen Konzerten während der letzten Jahre und - vor allem - für seine Steuergelder.
Meiner **Familie** danke ich für das gute Genmaterial und für alles, was Sie mir in den letzten 29 Jahren mit auf den Weg gegeben haben. Danke für eure ständige Unterstützung auf meinem Werdegang.
Und da das Beste immer zum Schluß kommt: Der größte Dank gilt vor allem **Teresa** für ihre ständige Unterstützung, dafür dass sie mir während der letzten Monate so viel vom Hals gehalten hat und für noch viel, viel mehr. Danke!

List of Publications

Publications in Journals

E. Janocha and C. Pettenkofer
ALD of ZnO using diethylzinc as metal-precursor and oxygen as oxidizing agent
Applied Surface Science 257 (2011), 10031 - 10035

Poster Presentations

E. Janocha and C. Pettenkofer, *Atomic Layer Deposition of TCO window layers for chalcopyrite solar cells*, 481. WE-Heraeus-Seminar: Energy Materials Research by Neutrons and Synchrotron Radiation, Bad Honnef, 09.05.2011 - 11.05.2011

E. Janocha, A. Hofmann, C. Pettenkofer, *Non-destructive depth profiling of the $CuInSe_2$ - ZnO interface by SR-PES*, Joint Users' Meeting 2010, BESSY, Berlin, 09.12.2010 - 10.12.2010

Oral Presentations

E. Janocha and C. Pettenkofer, *Investigation of the initial interface formation between $CuInSe_2$ (112) and ZnO grown by ALD*, DPG Frühjahrstagung, Dresden, 13.03.2011 - 18.03.2011

E. Janocha and C. Pettenkofer, *Initial Growth and Interface Reactions of Epitaxial ZnO Layers Grown by Atomic Layer Deposition*, MRS Fall Meeting, Boston, MA, USA, 28.11.2010 - 04.12.2010

E. Janocha and C. Pettenkofer, *In situ PES analysis of ultra-thin ZnO layers grown by atomic layer deposition (ALD)*, DPG Frühjahrstagung, Regensburg, 21.03.2010 - 26.03.2010

E. Janocha and C. Pettenkofer, *Growth of ALD-ZnO on Si(111):H and initial growth on $CuInS_2$ (112)*, CRG-Klausurtagung, Bischofsmühle, 12.02.2010 - 14.02.2010

C. Lehmann, E. Janocha, A- Hofmann, A. Dombrowa, C. Pettenkofer, *The ZnO - CIS interface*, CRG-Klausurtagung, Bischofsmühle, 12.02.2010 - 14.02.2010

E. Janocha and C. Pettenkofer, *Current status of ALD assembly*, CRG-Klausurtagung, Bischofsmühle, 30.01.209 - 01.02.2009